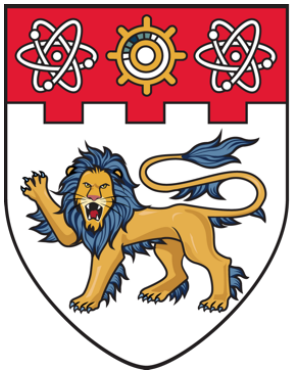

NANYANG TECHNOLOGICAL UNIVERSITY
SINGAPORE

Development of Molecular Catalysts for H_2 Evolution and Modified Copper Catalyst for CO_2 Reduction

Ho Xian Liang

SCHOOL OF PHYSICAL AND MATHEMATICAL SCIENCES

2020

Development of Molecular catalysts for H_2 Evolution and Modified Copper catalyst for CO_2 Reduction

Ho Xian Liang

SCHOOL OF PHYSICAL AND MATHEMATICAL SCIENCES

A thesis submitted to the Nanyang Technological University in partial fulfilment of the requirement for the degree of Doctor of Philosophy

2020

Statement of Originality

I hereby certify that the work embodied in this thesis is the result of original research done by me except where otherwise stated in this thesis. The thesis work has not been submitted for a degree or professional qualification to any other university or institution. I declare that this thesis is written by myself and is free of plagiarism and of sufficient grammatical clarity to be examined. I confirm that the investigations were conducted in accord with the ethics policies and integrity standards of Nanyang Technological University and that the research data are presented honestly and without prejudice.

12/05/2020

. . . . . .

Date

. . . . . .

Ho Xian Liang

Supervisor Declaration Statement

I have reviewed the content and presentation style of this thesis and declare it of sufficient grammatical clarity to be examined. To the best of my knowledge, the thesis is free of plagiarism and the research and writing are those of the candidate's except as acknowledged in the Author Attribution Statement. I confirm that the investigations were conducted in accord with the ethics policies and integrity standards of Nanyang Technological University and that the research data are presented honestly and without prejudice.

12/05/2020

. . . . . .

Date

. . . . . .

Assoc Prof. Richard D. Webster

Authorship Attribution Statement

This thesis contains material from 2 papers published in the following peer-reviewed journals in which I am listed as an author.

Chapter 3 is published as Ho, X. L.; Das, S. P.; Ng, L. K.-S.; Ng, A. Y. R.; Ganguly, R.; Soo, H. S., Cobalt Complex of a Tetraamido Macrocyclic Ligand as a Precursor for Electrocatalytic Hydrogen Evolution. *Organometallics*. **2019**, *38*, 1397–1406 DOI: 10.1021/acs.organomet.9b00032.

The contributions of the co-authors are as follows:

- Asst. Prof. Soo Han Sen provided the initial project direction and edited the completed manuscript drafts.
- I prepared the manuscript and revised it together with Asst. Prof. Siva Prasad Das.
- I designed the study together with Asst. Prof. Soo Han Sen and performed all the laboratory work at the School of Materials Science and Engineering (MSE) and School of Physical and Mathematical Sciences (SPMS).
- I analysed the data obtained from the experiments.
- I synthesised all the molecular compounds in the paper unless stated otherwise.
- I did all the molecular compounds characterisation and calculate the Faradaic efficiency of the catalyst.
- Dr. Ng Kia Shuen Leonard and Mr. Andrew Ng Yun Ru assisted in material characterisation.
- Dr. Rakesh Ganguly assisted in resolving the single crystal structure of the complex.

Chapter 4 is published as Ho, X. L.; Shao, H.; Ng, Y. Y.; Ganguly, R.; Lu, Y.; Soo, H. S., Visible Light Driven Hydrogen Evolution by Molecular Nickel Catalysts with Time-Resolved Spectroscopic and DFT Insights. Inorg. Chem. 2019, 58, 1469-1480. DOI: 10.1021/acs.inorgchem.8b03003.

The contributions of the co-authors are as follows:

- Asst. Prof. Soo Han Sen provided the initial project direction and edited the completed manuscript drafts.
- I prepared the manuscript and revised it with the help of Dr. Shao Haiyan.
- I designed the study together with Asst. Prof. Soo Han Sen and performed all the laboratory experiments at MSE and SPMS.
- I also analysed all the data obtained from the experiments.
- All the synthesis, characterisation and kinetics were carried out by me unless stated otherwise.
- Dr. Lu Yunpeng assisted in the density functional theory (DFT) calculation to provide mechanistic insight to the reaction mechanism.
- Dr. Ng Yik Yie helped with transient absorption measurement for the mechanistic studies of the complex.
- Dr. Rakesh Ganguly assisted in resolving the single crystal structure of the complex.

12/05/2020

. . . .

Date

. . . .

Ho Xian Liang

Abstract

In the first part of the thesis, a series of first row transition metal complexes have been synthesized in order to study their mechanism and efficiency as a H_2 evolution catalyst. The H_2 produced can served as an alternative clean fuel to tackle the issue on climate change. A comprehensive characterisation of the electrochemical and spectroscopic properties of these complexes has been performed. The efficiency and the mechanism of these materials and complexes have been studied.

In Chapter 3, the effects of the first coordination sphere on H_2 evolution was explored. A new Co and Ni tetraamido macrocyclic ligand (TAML) complexes were synthesised and their reactivity for electrocatalytic proton reduction were studied. The metal complexes have been extensively characterized with various spectroscopic techniques. The Co TAML complex appeared to be active for electrocatalytic H_2 evolution initially. However, detailed mechanistic studies revealed that Co nanomaterials were responsible for the catalysis.

In Chapter 4, the effect of the second coordination sphere modification on H_2 evolution activity was explored. An active Ni salicylaldimine catalyst was synthesized and found to be able to incorporate into a molecular photocatalytic H_2 evolution system with $[Ir^{III}(ppy)_2(dtbbpy)(]PF_6)$ (ppy = 2-phenylpyridinato; dtbbpy = 4,4'-di-*tert*-butyl-2,2'-bipyridine, $[Ir]^+$) as a light-harvester and triethylamine (TEA) as a sacrificial electron donor and reductive quencher. This new Ni complex possess a pair of peripheral ether arms in the second coordination sphere of the molecule. Various spectroscopic techniques such as nanosecond transient absorption spectroscopy (TAS), transient emission spectroscopy (TES) and, electron paramagnetic resonance (EPR), supported by intermediate isolation studies and density functional theory (DFT) calculations suggest the possible influence of balancing ligand redox noninnocence and second coordination sphere effects to effect H_2 evolution activity.

In the second part of the thesis, the surface modification on oxide-derived copper (OD-Cu) and its influence on the products distribution of CO_2 reduction on Cu were investigated. In Chapter 6 of the thesis, it was found that the majority of the crystal facets in the polycrystalline OD-Cu can dictate the major products formed and can greatly reduce the overpotentials for CO_2 reduction.

Acknowledgements

I would like to express my gratitude to my supervisors, Prof. Richard D. Webster and Dr. Soo Han Sen for their continuous guidance and support in the last four years. Thank you, Prof. Xu Rong and Prof. Leong Weng Kee, for being my Thesis Advisory Committee (TAC) members. I would like to thank Dr. Malcolm E. Tessensohn, Dr. Shao Haiyan, Dr. Siva Prasad Das, Dr. Lim Jia Hui and Dr. Sarifuddin Gazi for being great mentors and sources of inspiration during this journey.

Thank you to all my colleagues, Dr. Malcolm E. Tessensohn, Ms. Maja Budanovic, Ms. Tam Si Man, Mr. Arnold Subrata, Mr. Shi Rongsheng Raymond, Dr. Gan Sherli, Ms. Nur Farhanah Binte Rosli, Ms. Maric Tijana, Ms. Chia Hui Ling, Ms. Soh Yan Ni Annie, Dr. Adriano Ambrosi, Mr. Muhammad Shafique Bin Hamid, Dr. Shao Haiyan, Dr. Lim Jia Hui, Dr. Leonard Ng, Dr. Hong Zonghan, Dr. Wang Jing Yi, Dr. Dokic Milos, Dr. Ng Yik Yie, Dr. Kee Jun Wei, Dr. Chin Kek Foo, Mr. Dwaipayan Ghosh, Mr. Andrew Ng, for always being there to lend their helping hands and provide support during this period of time. I would also like to thank all the undergraduate and exchange students, Ms. Belvy Bay, Mr. Matthew Hutchesen, Mr. Samuel Lee, Wei Loong, Ms. Seah Hui Ling, Mr. Desmond Chang, Ms. Wu Shuxin, and Mr. Wayne Yeo, for the help that they extended. The many valuable lessons that I have learnt from my collaborators, Dr. Lu Yunpeng for the DFT calculations, Dr. Ganguly for all the single crystal XRD data, and Dr. Sheng Yuan for detection of gaseous products from CO_2 reduction, are also greatly appreciated. I am grateful for the support from the Solar Fuels Laboratory at NTU. Special thanks to Dr. Sun Libo and Mr. Tay Yingfan for the help at Solar Fuels Laboratory in NTU.

I would also like to express my gratitude to all the staffs from SPMS and CBC, from the Central Equipment Lab, Teaching Lab to the graduate office an finance department for the assistance they provided with regards to the various facilities and other administrative matters during the four years. Specially thanks to Susan and Clemence for the many helps they extended in handling purchases. Finally, I would like to thank my family and friends for the encouragement during this time.

\

Table of Contents

List of Abbreviations

$[(DBF)H]NTf_2$	Dibutylformamidium bis(trifluromethanesulfonyl)amide
abt	2-aminobenzenethiolate
bpy	bipyridine
Bu_4NPF_6	Tetrabutylammonium Hexafluorophosphate
CB	Conduction Band
CPE	Controlled Potential Electrolysis
CV	Cyclic Voltammogram
dap	2,9-di(p-anisyl)-1,10-phenanthroline
DAPy	2,3-diaminopyridine
DCM	Dichloromethane
DFT	Density Functional Theory
DI	Deionised
DLS	Dynamic Light Scattering
DMF	Dimethylformamide
DMSO	Dimethyl sulfoxide
dtppy	4,4'-di-tert-butyl-2,2'-bipyridine
EDS	Energy Dispersive X-ray Spectroscopy
en	Ethylenediamine
EPR	Electron Paramagnetic Resonance

Equiv	Equivalent
ESI	Electrospray Ionisation
Et_4N	Tetraethylammonium
EtOH	Ethanol
Fc^+/Fc	Ferrocenium/Ferrocene redox couple
FESEM	Field Emission Scanning Electron Microscopy
FID	Flame Ionisation Detector
GC	Gas Chromatography
h	Hour
HAABF-STEM	High-angle Annular Bright-field-scanning Transmission Electron Microscopy
HMDS	Hexamethyldisilazide
HOMO	Highest Occupied Molecular Orbital
HOTf	Triflic Acid
HRMS	High-resolution Mass Spectrometry
HRTEM	High-Resolution Electron Microscopy
LCMS	Liquid Chromatography Mass Spectrometry
LMCT	Ligand-to-metal Charge Transfer
LUMO	Lowest Unoccupied Molecular Orbital
M	Number of moles per liter

m/z	Mass-to-charge ratio
MBD	2-mercaptobenzimidazole
MBT	2-mercaptobenthiazole
MHz	Megahertz
MJ/L	Megajoules per liter
MO	Molecular Orbital
mV s^{-1}	Millivolt per second
n-Bu	n-butyl
NHE	Normal Hydrogen Electrode
NMR	Nuclear Magnetic Resonance
NW	Nanowire
OAc	Acetate
OD	Optical Density
OD-Cu	Oxide-derived Copper
ORTEP	Oak Ridge Thermal Ellipsoid Plot
PGMs	Platinum-group metals
Ph	Phenyl
ppm	parts per million
ppy	2-phenylpyridinato
PyS	Pyrindine-2-thionato

RHE	Reversible Hydrogen Electrode
RVC	Reticulated Vitreous Carbon
Sal	Salicylaldehyde
Saloph	*N,N'*-disalicylidene-*o*-phenylenediaminate
SCE	Saturated Calomel Electrode
SHE	Standard Hydrogen Electrode
SOMO	Singly Occupied Molecular Orbital
STEM	Scanning Transmission Electron Microscopy
TAML	Tetraamido Macrocyclic Ligand
TAS	Transient Absorption Spectroscopy
TCD	Thermal Conductivity Detector
TEA	Triethylamine
TEM	Transmission Electron Microscopy
TEOA	Triethanolamine
TES	Transient Emission Spectroscopy
TFA	Trifluoroacetic Acid
THF	Tetrahydrofuran
TMD	Transition Metal Dichalcogenides
TMPyP	Tetrakis(1-methy-pyridinium-4-yl) porphyrin
TOF	Turnover Frequency

TON	Turnover Number
UV	Ultraviolet
V	Volt
VB	Valence Band
XPS	X-ray Photoelectron Spectroscopy
XRD	X-ray Diffraction

Chapter 1

Introduction

1.1 Background Information

Anthropogenic activities have led to an increase in atmospheric CO_2 concentrations since the Industrial Revolution.[1] The concentration of CO_2 in the air has since reached an unprecedented level of 400 ppm and shows no sign of slowing down.[2] CO_2 is a greenhouse gas that is capable of absorbing electromagnetic radiation within the thermal infrared region.[3] As the concentration of CO_2 in the atmosphere increases, it acts like a giant blanket that traps heat within the Earth, leading to an increase in global temperature. As the Earth becomes warmer, many undesirable consequences will result. For instance, the polar ice caps will start to melt, leading to rising sea levels, which could cause floods in low-lying countries. Production of crops will also be disrupted due to the extreme weather patterns, changes in the global temperature and amounts of precipitation.[4] The implications of global warming are vast, covering areas from energy to food security, and should be mitigated.

There are various possible solutions that are thought to be able to arrest this rise in global temperature. Notably, reducing and ultimately eliminating the use of traditional fossil fuels by replacing them with renewable energy resources has been at the forefront in shaping government policies around the world to mitigate the effects of global climate change. One of the most promising sources of energy available is the solar energy. The Sun emits about 4.3×10^{20} J of energy to the Earth's surface in an hour, surpassing the annual energy expenditure of fossil fuels from the entire world at 4.1×10^{20} J, with visible light forming the bulk of the light that reaches the Earth's surface.[5]

However, in order to fully utilize the potential of solar power, the problems associated with energy storage must be solved to make it a reliable source of energy. Currently, solar energy is mainly harnessed by silicon-based photovoltaic cells that convert it directly into electrical energy for immediate use. However, due to the intermittent nature of sunlight, such direct conversion to electricity can never match the demand of energy across a day.

1.1.1. Artificial Photosynthesis

A hybrid artificial photosynthetic system aims to imitate the natural one where plants convert light into chemical energy. Similar to natural photosynthesis, the artificial system consists of three different components: a light harvester, and two molecular cocatalysts as illustrated in figure 1.1. The process begins when the semiconductor absorbs photons emitted from the Sun causing the electrons in the VB of the semiconductor to be excited and promoted to the CB leaving behind holes. This creates a charge separation between the electrons and holes. The excited electrons are then transported to the reduction molecular cocatalyst to catalyse reactions such as H_2 evolution or CO_2 reduction, while the oxidation cocatalyst draws electrons back into the holes of the VB by catalysing oxidation reactions.[6] This relay system reduces the recombination of charges and allows both oxidation and reduction reactions to occur at a higher probability. Such process provides us with an alternative way to store solar energy into chemical bond. In this thesis, the focus will be on the development of the molecular catalysts for the reduction half reaction.

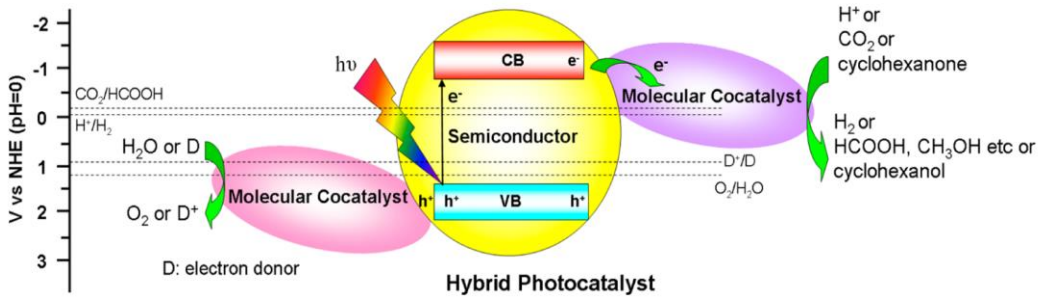

Figure 1.1. Proposed artificial photosynthetic unit. Adapted with permission from *Acc. Chem. Res*. **2013**, 46, 2355-2364. Copyright 2013 American Chemical Society.[7]

H_2 when combined with O_2, releases energy and H_2O as the only reaction by-product, resulting in zero carbon emission. It also possesses the highest specific energy per kilogram[8] compared to other fuels as shown in figure 1.2. This also makes H_2 a good choice as a fuel. For example, when used as a fuel in transportation, it does not increase the load

carried by cars. Materials such as metal-organic frameworks[9] and metal hydrides[10] have also shown potential in tackling the problem of low specific energy density (MJ/L) of H_2. As the technology advances, the prices of cars running on H_2 as fuel are projected to decrease.[11] Therefore, H_2 has been proposed as one of the most promising clean fuels in the near future.[12] However, the current production of H_2 is neither clean nor pollutant-free. Most of the H_2 used today is produced from natural gas by steam reforming which generates CO_2 as one of the by-products at high temperature. This method accounts for almost 50% of the world's supply of H_2.[13] It is an energy intensive process that requires more fossil fuels to be burnt in order to meet the world's raising energy demands.

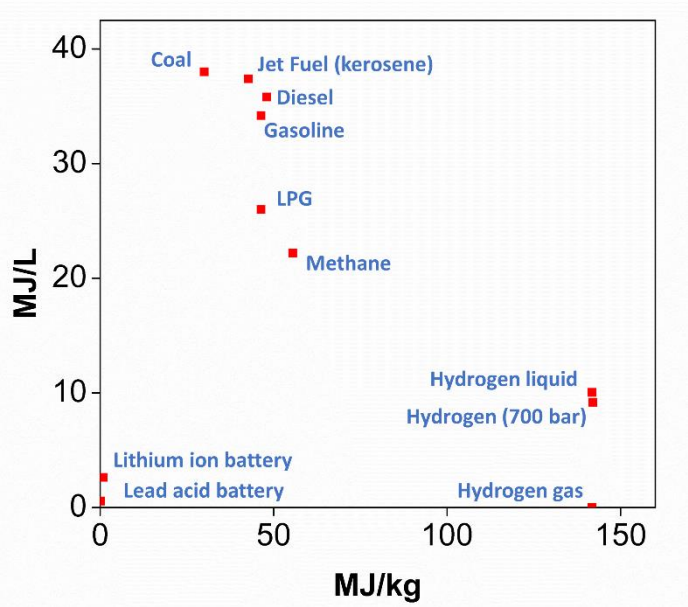

Figure 1.2. A plot of the energy densities of commonly used fuels.

In nature, H_2 is produced by many different microbes under anaerobic conditions. The three types of hydrogenases are the nickel-iron [NiFe] hydrogenase, the iron-iron [FeFe] hydrogenase, and the iron [Fe] only hydrogenase.[14] These hydrogenases have been reported to be able to produce up to 9000 moles of H_2 per mole of catalyst per second.[15] Notably, these catalysts consist only of cheap and earth-abundant metals as the core surrounded with organic ligands and proteins in the secondary coordination sphere.

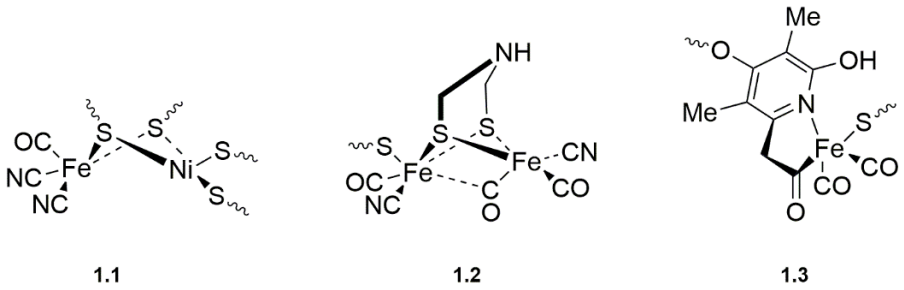

Figure 1.3. Proposed structure of the active sites of [NiFe], [FeFe] and [Fe] only hydrogenase.[14]

Inspired by these naturally occurring efficient H_2 evolution catalysts that use only earth-abundant metals, scientists have since conducted extensive studies to elucidate the mechanisms of these hydrogenases to replace the expensive platinum catalyst in the future.[16] As an alternative to the artificial photosynthesis system, the reduction of CO_2 using electricity also has a great prospect in attaining a sustainable global energy technology by converting the CO_2 generated from industrial emissions to fuels.

1.1.2. Electrocatalytic CO_2 Reduction

Electrocatalytic CO_2 reduction is a process that is compatible with many renewables such as wind and sunlight.[17] By harnessing these renewable energies to convert CO_2 to clean fuels and chemical precursors, it is potentially able to reduce the amount of CO_2 emitted through flue gas from the industry into the environment and, simultaneously, generate fuels (Figure 1.3). However, CO_2 is a very thermodynamic stable carbon compounds and hence, the direct electroreduction of CO_2 to fuels is very challenging.[18]

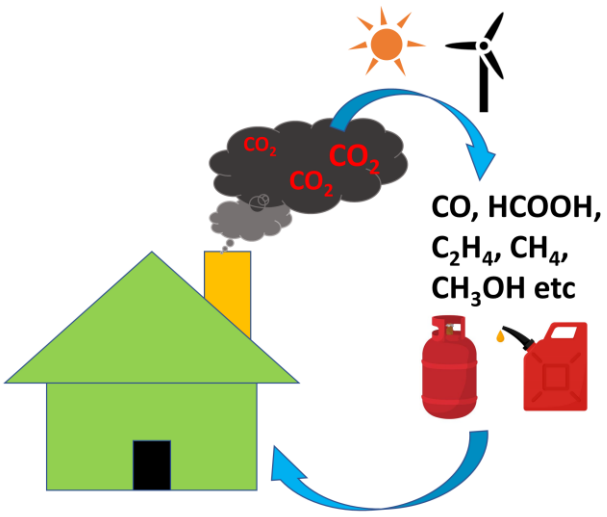

Figure 1.3. General Scheme for electrocatalytic conversion of CO_2.

Many catalysts, from homogenous to heterogenous, have been developed and studied in the past few years in the hope of achieving an industrial application for this process. These includes organometallic based complexes,[19] metallic electrodes,[20] metal chalcogenides,[17] carbon- based materials[21] and metal- organic frameworks.[22] However, the current catalysts often suffer from low catalytic rates, high overpotentials, low stability, low TON, use of organic solvents and/or low selectivity of products.[23] Furthermore, the reduction of CO_2 beyond 2 electrons is usually very challenging. Therefore, the current technology for the reduction of CO_2 to hydrocarbons is still not efficient and selective enough for large- scale industrial applications.

1.2 Objectives

There are two major parts to this thesis. In the first part, the objective of the project is to develop inexpensive, molecular, first-row transition metal catalysts that can replace expensive platinum metal as the conventional H_2 reduction catalyst. It can also be an alternative way to produce H_2 cleanly as compared to the polluting steam reforming process used currently. These catalysts can serve as the H_2 evolution materials in an artificial

photosynthetic system in order to store the energy from sunlight into chemical bonds. We first studied the functionality of the first coordination spheres of the catalysts and how they affect the evolution of H_2. Next, we explored the effect of the non-amino group second coordination sphere and the role it plays in assisting H_2 evolution.

In the second part of the thesis, we looked at the development of a catalyst for the electrochemical reduction of CO_2 into short-chain hydrocarbons that can be used as fuels. Since Cu was found to be able to produce various hydrocarbons via electrocatalytic CO_2 reduction, we seek to understand the effects of surface modification on Cu electrodes on the final distribution of products after reduction.

1.3 Dissertation Overview

This thesis describes the development of Earth abundant, first-row transition metal-based catalysts for H_2 evolution and CO_2 reduction.

Chapter 1 highlights the problems that this research aims to tackle, together with the research objectives.

Chapter 2 reviews published work on several topics, including (i) artificial photosynthesis, (ii) H_2 evolution catalysts in nature, and (iii) molecular catalysts, both biomimetic and non-biomimetic, for H_2 evolution. From this review, the problem statement and hypothesis are generated and subsequently, the project aims to address these questions.

Chapter 3 discusses the synthesis of various first-row transition metal complexes with the TAML. The reactivities of the complexes as catalysts for H_2 production are explored. It was found that only Co (TAML) exhibited H_2 evolution activity. Further studies showed that Co metal nanoparticles were electrodeposited on the working glassy carbon electrode during electrolysis and hence, act as the active catalyst for H_2 evolution. This work explores the effect of the first-row coordination sphere and its effect on H_2 evolution activity.

Chapter 4 discusses the synthesis and characterization of a new Ni^{II} complex consisting of a salen-type ligand. The reactivity of the complex as a catalyst for H_2 production in water was explored and the mechanism was probed using TAS and TES. DFT calculations suggest that the peripheral ether arms on the second coordination sphere are able to improve the catalytic activity for H_2 evolution by facilitating proton relay, similar to the mechanism found among [FeFe] hydrogenases in nature.

Chapter 5 reviews published work on several topics, including (i) the electrocatalytic CO_2 reduction, (ii) the different materials used, (iii) Cu metal, and (iv) the reaction mechanism. From this review, the problem statement and hypothesis are generated and subsequently, the project aims to address these questions.

Chapter 6 discusses the modification and characterisation of Cu foil and how it affects the product distribution of electrocatalytic CO_2 reduction reaction. The modification of the Cu surface was achieved through the combination of electrolysis and chemical oxidation.

Chapter 7 recaps the findings from the previous chapters and the new understanding on the development of molecular catalysts for H_2 evolution. A thorough review of the overall work in the context of the thesis hypothesis is given. This chapter also describes the future work on our comprehension on development of CO_2 reduction catalyst.

1.4 Findings and Outcomes/Originality

This research led to several outcomes by:

1. Assessing the effects of the primary coordination sphere of the catalyst on H_2 evolution by characterisation and quantification of the H_2 formed using GC.

2. Characterizing the photophysical properties of salen-type ligand Ni complex in an iridium complex/TEA photosensitiser system using nanosecond TAS to study the mechanism.
3. Assessing a possible formation of ligand-based reduction in the reaction mechanism for H_2 evolution using DFT calculations and spectroscopy using a salen-type ligand Ni complex.
4. Assessing the effects of secondary coordination sphere of the catalyst on H_2 evolution reactivity.
5. Modification of Cu surface via oxidation for CO_2 reduction to hydrocarbons.
6. Assessing the effect of surface modification of Cu on the product distribution for CO_2 reduction.

The following findings will contribute to the search for an effective molecular photocatalytic H_2 evolution catalyst that can be incorporated into an artificial photosynthesis system for generation of green energy. The modification of Cu surface also provides an insight towards the search for a selective CO_2 reduction catalyst for industrial application.

References

(1) Hansen, J. E.; Lacis, A. A. *Nature* **1990**, *346*, 713-719.

(2) Wenzel, S.; Cox, P. M.; Eyring, V.; Friedlingstein, P. *Nature* **2016**, *538*, 499-501.

(3) Hansen, J.; Lacis, A.; Prather, M. *J. Geophys. Res.* **1989**, *94*, 16417-16421.

(4) Hughes, L. *Trends Ecol. Evol.* **2000**, *15*, 56-61.

(5) Lewis, N. S.; Nocera, D. G. *Proc. Natl. Acad. Sci. U.S.A.* **2006**, *103*, 15729-15735.

(6) Tran, P. D.; Wong, L. H.; Barber, J.; Loo, J. S. C. *Energy Environ. Sci.* **2012**, *5*, 5902-5918.

(7) Wen, F.; Li, C. *Acc. Chem. Res.* **2013**, *46*, 2355-2364.

(8) Campen, A.; Mondal, K.; Wiltowski, T. *Int. J. Hydrog. Energy* **2008**, *33*, 332-339.

(9) Suh, M. P.; Park, H. J.; Prasad, T. K.; Lim, D. W. *Chem. Rev.* **2012**, *112*, 782-835.

(10) Sakintuna, B.; Lamaridarkrim, F.; Hirscher, M. *Int. J. Hydrog. Energy* **2007**, *32*, 1121-1140.

(11) Samuelsen, S. *IEEE Spectrum* **2017**, *54*, 38-43.

(12) Yu, K. M.; Tong, W.; West, A.; Cheung, K.; Li, T.; Smith, G.; Guo, Y.; Tsang, S. C. *Nat. Commun.* **2012**, *3*, 1230.

(13) Haryanto, A.; Fernando, S.; Murali, N.; Adhikari, S. *Energy Fuels* **2015**, *19*, 2098-2106.

(14) Tard, C.; Pickett, C. J. *Chem. Rev.* **2009**, *109*, 2245-2274.

(15) Helm, M. L.; Stewart, M. P.; Bullock, R. M.; DuBois, M. R.; DuBois, D. L. *Science* **2011**, *333*, 863-866.

(16) Du, P.; Eisenberg, R. *Energy Environ. Sci.* **2012**, *5*, 6012-6021.

(17) Zhang, W.; Hu, Y.; Ma, L.; Zhu, G.; Wang, Y.; Xue, X.; Chen, R.; Yang, S.; Jin, Z. *Adv. Sci.* **2018**, *5*, 1700275.

(18) Zhang, L.; Zhao, Z. J.; Gong, J. *Angew. Chem. Int. Ed.* **2017**, *56*, 11326-11353.

(19) Windle, C. D.; Perutz, R. N. *Coord. Chem. Rev.* **2012**, *256*, 2562-2570.

(20) Lim, R. J.; Xie, M.; Sk, M. A.; Lee, J.-M.; Fisher, A.; Wang, X.; Lim, K. H. *Catal. Today* **2014**, *233*, 169-180.

(21) Vasileff, A.; Zheng, Y.; Qiao, S. Z. *Adv. Energy Mater.* **2017**, *7*, 1700759.

(22) Al-Rowaili, F. N.; Jamal, A.; Ba Shammakh, M. S.; Rana, A. *ACS Sustain. Chem. Eng.* **2018**, *6*, 15895-15914.

(23) Grills, D. C.; Matsubara, Y.; Kuwahara, Y.; Golisz, S. R.; Kurtz, D. A.; Mello, B. A. *J. Phys. Chem. Lett.* **2014**, *5*, 2033-2038.

Chapter 2

Literature Review

2.1 Overview

Solar to chemical energy conversion offers an attractive solution to the current energy and climate woes that the world is facing today. This process has the potential to eliminate the problems associated with energy storage from renewable energy resources and allow solar energy to take the centre stage in energy production.[1] Nature has provided a long-standing model to convert solar to chemical energy. The plant converts atmospheric CO_2 into sugar as food by harnessing solar energy in the process known as natural photosynthesis. In the microscopic scale, this process, is known as the 'Z-scheme' as shown in Figure 2.1. It consists of two related systems, photosystem I and photosystem II. These systems are connected in a series of electron transfer relays and the processes that occurs can be classified into three major steps: (1) the light harvesting step, (2) the electron transfer step, and (3) the fuel production step. In the light harvesting step, the light harvesters, P680 and P700, absorb sunlight to form the excited P680* and P700*. These excited light harvesters then transfer the electrons to the catalysts for the reduction of CO_2 or protons at one end, and transfer holes for the water oxidation reaction at the manganese calcium oxide cluster at the other end. This electron transfer relay system employed by the photosystems creates a charge separation that prevents charge recombination, and thus improves the efficiency of the system.[2]

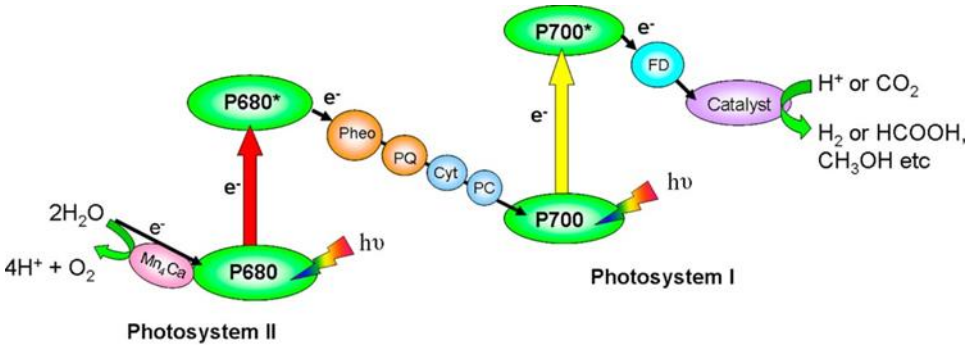

Figure 2.1. Z-scheme of natural photosynthesis. Adapted with permission from *Acc. Chem. Res*. **2013**, 46, 2355-2364. Copyright 2013 American Chemical Society.[2]

With this knowledge of nature's photosynthetic process, we intend to recreate it artificially to store solar energy in the form of chemical bonds that will enable us to utilise it whenever required. The artificial photosynthesis system was proposed and described in Chapter 1. In the context of artificial photosynthesis, the water splitting reaction provides a path towards a carbon neutral process for energy storage and usage. H_2, as discussed in Chapter 1, is one of the more promising candidates to replace the current carbon-based fuels. It combines with O_2 to release energy while producing H_2O as the only reaction by-product thus achieving zero carbon emission. This thesis will focus on the development of a molecular catalyst for the reduction of protons to H_2 that can be incorporated into the artificial photosynthesis system for future water splitting reactions.

The evolution of H_2 is a two-electron process that either involve two hydrogen atoms or the presence of a proton source.[3] Currently, the performance of Pt on H_2 evolution is still unrivalled by other metals, their oxides and complexes. Pt shows low overpotential, long durability, and high TOF in proton reduction.[4] However, Pt is a precious metal that is costly and in low abundance in the Earth's crust.

Fortunately, in nature, microorganisms metabolise H_2 by expressing hydrogenases, a type of metalloenzyme, that plays an essential role in this biological process.[5] These enzymes have garnered much interest recently in the search for a catalyst to replace the expensive Pt for H_2 production. They were found to catalyse proton reduction at a potential close to -0.40 V vs SHE and can produce up to 10 000 moles of H_2 per mole of catalyst per second, a feat comparable to that of the Pt catalyst. However, they are highly sensitive to O_2 and prone to degradation at ambient conditions. Furthermore, this macromolecule has a low active metal center density due to its sheer size, rendering them difficult to replace Pt in their original form currently.[5] Mechanistic and structural studies of these enzymes have thus been carried out in order to understand the reasons behind such high reactivity of

these enzymes so as to artificially replicate them through careful design of a new molecular catalysts of lower molecular mass.

2.2 Structural features of hydrogenases and design principle for H_2 evolution catalyst

The biomimetic approach to design a low molecular mass compound for catalysis requires a detailed understanding of the structures and the mechanisms of these natural enzymes in H_2 evolution. This includes all the functional structures and the active sites of the enzymes that directly or indirectly participate in the reaction mechanism. Fortunately, remarkable structural and mechanistic studies of hydrogenases have provided us with detailed molecular information regarding the active sites and the secondary coordination spheres of the hydrogenases. These insights into the biological system have set a strong foundation for a rational biomimetic approach. Several interesting structural models for the active sites of hydrogenases have since emerged over the last 10 years.

The first structural determination of [NiFe] hydrogenase was obtained from *Desulfovibrio gigas* in 1995 by J. C. Fontecilla-Camps' group.[6] The enzymes expressed from this sulphate reducing bacterium, were used by the group to obtain the first structure of [NiFe] hydrogenase at 2.46 Å resolution.[6] Following this work, the structural characterisations of the other enzymes from *D. fructosovorans*,[7] *D. vulgaris*,[8] and *D. desulfuricans* (ATCC 27774)[9] were also obtained. From the combination of these studies, a clear picture of the active site of [NiFe] hydrogenase can be derived. The active site of [NiFe] hydrogenase was found to consist of only earth-abundant metals, namely Ni and Fe, as the bimetallic centre. The Ni ion is coordinated by four cysteinates, with two of the cysteinates forming thiolate bridges between the metals. The Fe^{2+} ion is ligated by two CN^- and one CO ligands. In its oxidised form, an oxygenated ligand then makes a third bridge between the two metals.[10] The Ni-Fe distance was found to be 2.9 Å with a distorted square

pyramidal geometry with respect to the Ni centre and a distorted octahedral low spin environment with respect to the Fe centre (**1.1**, Figure 1.3).[5] The [FeFe] hydrogenase, on the other hand, consists of a six-Fe cluster, which includes two Fe subunit cysteine-sulfur bridged to a regular [4Fe-4S] cubane (**1.2**, Figure 1.3). In the Fe subunit, the Fe ions are ligated by two bridging thiolate groups and are terminated by CO and CN^- ligands.[11] The two Fe ions are further bridged by a CO group. It was found that the activity of [FeFe] hydrogenase is usually higher than the activity of [NiFe] hydrogenase.

With the structural features in hand, the mechanism of the reaction by hydrogenases was probed. In general, at atomic level, there is a fundamental difference in the H_2 evolution reaction mechanism when catalysed by Pt as compared to that by a molecular coordination complex. The H_2 evolution mechanism catalysed by Pt proceeds through a one-electron reduction of a proton into atomic hydrogen before the combination of two adsorbed hydrogen atoms on the surface to generate a H_2. This H_2 is then released from the metal surface to regenerate the active metal surface for further reaction. In contrast, for the reaction catalysed by homogeneous coordination complexes, they undergo either a heterolytic pathway or a homolytic pathway. In the heterolytic pathway, similar to hydrogenases, the active metal centre (M^+) first gets reduced to form M. Protonation followed by reduction with the addition of a second proton then releases a H_2 molecule. The other possible route for the heterolytic pathway is when M^+ gets reduced by two electrons and then protonated to form a metal hydride (MH). A H_2 molecule is formed when the second proton approaches MH as shown in Figure 2.2 (right).[3] In the homolytic pathway, two metal centres are usually in play for the H_2 evolution. Both the metal centres can be protonated to form two metal hydrides, MH, and through reductive elimination, give off H_2 as the product (left, Figure 2.2).

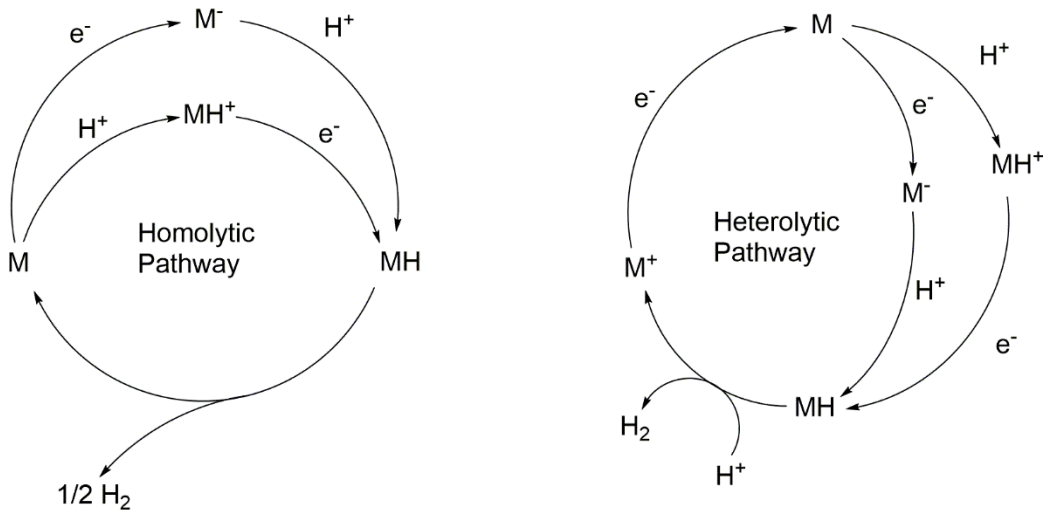

Figure 2.2. Homolytic (left) and heterolytic (right) pathways for proton reduction.

The mechanistic studies on the [FeFe] hydrogenase based on DFT and spectroscopy studies suggest that the [FeFe] hydrogenase undergoes a heterolytic mechanism via a Fe^{I} to Fe^{II} transition even though it is bimetallic in nature.[12] Furthermore, it was found that the first step of H_2 evolution catalysed by the [FeFe] hydrogenase catalyst is the protonation of the azapropanedithiolate ligand. This protonating step was found to facilitate the H_2 evolution by lowering the redox potential of the H-cluster. This protonated system, when reduced, formed a highly active terminal hydride. When in contact with proton, it can rapidly generates H_2 via a heterolysis mechanism.[13] Figure 2.3 below shows the transition state of the [FeFe] hydrogenase. This unique structural feature was hypothesised to be one of the reasons behind the high reactivity within this class of molecule.

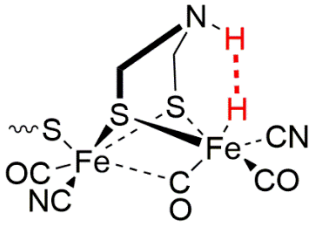

Figure 2.3. One of the transition states of the [FeFe] hydrogenase.

From mechanistic studies of the nature hydrogenase, several criteria that can contribute to the success of an effective H_2 evolution catalyst can be derived. Firstly, the ligand platform on the first coordination sphere should be able to stabilise the electron- rich, reduced metal species in order to lower the overpotential needed for the reaction. Secondly, the metal center should possess an open coordination site and be sufficiently basic enough for the formation of metal hydride species via protonation on the metal center. This can be achieved by modification of the first coordination sphere and ligand substituent. Finally, the incorporation of an appropriate secondary coordination sphere could assist in the H_2 evolution activity of the catalyst as shown in [FeFe] hydrogenase.

2.3 Biomimetic system

There are several molecular complexes designed for H_2 evolution that incorporate the structural features of the hydrogenase found in nature to reproduce their reactivity. The incorporation of an amino group on the secondary coordination sphere is the central theme of most biomimetic molecular catalysts.

2.3.1. Nickel complexes

Most notably, DuBois and co-workers have developed a class of excellent molecular catalysts for H_2 evolution by incorporating this key functional feature of the [FeFe] hydrogenase (Figure 2.4).[14-15] These $Ni(P^R_2N^{R'}_2)^{2+}$ complexes have shown high reactivity at low overpotential when they function as electrocatalysts in acidic acetonitrile/water solution (**2.2** to **2.8**). Due to their high reactivity, catalyst **2.2** was later incorporated into a photocatalytic system with either $[Ru(bpy)_3](Cl)_2$ or eosin Y as the photosensitiser, and ascorbic acid as the sacrificial reagent, to study its performance. A high TON of 2700 was observed.[16] However, the rate of H_2 produced was found to be low at only 18 mol h^{-1}. Further modification of the molecule uses a $Ni\ (P^R_2N^{R'})_2{}^{2+}$, where there is only a single amino group on each side of the ligands (**2.1**). This catalyst (**2.1**) was even

shown to catalyse H_2 production at a remarkable TOF of 100 000 s^{-1} at -0.49 V vs SHE in an acetonitrile/water solution (Figure 2.4**).**

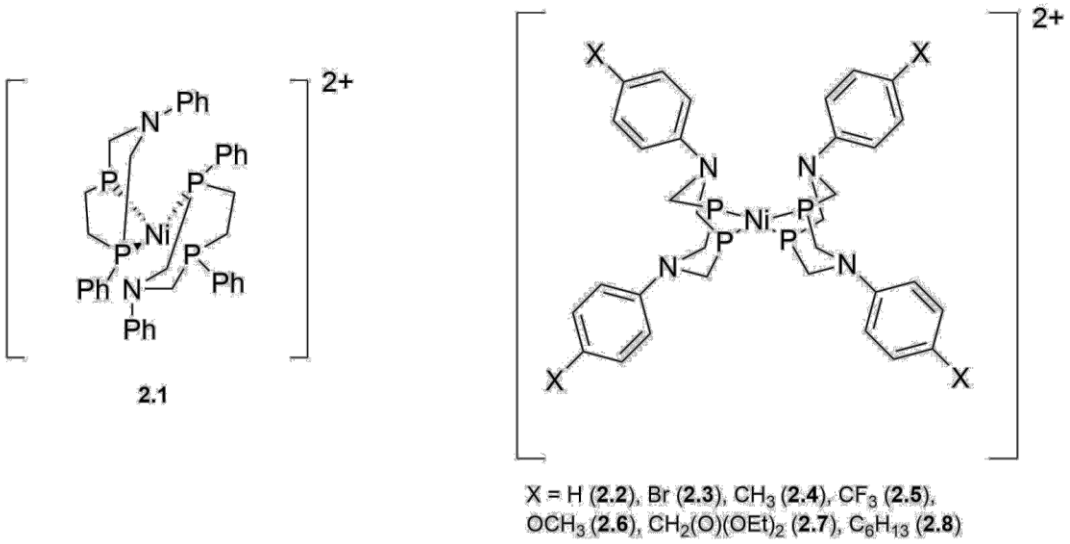

Figure 2.4. Structures of Ni catalysts developed by DuBois' group..[14-15, 17]

Further studies that were conducted to elucidate the mechanism of complexes **2.1** to **2.8** suggest that H_2 evolution is initiated by the protonation of the basic nitrogen as shown in figure 2.5, followed by two single-electron transfer processes. Subsequently, the proton is then transferred from one protonated nitrogen atom to the reduced-Ni species, forming a reactive Ni–H intermediate (Int, Figure 2.5). This reactive species eventually combines with the other proton on the nitrogen to generate a hydrogen molecule and regenerate the Ni catalyst. This mechanism is similar to the proposed mechanism of [FeFe] hydrogenase and [NiFe] hydrogenase where the protonation of the pendant amine arm occurred before the formation of metal hydride. Furthermore, the Ni $(P^R_2N^{R'})_2{}^{2+}$ catalyst (**2.1**), that consists of only a single amino group on each side of the ligands, was found to favour the formation of *endo* isomer (**Iso 2**, Figure 2.5) that allows the second N-H stabilisation and prevent the stabilisation of *exo- exo* form (**Iso 1**, Figure 2.5) in the previous $Ni(P^R_2N^{R'}_2)^{2+}$ (**Iso 1** and **Iso 3**, Figure 2.5). As **Iso 2** was found to be able to convert to Int readily, the resulting H_2 evolution efficiency improved as a result. In the subsequent study, it was shown that these

Ni P_2N_2 compounds exhibited surprisingly low TOF for photocatalytic proton reduction without the pendant amine arm in its second coordination sphere.[16]

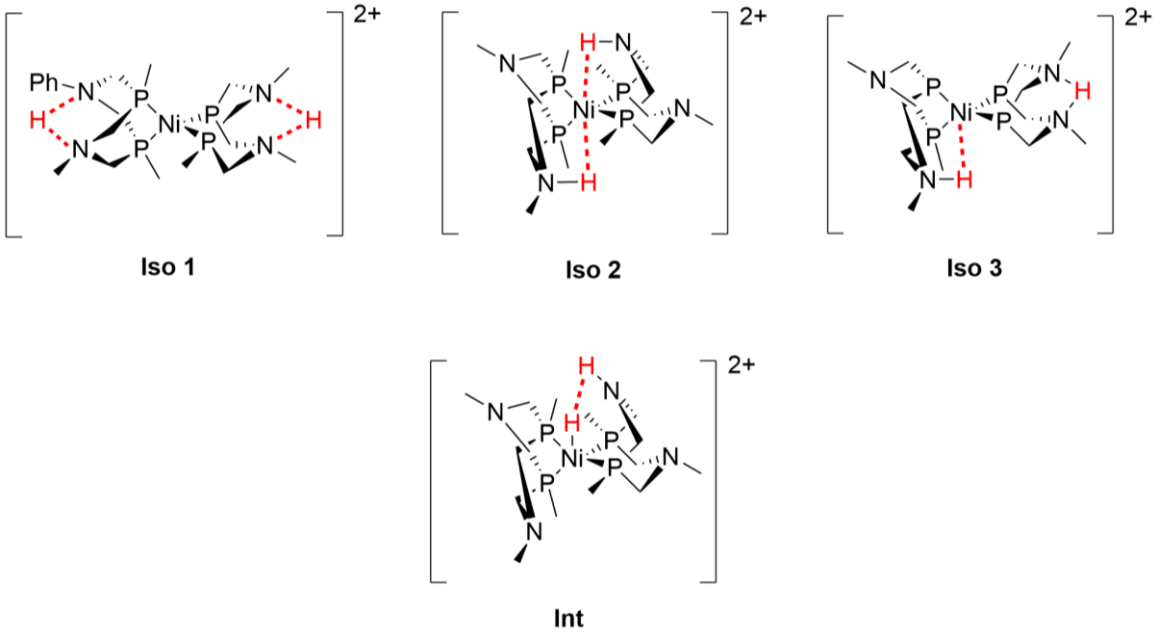

Figure 2.5. Proposed isomers of the transition state and reaction intermediate of complex **2.2.**

Eisenberg and co- workers. have also developed another class of novel bioinspired Ni catalyst for light-driven, noble-metal-free H_2 evolution in aqueous systems as illustrated in Scheme 2.1. Their strategy uses a mixed nitrogen and sulfur ligation, similar to that found in the [NiFe] hydrogenase. Their proposed mechanism suggests that the protonation of the pyrindine-2-thionato ligand acts as the key intermediate step in H_2 evolution (**Int 1**, Scheme 2.1). This is supported by nuclear magnetic resonance and electrochemical studies in the presence of acid. The pyrindine-2-thionato ligand functions as a proton relay system, similar to that seen in [FeFe] hydrogenase thus facilitating H_2 evolution. This class of catalyst can achieve up to TON of 7335 after 30 h of irradiation using a fluorescein photosensitiser.[18]

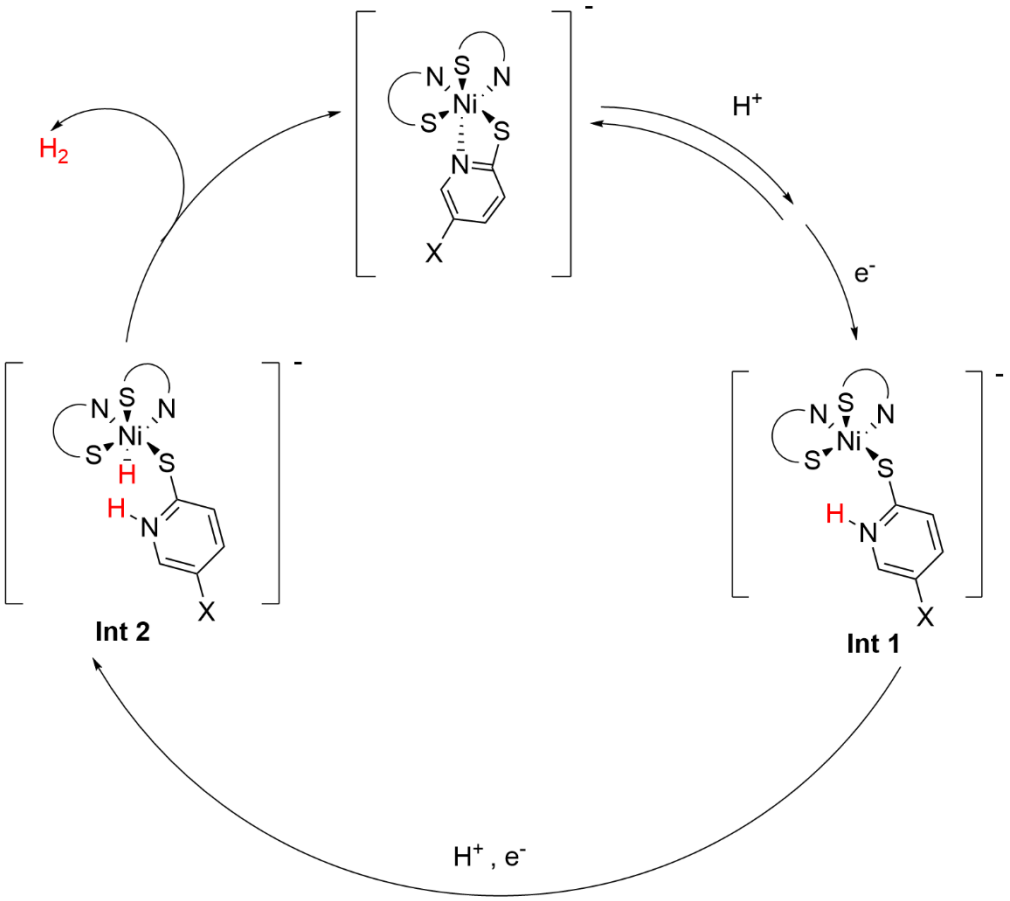

Scheme 2.1. Proposed mechanism of H_2 formation. with fluorescein as the photosensitiser.[18]

Fisher and Eisenberg have also developed a bioinspired Ni tetraazamacrocycle compound that is able to catalyse the H_2 evolution in an acetonitrile/water solution using a Hg electrode at -1.46 V vs SHE (**2.9**). Sauvage and co- workers then reported other Ni complexes that can catalyse H_2 evolution in neutral water with Hg as the working electrode (**2.10** and **2.11,** Figure 2.6). These catalysts possess both a vacant site on Ni for H_2 coordination and coordinated amino group that can control the electronic state of the metal centre and function as a proton relay simultaneously.[19] However, they suffer from a low TON and high overpotential. Furthermore, a Hg electrode must be used.

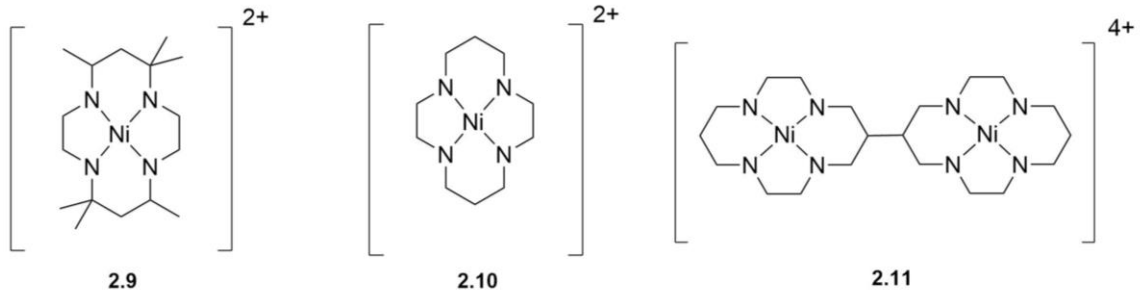

Figure 2.6. Structures of Ni complexes incorporating similar design features as an [FeFe] hydrogenase.

2.3.2. Iron Complexes

Diiron azadithiolate complexes (Figure 2.7) have also been synthesised to model the [FeFe] hydrogenase active site in order to study the role of the second coordination sphere in the mechanism of H_2 evolution. Through the combination of crystal structure, computational calculation and electrochemical studies, it is proposed that the azadithiolate cofactor helps to speed up the otherwise slow rate of proton transfer to the metal centre. This has in turn improved the TOF of the complex as a H_2 evolution catalyst. The complex in figure 2.7 can catalyse H_2 evolution in the presence of strong acid at -1.22 V vs ferrocenium/ferrocene (Fc^+/Fc). A TOF of 58 000 s^{-1} was achieved. All these studies highlight the importance of a secondary coordination sphere in improving catalytic activity.[13]

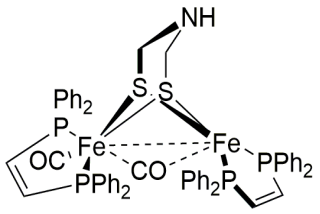

Figure 2.7. Structure of the diiron azadithiolate complex as a biomimetic catalyst of [FeFe] hydrogenase.

2.3.3. Cobalt Complexes

Earlier on, Fisher and Eisenberg also reported on a Co based azamacrocycle complex (**2.12**). This complex is reported to be able to produce H_2 in a pure water system at a potential of -1.36 V when Hg was used as the working electrode. The Faradaic yield is reported to reached 80% when an acetonitrile/water solvent system was used.[20] More recently, following up the work from Du and Wang **(2.13**, Figure 2.8), Dutta and co-workers functionalised the Co salen like core with secondary functionalities (**2.14** –**2.17**, Figure 2.8), such as phenol and carboxylic acid, and found that this modification transformed the otherwise inactive Co complex to an active H_2 evolution catalyst.[21-22] The highest TOF achieve was 277 s^{-1} at pH 1 at an overpotential of 0.84 V in a DMF/water mixed solvent using the Co salen like complex functionalised with tyrosine (**2.17**).

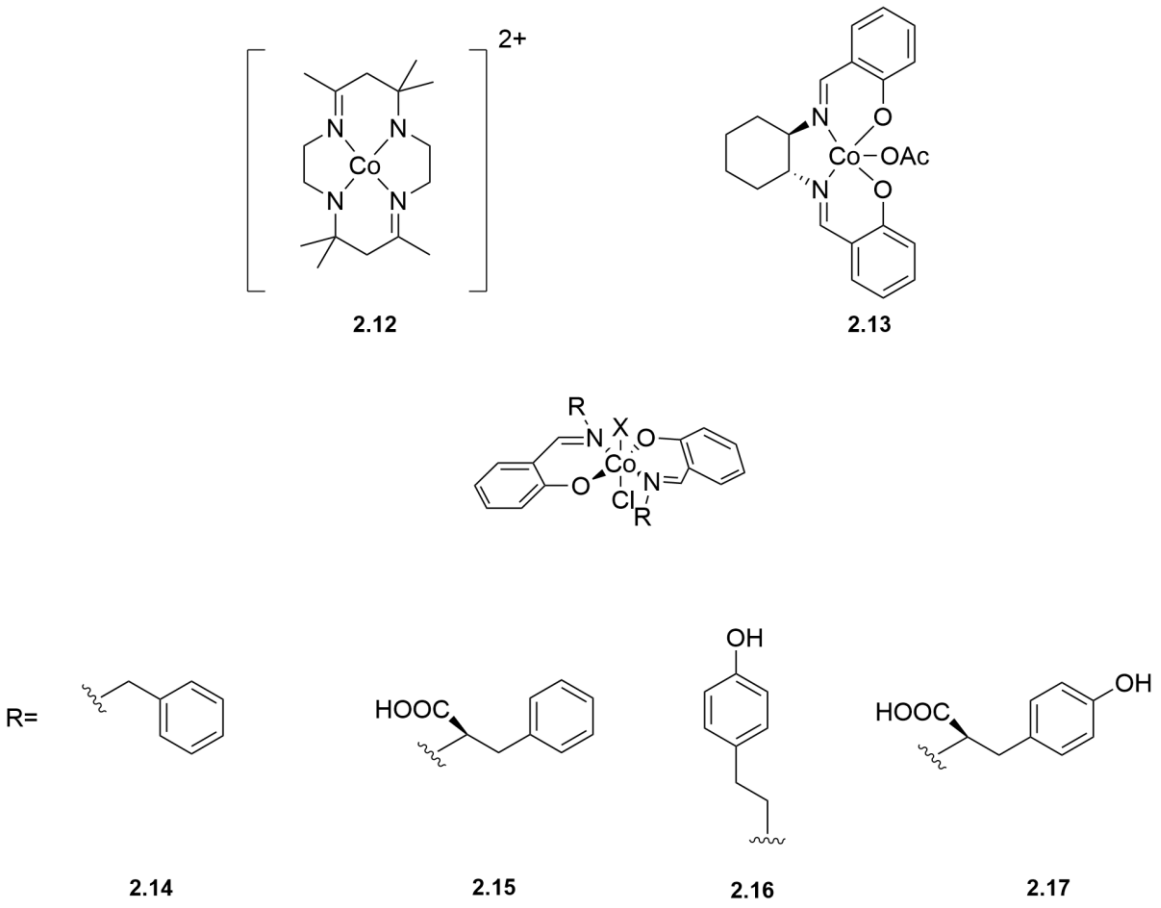

Figure 2.8. Some examples of Co complexes

Apart from the structural biomimetic catalysts of hydrogenase through the incorporation of pendant amine arm to facilitate H_2 evolution, the first coordination sphere of the molecule also play an important role in facilitating H_2 evolution. The first coordination sphere controls the electronic state of the metal center through its electron donating and withdrawing properties. Vitamin B_{12} is one of the most powerful nucleophiles in nature in its reduced state. The strongly nucleophilic reduced metal center favours the protonation of the complex, which is a key intermediate for proton reduction to take place. It is one of the most active molecular catalysts for H_2 evolution in a non-aqueous solution.[23] Cobaloximes which were developed by Schrazuer and coworkers mimic the Co-containing vitamin B_{12} complex.[24] These cobaloximes (**2.18- 2.20,** Figure 2.9) were found to show similar reactivity as vitamin B_{12} which is ligated by corrins. These complexes were studied extensively for their reactivity towards H_2 evolution in organic-aqueous solvents. In

particular, complex **2.20** (Figure 2.9) was found to be able to catalyse H_2 evolution in a photocatalytic system with rhodamine as the photosensitiser and triethanolamine as the sacrificial donor in an acetonitrile/water system. A high TON of 9000 was achieved in 8 h.[25] However, most of this cobaloxime complexes are unstable in acidic solution due to hydrolysis.[23]

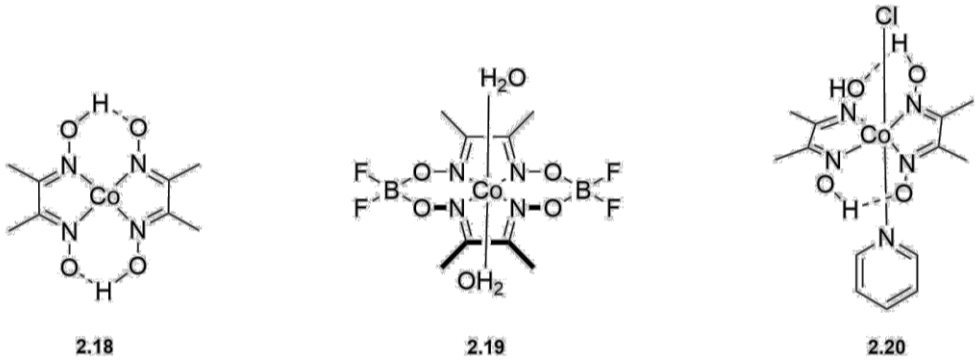

Figure 2.9. Some examples of cobaloxime complexes.

To improve the stability of the catalyst, the focus then shifted towards Co diimine-dioxime complexes, which contain only a single tetradentate equatorial ligand that is hardly displaced. Some examples of Co diimine-dioxime complexes are presented in Figure 2.10.[26] These complexes prove to be stable in an aqueous medium under a photocatalytic system using an Ir photosensitiser and TEA as the sacrificial agent.[26] These studies suggest that by careful design of the first coordination sphere of the complex, the stability and the reactivity of the complex can be improved through this electronic modification of the metal center.

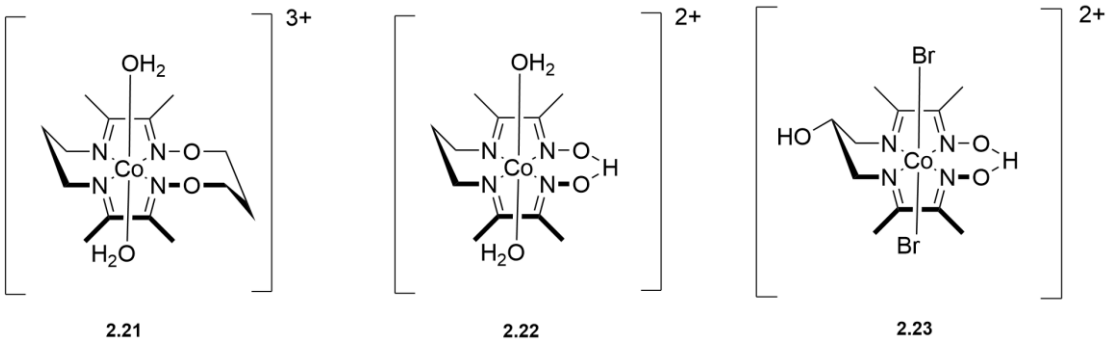

Figure 2.10. Some examples of Co diimine-dioxime complexes.[26]

2.4. Non-Biomimetic system

Besides the biomimetic catalysts, other molecular catalysts have been also developed for H_2 evolution. For example, Eisenberg and Holland reported that a bis(dithiolene) Co complex can reduce trifluoroacetic acid with a Faradaic efficiency of >99% on a glassy carbon electrode (**2.24 -2.25**, Figure 2.11).[27] Chang's group also reported on a series of Co pentapyridine complexes (**2.26 -2.28**, Figure 2.11), which are capable of producing H_2 in a pH 7 phosphate buffer with high Faradaic efficiency. These complexes can be stable up to 60 h in a reducing environment.[28-29] Notably, the complex **2.26** was found to be able to catalyse H_2 evolution at 99% Faradaic efficiency. Sakai and co-workers have also developed a new Co catalyst (**2.29**, Figure 2.11), that consist of a pentadentate macrocyclic ligand that can catalyse the production of H_2 in aqueous solution with a TOF of 2210 s^{-1}. Furthermore, this catalyst is found to be tolerant to both CO and O_2 with retention of 90% activity under either condition.[30]

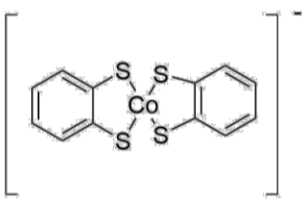

2.24

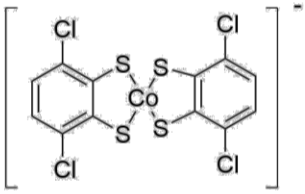

2.25

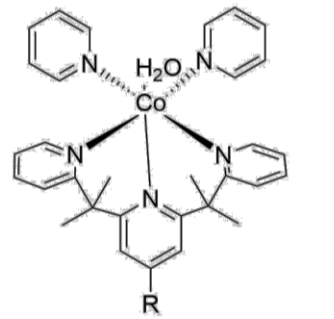

R = H (**2.26**), CF_3 (**2.27**), NMe_2 (**2.28**)

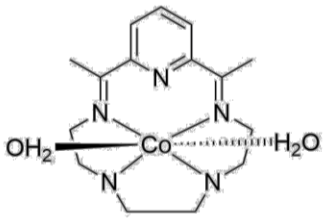

2.29

Figure 2.11. Some examples of non- biomimetic Co complexes[24,]

Table 2.1 and Table 2.2 summarized the conditions and efficiencies of the current molecular H_2 evolution catalysts in photocatalytic system and electrocatalytic system respectively.

Table 2.1. Molecular H_2 evolution catalysts performance in photocatalytic system.

Catalyst	Photosensitiser	Sacrificial Reagent	Conditions	TON	Ref
[Ni(4,4'-X-2,2'-bpy)(pyS)$_2$], (X= OCH$_3$) (4.0 μM)	Fluorescein (2.0 μM)	TEA (0.36 M)	EtOH/H_2O (v/v=1:1)	7335	[18]
(Et$_4$N)[Ni(X-pyS)$_3$], (X= 6-CH$_3$) (4.0 μM)	Fluorescein (2.0 μM)	TEA (0.36 M)	EtOH/H_2O (v/v=1:1)	5020	[18]

$Ni(abt)_2$ (20 μM)	Fluorescein (2.0 μM)	TEOA (0.35 M)	H_2O	6190	[31]
2.2 (0.14 mM)	$[Ru(bpy)_3]^{2+}$ (0.4 mM)	Ascorbic Acid (0.50 M)	CH_3CN/H_2O (v/v=1:1)	2700	[16]
$[Ni(L1)_2(H_2O)_2](BF_4)_2$ (0.02 mM)	Fluorescein (2.0 μM)	TEA (5% v/v)	$EtOH/H_2O$ (v/v=1:1)	3220	[32]
$Ni_2(MBD)_4$ (0.2 mM)	Fluorescein (2.0 mM)	TEOA (5% v/v)	CH_3CN/H_2O (v/v = 1:1)	320	[33]
$Ni_2(MBT)_4$ (0.2 mM)	Fluorescein (2.0 mM)	TEOA (5% v/v)	CH_3CN/H_2O (v/v = 1:1)	120	[33]
$[CoL2](BF_4)_2$ (0.1 mM)	$[Ir(ppy)_2(bpy)](PF_6)$ (0.1 mM)	TEA (10% v/v)	CH_3CN/H_2O (v/v = 1:1)	34	[34]
2.24 (0.05 mM)	$[Ru(bpy)_3]^{2+}$ (0.5 mM)	Ascorbic Acid (0.10 M)	CH_3CN/H_2O (v/v = 1:1)	2700	[27]
2.20 (0.5 mM)	$[ZnTMPyP](Cl_4)$ (0.04 mM)	TEOA (5% v/v)	CH_3CN/H_2O (v/v = 1:1)	280	[35]

L1=2-(2-pyridyl)-1,8-naphthyridine

L2= (2E)-2-N-(pyridin-2-ylmethylidene)-1-N,1-N-bis({2-[(E)-(pyridin-2-ylmethylidene)amino]phenyl})benzene-1,2-diamine

Table 2.2 Molecular H_2 evolution catalysts performance in electrocatalytic system.

Catalyst	Faradaic Efficiency (%)	Applied Potential (V vs. SHE)	Electrode	Condition	TOF (mol H_2/mol cat.h)	Ref
2.1	-	-0.49	Glassy carbon	DMF: HOTf, 1.2 M H_2O in CH_3CN	1.1×10^5	[17]
2.2	-	-0.20	Glassy carbon	DMF: HOTf, 0.034 M H_2O in CH_3CN	2.6×10^6	[36]
2.3	-	−0.17	Glassy carbon	DMF:HOTf, 0.27 M H_2O in CH_3CN	3.7×10^6	[36]
2.4	-	−0.24	Glassy carbon	DMF:HOTf, 0.05 M H_2O in CH_3CN	2.8×10^6	[36]
2.5	-	−0.18	Glassy carbon	DMF:HOTf, 0.27 M H_2O in CH_3CN	4.3×10^5	[36]
2.6	-	−0.21	Glassy carbon	DMF:HOTf, 0.08 M H_2O in CH_3CN	1.7×10^6	[36]
2.8	92	−1.0	Glassy carbon /RVC	H_2O in $[(DBF)H]NTf_2$	4.3×10^4	[37]
2.9	-	−1.46	Hg	H_2O/ CH_3CN (2:1)	-	[20]
2.10	-	−1.26	Hg	0.1 M $NaClO_4$ in H_2O	-	[38]
2.11	-	−1.26	Hg	0.1 M $NaClO_4$ in H_2O	-	[38]
2.12	<80	−1.36	Hg	H_2O	-	[20]
2.19	79	−0.69	Glassy carbon	pH 2.2 phosphate buffer	8.0	[29]

2.21	30	−0.69	Glassy carbon	pH 2.2 phosphate buffer	1.0	[29]
2.22	81	−0.69	Glassy carbon	pH 2.2 phosphate buffer	11.5	[29]
2.23	80	−0.69	Glassy carbon	pH 2.2 phosphate buffer	9.0	[29]
2.24	>99	−0.77	Glassy carbon	TFA, H_2O/ CH_3CN (1:1)	-	[39]

2.5. Research gap and PhD in context of literature

As described in section 2.2 and 2.3, recent efforts on the development of cheap molecular catalysts for H_2 evolution focusses mainly on biomimetic models of hydrogenases or vitamin B_{12}. The design principles involve the increase in basicity of the metal center by the careful selection of the first coordination sphere and the incorporation of the pendant amine arm that acts as a proton relay system for proton reduction. In this thesis, we will first study the effect of first coordination sphere on H_2 evolution reactivity follow by the effect of second coordination sphere using a non- amino group in the second coordination sphere modification

The Fe TAML complexes that are pioneered by Collins' group, have been applied in various oxidative applications such as pulp bleaching,[40-41] degradation of organic pollutants,[41-43] destruction of explosives,[44] and water oxidation.[45-46] Their applications have also recently been extended to C-H activation via high-valent transition metal TAML complexes.[40, 47] However, these studies focus on the oxidative applications of TAML systems with transition metals without considering the reductive reactivity of these potentially nucleophilic late transition metal-ate complexes. We hypothesised that with the strongly electron donating TAML, the basicity of the metal center will be increased, and

the protonation of metal center will be facilitated resulting in a higher reactivity in H_2 evolution than cobaloximes. Therefore, the H_2 evolution activity of the first-row transition metals modified with TAML will be explored in Chapter 3 of the thesis.

As discussed in section 2.2, the pendant amine arm was shown to play an essential role in H_2 evolution. However, most of the report focusses on the effect of amino-based modification on the second coordination sphere. Lately, polyether appended salicylaldimine complexes were found to be able to chelate to alkali metal cations effectively to form bimetallic complexes.[48-49] Furthermore, this coordination and hydration of alkali metal cations are able to operate as a non-amine proton relay to enhance H_2 evolution by directing water molecules towards metal center in electrocatalytic conditons.[50] This approach capitalises on principles in supramolecular chemistry where crown ethers effectively chelate alkali metal cations. The Lewis acids increases the Brønsted acidity of coordinated water molecules, thus resulting in enhanced activity for proton-dependent catalysis.[51-52] We therefore hypothesised that the unbound ether groups could also form hydrogen-bonding interactions with the water molecules, which will result in an increase in the local concentration of water around the catalytically active metal center, facilitating the multi-electron and multi-proton transfer processes for the H_2 evolution reaction. This study will be presented in Chapter 4. In conclusion, the careful modification of the first and second coordination spheres of the metal complexes will be studied independently in chapter 3 and chapter 4.

References

1. Tachibana, Y.; Vayssieres, L.; Durrant, J. R. *Nat. Photonics* **2012,** *6*, 511-518.

2. Wen, F.; Li, C. *Acc. Chem. Res.* **2013,** *46*, 2355-2364.

3. Artero, V.; Fontecave, M. *Coord. Chem. Rev.* **2005,** *249*, 1518-1535.

4. Khaselev, O.; Turner, J. A. *Science* **1998,** *280*, 425-427.

5. Canaguier, S.; Artero, V.; Fontecave, M. *Dalton Trans.* **2008**, 315-325.

6. Volbeda, A.; Charon, M. H.; Piras, C.; Hatchikian, E. C.; Frey, M.; Fontecilla-Camps, J. C. *Nature* **1995,** *373*, 580-587.

7. Rousset, M.; Montet, Y.; Guigliarelli, B.; Forget, N.; Asso, M.; Bertrand, P.; Fontecilla-Camps, J. C.; Hatchikian, E. C. *Proc. Natl. Acad. Sci. U.S.A* **1998,** *95*, 11625-11630.

8. Higuchi, Y.; Yagi, T.; Yasuoka, N. *Structure* **1997,** *5*, 1671-1680.

9. Matias, P. M.; Soares, C. M.; Saraiva, L. M.; Coelho, R.; Morais, J.; Le Gall, J.; Carrondo, M. A. *J. Biol. Inorg. Chem.* **2001,** *6*, 63-81.

10. Volbeda, A.; Martin, L.; Cavazza, C.; Matho, M.; Faber, B. W.; Roseboom, W.; Albracht, S. P.; Garcin, E.; Rousset, M.; Fontecilla-Camps, J. C. *J. Biol. Inorg. Chem.* **2005,** *10*, 239-249.

11. Carroll, M. E.; Barton, B. E.; Rauchfuss, T. B.; Carroll, P. J. *J. Am. Chem. Soc.* **2012,** *134*, 18843-18852.

12. Mulder, D. W.; Shepard, E. M.; Meuser, J. E.; Joshi, N.; King, P. W.; Posewitz, M. C.; Broderick, J. B.; Peters, J. W. *Structure* **2011,** *19*, 1038-1052.

13. Rauchfuss, T. B. *Acc. Chem. Res.* **2015,** *48*, 2107-2116.

14. DuBois, M. R.; DuBois, D. L. *Chem. Soc. Rev.* **2009,** *38*, 62-72.

15. Ho, M.-H.; O'Hagan, M.; Dupuis, M.; DuBois, D. L.; Bullock, R. M.; Shaw, W. J.; Raugei, S. *Dalton Trans.* **2015,** *44*, 10969-10979.

16. McLaughlin, M. P.; McCormick, T. M.; Eisenberg, R.; Holland, P. L. *Chem. Commun.* **2011,** *47*, 7989-7991.

17. Helm, M. L.; Stewart, M. P.; Bullock, R. M.; DuBois, M. R.; DuBois, D. L. *Science* **2011,** *333*, 863-866.

18. Han, Z.; Shen, L.; Brennessel, W. W.; Holland, P. L.; Eisenberg, R. *J. Am. Chem. Soc.* **2013,** *135*, 14659-14669.

19. Du, P.; Eisenberg, R. *Energy Environ. Sci,* **2012,** *5*, 6012-6021.

20. Fisher, B. J.; Eisenberg, R. *J. Am. Chem. Soc.* **1980,** *102*, 7361-7363.

21. Khandelwal, S.; Zamader, A.; Nagayach, V.; Dolui, D.; Mir, A. Q.; Dutta, A. *ACS Catal.* **2019,** *9*, 2334-2344.

22. Li, C.-B.; Gong, P.; Yang, Y.; Wang, H.-Y. *Catal. Lett.* **2018,** *148*, 3158-3164.

23. Artero, V.; Saveant, J. M. *Energy Environ. Sci.* **2014,** *7*, 3808-3814.

24. Schrauzer, G. N. *Acc. Chem. Res.* **1968,** *1*, 97-103.

25. McCormick, T. M.; Calitree, B. D.; Orchard, A.; Kraut, N. D.; Bright, F. V.; Detty, M. R.; Eisenberg, R. *J. Am. Chem. Soc.* **2010,** *132*, 15480-15483.

26. Kaeffer, N.; Chavarot-Kerlidou, M.; Artero, V. *Acc. Chem. Res.* **2015,** *48*, 1286-1295.

27. McNamara, W. R.; Han, Z.; Alperin, P. J.; Brennessel, W. W.; Holland, P. L.; Eisenberg, R. *J. Am. Chem. Soc.* **2011,** *133*, 15368-15371.

28. Khnayzer, R. S.; Thoi, V. S.; Nippe, M.; King, A. E.; Jurss, J. W.; El Roz, K. A.; Long, J. R.; Chang, C. J.; Castellano, F. N. *Energy Environ. Sci.* **2014,** *7*, 1477-1488.

29. Sun, Y.; Bigi, J. P.; Piro, N. A.; Tang, M. L.; Long, J. R.; Chang, C. J. *J. Am. Chem. Soc.* **2011,** *133*, 9212-9215.

30. Wang, J. W.; Yamauchi, K.; Huang, H. H.; Sun, J. K.; Luo, Z. M.; Zhong, D. C.; Lu, T. B.; Sakai, K. *Angew. Chem. Int. Ed.* **2019,** *58*, 10923-10927.

31. Das, A.; Han, Z.; Brennessel, W. W.; Holland, P. L.; Eisenberg, R. *ACS Catal.* **2015,** *5*, 1397-1406.

32. Yang, Y.; Wang, M.; Xue, L.; Zhang, F.; Chen, L.; Ahlquist, M. S.; Sun, L. *ChemSusChem* **2014,** *7*, 2889-2897.

33. Cui, H. H.; Wang, J. Y.; Hu, M. Q.; Ma, C. B.; Wen, H. M.; Song, X. W.; Chen, C. N. *Dalton Trans.* **2013,** *42*, 8684-8691.

34. Song, X.; Wen, H.; Ma, C.; Chen, C. *Polyhedron* **2014,** *81*, 639-645.

35. Lazarides, T.; Delor, M.; Sazanovich, I. V.; McCormick, T. M.; Georgakaki, I.; Charalambidis, G.; Weinstein, J. A.; Coutsolelos, A. G. *Chem. Commun.* **2014,** *50*, 521-523.

36. Kilgore, U. J.; Roberts, J. A.; Pool, D. H.; Appel, A. M.; Stewart, M. P.; DuBois, M. R.; Dougherty, W. G.; Kassel, W. S.; Bullock, R. M.; DuBois, D. L. *J. Am. Chem. Soc.* **2011,** *133*, 5861-5872.

37. Pool, D. H.; Stewart, M. P.; O'Hagan, M.; Shaw, W. J.; Roberts, J. A.; Bullock, R. M.; DuBois, D. L. *Proc. Natl. Acad. Sci. U.S.A* **2012,** *109*, 15634-15639.

38. Collin, J. P.; Jouaiti, A.; Sauvage, J. P. *Inorg. Chem.* **1988,** *27*, 1986-1990.

39. McNamara, W. R.; Han, Z.; Yin, C. J.; Brennessel, W. W.; Holland, P. L.; Eisenberg, R. *Proc. Natl. Acad. Sci. U.S.A* **2012,** *109*, 15594-15599.

40. Collins, T. J.; Kostka, K. L.; Uffelman, E. S.; Weinberger, T. L. *Inorg. Chem.* **1991,** *30*, 4204-4210.

41. Ellis, W. C.; Tran, C. T.; Roy, R.; Rusten, M.; Fischer, A.; Ryabov, A. D.; Blumberg, B.; Collins, T. J. *J. Am. Chem. Soc.* **2010,** *132*, 9774-9781.

42. Collins, T. J. *Acc. Chem. Res.* **2002,** *35*, 782-790.

43. Khetan, S. K.; Collins, T. J. *Chem. Rev.* **2007,** *107*, 2319-2364.

44. Kundu, S.; Chanda, A.; Khetan, S. K.; Ryabov, A. D.; Collins, T. J. *Environ. Sci. Technol.* **2013,** *47*, 5319-5326.

45. Demeter, E. L.; Hilburg, S. L.; Washburn, N. R.; Collins, T. J.; Kitchin, J. R. *J. Am. Chem. Soc.* **2014,** *136*, 5603-5606.

46. Panda, C.; Debgupta, J.; Díaz Díaz, D.; Singh, K. K.; Sen Gupta, S.; Dhar, B. B. *J. Am. Chem. Soc.* **2014,** *136*, 12273-12282.

47. Collins, T. J.; Nichols, T. R.; Uffelman, E. S. *J. Am. Chem. Soc.* **1991,** *113*, 4708-4709.

48. Kumar, A.; Lionetti, D.; Day, V. W.; Blakemore, J. D. *Chem. Eur. J.* **2018,** *24*, 141-149.

49. Van Staveren, C. J.; Van Eerden, J.; Van Veggel, F. C. J. M.; Harkema, S.; Reinhoudt, D. N. *J. Am. Chem. Soc.* **1988,** *110*, 4994-5008.

50. Shao, H.; Muduli, S. K.; Tran, P. D.; Soo, H. S. *Chem. Commun.* **2016,** *52*, 2948-2951.

51. Chang, C. T.; Chen, C. L.; Liu, Y. H.; Peng, S. M.; Chou, P. T.; Liu, S. T. *Inorg. Chem.* **2006,** *45*, 7590-7592.

52. Cacciapaglia, R.; Mandolins, L. *Chem. Soc. Rev.* **1993,** *22*, 221-231.

Chapter 3

Cobalt Complex of a Tetraamido Macrocyclic Ligand as a Precursor for Electrocatalytic Hydrogen Evolution

3.1. Foreword

Currently, the production H_2 is dominated by the energy intensive steam reforming reaction, that emits large amounts of CO_2 as one of the by-products as discussed in Chapter 1. Alternatively, the use of expensive, noble metal, Pt, as the electrocatalyst for water splitting can also generate high amounts of H_2 for industrial uses, but at a much higher cost than steam reforming. Therefore, we are interested in developing an earth-abundant first-row transition metal-based catalyst as a cheaper alternative for H_2 evolution.

Chapter 3 discusses the efforts in the synthesis and characterisation of new first-row transition metal complexes with the TAML. We hypothesise that with the electron-donating TAML, we can achieve a highly nucleophilic complex, similar to that of reduced vitamin B_{12}, to activate H^+ for H_2 evolution. The reactivity of the complexes as catalyst for H_2 production was explored with only the Co TAML variant and they exhibited H_2 evolution activity. Further studies revealed that Co metal nanoparticles were electrodeposited on the glassy carbon electrode during electrolysis and hence, act as the active catalyst for H_2 evolution. This chapter is based on work published in *Organometallics* (*Organometallics* **2019**, *3*, 86, 1397-1406). I am the first author for this paper. I analysed the experimental data obtained, prepared the manuscript drafts and revised it together with the help of Dr. Siva Prasad Das. I designed the study together with Asst. Prof. Soo Han Sen and performed all the laboratory work at the MSE and SPMS. All the synthesis and characterisation were carried out by myself unless stated otherwise. Dr. Leonard Kia-Shuen Ng and Mr. Andrew Yun Ru Ng helped with the material characterisation. Dr. Rakesh Ganguly assisted in resolving the single crystal structure of the complex.

Cobalt Complex of a Teteaamido Macrocyclic Ligand as a Precursor for Electrocatalytic Hydrogen Evolution

Xian Liang Ho, Siva Prasad Das, Leonard Kia- Shuen Ng, Andrew Yun Ru Ng, Rakesh Ganguly, and Han Sen Soo*

3.2. Abstract

H_2 is a clean fuel that can potentially store renewable energy and overcome some of the environmental problems that arise from fossil fuel consumption. One attractive approach is to produce H_2 from water electrocatalytically using molecular complexes that can be systematically improved through ligand modifications. Here, we report Co and Ni complexes supported by TAML, which consist of exclusively earth abundant elements. Although TAML systems are well established in high valent transition metal chemistry, little is known about their reactivity in reductive catalysis despite the electron-rich nature of the tetraanionic TAML. Thus, we explored the utility of these nucleophilic -ate complexes as potential electrocatalysts for H_2 evolution using water as the proton source. CPE experiments were performed, and the Co TAML variant exhibited catalytic H_2 evolution activity in acetonitrile containing 1.0 M water but was inactive in purely aqueous solutions. Further investigation revealed that Co metal nanoparticles were electrodeposited as the active catalyst for H_2 evolution.

3.3. Introduction

Electrocatalysis has experienced a renaissance lately with intense interest in their applications in materials,[1-3] energy,[4-7] and even synthetic organic chemistry.[8-10] Of special interest to us is the use of electrocatalysis as a fundamental component of artificial photosynthesis to address global climate change.[11] The consequences of increasingly palpable climate change have largely been recognised to originate from anthropogenic generation of greenhouse gases due to consumption of fossil fuels and the proliferation of volatile, halogenated organic compounds. A promising and more sustainable approach to overcome these problems is to harness solar or other renewable, but intermittent sources of energy to produce electricity, which can subsequently be employed in electrocatalytic processes to store energy in molecules such as H_2 and O_2 by splitting water.[11-14]

Although water splitting electrocatalysis has traditionally been dominated by platinum group metals,[15, 16] there has been increasing interest in the utilisation of more earth-abundant, molecular, first-row transition metal systems,[11, 17-22] main group compounds,[23, 24] and even recycled spent nuclear waste.[25-27] Molecular electrocatalysts for proton reduction are especially attractive since they can be systematically customised by ligand modifications and some of them have demonstrated outstanding TOF at modest overpotentials. For instance, inspired by natural hydrogenase enzymes, there have been reports of Fe,[19] Ni,[21, 22] and other late,[19, 28] first-row transition metal electrocatalysts that operate in water. Among these reports, one of the themes that has proven successful at enhancing proton reduction catalytic activity has been the careful management of second coordination sphere effects to create H^+ relays and reduce the kinetic barrier for H_2 evolution.[21, 22, 29-33] Notably, however, not many of these catalysts are nucleophilic –ate complexes.

The reduced vitamin B_{12} is one of the most powerful nucleophiles in nature in its reduced state. This strongly nucleophilic metal center favors the protonation of the

complex, a key intermediate for proton reduction.[34] The Fe TAML complexes had been pioneered by Collins and coworkers and have been utilised in many oxidative applications including pulp bleaching,[35-42] decomposition of organic pollutants,[38, 41-44] destruction of explosives,[45] and water oxidation.[46, 47] Furthermore, Nam, Fukuzumi, and others have recently extended the applications of TAML compounds to other applications such as oxidative C-H activation by high-valent Co and Ni complexes.[40, 48-57] These seminal studies highlight the oxidative robustness of TAML systems, but also underscore the paucity of reports on the reductive catalytic activity of these potentially nucleophilic late transition metal –ate complexes.

Herein, we explored the reactivity of Co and Ni TAML complexes under reductive conditions, specifically for electrocatalytic proton reduction. The TAML ligand is slightly modified compared to prior examples[50, 56, 57] and all the metal complexes have been extensively characterised, including with X-ray structural studies. The Co TAML complex appeared to be active for electrocatalytic H_2 evolution in acetonitrile containing 1.0 M water, but detailed studies revealed that Co nanomaterials were responsible for the catalysis.

3.4. Results and Discussions

3.4.1. Synthesis and NMR characterisation of the TAML complexes

The TAML compound was synthesised in a total of six steps (Scheme 3.1) from commercially available reagents. In the first step, 2,4-dibromo-2,4- dimethylpentanone (**3.1**) was subjected to S_N1 nucleophilic substitution conditions with sodium azide (NaN_3) to give 2,4-diazido-2,4- dimethylpentanone (**3.2**) under reflux conditions in ethanol. After extraction with pentane, the concentrated solution of **3.2** was used in the next step without further purification due to concerns over the safety of isolating large amounts of this potentially explosive, low molecular weight, organic aliphatic azide. Compound **3.2** was then reduced by lithium aluminium hydride to give 2,4-diamino-2,4-dimethylpentan-3-ol

(**3.3**) in 80% yield. The third step of the ligand synthesis was the formation of the first amide linkage with α-bromoisobutyryl bromide in DCM to give bis-2,4-(2-bromo-2-methylpropanamido)-2,4-dimethyl-pentan-3-ol (**3.4**) with a yield of 88%. The reaction with the acyl bromide is very exothermic and the reagent should be added slowly with care to avoid boiling the DCM. Compound **3.4** was then mixed with NaN_3 in another S_N1 nucleophilic substitution reaction to give bis-2,4-(2-azido-2-methylpropanamido)-2,4-dimethylpentan-3-ol (**3.5**) almost quantitatively.

Scheme 3.1. Synthetic route to access the sterically encumbering TAML ligand **3.7**.

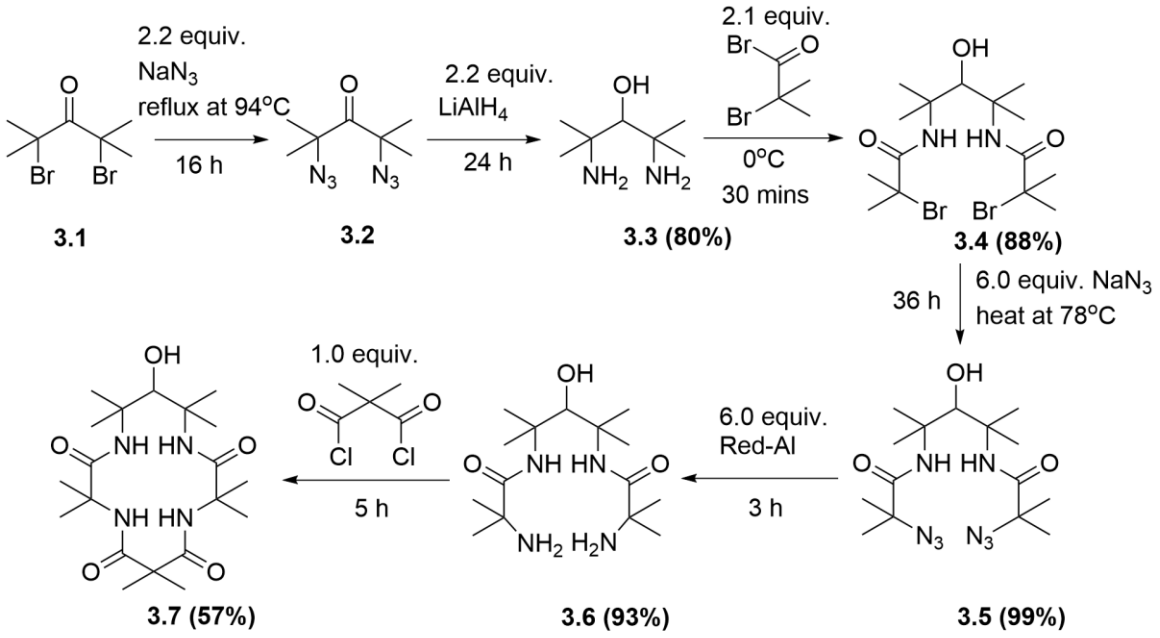

Likewise, **3.5** could be used without additional purification in the next step, where the azido groups were reduced using sodium bis(2-methoxyethoxy) aluminium hydride (Red-Al) in 70% toluene solution. Red-Al was found to be selective for reducing the azide without reacting with the amides and **3.6** was isolated in 93% yield. The final step for the ligand formation involved macrocycle ring closure with 2,2-dimethylmalonyl chloride *via* dropwise addition over 8 h under dilute conditions to prevent oligomerisation. Compound **3.7** was isolated after purification by silica gel column chromatography as a colourless, crystalline material in 57% yield.

The metal complexes were synthesised by using a strong base, LiHMDS, to deprotonate **3.7** before the addition of different metal precursors to give their respective TAML metal complexes (Scheme 3.2). These complexes were fully characterised by NMR spectroscopy, HRMS, and elemental analyses.

Scheme 3.2. Synthetic route to access the TAML complexes of Co^{III} and Ni^{II}.

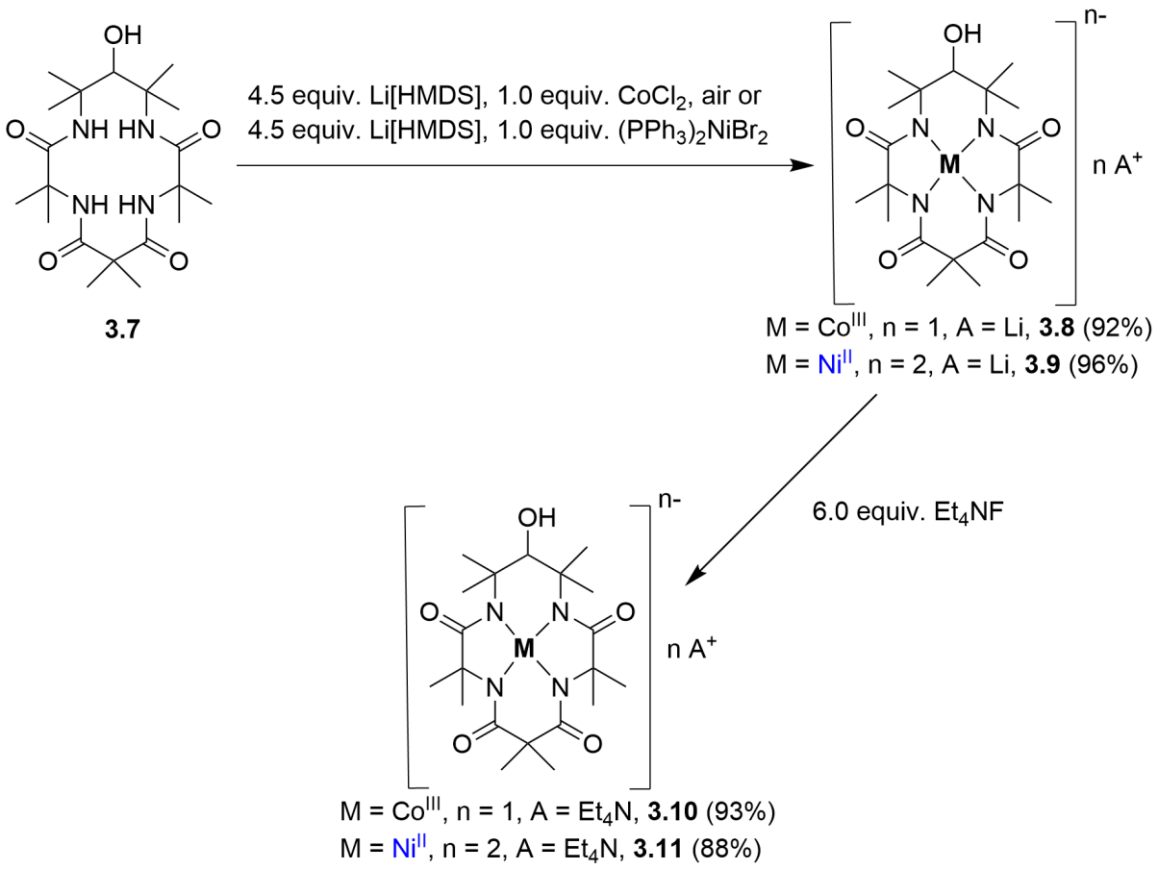

Complex **3.9** is diamagnetic and displayed typical ^{1}H NMR features consistent with a square planar d^8 electronic configuration containing mirror symmetry. Remarkably, the ^{1}H NMR of **3.8** suggested the formation of a paramagnetic Co^{III} complex, instead of the common low-spin diamagnetic, octahedral Co^{III}.[48] An Evan's method measurement was carried out to determine the magnetic susceptibility of the complex (Table A3, Appendix). Complex **3.8** is found to have an intermediate spin ground state with a spin-only magnetic moment of 2.91 μ_B, corresponding to a $S = 1$ ground state. In order to improve the solubility of complex **3.8** in organic solvent for further characterisation, it was subjected to cation exchange with tetraethylammonium fluoride to give **3.10**. As anticipated, **3.10** became

more soluble in a wider range of organic solvents, enabling the growth of single crystals for X-ray structural characterisation.

3.4.2. Structural characterisation by single crystal X-ray diffraction

Deep red plate-like single crystals of **3.10** were grown from DCM and diethyl ether, and a specimen was used for X-ray crystallography. The ORTEP of **3.10** is shown in Figure 3.1, and Table 3.1 summarises the salient bond lengths and angles. Detailed information about the crystallographic experiment, including the remaining bond parameters, are given in the Table A1 (Appendix).

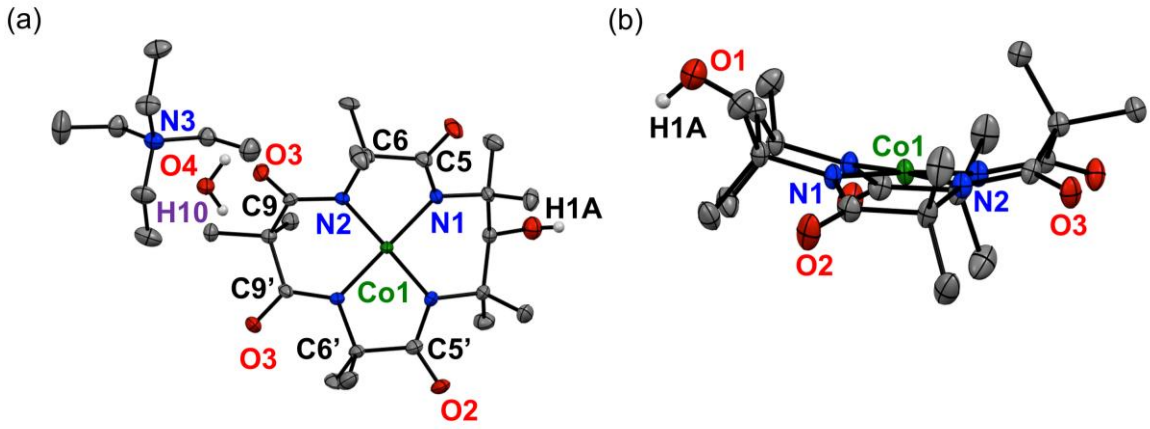

Figure 3.1. ORTEP of **3.10** with the thermal ellipsoids at 50% (a) with the tetraethylammonium cation and water included, and (b) showing the planar geometry around the Co center. The ellipsoids are colored according to their elements: Co (green), N (blue), O (red), C (gray), and H (white). A mirror plane bisects the Co centre. All hydrogen atoms have been omitted except for the ones on the water molecule and the alcohol group on the ligand.

Table 3.1. Selected bond distances and angles for **3.10**.

Parameter	Bond length (Å)
Co1-N1	1.8720(19)
Co1-N2	1.8630(91)
C2-N1	1.485(3)
C5-N1	1.351(3)
C5-O2	1.239(3)
C6-N2	1.469(3)
C9-N2	1.361(3)
C9-O3	1.237(3)
C1-O1	1.400(4)
	Bond angle (º)
N1-Co1-N1	96.47(12)
N1-Co1-N2	84.59(8)
N2-Co1-N2	94.15(12)
N2-Co1-N1	176.38(9)
Co1-N1-C2	127.79(15)
Co1-N1-C5	114.07(16)
Co1-N2-C6	115.44(15)
Co1-N2-C9	125.60(16)

The Co center shows a square planar geometry with 4 N atoms at almost equal distances around the metal. The average distance between the Co and N atoms in **3.10** is 1.868 Å, which is close to the reported values for Co^{III} complexes.[58] The cis and trans N bond angles N1-Co1-N1 and N2-Co1-N1 are 96.47(12)º and 176.38(9)º respectively, illustrating how the Co is sitting almost exactly within the plane of the four N atoms (Figure 3.1b). The slight distortions from 90º and 180º of a perfect square planar complex likely arise from the steric constraints afforded by the macrocycle. In addition, the lone pair of electrons on the N are all delocalised to form some partial double bond character between N and the carbonyl carbon, resulting in shorter bond distances of 1.351(3) and 1.361(3) Å for C5-N1 and C9-N2, respectively. In contrast, the *bona fide* single bonds of C2-N1 and C6-N2 are 1.485(3) and 1.469(3) Å, respectively. Overall, these bond parameters are similar to the (TAML)Co^{III} structural data reported by Collins and coworkers[59] and are consistent with the intermediate spin nature of the complex.

3.4.3. UV-visible spectroscopy of TAML complexes

Complex **3.8** exhibits two intense absorption bands at 392 nm and 584 nm with molar extinction coefficients of 2020 and 3530 M^{-1} cm^{-1} respectively (Figure 3.2a), obtained from the Beer-Lambert Law, $A = \varepsilon Cl$ (A = absorbance; ε = molar extinction coefficient; C = concentration; l = pathlength of cell). The magnitude of these absorption bands suggest that they should arise LMCT, since the aliphatic **3.7** will be a poor π-acceptor. We propose that the LMCT originates from the electron-rich amide N to the $d_{xz/yz}$ and d_{z2} orbitals of the Co^{III} center in the square planar geometry.[48]

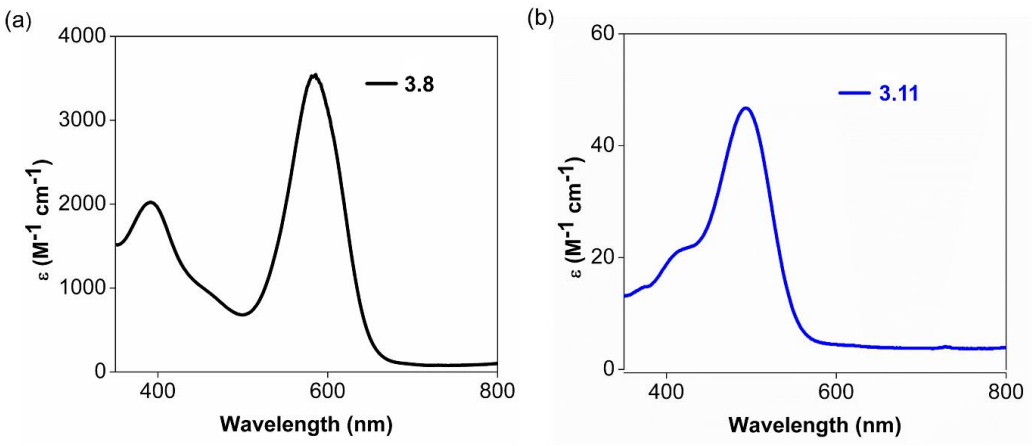

Figure 3.2. Plot of molar extinction coefficient against wavelength for (a) **3.8** (black), and (b) **3.11** (blue) in acetonitrile.

Complex **3.11**, however, exhibits only weak absorptions in the visible region with a peak at 492 nm, at an extinction coefficient of 47.1 M^{-1} cm^{-1} (Figure 2b). Complex **3.11** has a low-spin Ni^{II} d^8 electronic configuration with a high energy d_{x2-y2} orbital. Consequently, the LMCT transitions to the empty d_{x2-y2} orbital are likely to be much higher in energy. The weak absorption bands in the visible spectrum for **3.11** probably arise from d-d transitions instead.

3.4.4. Cyclic voltammetry of TAML complexes

The CV of **3.8** in acetonitrile shows an quasi-reversible redox wave with an $E_{1/2}$ at -0.41V vs silver/silver chloride (Ag/AgCl), which we assign to the Co^{III}/Co^{II} redox couple (Figure 3.3a).[60] On the other hand, **3.11** shows a reversible redox wave at +0.24 V (Figure 3.3b). This redox wave is assigned as the Ni^{III}/Ni^{II} redox couple.[61]

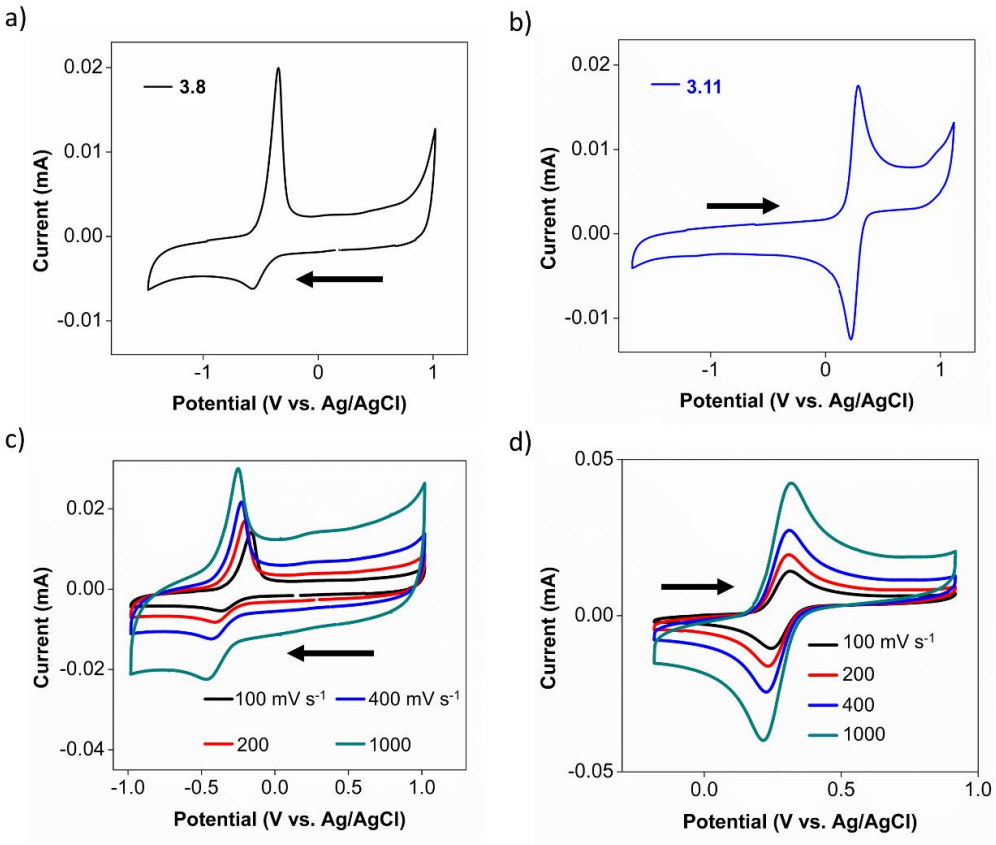

Figure 3.3. CVs of 1.0 mM (a) **3.8** (black) and (b) **3.11** (blue) in 0.10 M n-Bu_4NPF_6 solutions in acetonitrile. Each experiment is conducted with a glassy carbon electrode (3 mm diameter) at a scan rate of 100 mV s^{-1}. Plot of CVs at scan rates of 100 (black), 200 (red), 400 (blue), and 1000 (teal) mV s^{-1} for complexes (c) **3.8** and (d) **3.11**. The black arrows correspond to the direction in which the initial potential was applied.

We conducted CV experiments at different scan rates on each of these complexes as displayed in Figures 3c-d. The peak currents were then plotted against the square root of the scan rate according to the Randles-Sevcik equation for both complexes **3.8** and **3.11** (Figure 3.4). The redox wave for **3.8** is quasi-reversible, with the anodic wave at a higher current than the cathodic peak even up to 1000 mV s^{-1} (Figure 3.4a). On the other hand, the linear plots obtained from **3.11** confirm that the redox couple appear to be reversible at scan rates between 100 to 1000 mV s^{-1} (Figure 3.4b). The linear relation between the peak currents and the square root of the scan rates indicated that the redox processes for both **3.8**

and **3.11** are under diffusion control. With these results in hand, we sought to explore if the electron-rich **3.8** and **3.11** could exhibit electrocatalytic reductive behaviour.

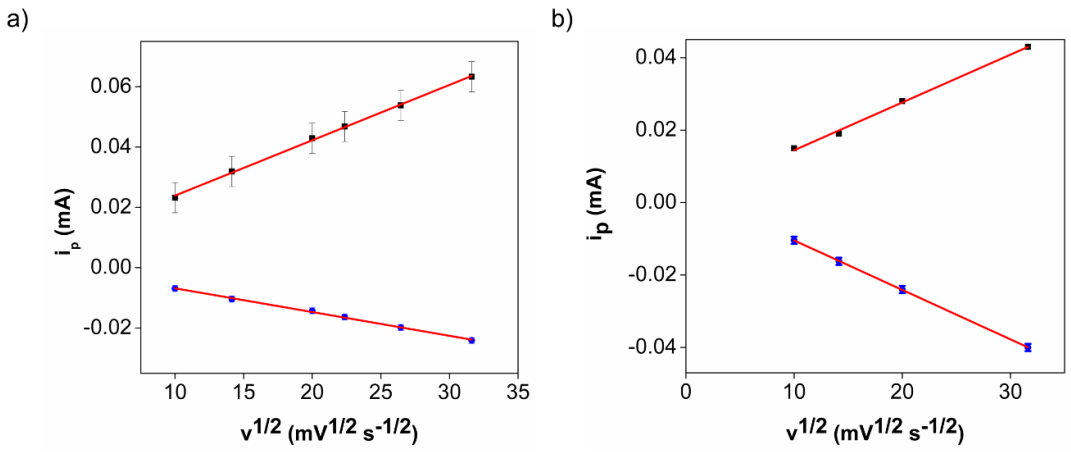

Figure 3.4. Plot of current against square root of the scan rates, fit to the Randles-Sevcik[62] equation from the CV data of a) Complex **3.8** for the redox wave at $E_{1/2}$ = -0.41 V (vs Ag/AgCl) and b) Complex **3.11** for the redox wave at $E_{1/2}$ = + 0.24 V.

3.4.5. Electrocatalytic proton reduction

A series of experiments were carried out with both **3.8** and **3.11** to study their reactivity in reductive catalytic H_2 evolution. The CVs of **3.11** in increasing concentrations of DI water in acetonitrile remained reversible, with no further increase in the cathodic current relative to the solution in the absence of **3.11**. On the other hand, upon the addition of 1.0 M of DI water to the acetonitrile, the CVs of **3.8** show an increase in catalytic current (Figure 3.5a). However, the onset of this catalytic current was observed when a potential of -1.7 V, beyond the Co^{III}/Co^{II} redox couple, was applied (Figure 3.5c). This suggested the possibility that **3.8** may just be a pre-catalyst, whereas the active species is formed from its electrochemical transformation.

To elucidate the origin of this unexpected increase in current, different concentrations of water were added and the CVs were analysed (Figure 3.5b). As the concentration of water increased from 0 to 0.10 M, both the anodic and cathodic wave

currents decreased. This change in redox behavior of **3.8**, suggested a chemical transformation of the complex in solution under these conditions. Notably, there was no significant increase in the current when a potential beyond -1.7 V was applied at these concentrations of water. However, as the concentration of water was increased to 1.0 M, three new cathodic and two anodic waves were observed, coupled with the dramatic increase in current at -1.7 V (pink line, Figure 3.5d). These new redox waves are attributed to the formation of new intermediates that arose from water coordination to **3.8**, and their subsequent chemical transformation during the CV.

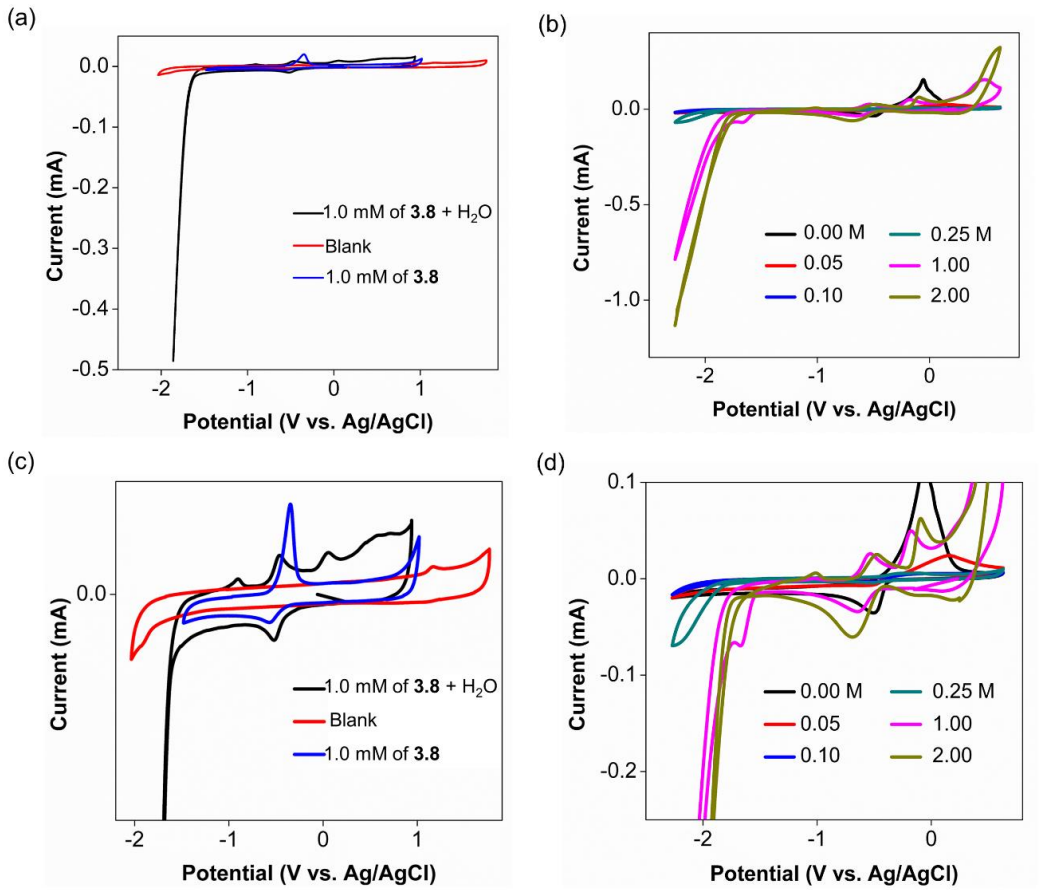

Figure 3.5. CVs of (a) 1.0 mM of **3.8** in the absence (blue) and presence (black) of 1.0 M of water in acetonitrile. (b) CVs of 1.0 mM of **3.8** with different concentrations of water in acetonitrile at scan rates of 100 mV s^{-1}. (c) Expansion of the data in (a) to show the detailed behavior. (d) Expansion of the data in (b) to show the detailed behavior.

CPE experiments were then conducted with a glassy carbon electrode to confirm the identity of and quantify the product via GC. The CPE measurements were performed with the same three-electrode setup as the CV experiments in 1.0 M of DI water in acetonitrile with a glassy carbon rod as the working electrode. A constant potential of –2.0 V was applied for 50 min. Samples of the headspace were removed by a gas-tight syringe and H_2 was identified as the product by GC (Figure 3.6). Both the current and charge were each plotted as a function of time (Figure 3.7). The current-time curve indicated that at least two different processes took place during the electrolysis (Figure 3.7a).

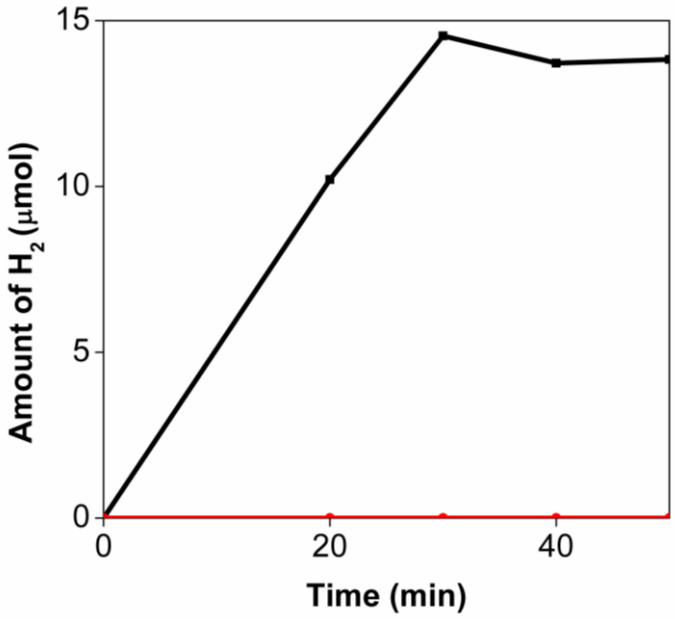

Figure 3.6. Amount of H_2 produced (µmol) in the presence (black) and absence (red) of **3.8**.

We hypothesise that during the first 1300 s, **3.8** was transformed into a new species, while the current gradually decreased. This was accompanied by the decolorisation of **3.8** in solution. Subsequently, the current stabilised at -4.95 mA until we stopped the CPE experiment at 2500 s, during which a steady current was observed over the span of 1200 s. We postulate that this latter behaviour could be a steady rate of H_2 production from the

actual heterogeneous catalyst. The UV-vis spectrum taken after the CPE displayed a remarkable loss of absorption in the visible region (Figure 3.8).

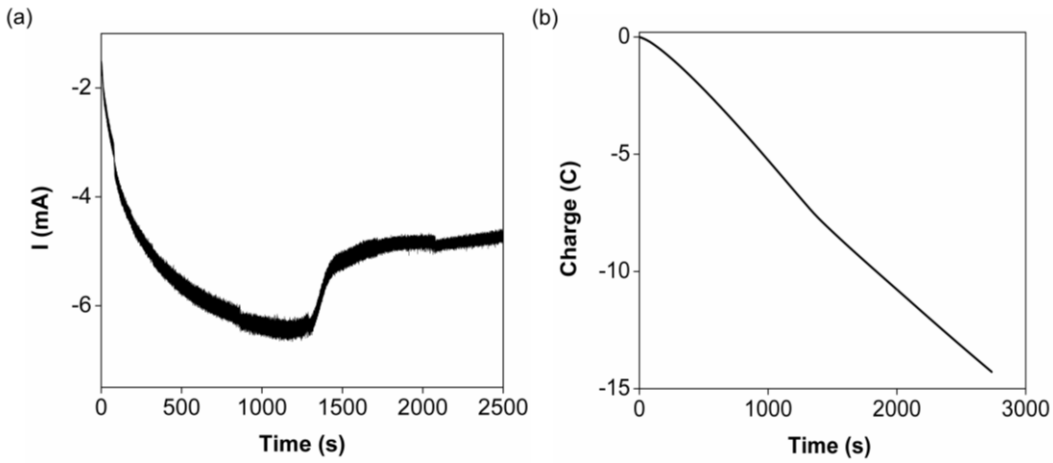

Figure 3.7. Plots of (a) current and (b) charge against time using 1.0 mM of **3.8** in acetonitrile (1.0 M of water).

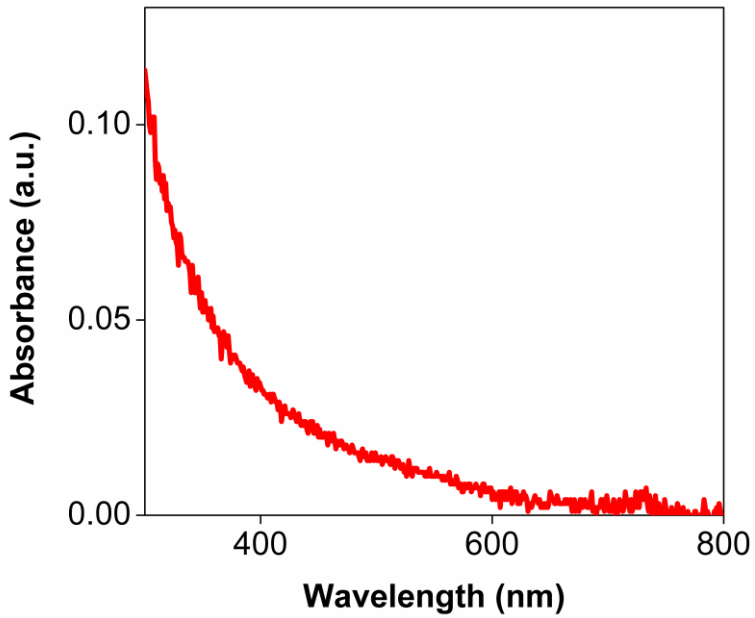

Figure 3.8. UV-vis spectrum of 1.0 mM **3.8** in acetonitrile (1.0 M of H_2O) after electrolysis.

Furthermore, based on the amount of H_2 obtained by GC, the Faradaic efficiency for H_2 evolution by **3.8** after 50 min was calculated to be only 18.2%. Thus, we believe that the lower than quantitative Faradaic efficiency could arise because current was consumed to transform **3.8** to the active H_2 evolution catalyst during the CPE experiments. As

expected, when the CPE was conducted with 1.0 mM of **3.8** in 1.0 M Na_2SO_4 solutions of DI water, no H_2 was detected above the levels produced by just the glassy carbon electrode alone (Figure 3.9).

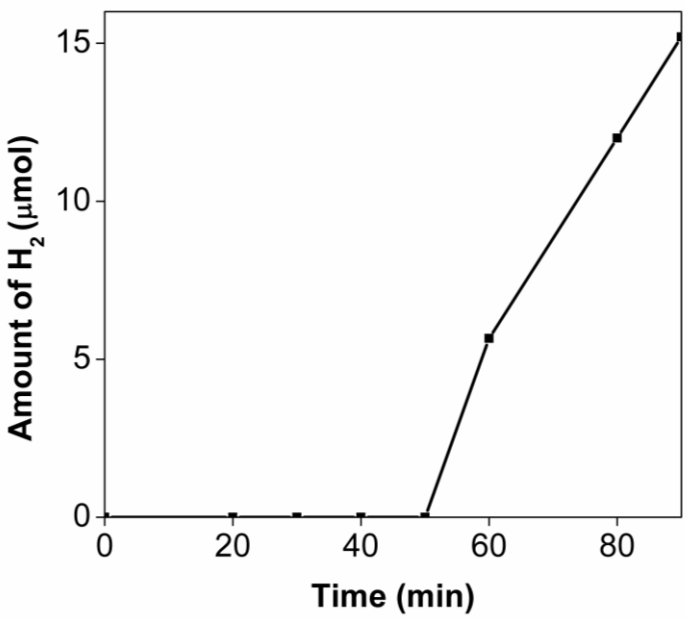

Figure 3.9. H_2 evolution of 1.0 mM of **8** dissolved in 1.0 M Na_2SO_4 solution. The electrolysis was carried out at an applied potential of -2.0 V *vs.* Ag/AgCl. The background levels of H_2 produced by the glassy carbon electrode in the absence of **3.8** has been subtracted from this data.

A rinse test was then carried out after the CPE. The same glassy carbon electrode was rinsed with DI water and acetone to wash away residual **3.8**. It was then used as the working electrode in acetonitrile containing 1.0 M of DI water for a second run. H_2 was detected once again as the electrolysis product. This clearly confirmed that the active species was a heterogeneous catalyst that had been deposited during the first round of electrolysis. The charge consumed within 1300 s of 7.1 C exceeded the charge required for the three-electron reduction of all the Co^{III} TAML in solution to Co^0 (2.3 C), suggesting that **3.8** may have been completely demetallated by the applied potential of -1.7 V in acetonitrile (1.0 M DI water) during CPE.

HRTEM, EDS, and XPS were carried out to further investigate the electrodeposited material. The HRTEM images showed nano-sized, non-uniform particles coated on the glassy carbon electrode (Figures 3.10a). The particles showed lattice d-spacings of 0.226 and 0.208 nm corresponding to the (111) and the (200) plane respectively, which are consistent with those of Co^0 nanoparticles (Figure 3.10d). Furthermore, HAABF-STEM together with elemental mapping verified the uniform distribution of Co in the sample, with some alumina present, likely from the abrasives used for polishing the carbon electrode (Figure 3.10).

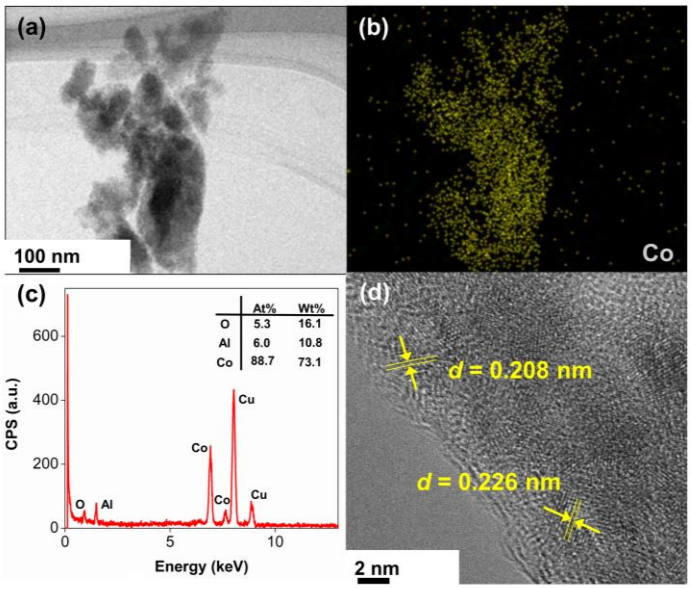

Figure 3.10. (a) HAABF-STEM of the Co particles. (b) Elemental mapping of Co particles (yellow) and (c) elemental distribution of particles using EDS. (d) lattice fringes with d-spacings of 0.226 nm and 0.208 nm corresponding to (111) plane and (200) plane of Co^0 nanoparticles.

The oxidation states and chemical nature of the electrodeposited film was further investigated by XPS experiments. Figure 3.11a shows the XPS spectrum in the Co 2p window for a sample of the nanoparticulate layer. The peak and shoulder of the Co 2p3/2 band can be fit to three distinct peaks with binding energies of 779.9, 782.1, and 785.9 eV.

These three peaks' binding energies are similar to those of the anhydrous $CoCl_2$ that we used as a reference for materials containing Co^{II} (Figure 3.11b). For the $CoCl_2$ sample, the two peaks of the Co $2p_{3/2}$ band are fitted with two components at higher binding that could be satellite or shake-up peaks, while the two more components at lower binding energies are consistent with Co^{II} interacting with Cl.[24] By comparing the data from the nanoparticulate film with those from $CoCl_2$, it appeared that there may be some Co^{II} present in the electrodeposited material, likely due to partial oxidation of the surface Co^0 by air.

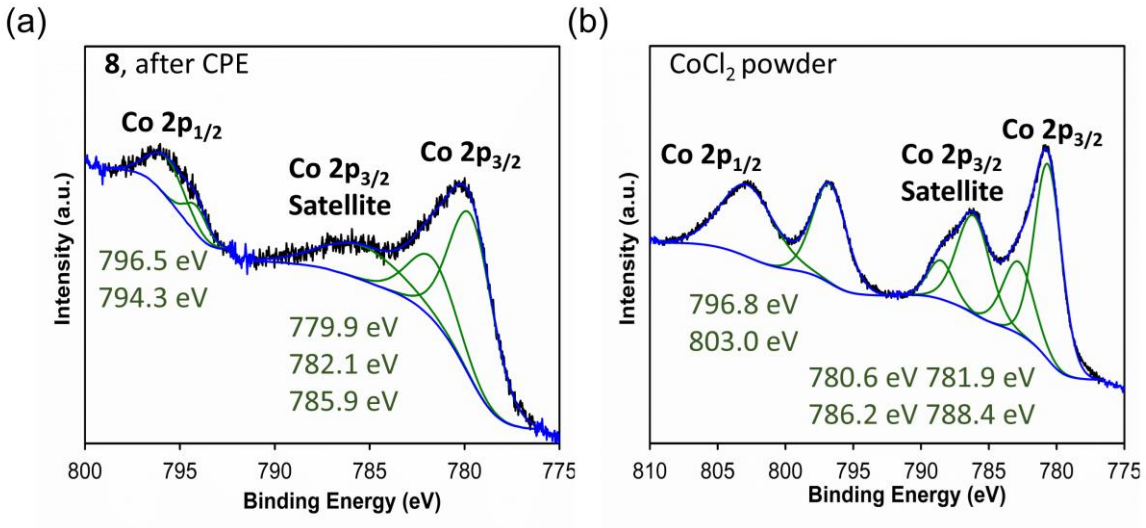

Figure 3.11. XPS spectra of (a) **3.8** after CPE and (b) anhydrous $CoCl_2$.

Since there had been previous reports of electrodeposited Co-based heterogeneous catalysts that were capable of proton reduction in aqueous buffer solutions,[63] we examined if the Co^0 nanoparticulate film on our electrode had the same properties as those reports. We conducted linear sweep voltammetry experiments on **3.8** to determine the overpotential of H_2 evolution for the Co^0 nanoparticulate layer in a phosphate buffer solution (KH_2PO_4/K_2HPO_4, 0.50 M, pH = 7.2). However, unlike what Saveant and coworkers observed,[63] the onset of the catalytic current occurred at a similar potential of -1.1 V, with or without **3.8**, suggesting that our Co^0 film was distinct from the ones in previous reports. Thus, it appears that there are subtle differences in the nature of the electrodeposited Co^0

heterogeneous catalyst that depend on the choice of the precursor. In our system, the Co^0 nanoparticulate film mainly showed electrocatalytic H_2 evolution activity at intermediate concentrations of water (around 1.0 M). The table 3.2 summarised the activity of the Co complex in comparison with other leading relevant catalysts reported in literature.

Table 3.2. Summary of the activity of the Co complex in comparison with other leading Co catalysts reported in literature.

Catalyst	Faradaic Efficiency (%)	Applied Potential (V vs. SHE)	Electrode	Condition	TOF (mol H_2/mol cat.h)	Ref
This work	-	-1.80	Glassy carbon	CH_3CN, 1.0 M of H_2O	0.018	-
2.1	-	-0.49	Glassy carbon	DMF: HOTf, 1.2 M H_2O in CH_3CN	1.1×10^5	[30]
2.2	-	-0.20	Glassy carbon	DMF: HOTf, 0.034 M H_2O in CH_3CN	2.6×10^6	[64]
2.3	-	−0.17	Glassy carbon	DMF:HOTf, 0.27 M H_2O in CH_3CN	3.7×10^6	[64]
2.4	-	−0.24	Glassy carbon	DMF:HOTf, 0.05 M H_2O in CH_3CN	2.8×10^6	[64]
2.5	-	−0.18	Glassy carbon	DMF:HOTf, 0.27 M H_2O in CH_3CN	4.3×10^5	[64]
2.6	-	−0.21	Glassy carbon	DMF:HOTf, 0.08 M H_2O in CH_3CN	1.7×10^6	[64]
2.8	92	−1.00	Glassy carbon /RVC	H_2O in $[(DBF)H]NTf_2$	4.3×10^4	[65]

2.9	-	−1.46	Hg	H_2O/ CH_3CN (2:1)	-	[66]
2.10	-	−1.26	Hg	0.1 M $NaClO_4$ in H_2O	-	[67]
2.11	-	−1.26	Hg	0.1 M $NaClO_4$ in H_2O	-	[67]
2.12	<80	−1.36	Hg	H_2O	-	[66]
2.19	79	−0.69	Glassy carbon	pH 2.2 phosphate buffer	8.0	[68]
2.21	30	−0.69	Glassy carbon	pH 2.2 phosphate buffer	1.0	[68]
2.22	81	−0.69	Glassy carbon	pH 2.2 phosphate buffer	11.5	[68]
2.23	80	−0.69	Glassy carbon	pH 2.2 phosphate buffer	9.0	[68]
2.24	>99	−0.77	Glassy carbon	TFA, H_2O/ CH_3CN (1:1)	-	[69]

3.5. Conclusion

Late first-row transition metal complexes supported by a new electron-rich TAML ligand were synthesised and characterised by spectroscopic and structural studies. Complex **3.11** exhibited reversible redox waves, whereas the **3.8** exhibited a quasi-reversible Co^{III}/Co^{II} redox couple. Both the **3.8** and **3.11** were then investigated for electrocatalytic proton reduction activity in aqueous solutions and acetonitrile containing neutral water. Interestingly, **3.8**, but not **3.11**, appeared to show electrocatalytic proton reduction, albeit only at intermediate concentrations of water around 1.0 M. However, upon careful examination, we discovered that an electrodeposited Co^0 nanoparticulate film was responsible for the catalytic activity, as verified by electron microscopy and XPS. We

propose that with different concentrations of water, **3.8** adopted distinct coordination geometries, with the kinetically labile square pyramidal intermediate being more susceptible to demetallation than the low-spin octahedral complex.

3.6. Experimental Section

Chemicals were obtained from Sigma-Aldrich, Alfa-Aesar, and Tokyo Chemical Industry Co., Ltd. (TCI). Unless otherwise noted, the commercial reagents were used as purchased. All reactions involving air- or moisture-sensitive compounds were performed by standard Schlenk techniques in oven-dried reaction vessels under an argon atmosphere.

The ^{1}H and ^{13}C NMR measurements were recorded on Bruker AV-400 (400 MHz) or BBFO-400 (400 MHz) NMR spectrometers. The ^{1}H and ^{13}C NMR spectra are reported in ppm downfield referenced to the residual protons of the deuterated solvents. UV-visible absorption measurements were carried out on a Shimadzu UV-3600 spectrophotometer. Elemental analyses were performed with an Elementar vario MICRO cube analyser. High-resolution mass spectra (HR-MS) were obtained with a Q-TOF Premier LC HR mass spectrometer.

Cyclic Voltammetry

The controlled-potential coulometric experiments were performed using a Biologic SP-300 potentiostat. A three-electrode electrochemical cell was used with a glassy carbon to the Ag/AgCl scale using E_{NHE} = E(Ag/AgCl) + 0.197 V. Before each experiment, the working electrode (glassy carbon) was polished using a 0.05 μm alumina suspension on a polishing pad, followed by sonication in DI water for 10 min, and dried in air. The saturated Ar solutions were prepared by bubbling Ar through the solvents for 30 min.

Scan Rate Dependence Study

In an electrochemical cell, 1.0 mM of **3.8** or **3.11** was dissolved in 0.10 M tetrabutylammonium hexafluorophosphate (n-Bu_4NPF_6) in acetonitrile (5 mL). CV

measurements were collected at various scan rates ranging from 100 mV s^{-1} to 1000 mV s^{-1}.

H_2O Dependence Study

In an electrochemical cell, 1.0 mM of **3.8** was dissolved in 0.10 M n- Bu_4NPF_6 in acetonitrile by adding 0 − 3.0 M H_2O at various scan rates. Plots of i_c/i_p versus [H_2O] were used to determine the order with respect to the H_2O concentration. In the plot, i_c is the catalytic current and i_p is the peak current observed for the catalyst in the absence of acid.

CPE for the Determination of Faradaic Efficiency, TON and TOF

The CPE measurements performed to calculate the Faradaic efficiency of the catalyst were performed on a CHI 660D workstation (CH Instruments. Inc.) with a customised gas-tight, three-neck, 63 mL electrolysis cell. A glassy carbon rod was employed as the working electrode, while a platinum coil counter electrode and an Ag/AgCl reference electrode were placed in the electrolyte solution. The electrolysis was carried out at an applied potential of -2.0 V. The solution was constantly stirred during the electrolysis experiments. Gas samples were taken from the headspace of the cell and injected into an Agilent 7890A gas-chromatograph/and a Shimadzu gas chromatograph GC-2010 (with a TCD, a 5 Å molecular sieve column (2 mm x 5 m), and Ar as the carrier gas). The amount of H_2 was quantified by a GC calibration curve derived by using H_2 samples of known concentration. The amount of H_2 generated from the electrolysis experiments and the amount of consumed charge of each CPE experiment were calculated based on the following equations:

$$TON = n_{hydrogen}/n_{cat} \text{ (mol } H_2 \text{ per mol catalyst)}$$

$$TOF = TON/ \text{ (duration of electrolysis) (mol } H_2 \text{ per mol catalyst per hour)}$$

The $n_{hydrogen}$ is the number of moles of H_2 generated from the electrolysis, and n_{cat} is the number of moles of catalyst used in the electrolysis experiment.

The Faradaic efficiency was calculated as follows:

$$\text{Faradaic efficiency for } H_2 = (2xF /Q) \times 100\%$$

The total amount of charge (Q) passed through the cell was obtained from the charge-time curve. The total amount of H_2 produced (x) was measured by a GC. Since two electrons are needed to make one H_2 molecule from two protons, there is a coefficient of 2 in the numerator.

Materials Characterisation

TEM

The morphology and structure of the samples were characterised by TEM with a JEOL JEM-1400 operated at 100 kV and a HRTEM with a JEOL JEM-2100F operated at 200 kV. The HRTEM is equipped with a STEM and an EDS for STEM images and elemental analysis, respectively. The sample preparation involved sonicating an aliquot of the electrodeposited material on the electrode in analytical-grade ethanol for 10 min. A single drop of the colloidal solution was dropped on a thin, lacey, carbon-coated Cu TEM grid and dried in air. This TEM grid was then used in the imaging experiments.

FESEM

The FESEM equipped with an energy-dispersive X-ray spectrometer was used to examine the samples using a JEOL JSM-7600F operated at 5 kV. Each sample was prepared by coating a uniform layer of the materials on SPI double-sided adhesive carbon tape and mounted on an aluminium (Al) SEM specimen stub.

XPS

XPS experiments were performed using a Phoibos 100 spectrometer and a Mg X-ray source (SPECS, Germany) working at 12.5 kV equipped with dual Al/Mg anodes. XPS measurements were performed on solid powder samples pressed onto SPI double-sided adhesive carbon tape. The XPS data obtained were processed using the CasaXPS software. The spectra were calibrated internally by setting the C 1s signal at 284.6 eV.

Synthesis of 2,4-diazido-2,4-dimethylpentanone (3.2):

This compound was synthesised according to the procedure described by Collins and coworkers.[40] To a solution of 2,4-dibromo-2,4-dimethylpentanone (**3.2**) (4.49 g, 16.5 mmol) in ethanol (60 mL) was added a solution of NaN_3 (2.36 g, 36.3 mmol, 2.2 equiv.) in water (30 mL). The solution was heated under reflux (external temperature set at 94 ºC) for 16 h to give pale yellow solution. The ethanol was removed under reduced pressure until the solution turned cloudy. The solution was then extracted with n-pentane (3 x 25 mL), dried over Na_2SO_4, and concentrated under reduced pressure. This concentrated solution was used in the next step without further purification due to concerns over the safety of isolating large amounts of this organic aliphatic azide. ^{1}H NMR (300 MHz, $CDCl_3$): 1.86 (s, 12 H) ppm. HRMS (ESI+, m/z) calculated for $C_7H_{13}N_6O$ $[M + H]^+$ m/z = 197.1151, found 197.1159.

Synthesis of 2,4-diamino-2,4-dimethylpentan-3-ol (3.3):

A 100 mL Schlenk flask was charged with anhydrous THF (45 mL) and $LiAlH_4$ (1.37 g, 36.0 mmol) under a nitrogen atmosphere. The mixture was cooled to –10 ºC and the concentrated solution of **3.2**, obtained in the previous step, was added slowly under a N_2 positive pressure. The resulting mixture's temperature was maintained below 0 ºC and was stirred for 30 min. Subsequently, the mixture was warmed to room temperature and stirred for another 24 h. The mixture was then cooled in an ice bath at –5 ºC and the $LiAlH_4$ was quenched by addition of aqueous NaOH solution (10%). The supernatant was decanted into a round bottom flask and the residue in the Schlenk flask was extracted with ethyl acetate (3 x 10 mL). The combined organic extracts were dried over Na_2SO_4 and the solvents were removed under reduced pressure. The viscous colorless oil thus obtained was dissolved in $CHCl_3$ and dried over Na_2SO_4. The solvent was removed under reduced pressure, and the residue was further dried under high vacuum until colorless crystals formed (1.92 g, 13.1 mmol, 80%). ^{1}H NMR (300 MHz, DMSO-d_6): 1.07 (s, 6 H), 1.08 (s, 6 H), 2.82 (s, 1 H)

ppm. ^{13}C NMR (75 MHz, DMSO-d_6): 29.25, 29.74, 53.85, 82.46 ppm. HRMS (ESI+, m/z) calculated for $C_7H_{19}N_2O$ $[M + H]^+$ m/z = 147.1497, found 147.1498. Elemental analyses for $C_7H_{18}N_2O$ calculated: C, 57.49; H, 12.41; N, 19.16%; found: C, 57.38; H, 12.52; N, 19.10%.

Synthesis of bis-2,4-(2-bromo-2-methylpropanamido)-2,4-dimethylpentan-3-ol (3.4):

To a 100 mL Schlenk flask, **3.3** (1.25 g, 8.55 mmol), triethylamine (TEA, 2.00 g, 19.8 mmol), and DCM (30 mL) were added under a N_2 atmosphere at room temperature. The solution was cooled to 0 ºC and α-bromoisobutyryl bromide (4.13 g, 18.0 mmol) was syringed in dropwise. The reaction is very exothermic, and the reagent should be added in very carefully to avoid boiling the solvent. After complete addition, the reaction mixture was stirred for 30 min at 0 ºC. The DCM was then removed under reduced pressure and the white solid thus obtained was dissolved in ethyl acetate (20 mL) and washed with brine (2 x 10 mL). The organic phase was dried over Na_2SO_4 and concentrated under reduced pressure. The obtained white solid was transferred to a frit, washed with hexane (5 x 5 mL), and dried under vacuum, yielding a white solid product (3.34 g, 7.53 mmol, 88 %). ^{1}H NMR (400 MHz, $CDCl_3$): 1.48 (s, 6 H), 1.50 (s, 6 H), 1.92 (d, J = 2 Hz, 12 H), 3.94 (s, 1 H), 5.29 (s, 1 H), 6.93 (s, 2 H) ppm. ^{13}C NMR (100 MHz, $CDCl_3$): 25.70, 25.79, 32.51, 32.57, 59.31, 63.31, 79.51, 172.28 ppm. HRMS (ESI+, m/z) calculated for $C_{15}H_{29}Br_2N_2O_3$ $[M + H]^+$ m/z = 443.0545, found 443.0540. Elemental analyses for $C_{15}H_{28}Br_2N_2O_3$ calculated: C, 40.56; H, 6.35; N, 6.31%; found: C, 40.93; H, 6.58; N, 5.98%.

Synthesis of bis-2,4-(2-azido-2-methylpropanamido)-2,4-dimethylpentan-3-ol (3.5):

To a solution of **3.4** (3.31 g, 7.45 mmol) in ethanol (60 mL) was added a solution of NaN_3 (2.91 g, 44.7 mmol, 6.0 equiv.) in water (20 mL). The solution was heated at 78 ºC for 36 h. The ethanol was removed under reduced pressure and the reaction mixture was extracted with DCM (3 x 15 mL) and dried over Na_2SO_4. The DCM was removed under reduced pressure and the remaining viscous oil was further dried under vacuum until it became

colorless crystals (2.71 g, 7.36 mmol, 99%). ^{1}H NMR (300 MHz, $CDCl_3$): 1.42 (s, 6 H), 1.45 (s, 6 H), 1.49 (s, 6 H), 1.49 (s, 6 H), 3.87 (d, J = 7.8 Hz, 1 H), 5.70 (d, J = 8.0 Hz, 1 H), 6.69 (s, 2 H) ppm. $^{13}C\{^{1}H\}$ NMR (75 MHz, $CDCl_3$): 24.41, 24.48, 25.96, 26.05, 58.96, 64.59, 79.64, 172.61 ppm. HRMS (ESI+, m/z) calculated for $C_{15}H_{29}N_8O_3$ $[M + H]^+$ m/z = 369.2363, found 369.2361. Elemental analyses for $C_{15}H_{28}N_8O_3$ calculated: C, 48.90; H, 7.66; N, 30.41%; found: C, 48.99; H, 7.41; N, 30.24%.

Synthesis of bis-2,4-(2-amino-2-methylpropanamido)-2,4-dimethylpentan-3-ol (3.6):

Red-Al (70% in toluene, 3.29 g, 16.3 mmol, 6 equiv.) was added dropwise to a solution of **3.5** (1.00 g, 2.71 mmol) in dry THF (20 mL) over 30 min under a N_2 atmosphere at –10 ºC and stirred for an additional 3 h. The excess Red-Al was quenched with NaOH (10% aqueous solution, 20 mL). The supernatant was decanted, and the solvent was removed under reduced pressure. The oily residue was dissolved in ethyl acetate (15 mL) and extracted with 1 M HCl (3 x 10 mL). The combined aqueous extracts were neutralised with Na_2CO_3 and dried under reduced pressure. The residue was subsequently extracted with chloroform (3 x 10 mL). The combined chloroform extracts were dried over Na_2SO_4, filtered, and the filtrate was concentrated by rotary evaporation. Additional drying in vacuo yielded a colorless solid (0.80 g, 2.53 mmol, 93%). ^{1}H NMR (500 MHz, $CDCl_3$): 1.32 (s, 6 H), 1.33 (s, 6 H), 1.43 (s, 6 H), 1.47 (s, 6 H), 3.86 (s, 1 H), 6.40 (s, 1 H), 7.95 (s, 2 H) ppm. $^{13}C\{^{1}H\}$ NMR (126 MHz, $CDCl_3$): 25.95, 26.38, 29.12, 29.17, 55.11, 58.28, 80.27, 177.96 ppm. HRMS (ESI+, m/z) calculated for $C_{15}H_{33}N_4O_3$ $[M + H]^+$ m/z = 317.2553, found 317.2561. Elemental analyses for $C_{15}H_{32}N_4O_3$ calculated: C, 56.93; H, 10.19; N, 17.71%; found: C, 56.77; H, 10.21; N, 17.53%.

Synthesis of TAML (3.7):

To a 200 mL Schlenk flask, **3.6** (0.200 g, 0.63 mmol), anhydrous TEA (0.185 mL, 0.134 g, 1.32 mmol) and anhydrous THF (140 mL) were added under nitrogen at room temperature. The solution was cooled to –10 ºC and a solution of 2,2-dimethylmalonyl chloride (0.083

mL, 0.107 g, 0.630 mmol) in anhydrous THF (60 mL) was added dropwise over 8 h by a dropping funnel. The reaction temperature was increased to 25 ºC and the mixture was stirred for another 5 h. Subsequently, the solvent was removed by rotary evaporation. The white residue was suspended in $CHCl_3$ (30 mL), washed with 10% aqueous brine (3 x 15 mL), dried over Na_2SO_4, and the solvent was removed by rotary evaporation. The white residue was purified by silica gel column chromatography (ethyl acetate as the solvent) to yield TAML (0.150 g, 0.360 mmol, 57%). ^{1}H NMR (500 MHz, $CDCl_3$): 1.31 (s, 6 H), 1.46 (s, 6 H), 1.51 (s, 6 H), 1.52 (s, 6 H), 1.54 (s, 3 H), 1.54 (s, 3 H), 3.53 (s, 1 H), 6.14 (s, 2 H), 6.34 (s, 2H) ppm. ^{13}C{^{1}H} NMR (126 MHz, $CDCl_3$): 20.62, 20.90, 25.81, 29.54, 52.41, 57.95, 58.46, 82.75, 171.49, 173.93 ppm. HRMS (ESI+, m/z) calculated for $C_{20}H_{37}N_4O_5$ $[M + H]^+$ m/z = 413.2764, found 413.2761. Elemental analyses for $C_{20}H_{36}N_4O_5$ calculated: C, 58.23; H, 8.80; N, 13.58%; found: C, 58.28; H, 9.16; N, 13.96%.

Synthesis of 3.8:

Solutions of **3.7** (25.0 mg, 0.060 mmol) in 5 mL anhydrous THF was added to a solution of LiHMDS (45.2 mg, 0.27 mmol, 4.5 equiv.) in 5 mL anhydrous THF in a 25 mL Schlenk flask under N_2 at room temperature. The mixture was stirred for 15 min before $CoCl_2$ (7.81 mg, 0.060 mmol) was added. The mixture became dark purple within 30 min. The reaction mixture was then stirred for another 2 h. The solvent was removed by rotary evaporation and the residue was washed with DCM (3 x 10 mL), followed by pentane (3 x 5 mL). The residue was then dried under vacuum. The dark red solid was suspended in THF (10 mL) and filtered. The dark red filtrate was dried in vacuo to yield the desired product (26.4 mg, 0.060 mmol, 92%).

Synthesis of 3.9:

A solution of **3.7** (50.0 mg, 0.12 mmol) in 10 mL anhydrous THF was added to a solution of lithium hexamethyldisilazide (LiHMDS, 90.4 mg, 0.54 mmol, 4.5 equiv.) in 5 mL anhydrous THF in a 25 mL Schlenk flask under N_2 at room temperature. The mixture was

stirred for 15 min under N_2. $(PPh_3)_2NiBr_2$ (89.2 mg, 0.12 mmol) was added and the mixture became a pale orange solution within 5 min. The solvent was removed under reduced pressure and the residue was washed with DCM (3 x 10 mL), followed by acetonitrile (3 x 5 mL). The pale orange solid obtained was dissolved in methanol (15 mL), filtered, and the filtrate was dried under reduced pressure to yield **3.9** (55.8 mg, 0.12 mmol, 96%).%). ^{1}H NMR (300 MHz, MeOD): 1.33 (s, 6 H), 1.39 (s, 6 H), 1.47 (s, 6 H), 1.48 (s, 6 H), 1.61 (s, 3 H), 1.73 (s, 3 H), 2.88 (s, 1 H) ppm. HRMS (ESI+, m/z) calculated for $C_{20}H_{35}N_4NiO_5$ $[M + 3H]^+$ m/z = 369.1961, found 369.1956. $[(TAML)Ni]^{2-}$: HRMS (ESI-, m/z) calculated for $C_{20}H_{33}N_4NiO_5$ $[M + H]^-$ m/z = 467.1804, found 467.1810 Elemental analyses for $C_{20}H_{32}Li_2NiN_4O_5$ calculated: C, 49.93; H, 6.71; N, 11.65%; found: C, 50.16; H, 6.70; N, 11.47%.

Synthesis of 3.10:

Complex **3.8** (8.00 mg, 0.017 mmol) was dissolved in 3 mL of water with Et_4NF (15.0 mg, 0.10 mmol, 6 equiv.) and stirred for 12 h. The water was removed under reduced pressure and the solid dark red residue was dissolved in DCM (5 mL). The DCM was removed under reduced pressure to give a deep red powder. (9.5 mg, 0.015 mmol, 93%). Vapor diffusion of diethyl ether into DCM gave deep red crystals suitable for XRD. Elemental analyses for $C_{28}H_{52}CoN_5O_5$ calculated: C, 56.27; H, 8.77; N, 11.72%; found: C, 56.52; H, 8.85; N, 11.52%. HRMS (ESI-, m/z) calculated for $C_{20}H_{32}N_4CoO_5$ $[M]^-$ m/z = 467.1705, found 467.1703.

Synthesis of 3.11:

Complex **3.9** (8.00 mg, 0.017 mmol) was dissolved in 3 mL of water. Et_4NF (15.0 mg, 0.10 mmol, 6 equiv.) was added and the reaction mixture was stirred for 12 h. The solvent was removed under reduced pressure and the residue was suspended in DCM (5 mL). The mixture was filtered, and the filtrate was dried by rotary evaporation to give **3.11** (10.2 mg, 0.014 mmol, 88%). ^{1}H NMR (300 MHz, MeOD): 1.37 (s, 6 H), 1.37 (s, 6 H), 1.48 (s, 6 H),

1.48 (s, 6 H), 1.62 (s, 3 H), 1.69 (s, 3 H), 1.88 (s, 1 H), 2.02 (s, 1 H) ppm. HRMS (ESI-, m/z) calculated for $C_{20}H_{33}N_4NiO_5$ $[M + H]^-$ m/z = 467.1804, found 467.1810. Elemental analyses for $C_{36}H_{72}N_6NiO_5$ calculated: C, 59.42; H, 9.97; N, 11.55%; found: C, 59.21; H, 10.14; N, 11.32%.

3.6. References

(1) Jin, H.; Guo, C.; Liu, X.; Liu, J.; Vasileff, A.; Jiao, Y.; Zheng, Y.; Qiao, S.-Z. *Chem. Rev.* **2018,** *118*, 6337-6408.

(2) Tao, H. C.; Gao, Y. A.; Talreja, N.; Guo, F.; Texter, J.; Yan, C.; Sun, Z. Y. *J. Mater. Chem. A* **2017,** *5*, 7257-7284.

(3) Mistry, H.; Varela, A. S.; Kuhl, S.; Strasser, P.; Cuenya, B. R. *Nat. Rev. Mater.* **2016,** *1*, 1-14.

(4) Savéant, J.-M. *Chem. Rev.* **2008,** *108*, 2348-2378.

(5) Vincent, K. A.; Parkin, A.; Armstrong, F. A. *Chem. Rev.* **2007,** *107*, 4366-4413.

(6) Costentin, C.; Robert, M.; Savéant, J.-M. *Acc. Chem. Res.* **2010,** *43*, 1019-1029.

(7) Rakowski Dubois, M.; Dubois, D. L. *Acc. Chem. Res.* **2009,** *42*, 1974-1982.

(8) Francke, R.; Schille, B.; Roemelt, M. *Chem. Rev.* **2018,** *118*, 4631-4701.

(9) Nutting, J. E.; Rafiee, M.; Stahl, S. S. *Chem. Rev.* **2018,** *118*, 4834-4885.

(10) Yan, M.; Kawamata, Y.; Baran, P. S. *Chem. Rev.* **2017,** *117*, 13230-13319.

(11) Dokic, M.; Soo, H. S. *Chem. Commun.* **2018,** *54*, 6554-6572.

(12) Faunce, T. A.; Lubitz, W.; Rutherford, A. W.; MacFarlane, D. R.; Moore, G. F.; Yang, P. D.; Nocera, D. G.; Moore, T. A.; Gregory, D. H.; Fukuzumi, S.; Yoon, K. B.; Armstrong, F. A.; Wasielewski, M. R.; Styring, S. *Energy Environ. Sci.* **2013,** *6*, 695-698.

(13) Khaselev, O.; Turner, J. A. *Science* **1998,** *280*, 425-427.

(14) Lewis, N. S.; Nocera, D. G. *Proc. Natl. Acad. Sci. U.S.A.* **2006,** *103*, 15729-15735.

(15) Pu, Z. H.; Amiinu, I. S.; Kou, Z. K.; Li, W. Q.; Mu, S. C. *Angew. Chem. Int. Ed* **2017,** *56*, 11559-11564.

(16) Seh, Z. W.; Kibsgaard, J.; Dickens, C. F.; Chorkendorff, I. B.; Norskov, J. K.; Jaramillo, T. F. *Science* **2017,** *355*, eaad4998.

(17) Thoi, V. S.; Sun, Y. J.; Long, J. R.; Chang, C. J. *Chem. Soc. Rev.* **2013,** *42*, 2388-2400.

(18) Zee, D. Z.; Chantarojsiri, T.; Long, J. R.; Chang, C. J. *Acc. Chem. Res.* **2015,** *48*, 2027-2036.

(19) Chen, L.; Wang, M.; Han, K.; Zhang, P. L.; Gloaguen, F.; Sun, L. C. *Energy Environ. Sci.* **2014,** *7*, 329-334.

(20) Helm, M. L.; Stewart, M. P.; Bullock, R. M.; DuBois, M. R.; DuBois, D. L. *Science* **2011,** *333*, 863-866.

(21) Koshiba, K.; Yamauchi, K.; Sakai, K. *Angew. Chem. Int. Ed.* **2017,** *56*, 4247-4251.

(22) Shao, H.; Muduli, S. K.; Tran, P. D.; Soo, H. S. *Chem. Commun.* **2016,** *52*, 2948-2951.

(23) Sherbow, T. J.; Fettinger, J. C.; Berben, L. A. *Inorg. Chem.* **2017,** *56*, 8651-8660.

(24) Thompson, E. J.; Berben, L. A. *Angew. Chem. Int. Ed.* **2015,** *54*, 11642-11646.

(25) Halter, D. P.; Heinemann, F. W.; Bachmann, J.; Meyer, K. *Nature* **2016,** *530*, 317-321.

(26) Halter, D. P.; Heinemann, F. W.; Maron, L.; Meyer, K. *Nat. Chem.* **2018,** *10*, 259-267.

(27) Halter, D. P.; Palumbo, C. T.; Ziller, J. W.; Gembicky, M.; Rheingold, A. L.; Evans, W. J.; Meyer, K. *J. Am. Chem. Soc.* **2018,** *140*, 2587-2594.

(28) Chen, H.; Sun, Z.; Ye, S.; Lu, D.; Du, P. *J. Mater. Chem. A* **2015,** *3*, 15729-15737.

(29) DuBois, M. R.; DuBois, D. L. *Chem. Soc. Rev.* **2009,** *38*, 62-72.

(30) Helm, M. L.; Stewart, M. P.; Bullock, R. M.; DuBois, M. R.; DuBois, D. L. *Science* **2011,** *333*, 863-866.

(31) Bang, S.; Lee, Y. M.; Hong, S.; Cho, K. B.; Nishida, Y.; Seo, M. S.; Sarangi, R.; Fukuzumi, S.; Nam, W. *Nat. Chem.* **2014,** *6*, 934-940.

(32) Dubois, M. R.; Dubois, D. L. *Acc. Chem. Res.* **2009,** *42*, 1974-1982.

(33) Tsui, E. Y.; Tran, R.; Yano, J.; Agapie, T. *Nat. Chem.* **2013,** *5*, 293-299.

(34) Artero, V.; Saveant, J. M. *Energy Environ. Sci.* **2014,** *7*, 3808-3814.

(35) Bartos, M. J.; Gordon-Wylie, S. W.; Fox, B. G.; James Wright, L.; Weintraub, S. T.; Kauffmann, K. E.; Münck, E.; Kostka, K. L.; Uffelman, E. S.; Rickard, C. E. F.; Noon, K. R.; Collins, T. J. *Coord. Chem. Rev.* **1998,** *174*, 361-390.

(36) Bartos, M. J.; Kidwell, C.; Kauffmann, K. E.; Gordon-Wylie, S. W.; Collins, T. J.; Clark, G. C.; Münck, E.; Weintraub, S. T. *Angew. Chem. Int. Ed.* **1995,** *34*, 1216-1219.

(37) Chanda, A.; Popescu, D. L.; Tiago de Oliveira, F.; Bominaar, E. L.; Ryabov, A. D.; Munck, E.; Collins, T. J. *J. Inorg. Biochem.* **2006,** *100*, 606-619.

(38) Collins, T. J. *Acc. Chem. Res.* **2002,** *35*, 782-790.

(39) Collins, T. J.; Kostka, K. L.; Munck, E.; Uffelman, E. S. *J. Am. Chem. Soc.* **1990,** *112*, 5637-5639.

(40) Collins, T. J.; Kostka, K. L.; Uffelman, E. S.; Weinberger, T. L. *Inorg. Chem.* **1991,** *30*, 4204-4210.

(41) Ellis, W. C.; Tran, C. T.; Denardo, M. A.; Fischer, A.; Ryabov, A. D.; Collins, T. J. *J. Am. Chem. Soc.* **2009,** *131*, 18052-18053.

(42) Ellis, W. C.; Tran, C. T.; Roy, R.; Rusten, M.; Fischer, A.; Ryabov, A. D.; Blumberg, B.; Collins, T. J. *J. Am. Chem. Soc.* **2010,** *132*, 9774-9781.

(43) Khetan, S. K.; Collins, T. J. *Chem. Rev.* **2007,** *107*, 2319-2364.

(44) Sen Gupta, S.; Stadler, M.; Noser, C. A.; Ghosh, A.; Steinhoff, B.; Lenoir, D.; Horwitz, C. P.; Schramm, K. W.; Collins, T. J. *Science* **2002,** *296*, 326-328.

(45) Kundu, S.; Chanda, A.; Khetan, S. K.; Ryabov, A. D.; Collins, T. J. *Environ. Sci. Technol.* **2013,** *47*, 5319-26.

(46) Demeter, E. L.; Hilburg, S. L.; Washburn, N. R.; Collins, T. J.; Kitchin, J. R. *J. Am. Chem. Soc.* **2014,** *136*, 5603-5606.

(47) Panda, C.; Debgupta, J.; Díaz Díaz, D.; Singh, K. K.; Sen Gupta, S.; Dhar, B. B. *J. Am. Chem. Soc.* **2014,** *136*, 12273-12282.

(48) Hong, S.; Pfaff, F. F.; Kwon, E.; Wang, Y.; Seo, M. S.; Bill, E.; Ray, K.; Nam, W. *Angew. Chem. Int. Ed.* **2014,** *53*, 10403-10407.

(49) Chandra, S.; Gupta, L. K. *Spectrachim. Acta A* **2005,** *61*, 2139-2144.

(50) Collins, T. J.; Nichols, T. R.; Uffelman, E. S. *J. Am. Chem. Soc.* **1991,** *113*, 4708-4709.

(51) Comba, P.; Kubeil, M.; Pietzsch, J.; Rudolf, H.; Stephan, H.; Zarschler, K. *Inorg. Chem.* **2014,** *53*, 6698-6707.

(52) Salavati-Niasari, M.; Abdolmohammadi, S. *J. Porous Mater.* **2009,** *16*, 19-26.

(53) Sangeetha, J. E.; Meenalochani, S.; Radha, K.; Chellappa, D. *Asian J. Chem.* **2008,** *20*, 4749-4754.

(54) Uffelman, E. S.; Doherty, J. R.; Schulze, C.; Burke, A. L.; Bonnema, K. R.; Watson, T. T.; Lee, D. W. *J. Chem. Educ.* **2004,** *81*, 182-185.

(55) Volov, A. N.; Zamilatskov, I. A.; Chernyshev, V. V.; Savinkina, E. V.; Chuvaev, V. F.; Kurochkina, N. M.; Tsivadze, A. Y. .*J. Coord. Chem.* **2014,** *67*, 3121-3134.

(56) Wang, H. X.; Butorin, S. M.; Young, A. T.; Guo, J. H. *J. Phys. Chem. C* **2013,** *117*, 24767-24772.

(57) Collins, T. J.; Uffelman, E. S. *Angew. Chem. Int. Ed.* **1989,** *28*, 1509-1511.

(58) Ghosh, A.; Ramidi, P.; Pulla, S.; Sullivan, S. Z.; Collom, S. L.; Gartia, Y.; Munshi, P.; Biris, A. S.; Noll, B. C.; Berry, B. C. *Catal. Lett.* **2010,** *137*, 1-7.

(59) Collins, T. J.; Powell, R. D.; Slebodnick, C.; Uffelman, E. S. *J. Am. Chem. Soc.* **1991,** *113*, 8419-8425.

(60) Popescu, D.-L.; Chanda, A.; Stadler, M.; de Oliveira, F. T.; Ryabov, A. D.; Münck, E.; Bominaar, E. L.; Collins, T. J. *Coord. Chem. Rev.* **2008,** *252*, 2050-2071.

(61) Sharma, S. K.; Upreti, S.; Gupta, R. *Eur. J. Inorg. Chem.* **2007,** *2007*, 3247-3259.

(62) Elgrishi, N.; Rountree, K. J.; McCarthy, B. D.; Rountree, E. S.; Eisenhart, T. T.; Dempsey, J. L. *J. Chem. Educ.* **2017,** *95*, 197-206.

(63) Anxolabéhère-Mallart, E.; Costentin, C.; Fournier, M.; Nowak, S.; Robert, M.; Savéant, J.-M. *J. Am. Chem. Soc.* **2012,** *134*, 6104-6107.

(64) Kilgore, U. J.; Roberts, J. A.; Pool, D. H.; Appel, A. M.; Stewart, M. P.; DuBois, M. R.; Dougherty, W. G.; Kassel, W. S.; Bullock, R. M.; DuBois, D. L. *J. Am. Chem. Soc.* **2011,** *133*, 5861-5872.

(65) Pool, D. H.; Stewart, M. P.; O'Hagan, M.; Shaw, W. J.; Roberts, J. A.; Bullock, R. M.; DuBois, D. L. *Proc. Natl. Acad. Sci. U.S.A* **2012,** *109*, 15634-15639.

(66) Fisher, B. J.; Eisenberg, R. *J. Am. Chem. Soc.* **1980,** *102*, 7361-7363.

(67) Collin, J. P.; Jouaiti, A.; Sauvage, J. P. *Inorg. Chem.* **1988,** *27*, 1986-1990.

(68) Sun, Y.; Bigi, J. P.; Piro, N. A.; Tang, M. L.; Long, J. R.; Chang, C. J. *J. Am. Chem. Soc.* **2011,** *133*, 9212-9215.

(69) McNamara, W. R.; Han, Z.; Yin, C. J.; Brennessel, W. W.; Holland, P. L.; Eisenberg, R. *Proc. Natl. Acad. Sci. U.S.A* **2012,** *109*, 15594-15599.

Chapter 4

Visible Light Driven Hydrogen Evolution by Molecular Nickel Catalysts with Time-Resolved Spectroscopic and DFT Insights

---

4.1. Foreword

In this study, we seek to understand the effect of ether arms on the secondary coordination on H_2 evolution activity. In this Chapter, we will discuss the effect of a Ni salicylaldimine catalyst, modified with pendant ether arms, on H_2 evolution activity in a photocatalytic system. The mechanism was probed using nanosecond TAS, TES, EPR, and UV-visible spectroscopic measurements. DFT calculations were also conducted to support the experimental data.

This chapter is based on the work published in *Inorganic Chemistry* (*Inorg. Chem.* **2019**, 58, 1469-1480). I am the first author for this paper. I analysed the obtained experimental data, prepared the manuscript drafts and revised it together with the help of Dr. Shao Haiyan. I designed the study together with Asst. Prof. Soo Han Sen and performed all the laboratory work at MSE and SPMS. All the synthesis, characterisation and kinetics were carried out by myself. Dr. Ng Yik Yie helped with the TAS and TES measurement for the mechanistic studies of the complex. Dr. Rakesh Ganguly assisted in resolving the single crystal structure of the complex. Dr. Lu Yunpeng assisted in the DFT calculations to provide mechanistic insight to the reaction mechanism.

Visible Light Driven Hydrogen Evolution by Molecular Nickel Catalyst with Time-Resolved Spectroscopic and DFT Calculation

Xian Liang Ho, Haiyan Shao, Yik Yie Ng, Rakesh Ganguly, Yunpeng Lu, and Han Sen Soo*

4.2. Abstract

H_2 is a clean fuel that can potentially be a future solution for the storage of intermittent renewable energy. However, current H_2 production is mainly dominated by the energy intensive steam reforming reaction, which consumes a fossil fuel, methane, and emits copious amounts of CO_2 as one of the by-products. To address this challenge, we report a molecular catalyst that produces H_2 from aqueous solutions, is composed of affordable, earth-abundant elements such as nickel, and has been incorporated into a system driven by visible light. Under optimised conditions, we observe a TON of 3880 in 6 h, among the best for photocatalytic H_2 evolution with Ni complexes from water-methanol solutions. Through nanosecond TAS, EPR, and UV-visible spectroscopic measurements, and supported by DFT calculations, we report a detailed study of this photocatalytic H_2 evolution cycle. We demonstrate that a one-electron reduced, predominantly ligand-centered, reactive Ni intermediate can be accessed under visible light irradiation using TEA as the sacrificial electron donor and reductive quencher of the initial photosensitiser excited state. In addition, the computational calculations suggest that the second coordination sphere ether arms can enhance the catalytic activity by promoting proton relay, similar to the mechanism among [FeFe] hydrogenases in Nature. Our study can form the basis for future development of H_2 evolution molecular catalysts that incorporate both ligand redox noninnocence and alternative second coordination sphere effects driven by visible light.

4.3. Introduction

With the growing threat of global climate change, intensified efforts have been devoted to the development of sustainable energy sources to reduce the reliance on fossil fuels.[1] The storage of solar energy in chemical bonds, also known as artificial photosynthesis, by splitting H_2O into H_2 (proton reduction) and O_2 (H_2O oxidation), has been explored as a potentially clean and carbon-free solution.[2] Semiconductor materials such as metal chalcogenides and phosphides have emerged as cost-effective replacements for the unsurpassed Pt as the photo- or electrocatalyst for proton reduction to H_2.[3-6] Nonetheless, although such heterogeneous systems exhibit remarkably high H_2 production rates or even self-healing abilities, detailed mechanistic investigations of the interfacial chemical processes remain challenging. In contrast, molecular photocatalytic systems are often highly selective and active, more amenable to spectroscopic probes for the elementary reaction steps and can be systematically designed and improved through ligand variations. Typically, molecular photocatalytic H_2 evolution systems consist of a light absorbing photosensitiser and a proton reduction catalyst, each of which can be independently optimised.[7,8] Thus, some critical aspects of creating improved artificial photosynthetic systems include the development of an affordable, efficient H_2 evolution catalyst, and a thorough understanding of the light absorption and electron transfer events.[9,10]

Historically, integrated photocatalytic systems comprising PGMs like Pt,[11,12] Rh,[13,14] Ir,[15] and Pd[16] have exhibited respectable performance for light absorption and H_2 evolution by the same molecule. However, new catalysts consisting of earth-abundant, first-row transition metals are increasingly sought after as more sustainable alternatives, due to the high price of PGMs.[17-19] For instance, Co-containing cobaloxime catalysts have been combined with a multitude of photosensitisers to produce H_2, although they have demonstrated modest stability and TON thus far.[20-23] Co polypyridyl complexes have also shown competent H_2 production activity under photodriven conditions.[24,25] On the other

hand, although DuBois, Bullock, and coworkers have reported Ni P_2N_2 complexes with exceptional electrocatalytic H_2 evolution activity exceeding that of even enzymatic systems,[26-28] the Ni P_2N_2 compounds exhibited surprisingly low TOF[29] for photocatalytic proton reduction until the second coordination sphere has been modified with phosphonic acid groups and the catalyst has been immobilised on metal oxide semiconductors.[30] In addition, Eisenberg and coworkers have presented seminal studies on homogeneous catalysis with redox noninnocent ligands by using Co dithiolene[31,32] and Ni thiolates[33,34] for the photogeneration of H_2 from aqueous organic solutions. Notably, their recent Ni pyridinethiolate molecular catalyst and photosensitiser system displayed an outstanding TON of 7300 in 30 h, with a proposed mechanism similar to the proton relays in natural hydrogenase enzymes.[34] Several other non-amine proton relays in small molecule redox catalysis have also been explored by Nocera and coworkers.[35,36] They reported that incorporating different proton relays on the second coordination sphere of metal complexes enhanced the H_2 evolution reaction and lowered the overpotential compared to the unmodified catalyst. These studies collectively demonstrated the importance of proton relays in the second coordination spheres of transition metal-based catalysts for efficient catalytic H_2 evolution reaction.

We had previously synthesised and employed new Ni salicylaldimine catalysts with pendant ether arms in the second coordination sphere to bind hydrated alkali metal cations and provide hydrogen-bonding stabilisation for enhanced electrocatalytic H_2 evolution reactivity.[37] Polyether appended salicylaldimine complexes have lately been explored by Yang, Blakemore, and others and shown to be effective for chelating alkali metal cations to form bimetallic complexes.[38-40] The coordinated and hydrated alkali metal cations can in turn act as non-amine proton relays to enhance H_2 evolution reaction by steering water molecules in close proximity to the metal center.[37] This approach capitalised on established principles in supramolecular chemistry that crown ethers effectively chelate alkali metal

cations and Lewis acids will increase the Bronsted acidity of coordinated water molecules, thus resulting in enhanced activity especially for proton-dependent catalysis.[41,42] In addition, the unbound ether groups can also form hydrogen-bonding interactions with water, which will raise the local concentration of water near the catalytically active metal center to promote the multi-electron and multi-proton transfer processes in H_2 evolution reaction.

We have now developed a more robust and active Ni salicylaldimine catalyst in two steps from affordable, commercially available reagents that can be incorporated into a molecular photocatalytic H_2 evolution system. This new Ni complex includes peripheral ether arms as well to allow us to investigate the effects of balancing ligand redox noninnocence and second coordination sphere effects on the H_2 evolution catalysis. Under optimised conditions, we utilised $[Ir^{III}(ppy)_2(dtbbpy)](PF_6)$ ($[Ir]^+$) as a light-harvester and TEA as a sacrificial electron donor and reductive quencher to achieve a photocatalytic H_2 evolution TON of 3880 within 6 h under visible light irradiation (> 420 nm), with H_2O and methanol as the proton sources. The $Ir]^+$ was chosen as the photosensitiser due to its long excited state lifetime, established photophysical characteristics, and highly reducing potential. Motivated by these results, we performed detailed experiments to elucidate the elementary steps of the H_2 evolution catalytic cycle through nanosecond TAS, EPR, and UV-visible spectroscopic measurements, further supported by intermediate isolation studies and DFT calculations. This study provides the mechanistic insights for small molecule activation and second coordination sphere effects in homogeneous catalysis, which can aid in the systematic improvement of H_2 evolution reaction activity not only for molecular systems,[18,31,43] but also for heterogeneous catalysts.

4.4. Results and Discussions

4.4.1. Synthesis and Characterisation of Nickel Complex

The nickel complex **4.2** was synthesised in high yields (83%) over two steps from affordable, commercially available reagents (Scheme 4.1). In the first step, 2,3-dihydroxybenzaldehyde was modified with a 2-methoxyethoxy ether arm to give 2-hydroxy-3-(2-methoxyethoxy)benzaldehyde (**4.1**). Subsequently, **4.1** reacted with 2,3-diamino-5-chloropyridine *via* a condensation reaction in the presence of nickel acetate in methanol (MeOH) to yield complex **4.2** as a deep red powder. Complex **4.2** was fully characterised by NMR spectroscopy, high- resolution mass spectrometry (HRMS), elemental analyses, and UV-visible spectroscopy.

Scheme 4.1. Synthetic Steps and X-ray Crystal Structure for Nickel Complex 4.2.

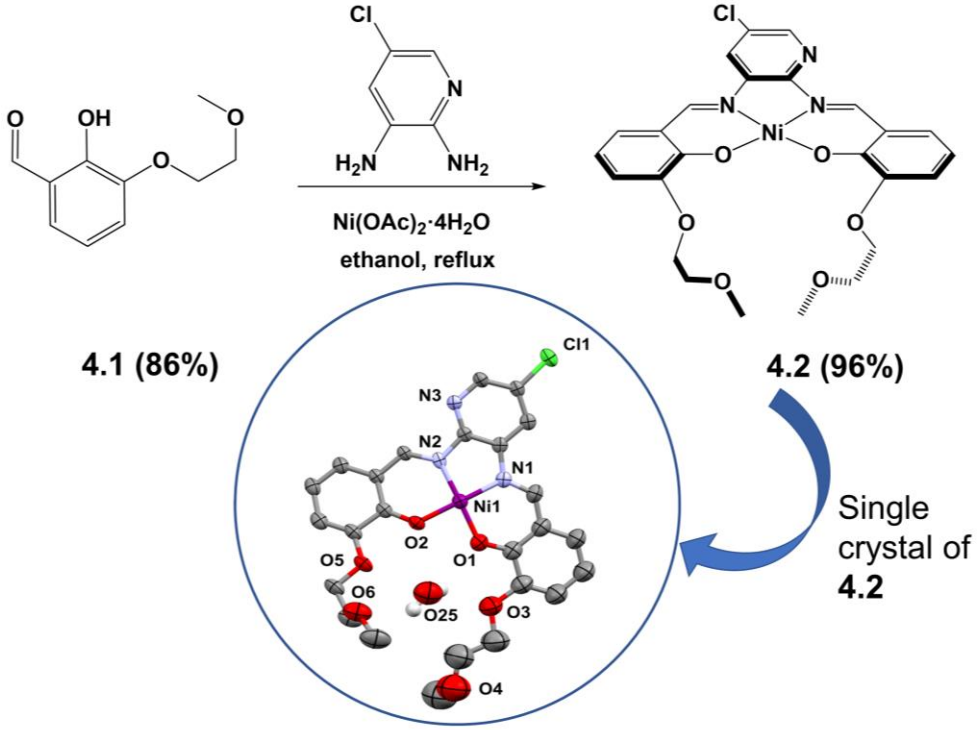

[a] Solvents and hydrogen atoms except the ones in H_2O are omitted for clarity.

The UV-visible spectrum of **4.2** exhibits two absorbance peaks at 380 and 488 nm in MeOH (containing 5% H_2O) with extinction coefficients of 18700 and 4820 $M^{-1}cm^{-1}$, which can be assigned to charge transfers arising from π–π* transitions of the

salicyaldimine ligand and a local excitation from the HOMO with spin density on the nickel to the LUMO that is largely localised on the pyridine (MLCT, Figure 4.1) respectively.

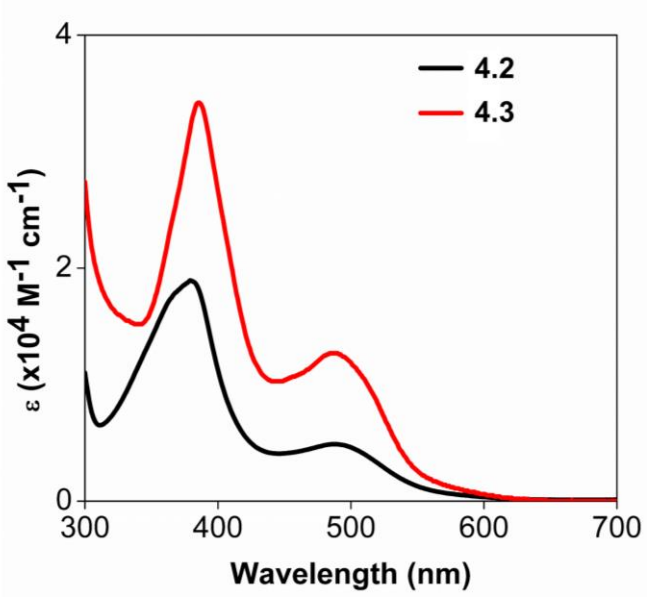

Figure 4.1. Plot of molar extinction coefficient against wavelength of **4.2** in methanol (MeOH) (5.0% H_2O) and **4.3** in DMF. From the Beer-Lambert Law, $A = \varepsilon Cl$ (A = absorbance; ε = molar extinction coefficient; C = concentration; l = pathlength of cell), the extinction coefficients of **4.2** at 488 and 380 nm are 4820 and 18700 $M^{-1}cm^{-1}$ respectively. The extinction coefficients of **4.3** at 490 and 385 nm are 12470 and 34355 $M^{-1}cm^{-1}$ respectively.

Single crystals of **4.2** were obtained by slow evaporation from a DCM solution, after which the molecular structure was determined by X-ray crystallography (Scheme 4.1). The coordination geometry of **4.2** is similar to the Ni complex in our previous report,[37] with a square planar geometry around Ni, corresponding to a d^8 electronic configuration. Notably, a H_2O molecule is trapped in the pendant ether arm of the secondary coordination sphere. The ether arm could thus potentially direct H_2O molecules and protons toward the Ni center during the catalytic cycle, assisting in the evolution of H_2. Other details of the crystallographic data can be found in Tables A2 (Appendix).

The CV of **4.2** (Figure 4.2a) in acetonitrile saturated with argon shows three redox waves. The quasi-reversible redox wave ($E_{1/2}$) at 0.30 V vs. Fc^+/Fc can be assigned to the **4.2**$^+$/**4.2** redox couple, whereas the irreversible reduction wave at –1.87 V can be attributed to the **Ni(SalDAPy)/ [Ni(SalDAPy●)**$^-$**]**redox couple (Figure 4.2b).[44] This access to multiple redox states implies that we may be able to employ **4.2** as a redox catalyst, especially for the H_2 evolution reaction. The irreversibility of the redox wave at -1.87 V, even at different scan rates, is likely due to an electron transfer followed by a chemical reaction (i.e. an EC process) where two ligand radicals dimerise under electrochemical conditions.[44] This dimerisation is a possible deactivation pathway[45] that can explain the absence of electrocatalytic H_2 evolution by **4.2**, despite the fact that it is active under dilute, photocatalytic conditions.

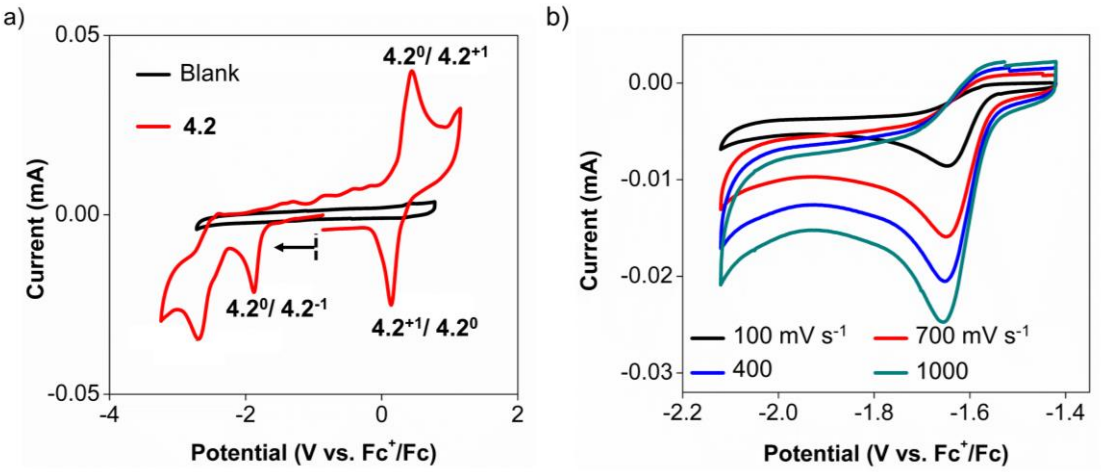

Figure 4.2. a) CV of 0.10 M n-Bu_4NPF_6 in acetonitrile with a glassy carbon electrode (3 mm diameter) in the absence (black) and presence of 1.0 mM **4.2** (red) at a scan rate of 100 mV s^{-1}. b) CV of the solution of 1.0 mM **4.2** in part a) with increasing scan rates from 100 to 1000 mV s-1 in the potential window of 1.63 to −2.35 V (vs Fc^+/Fc).

4.4.2. Photocatalytic H_2 Evolution

A series of photodriven H_2 evolution experiments were thus performed using a solution of **4.2** as the catalyst (GC, Table 4.1). Compound $[Ir]^+$ was eventually chosen as

the photosensitiser due to its long excited state lifetime, established photophysical characteristics, promising H_2 evolution result and highly reducing potential of –1.91 V vs Fc^+/Fc.[46,47] These properties will allow us to focus on investigating the role of **4.2** in the photocatalytic system. TEA was used as the sacrificial electron donor under visible light irradiation with 5% water in methanol as the solvent to solubilise all the components. During each catalytic experiment, the amount of H_2 built up in the headspace was quantified by gas chromatography (GC, Table 4.1) and calculated by subtracting the H_2 produced from the control experiments that were conducted in the absence of **4.2.**

Table 4.1. Summary of photocatalytic H_2 evolution experiments conducted comparing with other leading relevant molecular H_2 evolution catalysts reported in literature.

Entry	Conditions	Solvent	Time (h)	TON
1	10 μM **4.2**, 0.10 mM $[Ir]^+$, 0.10 TEA	MeOH (5% water)	6	1660
2	5.0 μM **4.2**, 0.10 mM $[Ir]^+$, 0.10 TEA	MeOH (5% water)	6	2370
3	2.0 μM **4.2**, 0.10 mM $[Ir]^+$, 0.10 TEA	MeOH (5% water)	6	3880
4	1.0 μM **4.2**, 0.10 mM $[Ir]^+$, 0.10 TEA	MeOH (5% water)	6	2100
5	2.0 μM **4.2**, 0.10 mM $[Ir]^+$, 0.10 TEA	MeOH only	6	1900
6	2.0 μM **4.2**, 0.10 mM $[Ir]^+$, 0.10 TEOA	MeOH (5% water)	4	0
7	2.0 μM **4.2**, 0.10 mM $[Ir]^+$, 0.10 BNAH	MeOH (5% water)	4	64
8	2.0 μM **4.2**, 0.10 mM $[Ir]^+$, 0.10 TEA	Acetone (5% water)	4	660

9	2.0 μM **4.2**, 0.10 mM $[Ir]^+$, 0.10 TEA (in dark)	MeOH (5% water)	6	0
10	2.0 μM **4.2**, 0.10 mM $[Ir]^+$	MeOH (5% water)	6	0
11	0.10 mM $[Ir]^+$, 0.10 TEA	MeOH (5% water)	6	-
12	2.0 μM **4.2**, 0.10 TEA	MeOH (5% water)	6	0
13	2.0 μM **4.2**, 0.50 mM [Ru],[a] 0.10 TEA	MeOH (5% water)	6	52
14	2.0 μM **4.2**$^-$, 0.10 mM $[Ir]^+$, 0.10 TEA	MeOH (5% water)	6	4303
15[37]	2.0 μM [NiL],[b] 0.10 mM $[Ir]^+$, 0.10 TEA	MeOH (5% water)	6	2800
16	2.0 μM **4.3**, 0.10 mM $[Ir]^+$, 0.10 TEA	MeOH(5% water)	6	0
17	2.0 μM **4.2**, 0.10 mM $[Cu(dap)_2]Cl$, 0.10 TEA	MeOH(5% water)	6	0
18[48]	2.0 μM **4.2**, 0.10 mM [Cu],[c] 0.10 TEA	MeOH(5% water)	6	0
19	2.0 μM **4.2**, 0.10 mM Eosin Y, 0.10 TEA	MeOH(5% water)	6	0
20	2.0 μM **4.2**, 0.10 Eosin B, 0.10 TEA	MeOH(5% water)	6	0
21[29]	0.14 mM $[Ni(P_2^{Ph}N_2^{Ph})_2](BF_4)_2$, 0.10 mM [Ru], 0.10	acetonitrile (50% water)	150	2700

	M ascorbic acid			
22[30]	NiP-RuP (TiO_2), 0.1 M ascorbic acid	Aqueous solution	2	723
23[34]	4.0 μM $(Et_4N)Ni(X\text{-}pyS)_3$, 2.0 mM fluorescein, 0.36 M TEA	EtOH (50% water)	30	7300
24[49]	0.010 mM $[Ni(L_4)]_2^+$, 1.0 mM $[Ir]^+$, 0.6 M TEA	THF (10% water)	70	5000

[a] [Ru] = $[Ru(bpy)_3](PF_6)_2$

[b] [NiL], L= 5,5'-((1E,1'E)-(1,2-phenylenebis(azaneylylidene))bis(methaneylylidene))bis(4-hydroxy-3-(2-methoxyethoxy)benzenesulfonate)

[c] [Cu] = [Cu (Xantphos)(bathocuproine)](PF_6)

The H_2 produced versus time profiles with different catalyst concentrations ranging from 1.0 to 10.0 μM are displayed in Figure 4.2a. For every experiment, we subtracted the amount of H_2 produced by $[Ir]^+$ only (Figure 4.3) from the total amount of H_2 measured.

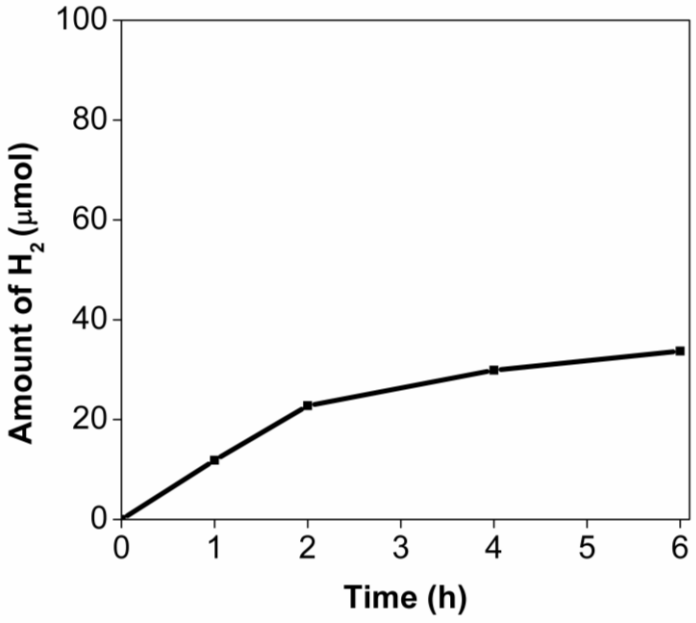

Figure 4.3. Baseline reactivity of $[Ir]^+$ photosensitiser in a solution containing 0.10 mM $[Ir]^+$, and 0.10 M TEA in methanol (5 % H_2O) solution under visible light irradiation.

Although the amount of H_2 that was produced increased as the concentration of **4.2** rose (Figure 4.4a), the highest TON of 3880 was achieved with only 2.0 μM of **4.2** (red line, Figure 4.4b). At even lower catalyst loadings when 1.0 μM of **4.2** was used, the TON was comparable to the ones with 2.0 μM of **4.2** only for the first 2 h of irradiation. However, the H_2 evolution activity for 1.0 μM of **4.2** decreased dramatically after the initial 2 h and the TON finally reached a value in between the experiments with 5.0 μM and 10.0 μM of **4.2** after 6 h, probably due to the inactivation of **4.2**. Our experiments indicated that at concentrations of **4.2** above 2 μM, the H_2 evolution performance per unit catalyst was lower, which may be caused by the formation of binuclear or polynuclear salicylaldimine complexes in the solution.[50] Furthermore, the H_2 evolution was also found to be terminated at 6 h for 5.0 μM and 10.0 μM as shown in Figure A.22.

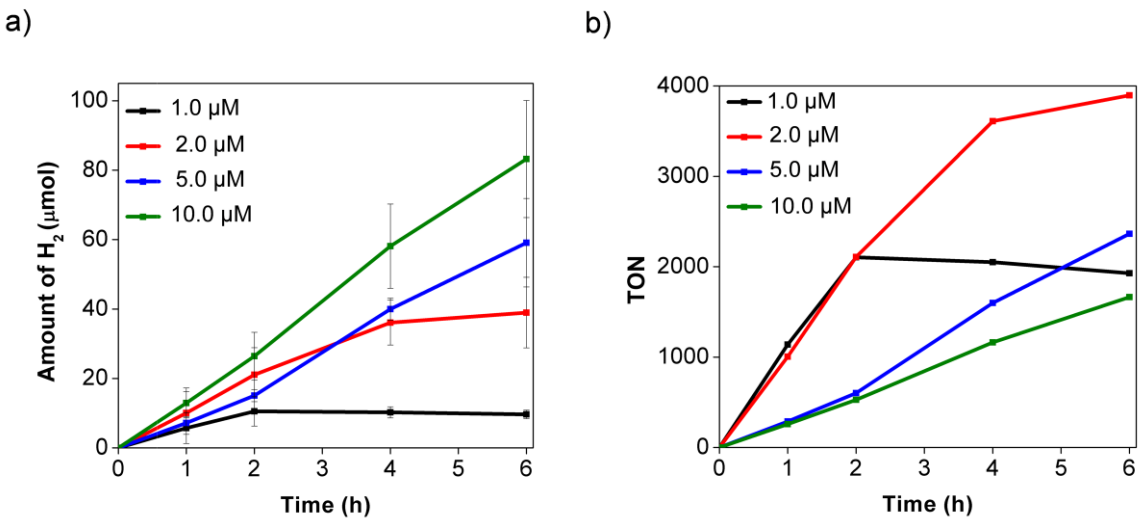

Figure 4.4. The (a) amount in μmol, and (b) TON of H_2 produced with **[4.2]** = 1.0 μM (black), 2.0 μM(red), 5.0 μM (blue), and 10 μM (green) in a methanol (5% H_2O) solution containing 0.10 mM of $[Ir]^+$ and 0.10 M TEA under 6 h of visible light irradiation. The amounts of H_2 generated for each data point was obtained as an average of at least three independent measurements.

To support this, we observed the presence of an intermediate with a *m*/*z* ratio of 1112.57 when we conducted liquid chromatography-mass spectrometry (LCMS) measurements on the one-electron reduced **4.2**$^-$ at high concentrations (Figure 4.5), which is consistent with a binuclear complex with a calculated *m*/*z* of 1112.13. The LCMS also displayed the presence of **4.2**$^-$ with a *m*/*z* of 556.25 (expected *m*/*z* of 556.62) and a product that is likely to be [**4.2**$^-$ + ligand] with the loss of one Ni center at a *m*/*z* ratio of 1056.92 (expected *m*/*z* of 1056.22). This suggested that the loss of Ni may be a pathway for the deactivation of **4.2** to form catalytically inoperative intermediates containing **4.2**$^-$ bound to a demetallated ligand. However, it is also possible that the loss of Ni by **4.2**$^-$ occurs only during the LCMS experiment, so we cannot definitively conclude that demetallation of **4.2** or **4.2**$^-$ is the major catalyst deactivation pathway.

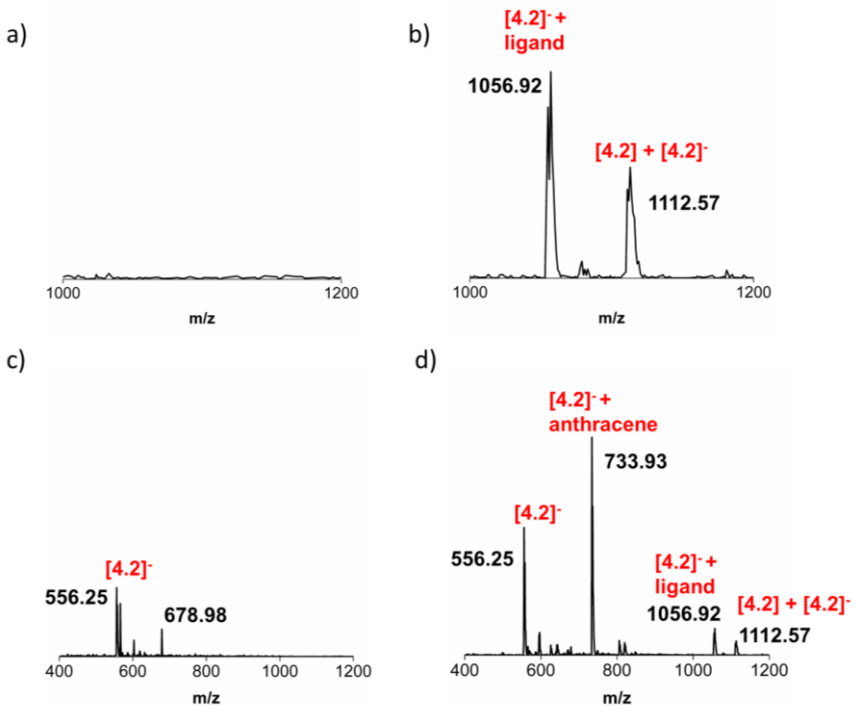

Figure 4.5. ESI mass spectra of 1.0 mM solutions of a) **4.2** and b) **4.2**$^-$ from m/z of 1000 to 1200. ESI mass spectra of c) **4.2** and d) **4.2**$^-$ from m/z of 400 to 1200.

A control experiment with 2.0 μM of **4.2** conducted in anhydrous methanol under otherwise identical conditions (entry 5, Table 4.1) revealed that the TON was almost halved to 1900, suggesting that H_2O was a more effective proton source, albeit not the only one in this photocatalytic system. An attempt to use $Ru(bpy)_3(PF_6)_2$ ([Ru]) as the light harvester led to a low TON of only 52 (Entry 13, Table 4.1), suggesting that a sufficiently reducing photosensitiser was required for optimal activity. Photosensitisers composed of only earth-abundant elements such as Cu and organic variants including Eosin Y and Eosin B were also evaluated, but the amount of H_2 produced was below the detection limits of our GC (Entries 17-20, Table 4.1). Catalyst **4.2** was also more active than our previously reported Ni salicylaldimine complex,[37] which led to a TON of 2800 under the same photocatalytic conditions at 2.0 μM of the catalyst (Entry 15, Table 4.1).

We observed that the rate of H_2 production slowed down drastically after 6 h of visible light irradiation in all the experiments. Furthermore, this decrease in the rate of H_2

production was accelerated at lower concentrations of **4.2**, prompting us to perform additional experiments to identify the cause. Since TEA was added in large excess, we ruled it out as the limiting reagent, and examined if the other components were responsible for this deactivation after 6 h. Using the optimised conditions with 2.0 μM of **4.2**, when 0.10 mM of fresh $[Ir]^+$ was added to the photocatalytic reaction after 6 h, the H_2 evolution did not resume. This indicated that photosensitiser deactivation was not the main reason that H_2 evolution slowed down. On the other hand, the addition of one extra equivalent of **4.2** led to an 80% recovery of H_2 production in the following 6 h (Figure 4.6). Control experiments were also carried out in the absence of **4.2**, $[Ir]^+$, TEA, or light, which verified that the amount of H_2 produced was reduced dramatically (Table 1). These results establish that all the components are essential for efficient H_2 gas production, and the deactivation of **4.2** is the main cause for the reduction in H_2 evolution reactivity.

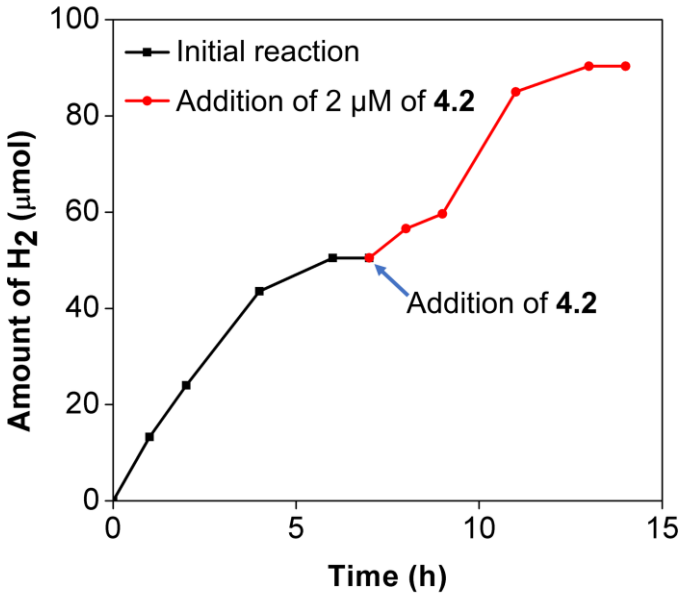

Figure 4.6. Changes in H_2 evolution with irradiation time before and after introducing an additional 2.0 μM of **4.2** to the photocatalytic system containing 2.0 μM of **4.2**, 0.10 mM $[Ir]^+$, and 0.10 M TEA in methanol (5 % H_2O) solution under visible light irradiation.

Furthermore, to investigate if the H_2 was produced from H_2O/methanol or from TEA, the reaction was conducted using D_2O and deuterated methanol (MeOD) with unlabelled TEA. Helium gas was employed as the carrier gas to distinguish between H_2 and D_2.[51-53] By comparing with the GC data of H_2 and D_2 standard gases, we observed a signal which confirmed that majority of the product formed was likely to be D_2, with H_2 below our detection limits (Figure 4.7). On the other hand, we mainly detected H_2 when undeuterated solvents and TEA were used. Therefore, we propose that H_2O, which undergoes rapid proton exchange with methanol, is probably the proton donor instead of TEA.

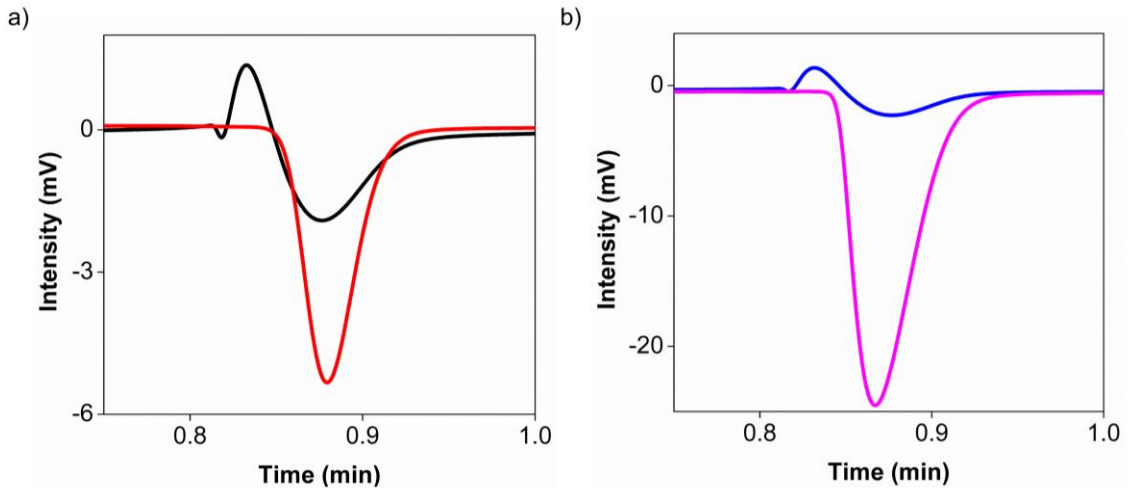

Figure 4.7. GC signals obtained using He (instead of Ar) as the carrier gas. (a) H_2 signals (black) when reaction was carried out in H_2O and MeOH, and D_2 signals (red) when the reaction was carried out with D_2O and MeOD with 2.0 μM of **4.2** in TEA. (b) H_2 (blue) and D_2 (pink) signals observed when standard gases were used.

Finally, to determine whether **4.2** was a precatalyst in a homogeneous or heterogeneous system since recent work[49,54,55] has shown that zero-valent nickel nanoparticles are capable of photocatalytic H_2 evolution as well, DLS experiments were carried out on the reaction mixture after 6 h of irradiation. No nanoparticles were observed in the reaction mixture (Figure 4.8), suggesting that **4.2** operated in a homogeneous molecular catalytic cycle.

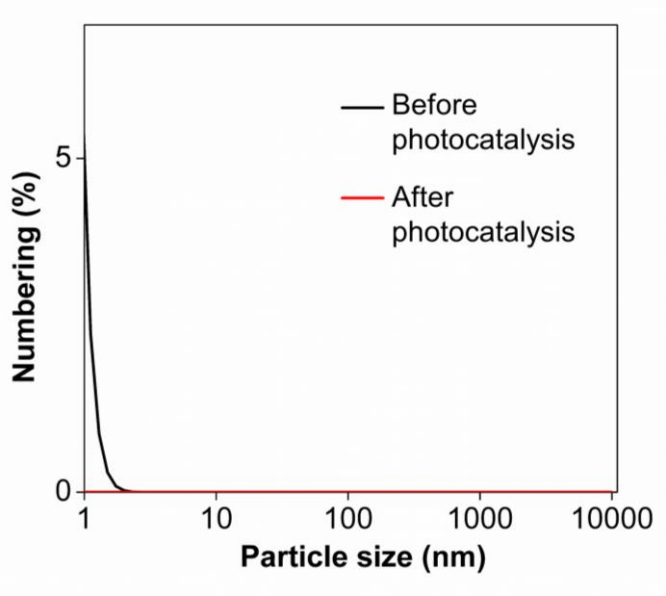

Figure 4.8. Particle distribution determined by DLS measurements before and after 6 h of H_2 evolution photocatalysis.

4.4.3. Mechanistic Insight via Transient Absorption and Transient Emission Spectroscopy

With the optimised catalytic conditions in hand, we sought a deeper understanding of the reaction pathway in the catalytic cycle through time-resolved spectroscopic experiments. There are two generally accepted pathways for the single photon absorption followed by electron transfer in molecular photosensitiser reactions. In one route, the photosensitiser absorbs light, after which its excited state is reduced by a sacrificial electron donor. The reduced photosensitiser is then recovered by transferring an electron to the catalyst enroute to producing H_2. Alternatively, the photosensitiser absorbs light, forms a transient excited state species, and transfers an electron to the catalyst directly. The oxidised photosensitiser is then reduced to its original oxidation state by the sacrificial electron donor. To gain some insights into the elementary reaction steps during the photocatalysis, nanosecond TAS and TES experiments were conducted with 355 nm pulsed irradiation of 0.10 mM $[Ir]^+$ in methanol containing 5% H_2O. The samples were probed by a broadband xenon lamp beam before and after 5 – 8 ns pulses. In all our TAS data, the detected intensity

of the transmitted signals is presented as the logarithm of the ratio (ΔOD) of the light intensity from the probe beam after laser excitation to the intensity before laser excitation. The ΔOD thus refers to increased absorption (positive ΔOD) or reduced absorption/emission (negative ΔOD) of the transient photoexcited species relative to the ground state.

At 570 nm near the emission maximum of $[Ir]^+$, the photoluminescence lifetime of $[Ir]^{+}$* is 390 ± 20 ns, which we define as τ0 (Figure 4.9a). We subsequently monitored the quenching effect of each component in the catalytic system on the $[Ir]^{+}$* lifetime (Figure 4.9b-d) in the presence of different concentrations of TEA and **4.2**.

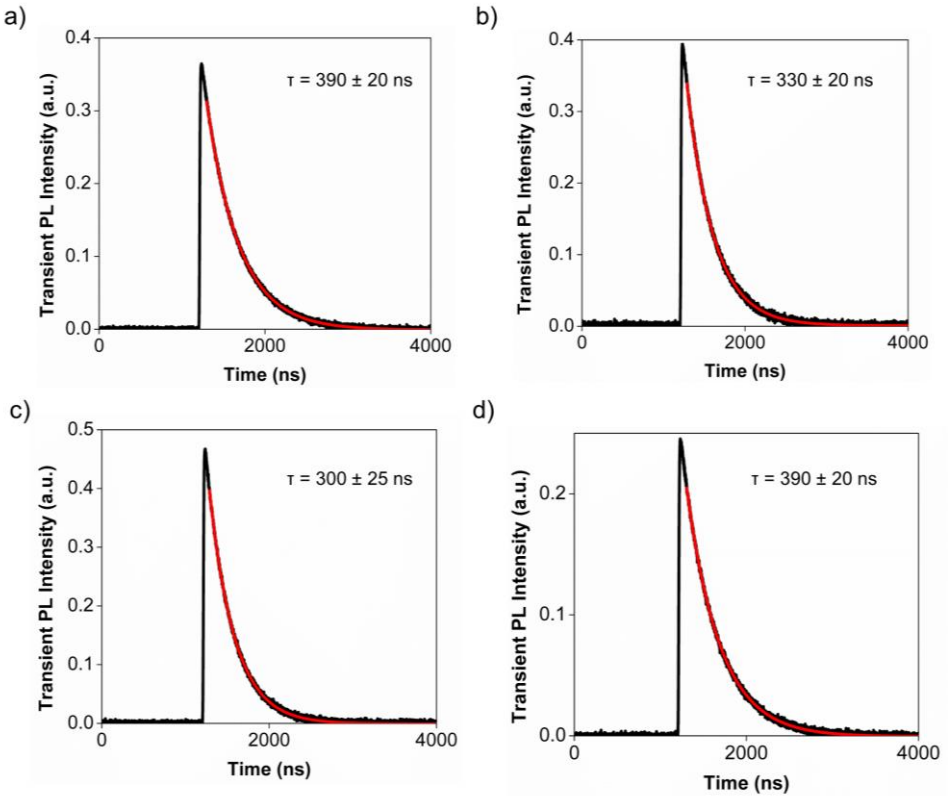

Figure 4.9. The excited lifetime of (a) $[Ir]^+$, (b) $[Ir]^+$ with 0.10 M of TEA, (c) $[Ir]^+$ with 0.10 M of TEA and 40 μM of **4.2**, and (d) $[Ir]^+$ and **4.2**.

The Stern-Volmer plots (Figure 4.10) were obtained after fitting the photoluminescence decay lifetimes of the signal at 570 nm to a single exponential, yielding a quenching rate constant, k_q, of 5.66 x 10^6 M^{-1} s^{-1} in the presence of TEA. Interestingly,

4.2 does not quench the photoexcited $[Ir]^+$ (Table 4.2), suggesting that $[Ir]^{+}$* is likely to be reductively quenched by TEA to form [Ir] first, after which [Ir] then transfers an electron to reduce **4.2** to **4.2**$^-$.

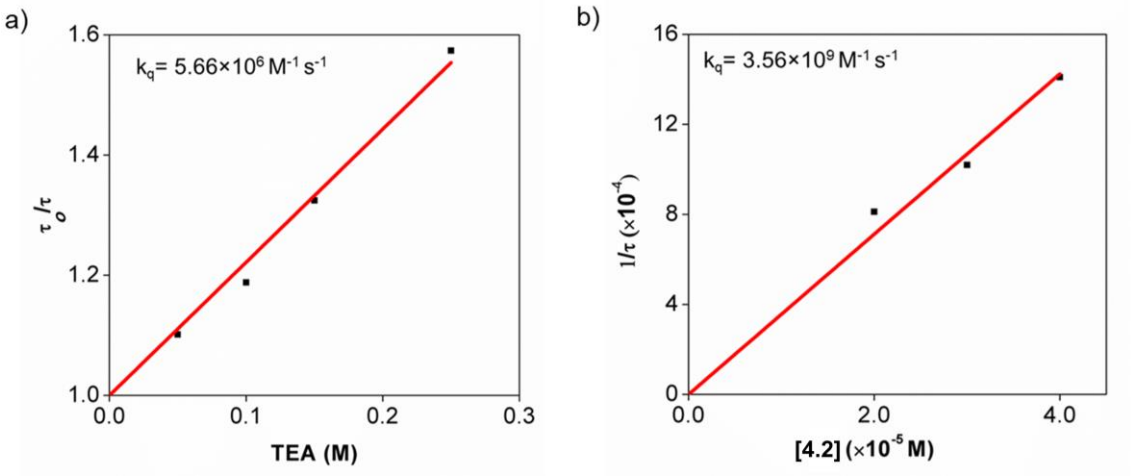

Figure 4.10. Stern–Volmer plot for quenching the transient emission spectroscopic signal of $[Ir]^{+*}$ at 570 nm by varying concentrations of a) TEA and b) **4.2** with 0.10 M of TEA.

Table 4.2. Summary of Ir emission lifetime at 570 nm with different concentration of **4.2**.

Entry	Concentration of 4.2 (μM)	Emission lifetime of $[Ir]^+$ at 570 nm (ns)
1	10	400 ± 40
2	20	400 ± 40
3	30	400 ± 40
4	40	390 ± 40

TAS experiments were then conducted on solutions of $[Ir]^+$ alone (Figure 4.11a) and with TEA, in the absence and presence of **4.2**, as depicted in Figures 3b and 3c, respectively. The spectra were recorded at μs timescales to monitor the long-lived intermediates during and after charge transfer processes have taken place. The transient absorption spectra in the absence of **4.2** shows the decay of the characteristic absorption maxima at 380 and 485 nm and the emission maximum at 590 nm of $[Ir]^{+}$*, concomitant with the formation of a new species with absorptions at 385, 448, 498, and 530 nm that

does not decay within 90 μs (Figure 4.11b). The spectral signatures at 385, 498, and 530 nm confirmed the formation of [Ir] through reductive quenching by TEA. In the presence of **4.2** (Figure 4.11c), the formation of [Ir] via reductive quenching by TEA was also observed from the spectral signature at 530 nm.

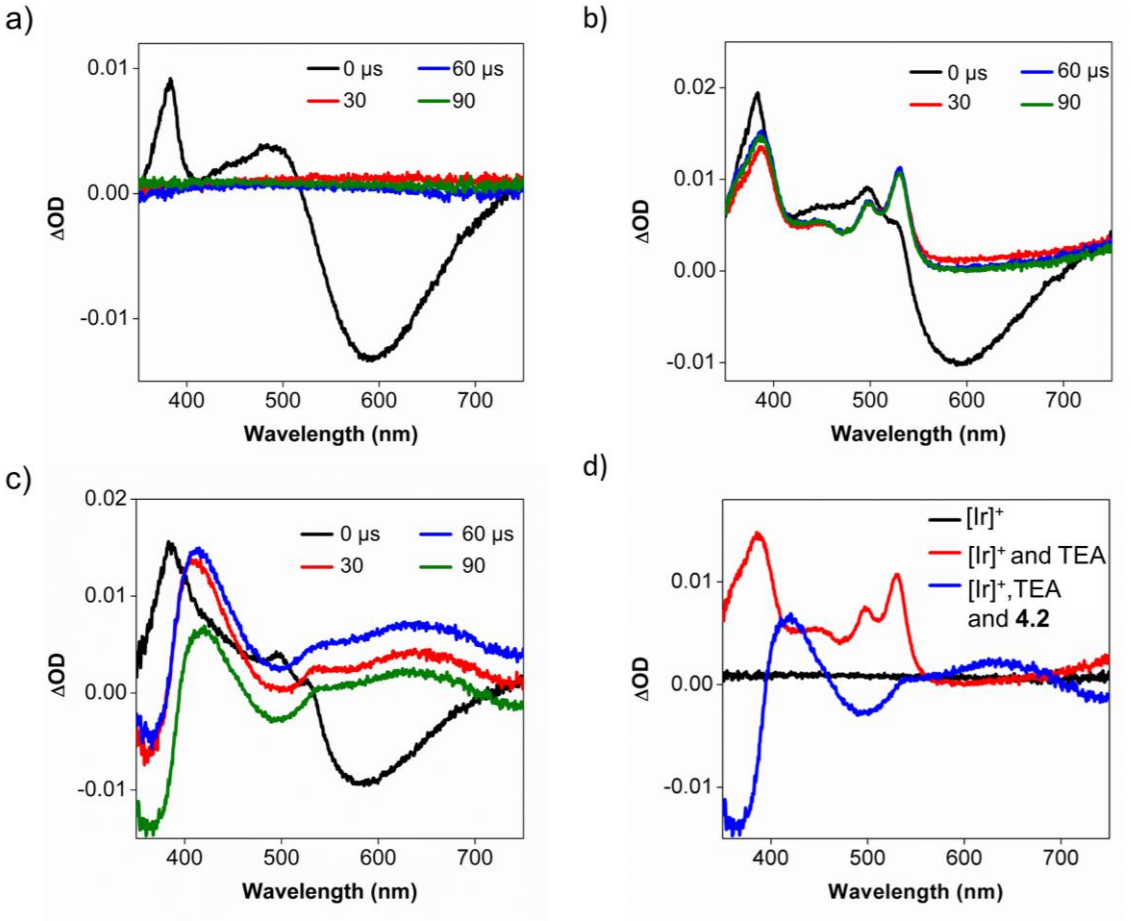

Figure 4.11. Transient absorption spectra upon 355 nm pulsed irradiation of (a) 0.10 mM of $[Ir]^+$, (b) 0.10 mM of $[Ir]^+$ with 0.10 M of TEA, and (c) 0.10 mM of $[Ir]^+$ with 0.10 M of TEA and 40 μM of **4.2**. (d) A comparison of the spectra at 90 μs of the three samples with different compositions. In parts (a) – (c), the 0 μs spectra correspond to the changes right after illumination, within the time resolution of the spectrometer.

However, the absorption bands at 385 and 498 decayed within 4 μs (Figure 4.12, decay of 530 nm band obscured by growing intermediate) and a new intermediate, likely $\mathbf{4.2}^-$, with a broad absorption spectral feature from 580 to 700 nm was formed (Figure 3d).

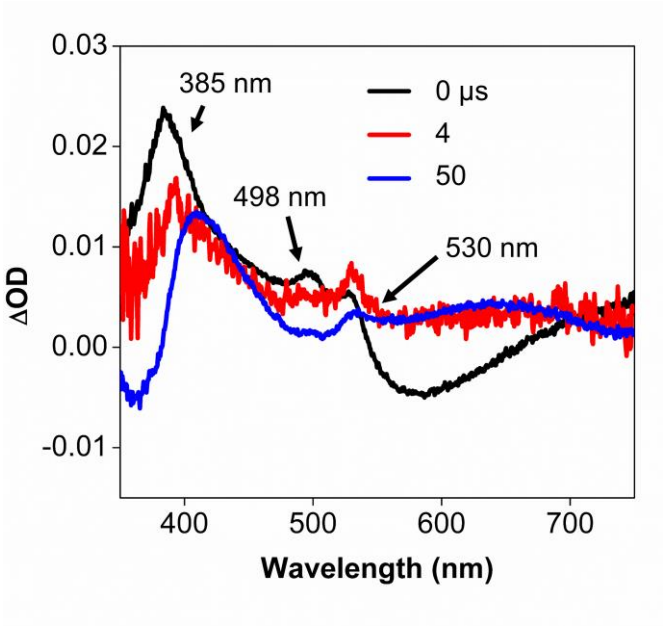

Figure 4.12. Transient absorption spectra highlighting the decay of the 385 and 498 nm absorption bands within 4 μs, upon 355 nm pulsed irradiation of 0.10 mM of $[Ir]^+$ with 0.10 M of TEA and 40 μM of **4.2**. The 0 μs spectra correspond to the changes right after illumination, within the time resolution of the spectrometer.

In addition, the kinetics of the absorption at 380 and 630 nm were explored. At and above 630 nm, the ΔOD for the formation of [Ir] is zero so it will have no contribution to the TAS. Thus, the two lifetimes obtained at this wavelength from the fits to the decay kinetics will then correspond to the decay of $[Ir]^{+}$* and the formation of **4.2**$^-$. At 380 nm, the longest time component corresponds to the decay of [Ir] (Figure 4.13). By comparing the longest time components at 380 and 630 nm, we find that the formation of **4.2** (Figure 4.13) is concurrent with the decay of [Ir], verifying the correlation between the two different processes. The shorter lifetimes obtained from absorption at 380 nm can be attributed to the decay processes of $[Ir]^{+}$*. Based on these TAS experiments, we propose that the proton reduction catalytic cycle is initiated by the reductive quenching of $[Ir]^+$ by TEA after photoexcitation, followed by electron transfer from [Ir] to **4.2**.

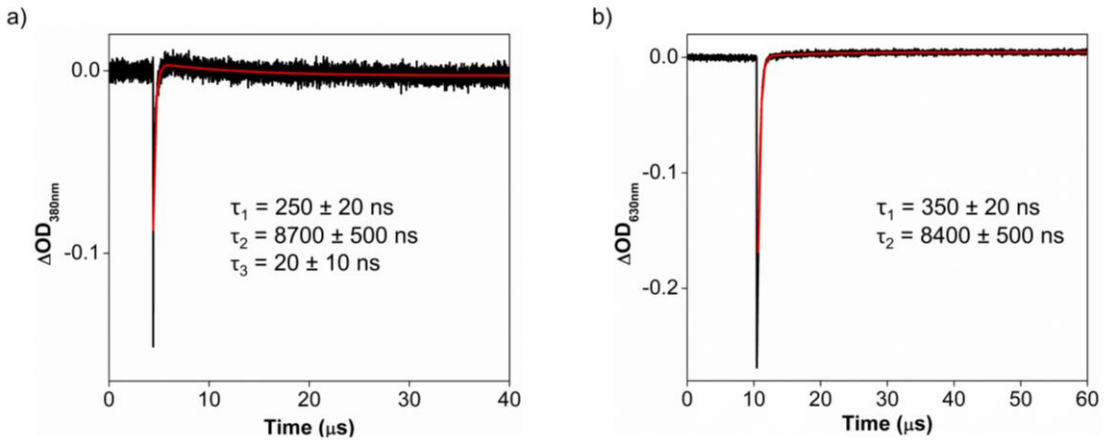

Figure 4.13. Transient absorption spectra at a) 380 nm and b) 630 nm showing the lifetimes of the decay of the $[Ir]^+$ intermediates and the formation of **4.2**$^-$. The short lifetime of 20 ns, measured at 380 nm, corresponds to a component that arises from the decay of $[Ir]^+$*, whereas, the longer lifetime of 8700 ns can be attributed to the decay of [Ir]. The lifetime of 8400 ns from transient absorption spectrum at 630 nm corresponds to the formation of **4.2**$^-$.

To verify that **4.2** can be reduced by [Ir] during the H_2 evolution cycle, we attempted to independently synthesise some of the possible intermediates of **4.2** during catalysis. We added one equivalent of magnesium anthracene as a one-electron chemical reductant[56,57] under anhydrous conditions at room temperature to **4.2**, and characterised the one-electron reduced product, **4.2**$^-$, by NMR, EPR and steady-state UV-visible spectroscopy. Further reduction is not expected since magnesium anthracene does not have sufficient potential to promote the second reduction of **4.2**. The ^{1}H NMR spectrum of the crude reaction mixture containing **4.2**$^-$ did not exhibit any signals from **4.2** itself or dissociated ligand, although anthracene was detected (Figure 4.14a). Even when the experiment was performed with a broader chemical shift range between -10 to 190 ppm, paramagnetically shifted or broadened signals were not observed (Figure 4.14b), suggesting that **4.2**$^-$ is probably paramagnetic.

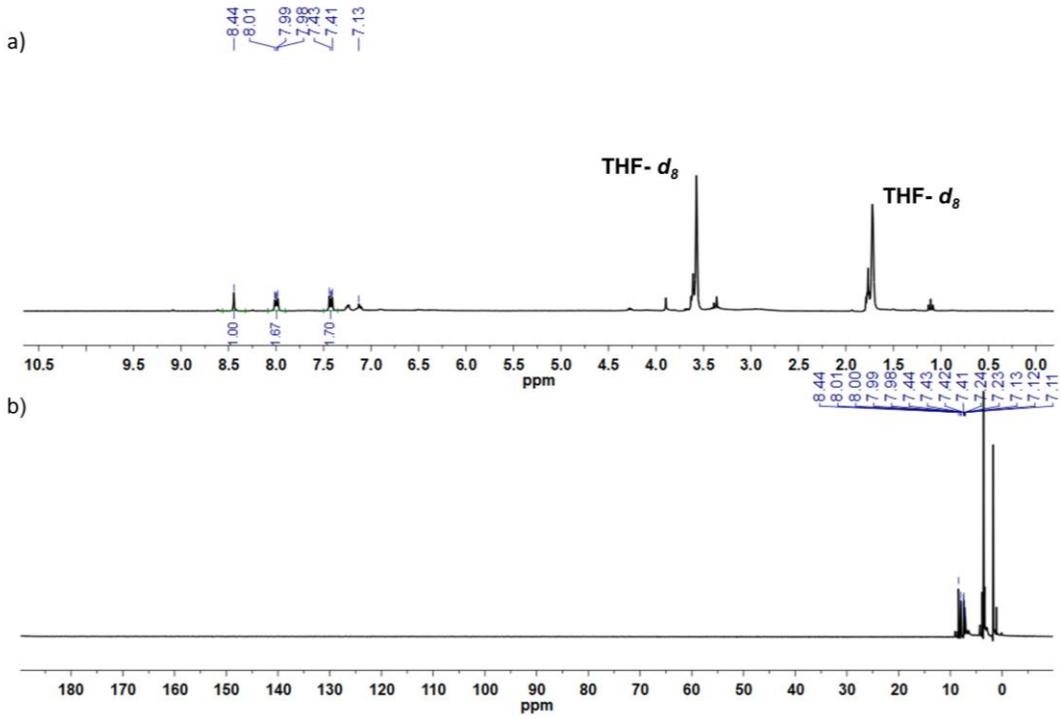

Figure 4.14. The ^{1}H NMR spectrum of **4.2**$^{-}$ from the unpurified reaction mixture in THF-d_8 with a) a scan width from 0 to 10.5 ppm and, b) a scan width of -10 to 190 ppm.

To complement this data, solid-state EPR spectroscopic measurements were performed to determine if the unpaired electron on **4.2**$^{-}$ was metal- or ligand-centered. The EPR spectrum exhibits axial symmetry with $g_{\parallel} = 2.0678$ and $g_{\perp} = 2.0081$ with no hyperfine splitting at room temperature (Figure 4.15a), indicating that **4.2**$^{-}$ likely contains an organic radical with the unpaired electron residing predominantly on the ligand, since these features are inconsistent with typical Ni(I) complexes that have *g* values of 2.12 to 2.15 and much larger anisotropies.[58] These *g* values also match those from structurally similar complexes such as [Ni(saloph)]$^{-}$, which was reported to arise from a ligand-centered reduction.[58] The EPR spectrum of sodium anthracenide only, as depicted in Figure 4.15b, displays an isotropic signal with g = 2.0023 as expected. Although we cannot fully rule out the presence of small amounts of anthracenide radical anion in the EPR sample for **4.2**$^{-}$, we had thoroughly rinsed the sample and do not anticipate much remaining. Furthermore, given the high sensitivity of EPR spectroscopy, we believe that the EPR signals in Figure 4a can

be mostly attributed to the radical anion localised on the ligand. We were not able to structurally characterise **4.2**$^-$ despite multiple attempts to recrystallise it and thus, we cannot definitively conclude that **4.2**$^-$ is a mononuclear Ni complex. However, we believe that the evidence based on the kinetics of **4.2**$^-$ for H_2 evolution catalysis, the converged structure of **4.2**$^-$ in the DFT calculations below, and the EPR spectra are not consistent with a dimer formed from radical coupling of two ligands each supporting Ni^{II}, which should be diamagnetic.

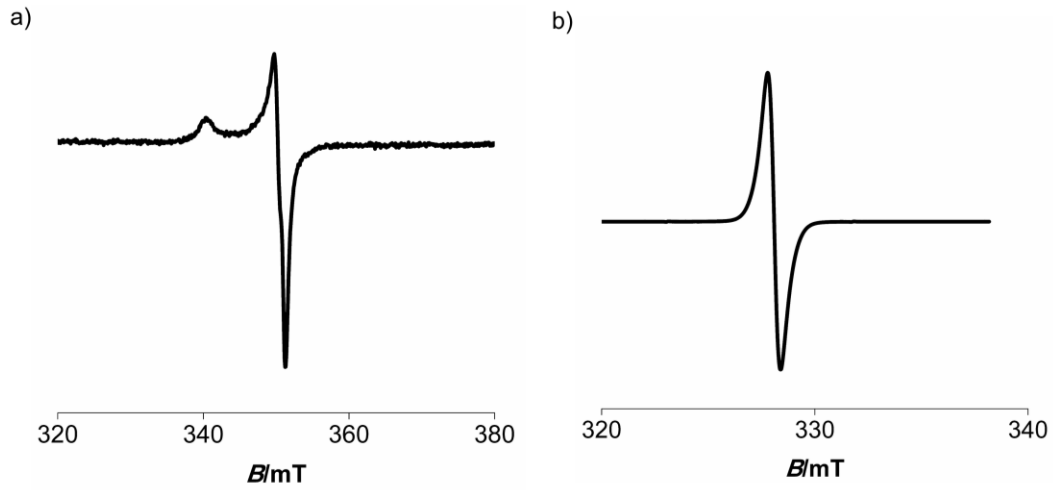

Figure 4.15. EPR spectra of (a) **4.2**$^-$ collected with a microwave frequency of 9850 Mhz and (b) sodium anthracenide collected with a microwave frequency of 9200 MHz.

DFT calculations with geometry optimisation in MeOH as the solvent were also performed by using the M06 functional. Notably, the SOMO of **4.2**$^-$ appeared to be predominantly localised on the ligand (Figure 4.16b). A natural population analysis on **4.2**$^-$ also demonstrated that the spin density population is almost zero on the Ni center, concurring with our proposal above that the unpaired electron after reduction was predominantly delocalised on the ligand. Overall, both the experimental and computational data support a ligand-centered reduction of **4.2**. This is consistent with recent results that demonstrate the importance of redox non-innocent ligands in facilitating charge transfer during H_2 evolution reactions.[18,59]

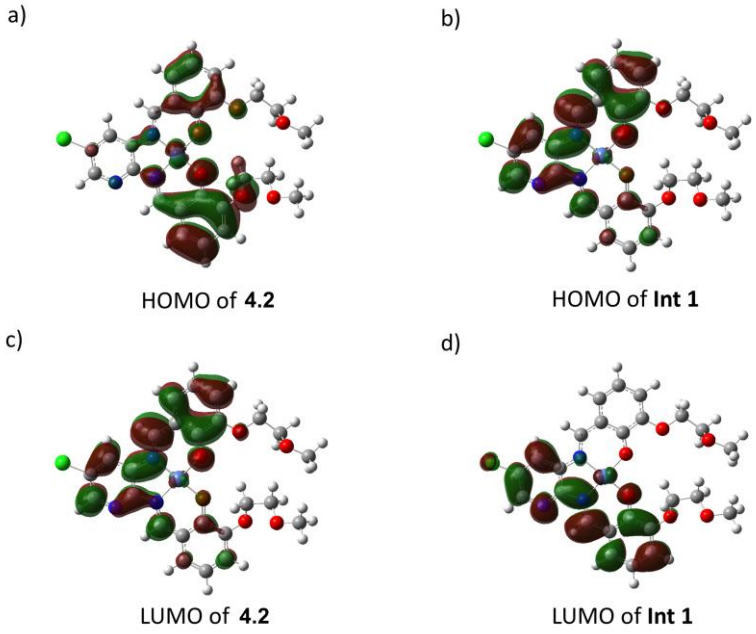

Figure 4.16. The HOMO of (a) **4.2** and (b) **Int 1**. The LUMO of (c) **4.2** and (d) **Int 1**.

With the **4.2**$^{-}$ accessed by chemical reduction in hand, we sought to compare and match its photophysical properties with those from the time-resolved measurements. Based on the TAS data at 90 μs, a long-lived intermediate had formed in the reaction mixture containing $[Ir]^{+}$, TEA, and **4.2** (blue line, Figure 4.11d). In addition, the steady-state UV-visible spectra of **4.2** and **4.2**$^{-}$ are illustrated in Figure 4.17a. By using the steady-state spectra of **4.2**$^{-}$ (red line, Figure 4.17a) and **4.2** (black line, Figure 4.17a), we can obtain the difference spectrum (red line, Figure 4.17b) and compare it with the TAS data at 90 μs, reproduced again from Figure 4.11d (black line). Interestingly, we observe spectral absorption signatures at 413 nm, 540 nm, and 580-700 nm for the steady-state data, similar to the 90 μs spectrum from the TAS measurements, as displayed in Figure 4.17b.

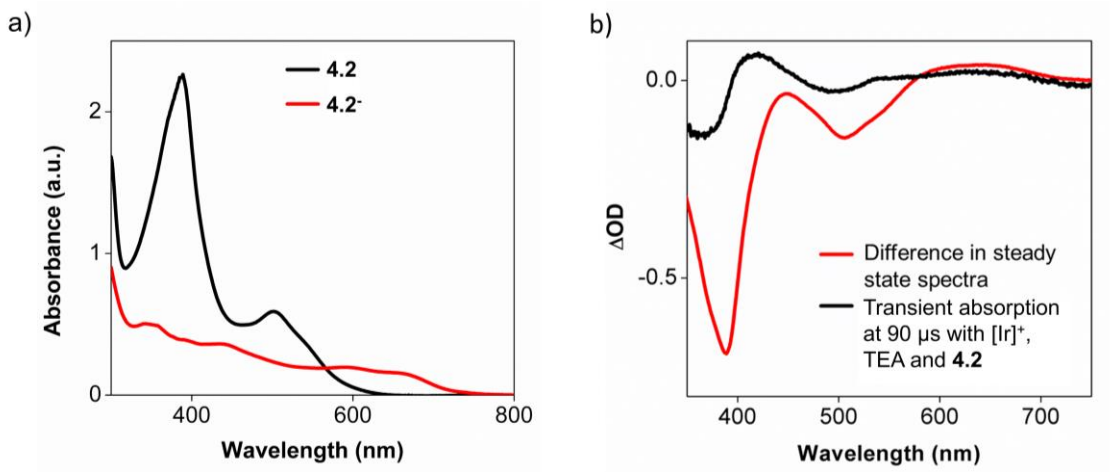

Figure 4.17. (a) The steady-state absorption spectra of **4.2** (black) and **4.2**$^{-}$ (red) in THF. (b) Difference in steady-state spectra by subtracting **4.2** from **4.2**$^{-}$ (red) in comparison to the TAS data at 90 μs of the mixture containing $[Ir]^{+}$, TEA, and **4.2** (black), the latter of which has been reproduced from Figure 4.11d.

In addition, we conducted HER experiments with **4.2**$^{-}$ and observed that the catalysis was first order (Figure 4.18) with respect to its concentration. The TON obtained with 2 μM of **4.2**$^{-}$ after 6 h (entry 14, Table 4.1) was also similar to the TON for the HER reactions with **4.2**, which suggested that **4.2**$^{-}$ was indeed an active intermediate in the catalytic cycle. Consequently, we believe that the optical spectroscopic and kinetic measurements concur with a model where $[Ir]^{+}$* is reductively quenched by TEA, which in turn then reduces **4.2** to **4.2**$^{-}$ in the first step of the photocatalytic H_2 evolution cycle.

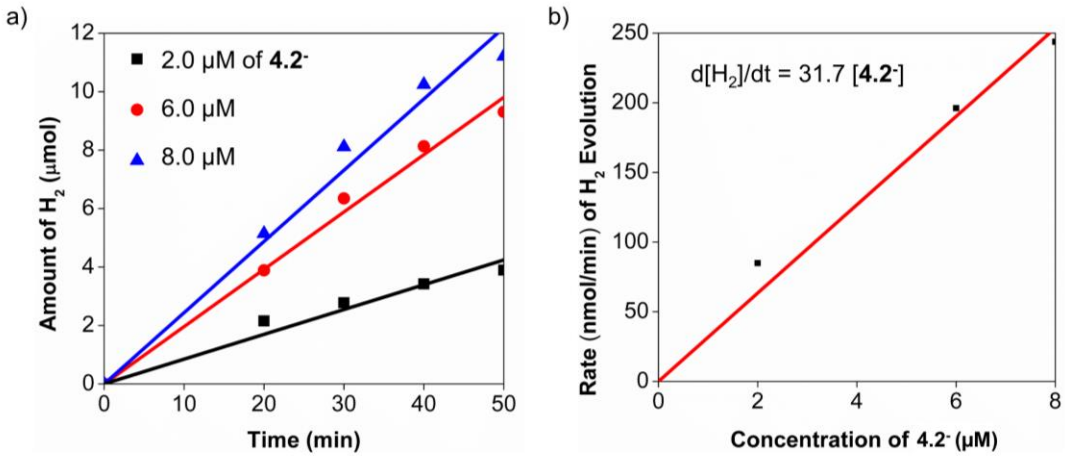

Figure 4.18. a) Amount of H_2 produced at different time intervals for 2, 6, and 8 μM of **4.2**$^{-}$. b) Plot of rate of H_2 produced against concentration of **4.2**$^{-}$.

In order to explore the effects of removing hydrogen bonding interactions with H_2O while still preventing the oligomerisation that is notorious among Ni salicylaldimine complexes, the ether arms were replaced with tert-butyl groups to give **4.3** (Scheme 4.2).

Scheme 4.2. Synthetic Steps for the *Tert*-Butyl Substituted 4.3.

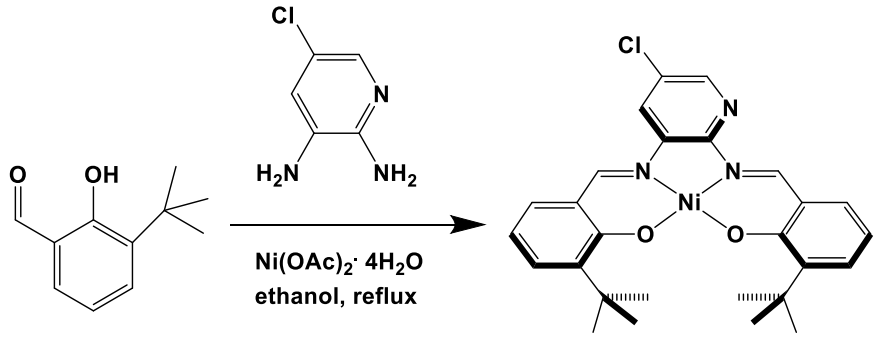

4.3

Complex **4.3** was then evaluated as a H_2 evolution catalyst under the same optimised conditions as above with $[Ir]^+$, TEA, and methanol with 5% H_2O under visible light irradiation. Remarkably, no H_2 was detected by GC, underscoring the essential function of the second coordination sphere ether arm in **4.2** (entry 16, Table 4.1). The CVs in THF illustrate a cathodic shift of the first reduction potential in **4.3** at -2.07 V, as compared to a potential of -1.85 V in **4.2** (Figure 4.19). Thus, both the cathodically shifted redox potential

and the lack of ether groups to hydrogen bond with H_2O molecules may contribute to the catalytic inactivity of **4.3**.

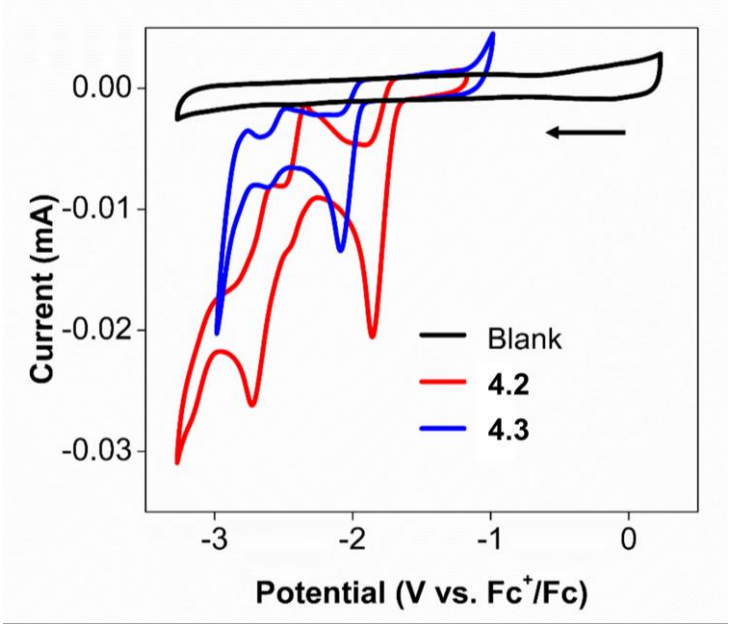

Figure 4.19. CV of 1.0 mM of **4.2** (red) and **4.3** (blue) in 0.10 M *n*-Bu_4NPF_6 in THF with a glassy carbon electrode (3 mm diameter) at a scan rate of 100 mV s^{-1}. The CV of just the 0.10 M *n*-Bu_4NPF_6 electrolyte solution in THF is the black line, confirming that THF is stable down to -3.0 V vs. Fc^+/Fc.

To elucidate the resting state of the **4.2** in the photocatalytic reaction, steady-state UV-visible spectroscopy was used to monitor the reaction over time. In the first 10 min of the reaction, the characteristic absorption of **4.2** at 380 nm decreases, while the weak absorption band from 580 – 700 nm, which is characteristic of the **4.2**$^-$, increases (Figure 4.20). These changes become more prominent after 20 min of irradiation. A separate experiment was also carried out, starting with **4.2**$^-$ instead of **4.2**, which showed a gradual recovery of the absorption band at 380 nm (Figure 4.20). The spectra obtained in both conditions suggest that **4.2**$^-$ is a likely resting state of **4.2** during the catalytic cycle under irradiation by visible light. With this in mind, further DFT calculations were carried out to

map out a plausible reaction pathway and verify the impact of the pendant ether arms on the H_2 evolution by **4.2**.

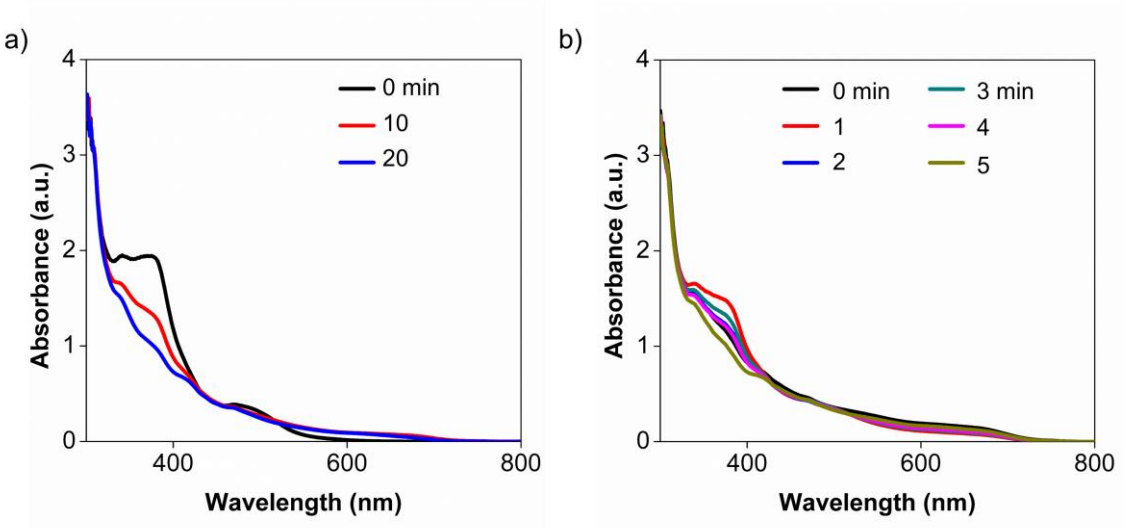

Figure 4.20. Steady state UV-visible spectra of a) 40 μM of **4.2**, 0.10 M of $[Ir]^+$, and 0.10 mM of TEA in MeOH (5% H_2O) over the course of 20 min, and b) 40 μM of **4.2**$^-$, 0.10 M of $[Ir]^+$, and 0.10 mM of TEA in MeOH (5% H_2O) over the course of 5 min. Both samples were monitored after visible light irradiation for the duration indicated.

4.4.4 DFT Calculations

DFT calculations were performed by using the M06 functional and the Def2-SVP basis set within the Gaussian 09 software. This combination of functional and basis set was found to provide a reasonable agreement with the experimentally observed physical parameters such as the experimental bond distances and angles of **4.2**, and also gave a reasonable calculated H_2 evolution route (Figure 4.21). Neutral H_2O, which could have been a potential proton donor in this reaction, was first considered for the DFT calculations. However, the calculation showed that H_2O was not capable of functioning as a proton donor since the O-H bond did not break with a reasonable barrier during the calculation. Instead, H_3O^+ ions were found to provide a reasonable mechanism.

We propose that **4.2** first undergoes an endothermic one-electron reduction by [Ir] to form **4.2**$^-$ (**Int 1**), with the unpaired electron delocalised on the ligand with little Ni

contribution. Subsequently, **Int 1** is protonated at one of the phenolic O atoms in an exergonic step (-38.3 kcal/mol) likely due to its largest spin density in the calculated highest occupied molecular orbital (HOMO). In the following step, a proton transfer from the phenolic O atom to Ni occurs to form **Int 3**, mediated by H_2O as a proton shuttle with a kinetic barrier of 33.6 kcal/mol.[60] **Int 3** is then reduced by [Ir] to give **Int 4**, and the Ni^{II} hydride is readily protonated to release a molecule of H_2 and regenerate **4.2** in a highly exergonic process (-84.7 kcal/mol).

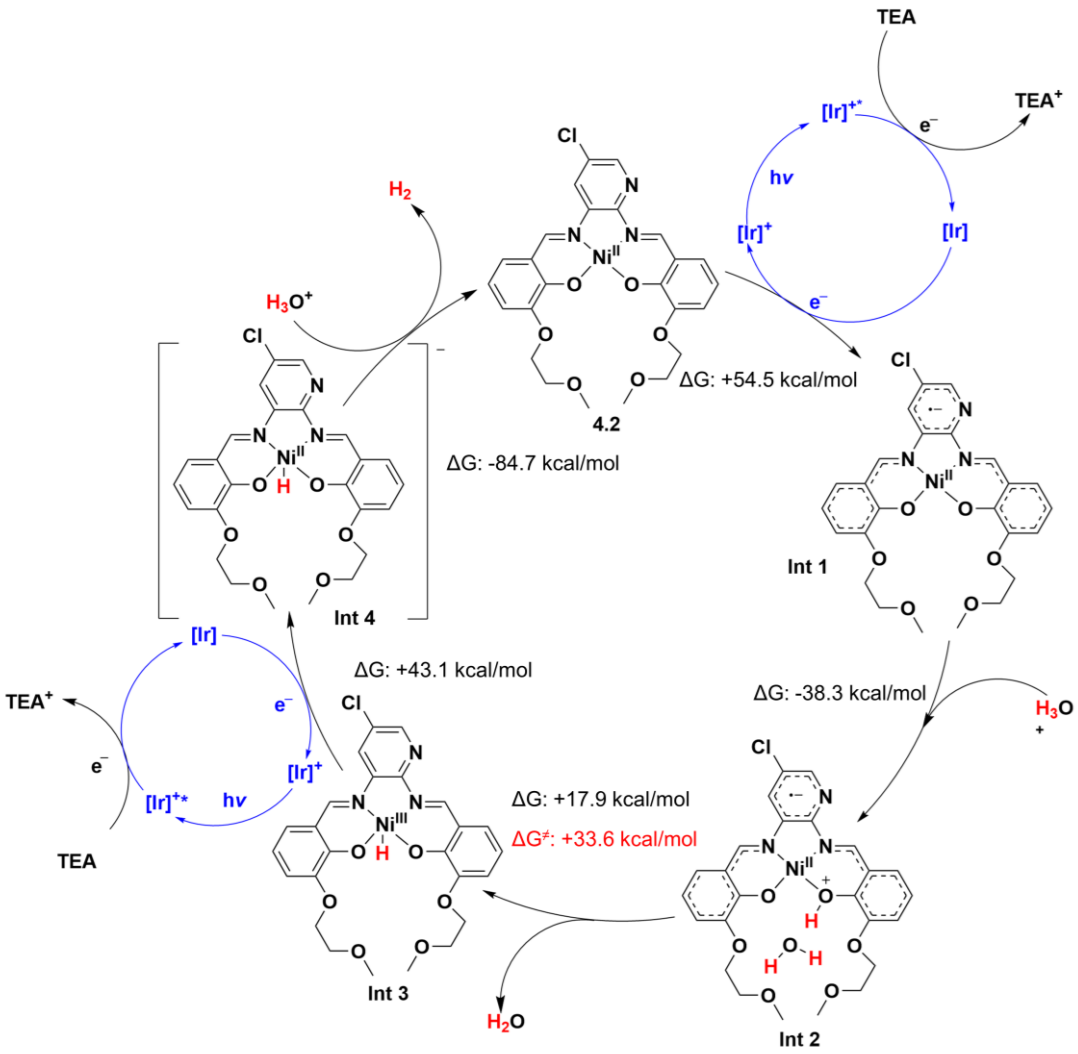

$\Delta G^{\neq}$: Energy barrier of transition state.

Figure 4.21. Proposed pathway for H_2 evolution catalysed by **4.2** based on DFT calculations of the energy levels of Ni-containing intermediates during the catalytic cycle. The thermodynamics in this cycle were obtained by including TEA as the sacrificial electron donor, whereas $[Ir]^+$ (blue parts of the cycle) was not included in the DFT calculations since it served only as a photocatalyst.

In addition, we also specifically probed the role of H_2O when it is cradled within the ether arms of **4.2**. The calculations show that H_2 evolution can only occur if a Ni hydride (**Int 4**) is formed, and the formation of the hydride **Int 3** required the presence of a H_2O molecule near Ni to act as a proton shuttle from the phenolic O atom. Without this crucial

Ni-H formation step, the second approach of H_3O^+ only results in further protonation of another phenolic O atom, after which there is no energetically accessible route for H_2 formation (Figure 4.22). The encapsulation of water molecules by supramolecular systems such as benzo crown ethers and rotaxanes have been previously reported to influence the pK_a and catalytic activity of the water,[61-63] lending support to our proposal that H_3O^+ trapping by the ether arms of **4.2** played a vital role in our photocatalytic system. As such, the DFT calculations highlight the importance of the second coordination sphere ether functionality in hydrogen bonding to H_2O as a proton shuttle to facilitate H_2 evolution. The full proposed mechanism is illustrated in Figure 4.21.

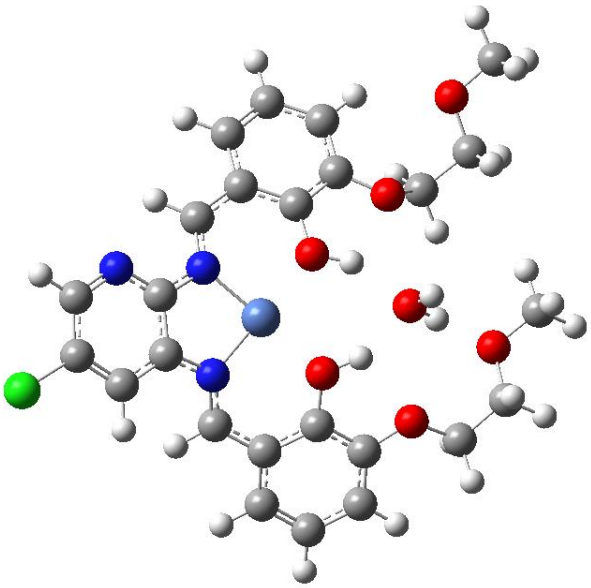

Figure 4.22. DFT calculations showing the double protonation on the ligand, which does not result in H_2 evolution.

4.5 Conclusion

In summary, we have shown that **4.2** can operate as an efficient homogeneous catalyst for H_2 evolution with TONs up to 3880, which is among the best for molecular Ni

complexes in molecular photocatalytic systems with neutral water as the proton source. Both steady-state and time-resolved optical spectroscopy combined with EPR spectroscopy provided insights into the initial elementary steps of the photocatalytic cycle involving a ligand-centered reduced intermediate. Moreover, DFT calculations supported a model where the second-sphere ether arms cradle H_2O as a proton shuttle in close proximity to the Ni center and promotes a vital proton transfer between the phenolic O atom and the metal center. Our detailed spectroscopic and computational studies have allowed us to extract critical insights into a catalytic cycle that could be a potential solution for the storage and utilisation of renewable energy. In addition, these results present a starting point for future developments of a broad class of H_2 evolution catalysts that employ alternative proton shuttles than amines in the second coordination sphere in artificial photosynthetic constructs driven by visible light in aqueous solutions.

4.6 Experimental Section

Materials and Methods Deuterated solvents were purchased from Cambridge Isotope Laboratories. Chemicals were obtained from Sigma-Aldrich, Alfa-Aesar, and Tokyo Chemical Industry Co., Ltd. (TCI). Unless otherwise noted, the commercial reagents were used as purchased. Compound $[Ir^{III}(ppy)_2(dtbbpy)](PF_6)$ was synthesised according to a previously published procedure.[64] The ^1H and ^{13}C spectra were recorded at room temperature on Bruker AVANCE 400 MHz and Bruker AV-300 (300 MHz) NMR spectrometers. The ^1H and ^{13}C chemical shifts (δ reported in ppm) are referenced to the residual solvent signal(s). UV-visible spectroscopic measurements were performed using a Shimadzu UV-3600 UV-Vis-NIR spectrophotometer. Elemental analyses were performed with an Elementar vario MICRO cube analyser. High-resolution mass spectra (HR-MS) were obtained with a Q-TOF Premier LC HR mass spectrometer.

Synthesis of complexes

Compound 2-Hydroxy-3-(2-methoxyethoxy)benzaldehyde (4.1).

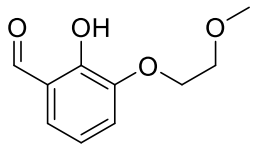

Compound **4.1** has been previously reported, and the current procedure we used was adapted from those published methods.[65] Sodium hydride (0.600 g of a 60% dispersion in oil, 15.2 mmol) was suspended in anhydrous dimethyl sulfoxide (DMSO, 10 mL) in an oven-dried Schlenk flask equipped with a dropping funnel. The suspension was cooled in an ice-bath. A solution of 2,3-dihydroxybenzaldehyde (1.00 g, 7.20 mmol) in anhydrous DMSO (10 mL) was added dropwise to the mixture under a flow of argon over the course of 1 h. Vigorous gas evolution occurred. After complete addition, the dark orange solution was stirred at ambient temperature, and (2-methoxyethoxy)-p- toluenesulfonate (1.36 mL, 7.2 mmol) was added in one portion. The solution was then stirred for another 2.5 h. Water (50 mL) was slowly added to quench the reaction, and the solution was extracted with chloroform (3 × 30 mL). The aqueous layer was acidified to pH 2 with 1 M aqueous hydrochloric acid (15 mL) and the color changed from dark orange to yellow. The aqueous layer was then extracted with chloroform (3 × 30 mL). The organic layer was subsequently rinsed with 1 M hydrochloric acid (2 × 30 mL), dried with anhydrous sodium sulphate, and filtered. The solvent was removed in vacuo to afford an orange viscous oil. The residue was purified by silica gel column chromatography (hexane:ethyl acetate = 4:1) and 1 (1.19 g, 86.0%) was isolated as a pale green-yellow solid. ^{1}H NMR (300 MHz, $CDCl_3$): δ = 3.46 (s, 3 H), 3.79 (t, J = 6.0 Hz, 2 H), 4.22 (t, J = 6.0 Hz, 2 H), 6.94 (t, J = 9.0 Hz, 1 H), 7.17 – 7.26 (m, 2 H), 9.94 (s, 1 H), 10.80 (s, 1 H) ppm. ^{13}C NMR (75 MHz, $CDCl_3$): δ = 59.7, 69.2, 70.9, 119.4, 121.0, 121.2, 125.3, 147.4, 152.2, 196.2 ppm. HR-MS (ESI^+) calcd for $C_{10}H_{12}O_4$, $[M+H]^+$ m/z = 197.0814, found 197.0805.

Ni pyridyl salicylaldimine complex (4.2).

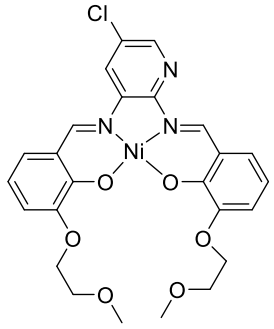

The current procedure we used was adapted from previous published methods.[37] To a solution of **4.1** (1.00 g, 5.10 mmol) and 2,3-diamino-5-chloropyridine (0.366 g, 2.55 mmol) in ethanol (20 mL) was added $Ni(OAc)_2{\cdot}4H_2O$ (0.750 g, 2.55 mmol). The mixture was heated under refluxing conditions for 12 h. After cooling to room temperature, the precipitate was collected by filtration, washed with cold ethanol followed by diethyl ether, and dried in vacuum. Complex **4.2** (1.36 g, 96%) was obtained as an orange powder. Single crystals were obtained by evaporating a solution of **4.2** in dichloromethane. ^{1}H NMR (400 Hz, $CDCl_3$): δ = 3.48 (s, 6 H), 3.83-3.87 (m, 4 H), 4.13 (t, J = 5.4 Hz, 2 H), 4.21 (t, J = 5.4 Hz, 2 H), 6.39 (t, J = 7.8 Hz, 1 H), 6.55 (t, J = 8.0 Hz, 1 H), 6.67 (d, J = 7.6 Hz, 1 H), 6.85 (t, J = 8.4 Hz, 2 H), 6.95 (d, J = 7.2 Hz, 1 H), 7.92 (d, J = 2.0 Hz, 1 H), 8.01 (d, J = 2.0 Hz, 1 H), 8.29 (s, 1 H), 8.76 (s, 1 H) ppm. ^{13}C NMR (100 MHz, $CDCl_3$): δ = 59.1 (2 C), 68.0, 68.1, 71.0 (2 C), 115.4, 115.6, 117.2, 119.8 (2 C), 122.9 (2 C), 125.6, 129.6, 136.4, 144.0, 149.8, 149.9, 151.9, 155.1 (2 C), 159.1 (2 C), 159.3 ppm. Anal. Calcd for $C_{25}H_{24}O_6N_3NiCl{\cdot}H_2O$ (%): C 52.35, H 4.54, N 7.33; found C 52.75, H 4.39, N 7.47. HR-MS (ESI^+) calcd. for $C_{25}H_{24}O_6N_3NiCl$, $[M+H^+]^+$ *m/z* = 556.0785, found 556.0789.

Ni pyridyl salicylaldimine complex (4.3).

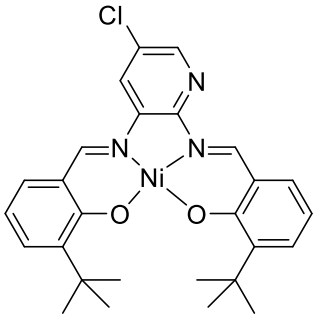

The current procedure we used was adapted from previous published methods.[37] To 3-*tert*-butyl-2-hydroxybenzaldehyde (0.100 g, 0.561 mmol) and 2,3-diamino-5-chloropyridine (0.0400 g, 0.281 mmol) in ethanol (2 mL) was added $Ni(OAc)_2{\cdot}4H_2O$ (0.0700 g, 0.281 mmol). The mixture was heated under refluxing conditions for 12 h. After cooling to room temperature, the precipitate was collected by filtration, washed with cold ethanol followed by diethyl ether, and dried in vacuum.

Complex **4.3** (0.124 g, 85%) was obtained as a red powder. ^{1}H NMR (400 Hz, $CDCl_3$): δ = 1.45 (s, 18 H), 6.61 (m, 2 H), 7.17 (m, 2 H), 7.39 (m, 2 H), 7.91 (s, 1 H), 8.13 (s, 1 H), 8.15 (s, 1 H), 8.94 (s, 1 H) ppm. ^{13}C NMR (100 MHz, $CDCl_3$): 29.6 (6 C), 35.7 (2 C), 115.9 (2 C), 120.1, 120.3, 129.1, 132.0 (3 C), 136.0, 141.6, 141.9, 143.9, 152.3, 155.1, 155.6 (2 C), 167.6 (2 C), 167.7 ppm. Anal. Calcd for $C_{27}H_{28}O_2N_3NiCl{\cdot}H_2O$ (%): C 60.26, H 5.61, N 7.80; found C 60.30, H 5.36, N 7.84. HR-MS (ESI^+) calcd. for $C_{27}H_{29}O_2N_3NiCl$, $[M+H^+]^+$ *m/z* = 520.1310, found 520.1302.

[Ir(ppy)$_2$(dtbbpy)](PF$_6$).

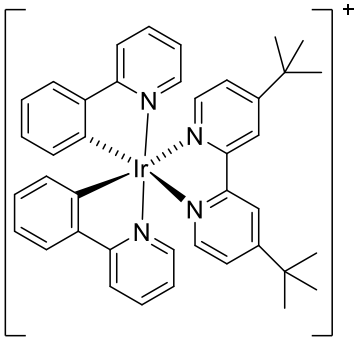

The synthesis of [Ir(ppy)$_2$(dtbbpy)](PF$_6$) was adopted from a literature procedure.[64] The spectroscopic data match the previously reported data. ^{1}H NMR (400 MHz, acetone-d_6): δ 1.40 (s, 18 H), 6.33 (d, J = 7.5 Hz, 2 H), 6.90 (s, 2 H), 7.02 (s, 2 H), 7.12 (s, 2 H), 7.69 (dd, J = 5.8, 1.6 Hz, 2 H), 7.77 (d, J = 5.6 Hz, 2 H), 7.88 (d, J = 7.7 Hz, 2 H), 8.04 – 7.92 (m, 4 H), 8.22 (d, J = 8.2 Hz, 2 H), 8.86 (d, J = 1.3 Hz, 2 H) ppm. ^{13}C NMR (100 MHz, acetone-d_6): δ 30.6 (6 C), 36.6 (2 C), 121.0 (2 C), 123.1 (2 C), 123.4 (2 C), 124.6 (2 C), 126.0 (2 C), 126.6 (2 C), 131.4 (2 C), 132.7 (2 C), 139.7 (2 C), 145.2 (2 C), 150.1 (2 C), 151.3 (2 C), 152.1 (2 C), 157.0 (2 C), 165.1 (2 C), 169.0 (2 C) ppm. HR-MS (ESI^+) calcd. for $C_{40}H_{40}N_4Ir^+$, $[M\text{-}PF_6]^+$ *m/z* = 769.2876, found 769.2866.

Cyclic Voltammetry

The controlled-potential coulometric experiments were performed using a Biologic SP-300 potentiostat. A three-electrode electrochemical cell was used with a glassy carbon working electrode (3 mm in diameter from BASi®), a Pt wire counter electrode, and another Pt wire as a pseudoreference electrode. Ferrocene (2 equiv. of catalyst, $E^0_{Fc^+/Fc}$ = +0.64 V vs.

NHE)[66] was added as the internal standard in anhydrous acetonitrile. Before each experiment, the working electrode (glassy carbon) was polished using a 0.05 μm alumina suspension on a polishing pad, followed by sonication in DI water for 10 min, and dried in air. The saturated Ar solutions were prepared by bubbling Ar through the solvents for 30 min.

Scan Rate Dependence Study In an electrochemical cell, 1.0 mM of **4.2** was dissolved in 0.10 M *n*-Bu_4NPF_6 in acetonitrile (5 mL). CV measurements were collected at various scan rates ranging from 100 mV s^{-1} to 1000 mV s^{-1}.

Photocatalytic H_2 Evolution Experiment The specific conditions, such as the reagent concentrations and reaction time intervals, have been summarised in Table 4.1. Typically, $[Ir]^+$, **4.2**, and TEA (0.10 M) in 5.0 mL MeOH (5% H_2O) were added to a 27 mL Schlenk tube together with a stir bar. The solution was deoxygenated by bubbling with Ar for 20 min after the Schlenk tube was sealed with a septum. The absence of O_2 in the Schlenk tube was verified by a GC (Agilent 7890A gas-chromatograph with a TCD, a 5 Å 2 mm × 5 m molecular sieve column, and Ar as the carrier gas) before irradiation. The tube was irradiated by visible light supplied by a 300 W xenon lamp with a 420 nm-cutoff UV light filter. After different time interval, a gas sample (0.50 mL) was taken from the headspace of the Schlenk tube and analysed by GC to determine the amount of generated H_2.

Preparation of TEA/acetic Acid Buffer A buffer solution for the photocatalytic reaction was prepared by adding 0.10 mL of acetic acid, 20.0 mL of TEA, and 2.50 mL of DI water to 50.0 mL of methanol.

Transient Absorption Measurements The transient absorption and emission measurements were performed using an Edinburgh Instruments LP920 transient absorption spectrometer equipped with a pulsed Xe probe lamp in conjunction with a Nd:YAG laser (Continuum Surelite II-10) as the excitation source. The laser pulse width is 5-8 ns and the repetition rate is 10 Hz. During transient absorption measurements, the pulses are

synchronised with the LP920 system at a frequency of 1 Hz. The pulse energy used was between 6-23 mJ/pulse.

The data were fit to single exponential or biexponential functions to obtain the time constants for the nanosecond transient optical spectroscopic signals according to the following equation:

$$y = y_0 + A_1 e^{-(t-\tau_0)/\tau_1}$$

The parameters y_0, τ_0, A_n, and τ_n were determined by a least-squares fitting procedure in Origin. The term y_0 corresponds to the vertical intercept at long lifetimes where the signal decays to a 'permanent' absorption (positive y_0) or bleach (negative y_0). The variable τ_0 is the delay time of the excitation pulse from the start of the probe measurement during each photoexcitation cycle. A_1 is the change in optical density after irradiation and τ_1 is the corresponding time constant.

Stern-Volmer Plot for the Quenching of $[Ir(ppy)_2(dtbbpy)]^{+}$* by TEA As the concentration of TEA increases, the lifetime τ of the signal owing to $[Ir]^{+}$* decreases. The bimolecular quenching rate constant, k_q, is related to the lifetime, τ of $[Ir]^{+}$* in the presence of TEA with a concentration of $[Q]$ by the Stern-Volmer equation:

$$\frac{\tau_0}{\tau} = 1 + k_q \tau_0 [Q]$$

where τ_0 is the lifetime of $[Ir]^{+}$* in the absence of TEA

The bimolecular rate constant, k_q, of the of $[Ir]^{+}$* by TEA can be obtained by plotting a graph of τ_0/τ against [Q] with a fixed vertical intercept of 1. The gradient ($k_q \tau_0$) was determined to be 2.22 ± 0.07 M^{-1} and τ_0 was determined to be 3.90 ± 0.20 μs. This gives a rate constant, k_q, of 5.66 x 10^6 M^{-1} s^{-1}.

Stern-Volmer Plot for the Quenching of $[Ir(ppy)_2(dtbbpy)]^{+}$* by 4.2 As the concentration of **4.2** increases, the lifetime τ of the signal owing to $[Ir]^{+}$* decreases. The

quenching rate constant, k_q, is related to the lifetime, τ, of $[Ir]^{+}$* in the presence of **4.2** with a concentration of $[Q]$ by the Stern-Volmer equation:

$$\frac{\tau_0}{\tau} = 1 + k_q \tau_0 [Q]$$

where τ_0 is the lifetime of $[Ir]^{+}$* in the absence of **4.2** and can be obtained by plotting a graph of τ_0 / τ against [Q] with a fixed vertical intercept of 1. This gives a rate constant, k_q, of 3.56 x 10^9 M^{-1} s^{-1}.

TON calculation The TON and TOF number of H_2 generated from the photocatalytic experiments were calculated by the following equations:

TON = n_{H_2}/n_{cat} (mol H_2 per mol catalyst)

In the equation, n_{H_2} is the number of moles of H_2 generated, and n_{cat} is the number of moles of catalyst used in the experiment.

DFT calculation All calculations were performed with the Gaussian 09 (Rev. E.01) program.[67] Geometry optimisation was conducted by using the M06 functional.[68] The Def2-SVP basis set was employed for all atoms.[69] The vibrational analysis and thermodynamic information at 298.15 K were calculated with the keyword Freq in Gaussian. The PCM solvent model was used in the geometry optimisations for all calculations.

EPR Measurements The X-band EPR spectra were recorded on either a JEOL FA200 spectrometer or a Bruker ELEXSYS spectrometer. The EPR spectra were obtained at room temperature with the microwave frequency from 9200 to 9850 MHz. The spectrum for **4.2**$^{-}$ was obtained in the solid–state EPR at room temperature. The microwave frequency modulation amplitude was 0.006, time constant was 0.08192, power used was 2 μW, and microwave frequency was at 9850 MHz. The EPR spectrum for sodium anthracenide was obtained as a solution in diethyl ether at room temperature. The microwave frequency was at 9200 MHz.

Preparation of Solid-State Sample for EPR Measurement The magnesium anthracene-THF complex (151 mg, 0.360 mmol) was added to **4.2** (200 mg, 0.360 mmol) in anhydrous THF and stirred at room temperature for 12 h. The solvent was removed under vacuum to obtain a dark green powder. The dark green residue was then washed with diethyl ether followed by pentane. The resulting solid was transferred to a J. Young EPR tube for the EPR experiment.

REFERENCES

(1) Barber, J. *Chem. Soc. Rev.* **2009**, *38*, 185-196.

(2) Han, Z.; Eisenberg, R. *Acc. Chem. Res.* **2014**, *47*, 2537-2544.

(3) Chen, X.; Shen, S.; Guo, L.; Mao, S. S. *Chem. Rev.* **2010**, *110*, 6503-6570.

(4) Sivula, K.; van de Krol, R. *Nat. Rev. Mater.* **2016**, *1*, 15010.

(5) Ran, J.; Zhang, J.; Yu, J.; Jaroniec, M.; Qiao, S. Z. *Chem. Soc. Rev.* **2014**, *43*, 7787-7812.

(6) Click, K. A.; Beauchamp, D. R.; Huang, Z.; Chen, W.; Wu, Y. *J. Am. Chem. Soc.* **2016**, *138*, 1174-1179.

(7) Bard, A. J.; Fox, M. A. *Acc. Chem. Res.* **1995**, *28*, 141-145.

(8) Sattler, W.; Ener, M. E.; Blakemore, J. D.; Rachford, A. A.; LaBeaume, P. J.; Thackeray, J. W.; Cameron, J. F.; Winkler, J. R.; Gray, H. B. *J. Am. Chem. Soc.* **2013**, *135*, 10614-10617.

(9) Esswein, A. J.; Nocera, D. G. *Chem. Rev.* **2007**, *107*, 4022-4047.

(10) Chang, C. J.; Chang, M. C.; Damrauer, N. H.; Nocera, D. G. *Biochim. Biophys. Acta.* **2004**, *1655*, 13-28.

(11) Pfeffer, M. G.; Kowacs, T.; Wächtler, M.; Guthmuller, J.; Dietzek, B.; Vos, J. G.; Rau, S. *Angew. Chem. Int. Ed.* **2015**, *54*, 6627-6631.

(12) Ozawa, H.; Haga, M.-a.; Sakai, K. *J. Am. Chem. Soc.* **2006**, *128*, 4926-4927.

(13) Cline, E. D.; Adamson, S. E.; Bernhard, S. *Inorg. Chem.* **2008**, *47*, 10378-10388.

(14) Xie, J.; Li, C.; Zhou, Q.; Wang, W.; Hou, Y.; Zhang, B.; Wang, X. *Inorg. Chem.* **2012**, *51*, 6376-6384.

(15) Pitman, C. L.; Miller, A. J. *ACS Catal.* **2014**, *4*, 2727-2733.

(16) Curtin, P. N.; Tinker, L. L.; Burgess, C. M.; Cline, E. D.; Bernhard, S. *Inorg. Chem.* **2009**, *48*, 10498-10506.

(17) Du, P.; Eisenberg, R. *Energy Environ. Sci.* **2012**, *5*, 6012-6021.

(18) Koshiba, K.; Yamauchi, K.; Sakai, K. *Angew. Chem. Int. Ed.* **2017**, *56*, 4247-4251.

(19) Beyene, B. B.; Mane, S. B.; Hung, C. H. *Chem. Commun.* **2015**, *51*, 15067-15070.

(20) Fihri, A.; Artero, V.; Razavet, M.; Baffert, C.; Leibl, W.; Fontecave, M. *Angew. Chem. Int. Ed.* **2008**, *120*, 574-577.

(21) Dempsey, J. L.; Brunschwig, B. S.; Winkler, J. R.; Gray, H. B. *Acc. Chem. Res.* **2009**, *42*, 1995-2004.

(22) McCormick, T. M.; Calitree, B. D.; Orchard, A.; Kraut, N. D.; Bright, F. V.; Detty, M. R.; Eisenberg, R. *J. Am. Chem. Soc.* **2010**, *132*, 15480-15483.

(23) Kaeffer, N.; Chavarot-Kerlidou, M.; Artero, V. *Acc. Chem. Res.* **2015**, *48*, 1286-1295.

(24) Khnayzer, R. S.; Thoi, V. S.; Nippe, M.; King, A. E.; Jurss, J. W.; El Roz, K. A.; Long, J. R.; Chang, C. J.; Castellano, F. N. *Energy Environ. Sci.* **2014**, *7*, 1477-1488.

(25) Nippe, M.; Khnayzer, R. S.; Panetier, J. A.; Zee, D. Z.; Olaiya, B. S.; Head-Gordon, M.; Chang, C. J.; Castellano, F. N.; Long, J. R. *Chem. Sci.* **2013**, *4*, 3934-3945.

(26) Helm, M. L.; Stewart, M. P.; Bullock, R. M.; DuBois, M. R.; DuBois, D. L. *Science* **2011**, *333*, 863-866.

(27) Jacobsen, G. M.; Yang, J. Y.; Twamley, B.; Wilson, A. D.; Bullock, R. M.; DuBois, M. R.; DuBois, D. L. *Energy Environ. Sci.* **2008**, *1*, 167-174.

(28) Rakowski Dubois, M.; Dubois, D. L. *Acc. Chem. Res.* **2009**, *42*, 1974-1982.

(29) McLaughlin, M. P.; McCormick, T. M.; Eisenberg, R.; Holland, P. L. *Chem. Commun.* **2011**, *47*, 7989-7991.

(30) Gross, M. A.; Reynal, A.; Durrant, J. R.; Reisner, E. *J. Am. Chem. Soc.* **2014**, *136*, 356-366.

(31) McNamara, W. R.; Han, Z.; Alperin, P. J.; Brennessel, W. W.; Holland, P. L.; Eisenberg, R. *J. Am. Chem. Soc.* **2011**, *133*, 15368-15371.

(32) McNamara, W. R.; Han, Z.; Yin, C.-J. M.; Brennessel, W. W.; Holland, P. L.; Eisenberg, R. *Proc. Natl. Acad. Sci. U.S.A.* **2012**, *109*, 15594-15599.

(33) Han, Z.; McNamara, W. R.; Eum, M. S.; Holland, P. L.; Eisenberg, R. *Angew. Chem. Int. Ed.* **2012**, *51*, 1667-1670.

(34) Han, Z.; Shen, L.; Brennessel, W. W.; Holland, P. L.; Eisenberg, R. *J. Am. Chem. Soc.* **2013**, *135*, 14659-14669.

(35) Lee, C. H.; Dogutan, D. K.; Nocera, D. G. *J. Am. Chem. Soc.* **2011**, *133*, 8775-8777.

(36) Graham, D. J.; Nocera, D. G. *Organometallics* **2014**, *33*, 4994-5001.

(37) Shao, H.; Muduli, S. K.; Tran, P. D.; Soo, H. S. *Chem. Commun.* **2016**, *52*, 2948-2951.

(38) Kumar, A.; Lionetti, D.; Day, V. W.; Blakemore, J. D. *Chem. Eur. J.* **2018**, *24*, 141-149.

(39) Van Staveren, C. J.; Van Eerden, J.; Van Veggel, F. C. J. M.; Harkema, S.; Reinhoudt, D. N. *J. Am. Chem. Soc.* **1988**, *110*, 4994-5008.

(40) Reath, A. H.; Ziller, J. W.; Tsay, C.; Ryan, A. J.; Yang, J. Y. *Inorg. Chem.* **2017**, *56*, 3713-3718.

(41) Chang, C. T.; Chen, C. L.; Liu, Y. H.; Peng, S. M.; Chou, P. T.; Liu, S. T. *Inorg. Chem.* **2006**, *45*, 7590-7592.

(42) Cacciapaglia, R.; Mandolins, L. *Chem. Soc. Rev.* **1993**, *22*, 221-231.

(43) Suneesh, C. V.; Balan, B.; Ozawa, H.; Nakamura, Y.; Katayama, T.; Muramatsu, M.; Nagasawa, Y.; Miyasaka, H.; Sakai, K. *Phys. Chem. Chem. Phys.* **2014**, *16*, 1607-1616.

(44) Isse, A. A.; Gennaro, A.; Vianello, E. *Electrochim. Acta* **1992**, *37*, 113-118.

(45) Costentin, C.; Passard, G.; Robert, M.; Saveant, J. M. *J. Am. Chem. Soc.* **2014**, *136*, 11821-11829.

(46) Lv, H.; Guo, W.; Wu, K.; Chen, Z.; Bacsa, J.; Musaev, D. G.; Geletii, Y. V.; Lauinger, S. M.; Lian, T.; Hill, C. L. *J. Am. Chem. Soc.* **2014**, *136*, 14015-14018.

(47) Prier, C. K.; Rankic, D. A.; MacMillan, D. W. C. *Chem. Rev.* **2013**, *113*, 5322-5363.

(48) Luo, S. P.; Mejia, E.; Friedrich, A.; Pazidis, A.; Junge, H.; Surkus, A. E.; Jackstell, R.; Denurra, S.; Gladiali, S.; Lochbrunner, S.; Beller, M. *Angew. Chem. Int. Ed.* **2013**, *52*, 419-423.

(49) Chen, L.; Chen, G.; Leung, C.-F.; Yiu, S.-M.; Ko, C.-C.; Anxolabéhère-Mallart, E.; Robert, M.; Lau, T.-C. *ACS Catal.* **2014**, *5*, 356-364.

(50) Cozzi, P. G. *Chem. Soc. Rev.* **2004**, *33*, 410-421.

(51) Zhang, W.; Wang, Y.; Wang, Z.; Zhong, Z.; Xu, R. *Chem. Commun.* **2010**, *46*, 7631-7633.

(52) Gartner, F.; Sundararaju, B.; Surkus, A. E.; Boddien, A.; Loges, B.; Junge, H.; Dixneuf, P. H.; Beller, M. *Angew. Chem. Int. Ed.* **2009**, *48*, 9962-9965.

(53) Thermal Conductivity/E-4W/mK(Fa. Messer,Switzerland): H2(1861)>He(1500)>D2(1310).

(54) Wang, C.; Cao, S.; Fu, W. F. *Chem. Commun.* **2013**, *49*, 11251-11253.

(55) Yamada, Y.; Miyahigashi, T.; Kotani, H.; Ohkubo, K.; Fukuzumi, S. *Energy Environ. Sci.* **2012**, *5*, 6111-6118.

(56) Bogdanovic, B. *Acc. Chem. Res.* **1988**, *21*, 261-267.

(57) Bogdanovic, B.; Janke, N.; Kinzelmann, H.-G. *Chem. Ber.* **1990**, 1507-1515.

(58) Azevedo, F.; Freire, C.; de Castro, B. *Polyhedron* **2002**, *21*, 1695-1705.

(59) Solis, B. H.; Maher, A. G.; Dogutan, D. K.; Nocera, D. G.; Hammes-Schiffer, S. *Proc. Natl. Acad. Sci. U.S.A* **2016**, *113*, 485-492.

(60) Das, A.; Jha, A.; Gera, R.; Dasgupta, J. *J. Phys. Chem. C* **2015**, *119*, 21234-21242.

(61) Costes, J.-P.; Dahan, F.; Laurent, J.-P. *Inorg. Chem.* **1994**, *33*, 2738-2742.

(62) Kusaka, R.; Inokuchi, Y.; Ebata, T. *Phys. Chem. Chem. Phys.* **2008**, *10*, 6238-6244.

(63) Ragazzon, G.; Schafer, C.; Franchi, P.; Silvi, S.; Colasson, B.; Lucarini, M.; Credi, A. *Proc. Natl. Acad. Sci. U. S. A.* **2018**, *115*, 9385-9390.

(64) Querard, P.; Perepichka, I.; Zysman-Colman, E.; Li, C. J. *Beilstein J. Org. Chem.* **2016**, *12*, 2636-2643.

(65) Schall, O. F.; Robinson, K.; Atwood, J. L.; Gokel, G. W. *J. Am. Chem. Soc.* **1993**, *115*, 5962-5969.

(66) Thoi, V. S.; Sun, Y.; Long, J. R.; Chang, C. J. *Chem. Soc. Rev.* **2013**, *42*, 2388-2400.

(67) M. J. Frisch, G. W. T., H. B. Schlegel, G. E. Scuseria, M. A. Robb, J. R. Cheeseman, G. Scalmani, V. Barone, G. A. Petersson, H. Nakatsuji, X. Li, M. Caricato, A. Marenich, J. Bloino, B. G. Janesko, R. Gomperts, B. Mennucci, H. P. Hratchian, J. V. Ortiz, A. F. Izmaylov, J. L. Sonnenberg, D. Williams-Young, F. Ding, F. Lipparini, F. Egidi, J. Goings, B. Peng, A. Petrone, T. Henderson, D. Ranasinghe, V. G. Zakrzewski, J. Gao, N. Rega, G. Zheng, W. Liang, M. Hada, M. Ehara, K. Toyota, R. Fukuda, J. Hasegawa, M. Ishida, T. Nakajima, Y. Honda, O. Kitao, H. Nakai, T. Vreven, K. Throssell, J. A. Montgomery, Jr., J. E. Peralta, F. Ogliaro, M. Bearpark, J. J. Heyd, E. Brothers, K. N. Kudin, V. N. Staroverov, T. Keith, R. Kobayashi, J. Normand, K. Raghavachari, A. Rendell, J. C. Burant, S. S. Iyengar, J. Tomasi, M. Cossi, J. M. Millam, M. Klene, C. Adamo, R. Cammi, J. W. Ochterski, R. L. Martin, K. Morokuma, O. Farkas, J. B. Foresman, and D. J. Fox Gaussian, Inc., Wallingford CT, 2016.

(68) Zhao, Y.; Truhlar, D. G. *Theor. Chem. Acc.* **2007**, *120*, 215-241.

(69) Weigend, F.; Ahlrichs, R. *Phys. Chem. Chem. Phys.* **2005**, *7*, 3297-3305.

Chapter 5

Literature Review for CO_2 reduction

5.1 Overview

CO_2 is a linear, centrosymmetric molecule that is one of the more thermodynamically stable carbon compounds. The two C=O bonds are equal in bond lengths. These bonds are found to be 0.04 Å shorter than the C=O bond in a typical ketone structure.[1-3] Owing to the large bond dissociation energy in the C=O bonds, CO_2 can only be converted into other carbon compounds under harsh reaction conditions.[1] However, reduction of CO_2 from flue gas to hydrocarbon fuels for energy storage is a potentially attractive solution to tackle current environmental issues. By harnessing solar energy to convert CO_2 to fuels, we can reduce the emissions of CO_2 in the atmosphere and diminish our reliance on the burning of fossil fuels for energy.

In particular, the electrochemical reduction of CO_2 using electrical power is an important transformation with a high possibility of finding practical applications in industries, as it is compatible with many renewable energies, including solar energy.[4] However, the process of electrochemically reducing CO_2 to hydrocarbon fuels as products requires a significant energy input. Equations (1) – (9) below summarise the electrode potentials required to drive the reactions to obtain different products in the electrochemical reduction of CO_2 in water. The value of E^0 refers to the standard hydrogen electrode (SHE) in an aqueous solution at pH 7, with electrolyte concentration at 1.0 M, at room temperature and 1 atm gas pressure.[5] According to equations (5) – (8), the multi-protons coupled electrons reduction of CO_2 to methane, ethane, methanol and ethanol are more thermodynamically favourable than the competing H_2 evolution reaction, which is illustrated in equation (9). However, the kinetics for CO_2 reduction to these products are usually sluggish due to the need for the first electron reduction, which occurs only at -1.90 V vs SHE. The first electron reduction converts the linear CO_2 structure to a bent CO_2 anion radical (Equation (1)) for further transformation.[6] This intermediate state requires a large overpotential and is widely thought to be the rate determining step for CO_2 reduction.[6]

Therefore, the formation of CO_2-reduction products are usually in smaller quantities as compared to H_2 formation. Furthermore, the reduction of CO_2 usually gives a variety of products because of the small potential differences between them. This is the reason behind the poor selectivity of products for CO_2 reduction.

$$CO_2 + e^- \longrightarrow CO_2^{\bullet -} \qquad E^0 = -1.90\ V \qquad (1)$$

$$CO_2 + 2H^+ + 2e^- \longrightarrow CO + H_2O \qquad E^0 = -0.52\ V \qquad (2)$$

$$CO_2 + 2H^+ + 2e^- \longrightarrow HCOOH \qquad E^0 = -0.61\ V \qquad (3)$$

$$CO_2 + 4H^+ + 4e^- \longrightarrow HCHO + H_2O \qquad E^0 = -0.51\ V \qquad (4)$$

$$CO_2 + 8H^+ + 8e^- \longrightarrow CH_4 + 2H_2O \qquad E^0 = -0.24\ V \qquad (5)$$

$$2CO_2 + 12H^+ + 12e^- \longrightarrow C_2H_4 + 4H_2O \qquad E^0 = -0.34\ V \qquad (6)$$

$$CO_2 + 6H^+ + 6e^- \longrightarrow CH_3OH + H_2O \qquad E^0 = -0.38\ V \qquad (7)$$

$$2CO_2 + 12H^+ + 12e^- \longrightarrow C_2H_5OH + 3H_2O \qquad E^0 = -0.33\ V \qquad (8)$$

$$2H^+ + 2e^- \longrightarrow H_2 \qquad E^0 = -0.42\ V \qquad (9)$$

5.2 Materials for Electrocatalytic CO_2 Reduction

In order to address the problems associated with CO_2 reduction, scientists have been looking at different materials that can 1) reduce the overpotential required for CO_2 reduction, 2) improve the selectivity towards CO_2 reduction and/or 3) increase selectivity in products formation. These materials are generally categorised into metals, metal chalcogenides and carbon-based materials. Recently, different hybrid materials such as metal organic frameworks (MOFs) have also shown reactivity towards electrocatalytic CO_2 reduction.[7,8] However, hybrid materials are beyond the scope of this thesis and will not be discussed in this literature review.

5.2.1. Metals

Studies of different elemental metals on CO_2 reduction have been conducted since the 1980s by Hori *et al.*[9] The metals are generally divided into three different groups based

on the products formed from the CO_2 reduction reaction. The first group of metals consist of Pt, Ni, Ti and Fe. These metals favour the formation of H_2 as products due to low overpotential for H_2 evolution and strong CO adsorption capability. The second group of metals include Au, Ag, Zn, Pd and Ga. They can bind to the CO_2 anion radical for the reduction to CO to take place. However, further reduction cannot occur as the reduced product, CO, desorbs from the metal surface readily. The last group of metals are Sn, Pb, Bi and In. They do not bind well to the CO_2 anion radical. The result is the desorption of the CO_2 anion radical that rapidly gets protonated in the solution, forming formic acid as the major product. This prevent the further reduction of the CO_2 to other hydrocarbons and liquid fuel. Amongst the elemental metals studied, Cu has proved to be unique. It has been found to catalyse the formation of products beyond the two-electron reduction. This is due to the unique bonding properties that Cu has with CO. Cu has intermediate bonding strengths with both CO and COOH, thus allowing the formation of further reduced products on the Cu surface before desorption occurs.[9-11] Therefore, Cu metal for CO_2 reduction is the main focus of this Chapter.

5.2.2. Metal Chalcogenides

Apart from the elemental metals, layered TMD, such as MoS_2 have also been investigated for their reactivity towards CO_2 reduction. Commonly known for their high reactivity towards the H_2 evolution reaction, it was found that the bulk MoS_2 can also function as a highly selective CO_2 reduction catalyst to produce CO selectively at a low overpotential of 0.54 V. Notably, at an overpotential of 0.65 V, a cathodic current density of 65 mA cm^{-2} and a CO Faradaic efficient of 98% were achieved.[12] Further studies on dichalcogenides were also conducted and WSe_2 nanoflakes were found to be the most active. At an overpotential of 54 mV, a current density of 19 mA cm^{-2} with a CO Faradaic efficiency of 24% in 50:50 vol% ionic liquid/water electrolyte were achieved. As the overpotential increased to 0.65 V, the recorded current density for WSe_2 increases to reach

330 mA cm^{-2}. A Faradaic efficiency of 85% for CO, a feat not previously achieved by any other catalyst.[13] However, while layered TMDs show potential to achieve good product selectivity at a relatively low overpotential, it requires the use of ionic liquids to supress the H_2 evolution reaction and to stabilise the CO_2 molecule.

5.2.3. Carbon-based Materials

Carbon-based materials were also found to be effective for CO_2 reduction when they were doped with heteroatoms. Doping creates structural defects and introduced charge density on adjacent carbon atoms that induces reactivity towards the otherwise inert pristine carbonaceous materials. Asadi *et al.* prepared a N-doped carbon nanofiber that demonstrated the potential for carbonaceous material to activate CO_2 reduction. At a low onset potential of 0.17 V, in the presence of an ionic liquid, selective CO_2 reduction to CO was observed. It was proposed that the active site for the reduction of CO_2 is the highly positive carbon atom that is adjacent to the nitrogen dopant.[14] B- doped diamond was also found to be able to catalyse the selective reduction of CO_2 to formaldehyde with methanol or seawater as the solvent.[15] Notably, carbon-based materials show the potential to reduce CO_2 beyond a two-electron reduction. Wu *et al.* reported using N-doped graphene quantum dots to achieve multi-hydrocarbons and oxygenated hydrocarbons as the products for CO_2 reduction.[16] However, the mechanism of these unique N-doped graphene quantum dots remains elusive and more mechanistic studies have to be carried out to elucidate the mechanism of this reaction.[17]

5.3. Cu for CO_2 reduction

As discussed in the previous section, Cu is the only metal that was found to be able to produce products beyond the 2-electron reduction of CO_2. In fact, Jaramillo and co-workers found that the reduction of CO_2 on Cu surface can produce up to 16 different products including olefins containing six carbon atoms.[11] This provides the opportunity to convert CO_2 to more energy dense fuels and chemical precursors. To promote the electrocatalytic performance of the Cu metal, careful control of the surface morphology is essential for the selectivity of the products. Mechanistic studies with the aid of theoretical MO based calculations have been at the forefront to elucidate the mechanism and explain the reasons behind this selectivity. The modification of polycrystalline Cu surfaces with different structures allows for stable electrode performance in aqueous solutions and energy efficient transformation routes towards energy dense products. Apart from surface modification, the electrolyte used, pH of the reaction vessel and the applied potential all contribute to the selectivity of the products formed.

5.3.1. Surface modification

To understand the fundamentals of CO_2 reduction on Cu surfaces, single crystal Cu was used to study the effect of the crystal facet on CO_2 reduction products. Frese and co-workers found that the crystal facet greatly influenced the product distribution of the CO_2 reduction reaction. In one study conducted by the Frese's group, they observed that the formation of methane is greatly favoured on the (111) surface compared to that of the (110) and (100) surfaces with 0.5 M of $KHCO_3$ at various potentials.[18] In a separate study by Hori *et al.,* using [*n*(100) × (111)], [*n*(100) × (110)], [*n*(111) × (100)], [*n*(111) × (111)] and [*n*(110) × (100)] Cu electrodes in 0.1 M of $KHCO_3$, reported that Cu with predominantly Cu (100) has high selectivity towards ethylene formation whereas methane is favoured when Cu (111) is predominant.[19] The effects of the surface crystal facet on CO_2 reduction products were also highlighted in a seminal study conducted by Nilssen and co- workers.

In this work, nanocube- covered Cu surface (Figure 5.1a) with predominately Cu (100) terrace shows near complete suppression of methane formation, and selectivity towards ethylene as the major product as compared to polycrystalline Cu (Figure 5.1b).[20] More recently, Jiang *et al.* also demonstrated that Cu (100) and stepped (211) facet were more favourable to the formation of C_{2+} products compared to Cu (111).[21] Computational studies suggest that the different Cu surfaces possess different degrees of stabilising effects on the reaction intermediates, resulting in different reaction pathways of product distributions, which will be discussed further in section 5.4.

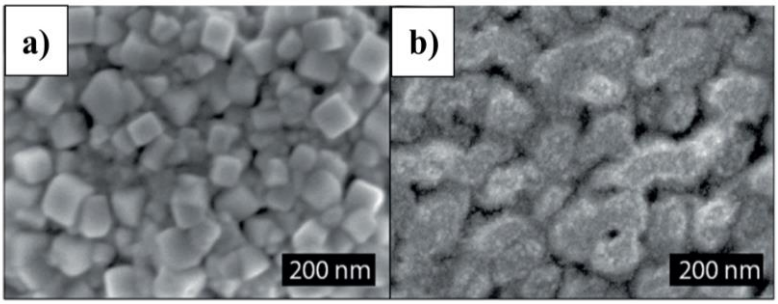

Figure 5.1. SEM images of a) Cu cube formed by cycling a polycrystalline Cu electrode between -1.15 and 0.9V three times in the presence of 4.0 mM KCl in 0.1 M $KHCO_3$ b) a polycrystalline electrode after cycling in the absence of KCl in 0.1 M $KHCO_3$. Adapted with permission from *Angew. Chem. Int. Ed.* **2015**, *54*, 5179-5182. Copyright 2015 WILEY-VCH Verlag GmbH & Co. KGaA, Weinheim.[20]

Apart from the crystal facet of the Cu, the particle size also greatly affects the product distribution of the reaction. Nanosized particles have been gaining traction in material research due to their increase in surface area and the unique catalytic activity they exhibit as compared to their bulk material. Predictably, the study of Cu nanoparticles by Strasser and co-worker found great enhancement of the current density compare to bulk Cu due to an increase in surface area. However, the selectivity of the products was found to be mainly H_2 and CO, with the suppression of hydrocarbon formation with a decrease in particle size, especially at less than 5 nm.[22] DFT calculations rationalized that the smaller

Cu nanoparticles provide more undercoordinated atoms that can bind strongly to H and COOH, thus accelerating the formation of H_2 and CO, while supressing the formation of hydrocarbons. However, conflicting results have been reported.

Kim *et al.* also found that in-situ structural modification during electrolysis of densely packed Cu nanoparticles to catalytic cube like structures resulted in the formation of C_2 - C_3 compounds at a Faradaic efficiency of more than 50% at only -0.75 V (Figure 5.2b).[23] The study conducted by Bell and co-workers on CO_2 reduction on Cu electrodes also supported a surface reconstruction for electrocatalytic conditioning the electrodes. By cycling the polycrystalline Cu from an oxidising potential to a reducing potential, they observed the formation of cubic shape Cu nanoparticles (Figure 5.2b) that lead to the suppression of methane and enhancement of the formation ethylene.[24] Sargent and co-workers also reported the electro-redeposition of Cu to control nanoscale morphology and achieve an ethylene/methane ratio of 200.[25] Figure 5.2c shows the change in surface morphology after 2 to 40 mins of electrolysis.

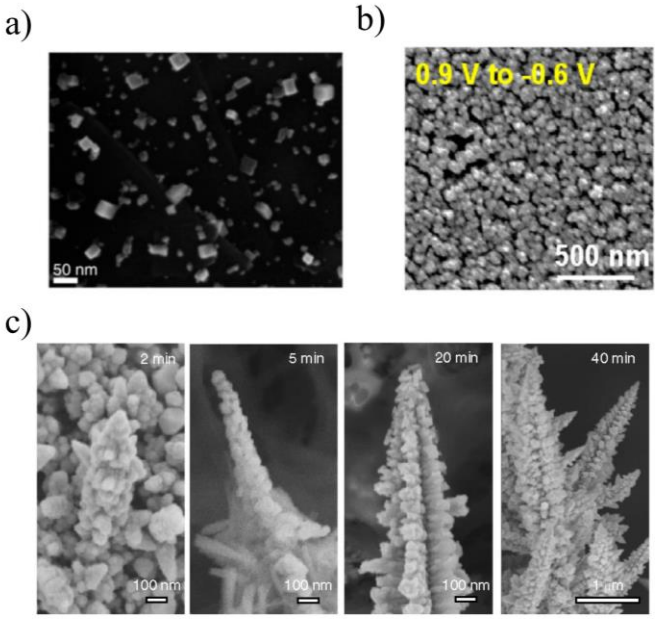

Figure 5.2. SEM images of (a) 22.5 times loaded Cu nanoparticles assembles on carbon-paper support electrode after 7 min of electrolysis at -0.81 V vs RHE. Adapted with permission from Proc. Natl. Acad. Sci. U.S.A. 2017, 114, 10560-10565. Copyright 2017 National Academy of Sciences.[23] (b) Cu cube formed by cycling a polycrystalline Cu electrode between -0.6 and 0.9 V in the presence of 4.0 mM KCl Adapted with permission from *ChemElectroChem* **2016**, *3*, 1012-1019. Copyright 2016 WILEY-VCH Verlag GmbH & Co. KGaA, Weinheim.[24] (c) Electro- redeposition Cu under -1.0 V vs RHE taken at 2, 5, 20 and 40 mins from left to right.. Adapted with permission from *Nat. Catal.* **2018**, *1*, 103-110. Copyright 2018 Macmillan Publishers Limited, part of Springer Nature.[25]

The surface roughening of the Cu electrode was also found to have influence over the product formation. The increase in surface area and the presence of more active surfaces are credited for this increase in the selectivity and reactivity.[26] Notably, the discovery of the reactivity of Cu nanofoams also highlight the importance of the surface on CO_2 reduction. This Cu nanofoam favours the reduction of CO_2 to hydrocarbons on the Cu at a much lower overpotential. This is attributed to the porosity of the Cu, providing channels for intermediate to undergo further reduction.[27]

The surface structure of the Cu can also affect the local condition of the working electrode. This has a great influence on the distribution of products. Ma *et al.* synthesised a group of Cu wires with different lengths to explore how the nanowire size affected the local pH and the effect it had on the product distribution. They demonstrated that an increase in the local pH correlates to the increase in C_2 product distribution.[28] From this work, we can see the effect of the local environment on the product distribution for CO_2 reduction.

Oxide derived Cu foils (OD-Cu) were reported to favour the formation of $C_2<$ products and shown to catalyse the reduction of CO_2 at a lower overpotential compared to a polycrystalline Cu surface. The foils can be obtained from various synthesis methods such as thermal,[29] chemical,[30,31] electrochemical oxidation[32,33] followed by electrochemical reduction. Oxidation-reduction cycling, anodisation and anodic-pulsing, were also used to obtain OD-Cu. Li *et al*. reported a OD-Cu that is composed of 20 nm particles in the shape of a rod that is 100-1000 nm in length. It is obtained by annealing in air at 500 °C for 12 h. By measuring the non-Faradaic capacitance, a surface roughness factor of 480 is obtained. It was found that the current density was 30 times higher than the regular polycrystalline Cu that catalysed the reduction of CO_2 at a low overpotential.[29] However, at this low onset potential, the majority of the products obtained were H_2 and CO. As the overpotential increased, the product distribution started to move towards C_{2+} chain products. The reasons behind this selectivity are still debatable and further investigation of this is needed to understand the mechanism. However, it is often attributed to the surface morphology of these OD-Cu.

5.3.2. pH

As discussed in section 5.3.1, the product distribution for CO_2 reduction with Cu plates can be affected by the local conditions. One of the most important conditions is the pH of the solution. In a follow up study by Smith and co-workers using in-situ surface

enhanced infrared absorption spectroscopy and computational modelling, they discovered the persistent alkalinity near the Cu surface, creating a local alkaline environment even in buffered solutions.[34] In the seminal study conducted by Sargent and co-workers with a gas diffusion electrode, it was found that the increase in pH reduces the overpotential and improves the selectivity of ethylene dramatically. A 70% Faradaic efficiency for ethylene was achieved at -0.55 V vs RHE.[35] Hori *et al.* also found a strong correlation between the pH and the applied potential on the selectivity towards CH_4 and C_2H_4 products. [36-38]

5.3.3. Electrolyte

Apart from the local pH, the choice of electrolyte, which was initially assumed to have no direct involvement in the selectivity of products, was shown otherwise by experiments conducted by Hori *et al*.[37,39] The group demonstrated that different electrolytes used can affect the product distribution at -0.5 mA current. The table below summarised the results obtained using different electrolytes for the reaction.

Table 5.1. Current efficiencies of CO_2 reduction products on a Cu electrode in various solutions at −5 mA cm^{-2} reported by Hori *et al.*. [37]

Electrolyte	Potential (V vs SHE)	Current efficiency (%)							
		CH_4	C_2H_4	alcohols	CO	$HCOO^-$	H_2	Total	C_2H_4/CH_4
0.1 M $KHCO_3$	-1.41	29.4	30.1	9.9	2	9.7	10.9	2	1.02
0.1 M KCl	-1.44	11.5	47.8	25.5	2.5	6.6	5.9	99.8	4.16
0.1 M K_2SO_4	-1.40	12.3	46	22.2	2.1	8.1	8.7	99.4	3.74
0.1 M K_2HPO_4	-1.23	17.0	1.8	0.7	1.3	5.3	72.4	98.5	0.11

The effect of cations on the product distribution was later studied in detail by Bell and co-workers. The group demonstrated how the hydrolysis of cations can affect the local

pH of the solution resulting in a different product distribution for Cu.[40] Figure 5.3a shows that as the cationic size increases, the current density increases. The increases in cation size for the electrolyte also correlates to the decrease in H_2 evolution, with an increase in carbon-based products (Figure 5.3b). The group suggest that the larger the cation, the better it can serve as a buffer, hence, controlling the pH of solution near the electrode surface. As discuss in section 5.3.2., this change in pH thus changes the products observed during electrolysis.

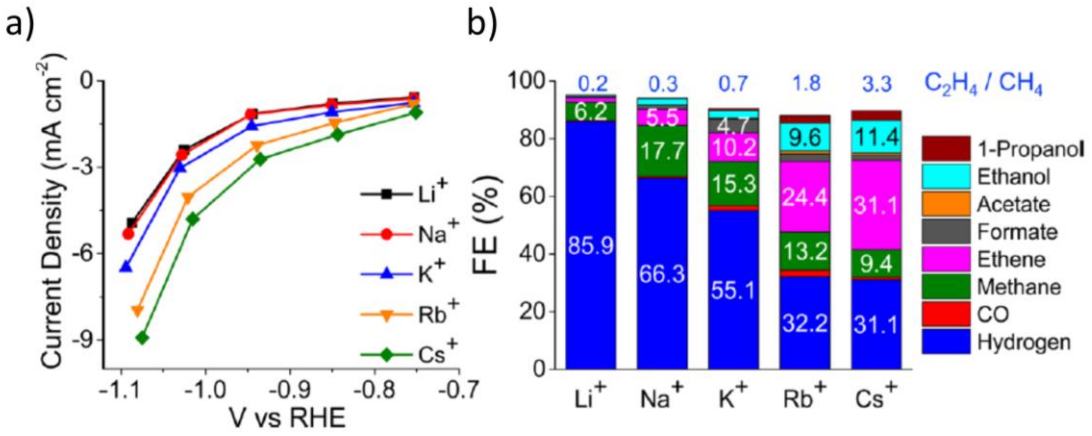

Figure 5.3. (a) Current density versus applied potential on Cu cathode in different cations. (b) Faradaic efficiencies for CO_2 reduction products produced over Cu at -1.0 V vs RHE in CO2 saturated 0.1 M $MHCO_3$ M= Li, Na, K, Rb, Cs) electrolyte. Adapted with permission from *J. Am. Chem. Soc.* **2016**, *138*, 13006-13012. Copyright 2016 American Chemical Society.[40]

5.3.4. Applied Potential

The potential applied also greatly influence the product distribution of the reaction. In the earlier work by Noda *et al.,* it was found that at low overpotentials, CO, $HCOO^-$ and H_2 are the major products that were detected. As the potential increases, the selectivity towards H_2 decreases with the increase in CO and $HCOO^-$. With further increases in potential, the selectivity of H_2 continue to decline and the formation of C_2H_4 was observed at -1.1 V and CH_4 at -1.2 V. However, as the potential increased to -1.5 V and above (more negative), H_2 selectivity began to increase again and dominate as the major product

formed.[41] This is usually attributed to the low solubility and the limitation of mass transport of dissolved CO_2 to the electrode surface for efficient CO_2 reduction. Some of the independent work by other groups have also verified this potential dependence selectivity with Cu as the electrocatalyst.[11,24]

5.4 Mechanistic Studies

Mechanistic studies on CO_2 reduction on Cu electrodes prove to be difficult due to the number of products that can be produced. As reported by Kuhl *et al*., sixteen different products, ranging from C_1, C_2 and oxygenated C_2, to C_3 and oxygenated C_3 compounds were detected during CO_2 reduction on Cu.[11] Many studies have been conducted to try to elucidate the mechanism of CO_2 reduction on the Cu surface. Schouten *et al*. attempted to study the mechanism of CO_2 reduction via experimental studies.[42] They fed the postulated intermediate of CO_2 reduction as the feedstock for reduction on the Cu surface and analysed the products formed. However, not all the products from the reduction of CO_2 can be determined by this method. In addition, only stable molecules can be used as the feedstock in this reaction and they do not necessarily be the reaction intermediates that have the lowest thermodynamic and kinetic barriers. Therefore, the use of computational calculations have been at the forefront to rationalise the product distribution on Cu surfaces with the support of experimental data.

Norskov and co-workers found that CO formation is the key step towards the formation of hydrocarbons such as CH_4 and C_2H_4.[43] Briefly, the key intermediate species, CO, is formed via the reduction of the carboxyl intermediate that is formed from the protonation of the $CO_2^{\bullet-}$ radical. This CO molecule can further be reduced to hydrocarbons or other oxygenated compounds. However, two different mechanisms have been proposed by different groups. In the first pathway as proposed by Peterson *et al*, which uses a computational hydrogen electrode (CHE) model on a (211) Cu surface, the absorbed CO is

reduced to CH_2O, followed by the formation of CH_3O and the eventual release of CH_4 after further reduction, leaving the O on the Cu surface to be reduced to H_2O.[43] They proposed that the reduction of CO_2 to CH_4 undergoes a similar mechanism on a Cu (100) face (Scheme 6.1, red). Nie *et al*, however, suggested an alternative pathway for the formation of CH_4 via the formation of a surface carbene (CH_2) before the formation of CH_3 and the eventual release of CH_4 (Scheme 6.1, blue).[44] By including the role of water in the computation, they found that the activation barrier is much higher through the CHO intermediate. In such case, methanol production is greatly favoured over the formation of methane. However, if the reaction pathway proceeds via a COH mechanism, which further reduces to C, the calculation favours the formation of methane over methanol. As the activation barrier for the formation of CHO and COH were calculated to be 0.39 eV and 0.21 eV, the formation of methane is preferred.[44] This is consistent with the experimental observation where methane is produced more than that of methanol.

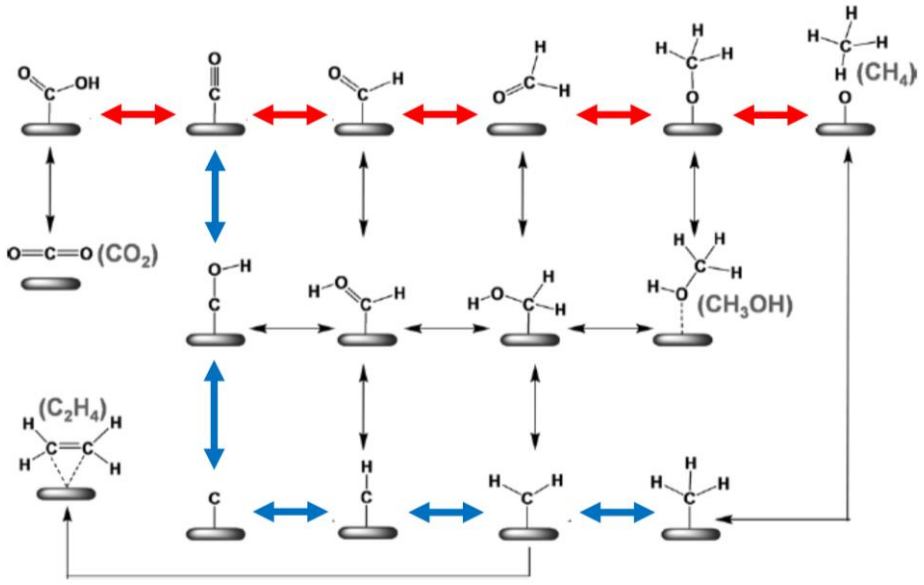

Scheme 6.1. Proposed reaction paths for production of CH_4, CH_3OH, C_2H_4 on Cu (111) based on previous experimental studies[11,37,42] as well as DFT work by Peterson and co-workers.[43,45] Electrochemical elementary steps for CH_4 and CH_3OH formation involve electron and proton transfer, whereas C_2H_4 is produced through nonelectrochemical CH_2 dimerisation. Adapted with permission from *Angew. Chem. Int. Ed.* **2013**, *52*, 2459-2462. Copyright 2013 WILEY-VCH Verlag GmbH & Co. KGaA, Weinheim

In their further studies of the system, they found that the different Cu surface facet of the Cu metal, such as fcc (211), can better stabilise the intermediates for CO_2 reduction, resulting in better selectivity towards CH_4 and C_2H_4 formation .[45,46]

Recently, Bell and Head-Gordon studied the formation of 7 different C_2 compounds on a Cu surface.[47] This study included the surface charges of the electrode that is present during electrolysis, which is usually not accounted in previous work, to understand the mechanism for product formation.[46,48] They showed that the formation of ethylene, while not pH dependent, is highly dependent on the surface facet and applied potential. They also suggest that the intermediates in ethylene formation differ when the surface changes from (111) facet to (100), as the Cu(100) favours the dimerisation of CO to form *COCO as the intermediate, while this pathway is not energetically favourable on Cu(111). They proposed

the formation of •CHO followed by coupling with CO to form •COCHO, which is in contrast with previous studies.

However, all these mechanistic studies discussed above assume that the surface is purely metallic Cu devoid of any presence of oxide layers or subsurface oxygen. More recently, the effect of oxygen on the Cu subsurface and their role in CO_2 reduction was explored. This a is particularly interesting area of study as oxide- derived Cu was shown to possess high selectivity towards C_2 products by various groups. Nilssen and co-workers reported, using ex-situ XPS and electron- energy spectroscopy (EELS), the presence of oxygen residing in the Cu subsurface.[49] They suggested that the electronic structure of the Cu was altered due to the presence of oxygen, thus, generating a high CO binding active site. Independently, Cuenya and co-workers also found that a large fraction of the oxide layer can be resistant to reduction even under strong reducing conditions.[50] Their calculation found that the presence of oxygen would help absorbed H_2O on the active surface, which lowers the first reduction potential by stabilising the CO_2 molecule through chemisorption of CO_2 with H_2O on the surface. A mixture of Cu^+ and Cu on the surface were also shown to act cooperatively to suppress the formation of C_1 products and promote the formation of C_2 products simultaneously.[50] However, further study by Ager and co-workers with isotope labelling, coupled with ex-situ secondary-ion mass spectrometry, suggested that these residual oxides are not stable during the CO_2 reduction process.[51] This is further supported by the calculations done by Head-Gordon and co- workers which suggest that the oxygen seen by the other groups might be a result of unintentional introduction of O_2 during the purification process.[52] Verdaguer-Casadevall *et al*. suggest that the high selectivity is likely due to the high density of the grain boundary as reported by Kanan and co-workers.[53]

5.5. Research gap and PhD in context of literature

As discussed in section 5.3, Cu was shown to produce up to 16 different products during the reduction of CO_2. The modification of the Cu surface has also shown great potential for tuning the selectivity of the products produced from CO_2 reduction. Notably, the oxide-derived Cu has shown high activity towards the formation of ethylene. The selective modification of the Cu oxide surface has been well studied using chemical oxidants in different pH to achieve desirable surface morphologies. In this thesis, we will study the effect of the Cu surface morphology, in particular, the crystal facets, on the selectivity of products via OD-Cu. In the studies on OD-Cu, the influence of the crystal facets of the OD-Cu on product distribution were never explored. In chapter 6, the synthesis of OD-Cu nano-scroll will be reported and characterised. The reactivity of the OD-Cu nano-scroll will also be studied and a discussion on product distribution with respect to different crystal facets of the OD-Cu will be presented.

References

(1) Zhang, L.; Zhao, Z. J.; Gong, J. *Angew. Chem. Int. Ed.* **2017**, *56*, 11326-11353.

(2) Glockler, G. *J. Phys. Chem.* **1958**, *62*, 1049-1054.

(3) Sun, Z.; Ma, T.; Tao, H.; Fan, Q.; Han, B. *Chem* **2017**, *3*, 560-587.

(4) Zhang, W.; Hu, Y.; Ma, L.; Zhu, G.; Wang, Y.; Xue, X.; Chen, R.; Yang, S.; Jin, Z. *Adv. Sci.* **2018**, *5*, 1700275.

(5) Bard, A. J.; Parsons, R.; Jordan, J. *CRC Press, New York* **1985**.

(6) Benson, E. E.; Kubiak, C. P.; Sathrum, A. J.; Smieja, J. M. *Chem. Soc. Rev.* **2009**, *38*, 89-99.

(7) Han, N.; Wang, Y.; Ma, L.; Wen, J.; Li, J.; Zheng, H.; Nie, K.; Wang, X.; Zhao, F.; Li, Y.; Fan, J.; Zhong, J.; Wu, T.; Miller, D. J.; Lu, J.; Lee, S.-T.; Li, Y. *Chem* **2017**, *3*, 652-664.

(8) Senthil Kumar, R.; Senthil Kumar, S.; Anbu Kulandainathan, M. *Electrochem. Commun.* **2012**, *25*, 70-73.

(9) Hori, Y.; Wakebe, H.; Tsukamoto, T.; Koga, O. *Electrochim. Acta* **1994**, *39*, 1833-1839.

(10) Hori, Y.; Murata, A.; Yoshinami, Y. *J. Chem. Soc., Faraday Trans.* **1991**, *87*, 125-128.

(11) Kuhl, K. P.; Cave, E. R.; Abram, D. N.; Jaramillo, T. F. *Energy Environ. Sci.* **2012**, *5*, 7050-7059.

(12) Asadi, M.; Kumar, B.; Behranginia, A.; Rosen, B. A.; Baskin, A.; Repnin, N.; Pisasale, D.; Phillips, P.; Zhu, W.; Haasch, R.; Klie, R. F.; Kral, P.; Abiade, J.; Salehi-Khojin, A. *Nat. Commun.* **2014**, *5*, 4470.

(13) Asadi, M.; Kim, K.; Liu, C.; Addepalli, A. V.; Abbasi, P.; Yasaei, P.; Phillips, P.; Behranginia, A.; Cerrato, J. M.; Haasch, R.; Zapol, P.; Kumar, B.; Klie, R. F.; Abiade, J.; Curtiss, L. A.; Salehi-Khojin, A. *Science* **2016**, *353*, 467-470.

(14) Kumar, B.; Asadi, M.; Pisasale, D.; Sinha-Ray, S.; Rosen, B. A.; Haasch, R.; Abiade, J.; Yarin, A. L.; Salehi-Khojin, A. *Nat. Commun.* **2013**, *4*, 2819.

(15) Nakata, K.; Ozaki, T.; Terashima, C.; Fujishima, A.; Einaga, Y. *Angew. Chem. Int. Ed.* **2014**, *53*, 871-874.

(16) Wu, J.; Ma, S.; Sun, J.; Gold, J. I.; Tiwary, C.; Kim, B.; Zhu, L.; Chopra, N.; Odeh, I. N.; Vajtai, R.; Yu, A. Z.; Luo, R.; Lou, J.; Ding, G.; Kenis, P. J.; Ajayan, P. M. *Nat. Commun.* **2016**, *7*, 13869.

(17) Zou, X.; Liu, M.; Wu, J.; Ajayan, P. M.; Li, J.; Liu, B.; Yakobson, B. I. *ACS Catal.* **2017**, *7*, 6245-6250.

(18) Frese, K., Jr. Electrochemical Reduction of CO_2 at Solid Electrodes. *In Electrochemical and Electrocatalytic Reaction of Carbon Dioxide*; Sullivan, B,: Krist, K., Guard, H., Eds.; Elsevier; New York, **1993**, *Chapter 6* 145-216.

(19) Hori, Y.; Takahashi, I.; Koga, O.; Hoshi, N. *J. Mol. Catal. A: Chem.* **2003**, *199*, 39-47.

(20) Roberts, F. S.; Kuhl, K. P.; Nilsson, A. *Angew. Chem. Int. Ed.* **2015**, *54*, 5179-5182.

(21) Jiang, K.; Sandberg, R. B.; Akey, A. J.; Liu, X.; Bell, D. C.; Nørskov, J. K.; Chan, K.; Wang, H. *Nat. Catal.* **2018**, *1*, 111-119.

(22) Reske, R.; Mistry, H.; Behafarid, F.; Roldan Cuenya, B.; Strasser, P. *J. Am. Chem. Soc.* **2014**, *136*, 6978-6986.

(23) Kim, D.; Kley, C. S.; Li, Y.; Yang, P. *Proc. Natl. Acad. Sci. U.S.A.* **2017**, *114*, 10560-10565.

(24) Kwon, Y.; Lum, Y.; Clark, E. L.; Ager, J. W.; Bell, A. T. *ChemElectroChem* **2016**, *3*, 1012-1019.

(25) De Luna, P.; Quintero-Bermudez, R.; Dinh, C.-T.; Ross, M. B.; Bushuyev, O. S.; Todorović, P.; Regier, T.; Kelley, S. O.; Yang, P.; Sargent, E. H. *Nat. Catal.* **2018**, *1*, 103-110.

(26) Tang, W.; Peterson, A. A.; Varela, A. S.; Jovanov, Z. P.; Bech, L.; Durand, W. J.; Dahl, S.; Norskov, J. K.; Chorkendorff, I. *Phys. Chem. Chem. Phys.* **2012**, *14*, 76-81.

(27) Sen, S.; Liu, D.; Palmore, G. T. R. *ACS Catal.* **2014**, *4*, 3091-3095.

(28) Ma, M.; Djanashvili, K.; Smith, W. A. *Angew Chem Int Ed Engl* **2016**, *55*, 6680-6684.

(29) Li, C. W.; Kanan, M. W. *J. Am. Chem. Soc.* **2012**, *134*, 7231-7234.

(30) Ma, M.; Djanashvili, K.; Smith, W. A. *Phys. Chem. Chem. Phys.* **2015**, *17*, 20861-20867.

(31) Chi, D.; Yang, H.; Du, Y.; Lv, T.; Sui, G.; Wang, H.; Lu, J. *RSC Adv.* **2014**, *4*, 37329-37332.

(32) Kas, R.; Kortlever, R.; Yılmaz, H.; Koper, M. T. M.; Mul, G. *ChemElectroChem* **2015**, *2*, 354-358.

(33) Kas, R.; Kortlever, R.; Milbrat, A.; Koper, M. T.; Mul, G.; Baltrusaitis, J. *Phys Chem Chem Phys* **2014**, *16*, 12194-12201.

(34) Yang, K.; Kas, R.; Smith, W. A. *J. Am. Chem. Soc.* **2019**, *141*, 15891-15900.

(35) Dinh, C. T.; Burdyny, T.; Kibria, M. G.; Seifitokaldani, A.; Gabardo, C. M.; Garcia de Arquer, F. P.; Kiani, A.; Edwards, J. P.; De Luna, P.; Bushuyev, O. S.; Zou, C.; Quintero-Bermudez, R.; Pang, Y.; Sinton, D.; Sargent, E. H. *Science* **2018**, *360*, 783-787.

(36) Hori, Y.; Murata, A.; Takahashi, R.; Suzuki, S. *J. Chem. Soc., Chem. Commun.* **1988**, 17-19.

(37) Hori, Y.; Murata, A.; Takahashi, R. *J. Chem. Soc., Faraday Trans. 1* **1989**, *85*, 2309-2326.

(38) Hori, Y.; Murata, A.; Takahashi, R.; Suzuki, S. *J. Am. Chem. Soc.* **1987**, *109*, 5022-5023.

(39) Murata, A.; Hori, Y. *Bull. Chem. Soc. Jpn.* **1991**, *64*, 123-127.

(40) Singh, M. R.; Kwon, Y.; Lum, Y.; Ager, J. W., 3rd; Bell, A. T. *J. Am. Chem. Soc.* **2016**, *138*, 13006-13012.

(41) Noda, H.; Ikeda, S.; Oda, Y.; Ito, K. *Chem. Lett.* **1989**, *18*, 289-292.

(42) Schouten, K. J. P.; Kwon, Y.; van der Ham, C. J. M.; Qin, Z.; Koper, M. T. M. *Chem. Sci.* **2011**, *2*, 1902-1909.

(43) Peterson, A. A.; Abild-Pedersen, F.; Studt, F.; Rossmeisl, J.; Nørskov, J. K. *Energy Environ. Sci.* **2010**, *3*, 1311-1315.

(44) Nie, X.; Esopi, M. R.; Janik, M. J.; Asthagiri, A. *Angew. Chem. Int. Ed.* **2013**, *52*, 2459-2462.

(45) Durand, W. J.; Peterson, A. A.; Studt, F.; Abild-Pedersen, F.; Nørskov, J. K. *Surf. Sci.* **2011**, *605*, 1354-1359.

(46) Luo, W.; Nie, X.; Janik, M. J.; Asthagiri, A. *ACS Catal.* **2015**, *6*, 219-229.

(47) Garza, A. J.; Bell, A. T.; Head-Gordon, M. *ACS Catal.* **2018**, *8*, 1490-1499.

(48) Cheng, T.; Xiao, H.; Goddard, W. A., 3rd *Proc. Natl. Acad. Sci. U.S.A.* **2017**, *114*, 1795-1800.

(49) Eilert, A.; Cavalca, F.; Roberts, F. S.; Osterwalder, J.; Liu, C.; Favaro, M.; Crumlin, E. J.; Ogasawara, H.; Friebel, D.; Pettersson, L. G.; Nilsson, A. *J. Phys. Chem. Lett.* **2017**, *8*, 285-290.

(50) Mistry, H.; Varela, A. S.; Bonifacio, C. S.; Zegkinoglou, I.; Sinev, I.; Choi, Y. W.; Kisslinger, K.; Stach, E. A.; Yang, J. C.; Strasser, P.; Cuenya, B. R. *Nat. Commun.* **2016**, *7*, 12123.

(51) Lum, Y.; Ager, J. W. *Angew. Chem. Int. Ed.* **2018**, *57*, 551-554.

(52) Garza, A. J.; Bell, A. T.; Head-Gordon, M. *J. Phys. Chem. Lett.* **2018**, *9*, 601-606.

(53) Verdaguer-Casadevall, A.; Li, C. W.; Johansson, T. P.; Scott, S. B.; McKeown, J. T.; Kumar, M.; Stephens, I. E.; Kanan, M. W.; Chorkendorff, I. *J. Am. Chem. Soc.* **2015**, *137*, 9808-9811.

Chapter 6

Modification of Oxide-Derived Copper Surface for Selective CO_2 Reduction

6.1 Foreword

In this study, we seek to explore the effect of surface modification on the product distribution of OD-Cu on electrocatalytic CO_2 reduction. OD-Cu nanoscrolls were synthesised via chemical oxidation followed by electrochemical reduction. The Cu surface was characterised using SEM and XRD. Comparing with reported OD-Cu from the literature, we hypothesised that the majority crystal face in the polycrystalline OD-Cu plays an important role in the selectivity of the products and the overpotentials required to attain such selectivity.

In this Chapter, I analysed the obtained experimental data, prepared the manuscript. I designed the study together with Assoc. Prof. Richard D. Webster and performed all the laboratory work at CREATE NUS and SPMS. All the synthesis and analysis were carried out by myself unless otherwise stated. Mr. Arnold Subrata helped with XPS measurement for material characterization. Dr. Sheng Yuan aided in gaseous products identification and Dr. Sebastian Quek assisted in XRD measurement.

6.2. Introduction

Electrochemical reduction of CO_2 coupled with advancement in photovoltaic cells is one of the most promising processes for future energy storage and fuel production.[1] This system can effectively close the carbon cycle by utilizing the fuels derived from the reduction of CO_2.[2] Among the various metal electrodes that were discussed in Chapter 5, the Cu electrode has shown its unique ability to produce hydrocarbons via multiple electron reduction of CO_2.[3-6] Furthermore, the production of these hydrocarbons occurs at reasonable currents and efficiencies.[5, 7] However, a large overpotential and poor selectivity of products currently limit the use of Cu as a catalyst for any practical implementation of the technology.[8]

Previous studies have suggested that the selectivity of CO_2 reduction is dependent on the Cu surface morphology.[9, 10] Frese *et al.* in their review on the influence of Cu surfaces on the selectivity of methane, stated that the different crystal faces of Cu give different products distribution after electrolysis.[11] In particular, Cu (111) favours the formation of methane as compared to (110) and (100) surfaces, whereas Cu (100) favours the formation of ethylene.[11] Hori *et al.* conducted experiments independently and reported the influence of the crystal surface, including step edges, on the product distribution and overpotential. These findings also suggest that the (100) crystal face of Cu favours the formation of ethylene at low overpotentials while the Cu (110) surface requires higher overpotentials that is selective for C_2 and C_3 products.[6] However, single and polycrystalline Cu still suffer from large required overpotentials and low selectivity of products with current efficiency of not more than 50% for C_2 products at low overpotentials.[6, 12]

In recent years, the discovery of oxide-derived Cu (OD-Cu) was found to favour the formation of C_2 and C_3 products.[13-15] Some studies were carried out to try to understand the reason behind this high selectivity towards C_2 and C_3 products. Notably, Kanan and Chorkendorff first reported the effect of grain boundary on CO binding to Cu. They

proposed that the grain boundary on the OD-Cu support strong CO binding sites, resulting in the further reduction to C_2 and C_3 products.[14] In a follow-up work, Kanan and co-workers reported the correlation between the grain boundary and the electroreduction of CO on Cu nanoparticles.[16] A high Faradaic efficiency for C_2 products of 70% was achieved when grain- boundary rich Cu nanoparticles were used for CO reduction reaction. Other groups also explored the effect of subsurface oxygen in OD-Cu as a possible explanation to the high selectivity towards C_2 and C_3 products.[17-19] However, in-situ measurements done by Ager and co-workers using secondary-ion mass spectrometry coupled with ^{18}O enriched OD-Cu found that less than 1% of the original ^{18}O was detected during the CO_2 reduction reaction. This study supports the hypothesis proposed by Kanan and co-workers that grain boundary is more likely the reason for this high selectivity towards C_2 and C_3 products.[15]

While the reasons for this high selectivity to C_2 and C_3 products are still debatable, OD-Cu possesses an opportunity for the tuning of Cu electrode morphology towards high selectivity of products. Modifications of the surface Cu oxides using electrochemical and chemical oxidation methods are well studied.[20] By utilising these known procedures, we can control the surface morphology of the OD-Cu to tune the selectivity of the Cu catalyst. The effects of the different surface morphologies of OD-Cu on the distribution of products can be explored to help elucidate the mechanism for this high selectivity.

In this work, we will present the synthesis of a OD-Cu "nano-scroll" by the chemical oxidation of Cu to the oxides of Cu followed by the electrochemical reduction to obtain the desired product OD-Cu nano-scroll. The OD-Cu nano-scroll obtained has been fully characterised and no residual of CuO was detected via X-ray diffraction and XPS before the electrocatalytic reduction of CO_2. It has been found that when the OD-Cu nano-scroll was used as the catalyst in the electrocatalytic reduction of CO_2, it favoured the formation of CO and H_2 at a low overpotential with up to a tenfold increase in the current efficiency as compared to the use of polycrystalline Cu. The production of CH_4 was completely

supressed. It was also discovered that the different crystal facets of Cu after electrochemical reduction have a strong influence on the product distribution at a low applied potential. The selectivity of products is also different between OD-Cu and that of polycrystalline Cu with the similar crystal face. Comparing the Faradaic efficiency of different OD-Cu with different morphologies, we hypothesize that although grain boundary might play an important role in the higher selectivity towards C_2 products, the crystal facet ultimately determines the product distribution, along with the applied overpotential.

6.3. Experimental Section

6.3.1. General Considerations

All chemicals used were of analytical grade and used as received without further purification. In a typical experiment, 2.0 × 1.0 × 0.1 cm^3 pieces of Cu foil were ultrasonically cleaned with deionised water, ethanol, and acetone for 10 min. The pre-cleaned Cu foils were then dried in air. A parafilm was used to cover the Cu plates such that only 1.0 × 1.0 × 0.1 cm^3 were exposed. The Cu oxide plates were then fabricated based on the published method by Zhang *et al.*[21] The Cu plate was first immersed in a solution containing 4.0 mL of 4.0 M NaOH, 2.0 mL of 1 M $(NH_4)_2S_2O_8$, and 9.0 mL of deionized water from 30 min to 90 min. The substrates were then rinsed with deionized water and acetone before drying under vacuum. The morphology and structure of the samples were characterised by a JEOL JSM-7600F SEM equipped with an EDS that was operated at 5.0 kV. Each sample was prepared by placing the materials on a SPI double-sided adhesive carbon tape and mounted on an Al SEM specimen stub. XPS experiments were performed using a Phoibos 100 spectrometer and a Mg X-ray source (SPECS, Germany), equipped with dual Al/Mg anodes, working at 12.5 kV. XPS measurements were performed similar to SEM, by adhering the Cu film onto SPI double-sided adhesive carbon tape. The XPS data obtained were processed using the CasaXPS software. The spectra were calibrated internally by setting the C 1s signal at 284.6 eV.

CV was performed using the Cu substrate as the working, a Pt rod as the counter electrode and Ag/AgCl in 3.5 M KCl, a reference electrode. Measurements were performed in 0.1 M $KHCO_3$ aqueous solution at different scan rates from 40 mV/s to 200 mV/s. The phase composition and crystal structure were also examined by X-ray diffraction (Bruker Bruckee d8 advance, Cu K radiation, $\lambda = 0.1542$ nm, 30 mA). The resulting Cu oxide film was then placed into 0.1 M of $KHCO_3$ electrolyte solution and -1.20 V (vs Ag/AgCl) was applied to reduce the Cu oxide back to the Cu metal. The resulting oxide derived Cu plate was used for CO_2 reduction experiments.

6.3.2. Gaseous Products Analysis and Electrochemical Measurements

All CO_2 reduction experiments for products detection were performed using a Metrohm Autolab PGSTAT302N electrochemical workstation using at saturated calomel electrode as reference. Electrode potentials were rescaled to reversible hydrogen electrode (RHE) reference by $E_{RHE} = E_{SCE} + 0.244\ V + 0.0591 \times pH$.[22] All reported currents were obtained by averaging over a timespan of at least 150 s for each applied potential. A conventional three-electrode compartment H-cell was used with a Pt plate as the counter electrode, saturated calomel electrode as the reference electrode and the prepared Cu foil as the working electrode. An anion exchange membrane was used to separate the anode side from the cathode side and to avoid the back-oxidation reduction of the cathode products on the anode electrode. Each cell was filled with 30 mL of 0.10 M $KHCO_3$ and was saturated with CO_2 gas for 20 minutes. The CO_2 gas was supplied at a constant flow rate of 20 cm^3/min for the period of the reaction and a constant potential was applied to the cell for 1.0 hour.

Gas products were analysed using a gas chromatograph (Agilent Technologies gas chromatograph GC system 7890B) coupled with a thermal conductivity detector (TCD) and a flame ionization detector (FID). The gas chromatograph was equipped with a Molecular

Sieve 5A capillary column and a packed Carboxen-1000 column. The current efficiency for the gaseous products was calculated based on the flow rate of CO_2.

The current efficiency was calculated with the following equation:

$$\text{Current Efficiency} = (ncf_1F/60)/I \times 100\%$$

The current (I) is obtained from the current time curve averaging over a timespan of at least 150s for each applied potential. The concentration of products produced (c) was measured by GC. The flow rate (f_1) was 20 cm^3/min. The multiplication of the concentration with flow rate gives the amount of products produced per min.

6.3.3. Liquid Products Identification

After each electrolysis at a constant applied potential, 600 μL of the catholyte solution was mixed with 5 μL of an internal standard dimethyl sulfoxide (DMSO, Sigma-Aldrich, 99.9%) with 10% of D_2O (Cambridge Isotope Laboratories, Inc., 99.9 atom % D) into a NMR sample tube and was analysed by ^1H NMR spectroscopy with 300 MHz spectrometer (Bruker AV 300 spectrometer) to identify liquid products. The peak of water was suppressed by a water suppression sequence.

6.4. Results and Discussions

6.4.1. Copper plate composition and structures

The Cu plates were submerged into two different solutions for different periods of time. The first solution contained 4.0 mL of 4.0 M NaOH, 2.0 mL of 1.0 M $(NH_4)_2S_2O_8$, and 9.0 mL of water. The second solution used KOH in place of NaOH (at the same concentration) in 1.0 M of $(NH_4)_2S_2O_8$, and 9.0 mL of water. The surface structure of Cu with the layer of formed oxides was probed using SEM. Nanofibers with a diameter of about 70 nm were observed after 30 mins of reaction in a solution containing NaOH (Figure

6.1a). As the reaction time increased from 30 to 45 mins, the nanofiber transformed into oxides of Cu in a nano-scroll morphology (Figure 6.1b). From 60 to 90 mins, the oxides of the Cu nano-scroll dominated the surface with a few sheet-like oxides of Cu observed. However, when KOH was used in place of NaOH, the Cu nano-scrolls were observed to form in a shorter reaction time of 30 mins (Figure 6.1e). In KOH, the nanofibers were not observed between 30 mins to 90 mins reaction time (Figure 6.1 e-h). The formation of the Cu oxide nano-scroll is likely due to the presence of the high concentration of base. This causes the weakening of the interlayer H-bond linkage of 3D $Cu(OH)_2$ crystal between the sheet edges, resulting in stress in the layer. In order to relieve the stress, the oxides of Cu sheet fold up into a roll, forming a tubular structure, similar to that of a scroll.[21]

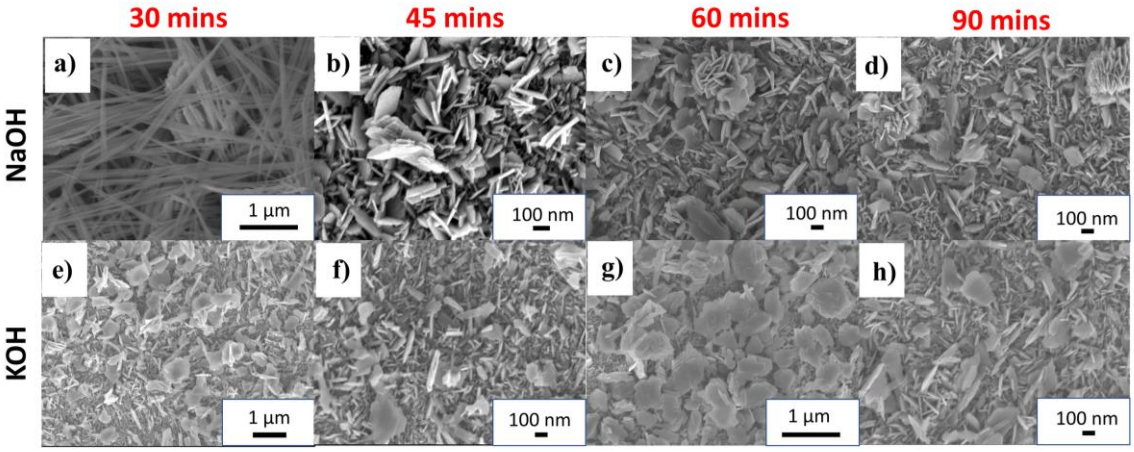

Figure 6.1. (a-d) shows the SEM images of Cu plate in solution containing NaOH from 30 to 90 mins. (e-h) shows the SEM images of Cu plate in solution containing KOH from 30 to 90 mins.

The oxides of Cu obtained after 90 min reaction time in NaOH were then electrocatalytically reduced at -1.20 V vs Ag/AgCl in 0.1 M of $KHCO_3$ solution for 200 s to form metallic Cu. From the current-time curve (Figure 6.2a), the reduction of the oxide surface takes approximately 70 s. However, the charge obtained cannot be directly used to quantify the amount of oxide that was reduced due to the presence of different oxidation

states of the oxidised Cu and possible competition reaction from H_2 evolution. After reduction, the SEM image of the reduced Cu plate shows the same surface morphology as the oxides of Cu surface before electrochemical reduction (Figure 6.2b) with nano-scrolls dominating the surface.

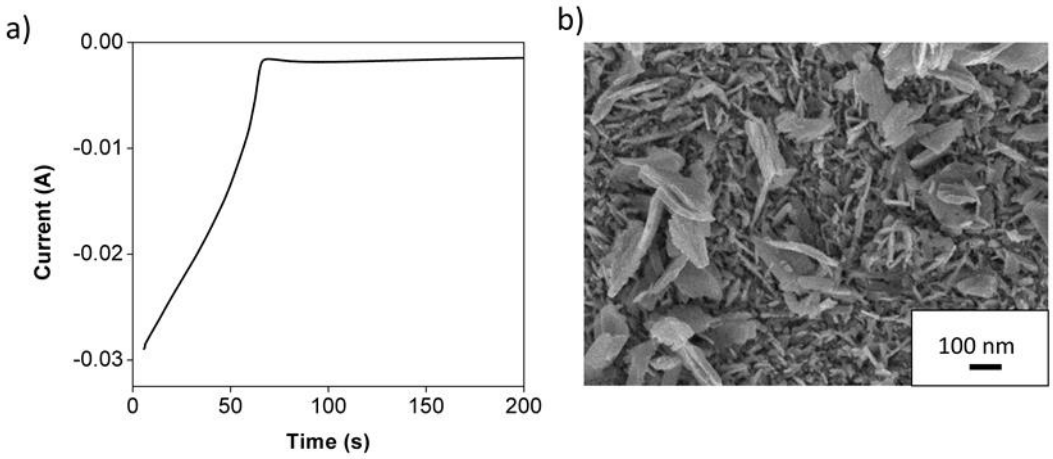

Figure 6.2. (a) Current-time curve for the reduction to metallic Cu for 200s at -1.2 V vs Ag/AgCl and (b) SEM image of oxides of Cu nano-scroll after electrochemical reduction at -1.2 V.

To further investigate the reduction of the Cu oxide nano-scrolls to metallic Cu nano-scrolls, XPS measurements were conducted. Figure 6.3 shows the Cu 2p XPS data recorded for the OD-Cu nano-scroll before and after electrochemical reduction. The strong Cu^{2+} satellites that were observed coupled with a shift in the Cu $2p_{3/2}$ peak to 933.5 eV before the electrochemical reduction, suggests that the Cu plate consists mainly of CuO after the initial oxidation with $(NH_4)_2S_2O_8$ in NaOH solution. The electrochemical reduction of the CuO plate at -1.20 V vs Ag/AgCl results in the disappearance of the strong Cu^{2+} satellite signals, indicating the conversion of CuO to Cu. However, a weak satellite at 945 eV is observed, thus we cannot eliminate the possibility of the presence of some Cu_2O after the electrochemical reduction at this point. The formation of Cu_2O could be during the transferring process before XPS measurements, as the plate was exposed to atmospheric O_2. The result obtained is similar to that of Ager and co-workers where their oxide-derived

nanowire was synthesised via a chemical oxidation followed by electrochemical reduction to obtain the OD-Cu nanowires.[23] Their nanomaterial also showed the complete conversion of the oxides of Cu to metallic Cu at an applied potential of -1.20 V in 200 s.

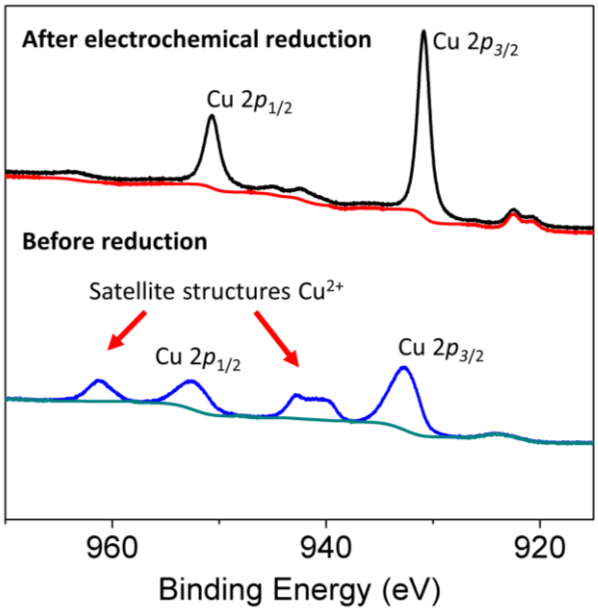

Figure 6.3. XPS narrow scans on the Cu 2p region after and before electrochemical reduction in 0.1 M of $KHCO_3$ for 200 s at -1.20 V vs Ag/AgCl.

X-ray diffraction was also conducted to determine the components and crystal facets of the CuO nano-scrolls and the reduced Cu nano-scrolls. The X-ray diffraction pattern of the oxides of Cu derived from chemical oxidation shows the presence of CuO, Cu_2O and $Cu(OH)_2$ before reduction (Figure 6.4a). After the electrochemical reduction of the CuO plate, the peaks corresponding to CuO, Cu_2O and $Cu(OH)_2$ disappeared and the peaks corresponding to Cu (220), Cu (200) and Cu (111) were observed (Figure 6.4b). This indicates that the oxide layer has been completely reduced to metallic Cu and is found to be polycrystalline in nature. Notably, the OD-Cu nano-scroll shows a stronger preference to form Cu (200) and Cu (220) facets after electrochemical reduction. This in in contrast with the OD-Cu reported by Ager and co-workers,[23] which shows mainly the Cu (111) facet.

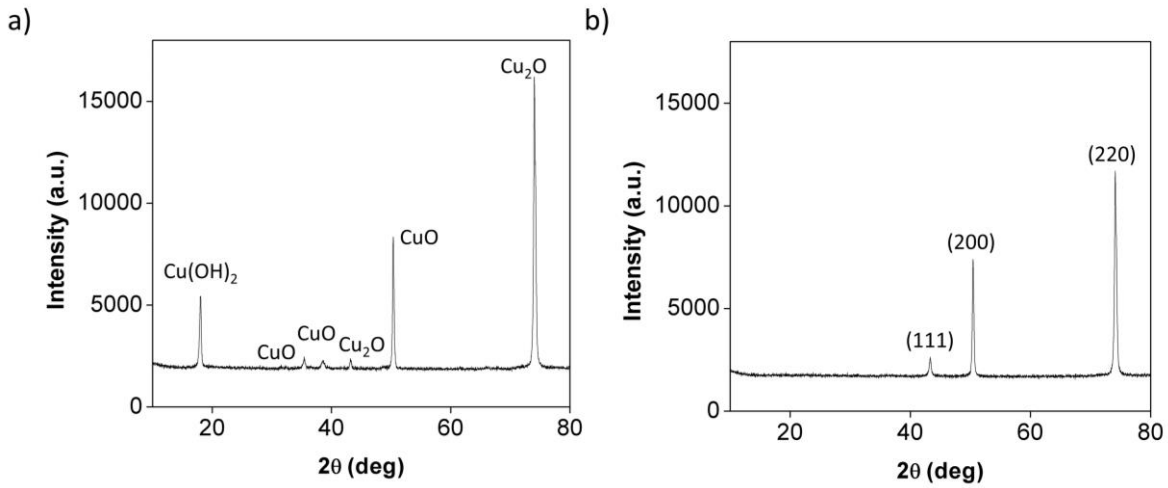

Figure 6.4. X-ray diffraction patterns of (a) oxidised Cu and (b) Cu after electrochemical reduction.

The surface roughness of the OD-Cu nano-scroll was also determined via the measurement of the double layer capacitance using the procedure described by Kanan and co-workers.[13] Since the double layer capacitance is directly related to the surface area, the surface roughness of the OD-Cu nano-scroll was determined relative to the polycrystalline Cu. A surface roughness factor of 119 was obtained. This value (Table 6.1, entry 1) appears to be slightly higher than the value obtained from the oxide-derived Cu as reported by Ager and co-workers (Table 6.1, entry 2-6).[23] However, since a different electrolyte was used, the comparison of the surface roughness can only be used as a guide.

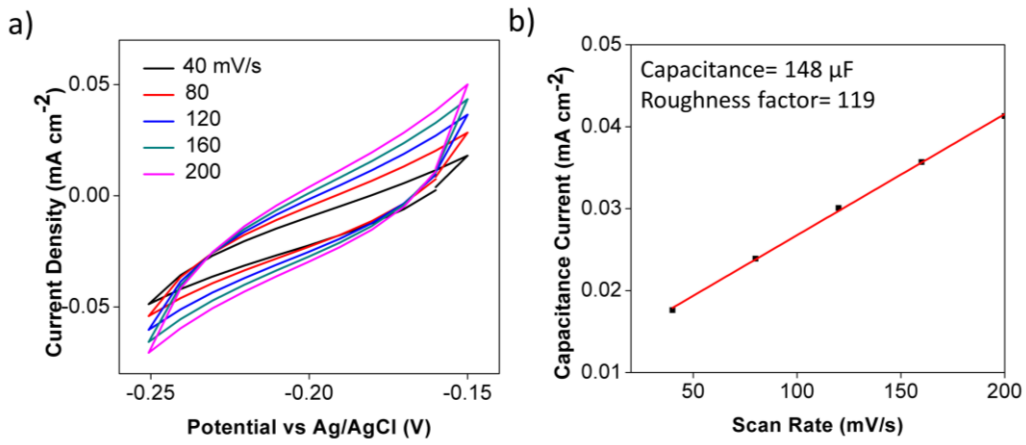

Figure 6.5. (a) Plot of the capacitance current vs applied potential from 40 to 200 mV/s using OD-Cu nano-scroll as the working electrode. (b) Plot of capacitance current vs different scan rate. The slope of the graph gives the double layer capacitance and the ratio of this value compared to the polycrystalline Cu gives the roughness factor.

Table 6.1. Comparison of the roughness factor of OD-Cu nano-scroll (this work) with other OD-Cu reported by Ager and co-workers.[23]

Entry	Cu material used	Roughness Factor
1	This work	119
2	OD-Cu	103
3	OD NWs 75s	7.50
4	OD NWs 150s	9.5
5	OD NWs 300s	15.6
6	OD NWs 600s	28.4
7	Polycrystalline Cu	1

6.4.2. CO_2 Reduction

The activity of the reduced OD-Cu nano-scrolls for CO_2 reduction were conducted at different potentials from -0.7 V to -1.2 V vs RHE. The current densities of the reduced OD-Cu nano-scrolls compared to the results obtained at the polycrystalline Cu are shown

in Figure 6.6. The oxidation followed by the reduction of the Cu foil shows significant positive effects on the current density of the reaction. The reduced OD-Cu nano-scroll has a higher current density as compared to the polycrystalline Cu plate at the applied potential. This can be partially attributed to the increase in surface roughness of the OD-Cu by a factor of 119 as compared to the polycrystalline Cu.

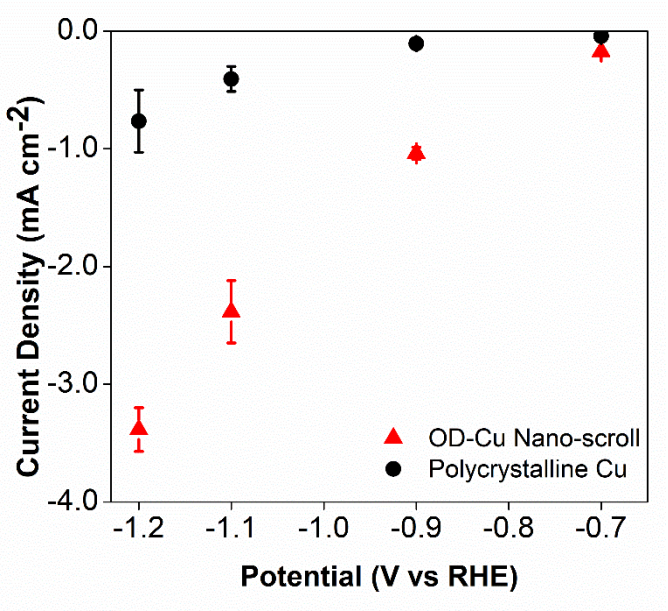

Figure 6.6. Plot of current density of OD-Cu nano-scroll (red triangle) and polycrystalline Cu (black circle) against the applied potential.

The gaseous products derived from different applied potentials for the reduced OD-Cu nano-scrolls are summarised in Figure 6.7 below. When reduced OD-Cu nano-scrolls (red, Figure 6.7) with a geometrical surface area of 1.0 × 1.0 cm^2 were used at a low overvoltage of -0.7 V, although the major product detected was CO, it was a very low concentration of 78 ppm. The absence of H_2 formed might be due to the low current observed and the low detection limit of the TCD detector (100 ppm). As the potential increased, both H_2 and CO were observed. The highest amount of H_2 production occurred at a low potential of -0.9 V with a current efficiency of 58% (black, Figure 6.7). Interestingly, at a higher applied voltage at -1.10 V, the current efficiency of CO to H_2 ratio reaches close to 1:1 with high selectivity towards CO production at a current efficiency of

25%. The efficiency for H_2 evolution was also suppressed at this potential, reaching a low of 37%. However, the production of C_2 gases are low with a complete suppression of CH_4 formation. At a potential of -1.20 V, there is a threefold increase in C_2H_4 and C_2H_6 formation as well as H_2 production coupled with a decrease in the CO formed.

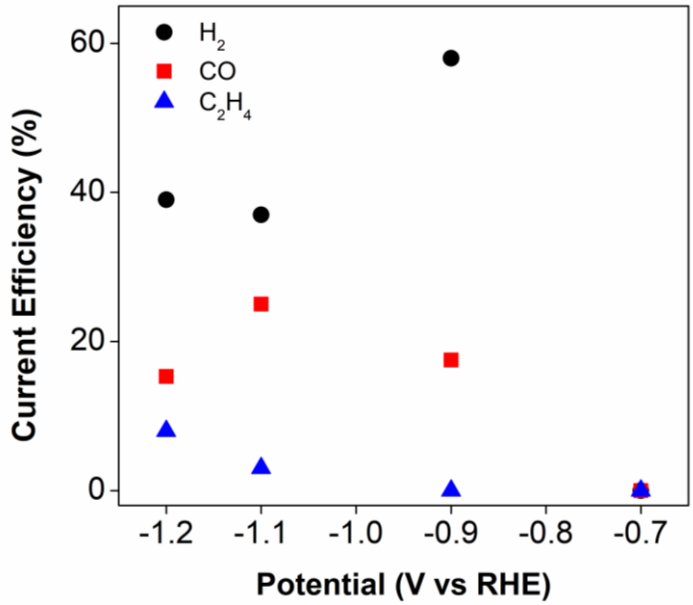

Figure 6.7. Plots comparing the current efficiency of CO (red square), H_2 (black circle) and C_2H_4 (blue triangle) at various applied potentials using OD-Cu nano-scroll as the working electrode in 0.10 M $KHCO_3$ solution.

In contrast, the polycrystalline Cu plate, shows a high current efficiency for H_2 evolution across the range of potentials from -0.7 V to -1.20 V compared to the OD-Cu nano-scroll. At a potential of -1.10 V, the current efficiency of the polycrystalline Cu remains low at 0.4%. This is consistent with the result reported by Hori *et al.* with Cu (111) and Cu (100) showing the production of CO at a low Faradaic efficiency.[6] Kuhl *et al.* has also reported low current efficiency for CO when polycrystalline Cu foil was used.[5] Apart from the trace amount of C_2H_4 and C_2H_6 observed, there is a near suppression of all oxygenated compounds and C_2 compounds when reduced OD-Cu nano-scrolls were used. The liquid products were also detected using ^1H NMR by the water suppression method. Formic acid was detected as the only liquid product.

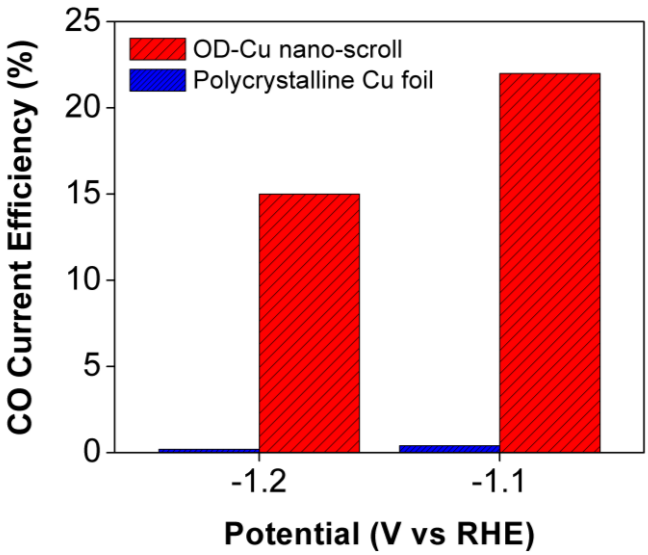

Figure 6.8. Plots comparing the current efficiency of CO and H_2 at various applied potential between the reduced OD-Cu nano-scrolls and polycrystalline Cu

These results obtained are significantly different from the OD-Cu nanowires as reported by Ager and co-workers.[23] Their OD-Cu nanowires showed a consistently low Faradaic efficiency of less than 10% for the production of CO across the potential -0.70 to -1.00 V. However, the OD-Cu nanowires obtained by Ager's group consisted mainly of Cu (111) as the dominant crystallite orientation after reduction.[23] A different product distribution was reported by Kanan and co-workers when they annealed their OD-Cu at 500 °C to get mainly Cu (200). At a low potential, there is high selectivity towards H_2 and CO evolution with low C_2H_4 and C_2H_6 production.[24] Similarly, the reduced OD-Cu nano-scroll that we report consists mainly of Cu (220) as the dominant crystallite orientation on the Cu surface. It shows a preference towards the formation of CO at low overpotential, instead of C_2 and C_3 products.

Kanan and co-workers have suggested that the grain boundary on the OD-Cu nano-scroll supports the strong CO binding sites, resulting in further reduction of CO to hydrocarbons.[14] However, the reduced OD-Cu nano-scrolls as described in this thesis, suggests that the grain boundary that supports strong CO binding might only be applicable in the presence of certain Cu facets or when CO is used directly as the feedstock. This is

evident from the high CO production shown by the reduced OD-Cu nano-scroll with (220) as the major crystal facet. Kanan and co-workers also reported an OD-Cu with (200) as the major crystallite orientation that shows high CO current efficiency of more than 40% at low potential.[24]

In addition, the higher surface roughness of the reduced OD-Cu nano-scroll does not seem to have an impact on the product selectivity. The OD-Cu and OD-Cu nanowires reported by Ager and co-workers, which are lower in surface roughness, show higher Faradaic efficiencies towards C_2 products compared to that of our reduced OD-Cu nano-scroll. This is consistent with work that shows that the surface roughness of the Cu affects the current density but not on the product distribution upon CO_2 reduction at low overpotentials.[23] The Table 6.2 summarised the Faradaic efficiencies for the products distribution obtained from the OD-Cu nano-scroll and compared it with the other published OD-Cu by other group.

Table 6.2. Summary of electrocatalytic CO_2 reduction of the OD-Cu nano-scroll compared to the OD-Cu synthesized by other research groups.

Cu	E vs RHE/V	Major Surface Facets	Faradaic Efficiency/%					Ref
			$HCOO^-$	EtOH	CO	C_2H_4	C_2H_6	
This work	-1.1 V	(220)	Trace	-	25	9.0	-	-
Polycrystalline Cu foil	-1.1 V	-	5.9	5.3	1.3	20.0	-	[25]
OD-Cu annealed at 500 ◦C for 12 h	-0.35 V	(200)	11.0	-	47.0	-	-	[24]

OD-Cu annealed at 500 ◦C for 12 h	-0.85 V	(200)	10.0	4.7	6.4	3.9	6.6	[24]
OD-Cu foil obtained by cycling in 4mM KF for 5 cycles to 0.9 V	-1.0 V	(100)	5.8	7.6	1.5	16.0	-	[26]
OD-Cu with O_2 plasma pretreatment for 20s	-1.0 V	(100)	5.0	23.0	-	45.0	0.1	[27]
OD-Cu with Ar plasma pretreatment for 5 min	-1.0 V	(100)	0.1	18.0	-	37.0	-	[27]
OD-Cu with H_2 plasma pretreatment for 4 min	-1.0 V	(100)	-	10.0	2.5	31.0	-	[27]
OD-Cu NW	-1.1 V	(111)	1.4	8.8	0.36	18.0	-	[23]

OD-Cu from electrodeposition of Cu_2O	-1.1 V	(200)	1.7	7.6	0.20	21.0	-	[23]
OD-Cu from electrochemical oxidation-reduction cycling	-1.1 V	(111)	1.7	8,7	0.33	23.0	-	[23]

The OD-Cu nano-scrolls was also found to be stable under the electrocatalytic conditions for the reaction time of 90 mins based on the current-time curve obtained at -1.1 V (Figure A.22.). Jinmo *et. al*. has previously reported the stability of OD-Cu to be 10 h before the current density decreases to 0 mA cm^{-2}.[28]

6.5. Conclusion

While most of the previous work on OD-Cu have focussed on determining if grain boundary or subsurface oxygen is the reason for the high selectivity towards C_2 to C_3 products, our work suggests that the Cu surface facets produced after the electrochemical reduction plays an important role in product selectivity, especially in low potential conditions. Furthermore, the selectivity of products between regular polycrystalline Cu and OD-Cu are different. A thorough study on this area will allow us to understand the mechanism behind the selectivity shown by OD-Cu.

References

(1) Tang, W.; Peterson, A. A.; Varela, A. S.; Jovanov, Z. P.; Bech, L.; Durand, W. J.; Dahl, S.; Norskov, J. K.; Chorkendorff, I. *Phys. Chem. Chem. Phys.* **2012,** *14*, 76-81.

(2) Lewis, N. S.; Nocera, D. G. *Proc. Natl. Acad. Sci. U.S.A* **2006,** *103*, 15729-15735.

(3) Hori, Y.; Kikuchi, K.; Murata, A.; Suzuki, S. *Chem. Lett.* **1986,** *15*, 897-898.

(4) Hori, Y.; Murata, A.; Takahashi, R.; Suzuki, S. *J. Chem. Soc., Chem. Commun.* **1988**, 17-19.

(5) Kuhl, K. P.; Cave, E. R.; Abram, D. N.; Jaramillo, T. F. *Energy Environ. Sci.* **2012,** *5*, 7050-7059.

(6) Hori, Y.; Takahashi, I.; Koga, O.; Hoshi, N. *J. Mol. Catal. A: Chem.* **2003,** *199*, 39-47.

(7) Raciti, D.; Wang, C. *ACS Energy Lett.* **2018,** *3*, 1545-1556.

(8) Sun, Z.; Ma, T.; Tao, H.; Fan, Q.; Han, B. *Chem* **2017,** *3*, 560-587.

(9) Jiang, K.; Sandberg, R. B.; Akey, A. J.; Liu, X.; Bell, D. C.; Nørskov, J. K.; Chan, K.; Wang, H. *Nat. Catal.* **2018,** *1*, 111-119.

(10) Kim, D.; Kley, C. S.; Li, Y.; Yang, P. *Proc. Natl. Acad. Sci. U.S.A.* **2017,** *114*, 10560-10565.

(11) Frese, K., Jr. Electrochemical Reduction of CO_2 at Solid Electrodes. *In Electrochemical and Electrocatalytic Reaction of Carbon Dioxide*; Sullivan, B,: Krist, K., Guard, H., Eds.; Elsevier; New York, **1993,** *Chapter 6* 145-216.

(12) Noda, H.; Ikeda, S.; Oda, Y.; Ito, K. *Chem. Lett.* **1989,** *18*, 289-292.

(13) Li, C. W.; Ciston, J.; Kanan, M. W. *Nature* **2014,** *508*, 504-507.

(14) Verdaguer-Casadevall, A.; Li, C. W.; Johansson, T. P.; Scott, S. B.; McKeown, J. T.; Kumar, M.; Stephens, I. E.; Kanan, M. W.; Chorkendorff, I. *J. Am. Chem. Soc.* **2015,** *137*, 9808-9811.

(15) Lum, Y.; Ager, J. W. *Angew. Chem. Int. Ed.* **2018,** *57*, 551-554.

(16) Feng, X.; Jiang, K.; Fan, S.; Kanan, M. W. *ACS Cent. Sci.* **2016,** *2*, 169-174.

(17) Lee, S.; Kim, D.; Lee, J. *Angew. Chem. Int. Ed.* **2015,** *54*, 14701-14705.

(18) Mistry, H.; Varela, A. S.; Bonifacio, C. S.; Zegkinoglou, I.; Sinev, I.; Choi, Y. W.; Kisslinger, K.; Stach, E. A.; Yang, J. C.; Strasser, P.; Cuenya, B. R. *Nat. Commun.* **2016,** *7*, 12123.

(19) Eilert, A.; Roberts, F. S.; Friebel, D.; Nilsson, A. *J. Phys. Chem. Lett.* **2016,** *7*, 1466-1470.

(20) Zhang, Q.; Zhang, K.; Xu, D.; Yang, G.; Huang, H.; Nie, F.; Liu, C.; Yang, S. *Prog. Mater. Sci.* **2014,** *60*, 208-337.

(21) Zhang, W.; Wen, X.; Yang, S. *Inorg. Chem.* **2003,** *42*, 5005-5014.

(22) Ng, W. Y. *J. Chem. Educ.* **1988,** *65*.

(23) Lum, Y.; Yue, B.; Lobaccaro, P.; Bell, A. T.; Ager, J. W. *J. Phys. Chem. C* **2017,** *121*, 14191-14203.

(24) Li, C. W.; Kanan, M. W. *J. Am. Chem. Soc.* **2012,** *134*, 7231-4.

(25) Loiudice, A.; Lobaccaro, P.; Kamali, E. A.; Thao, T.; Huang, B. H.; Ager, J. W.; Buonsanti, R. *Angew. Chem. Int. Ed.* **2016,** *55*, 5789-5792.

(26) Kwon, Y.; Lum, Y.; Clark, E. L.; Ager, J. W.; Bell, A. T. *ChemElectroChem* **2016,** *3*, 1012-1019.

(27) Gao, D.; Zegkinoglou, I.; Divins, N. J.; Scholten, F.; Sinev, I.; Grosse, P.; Roldan Cuenya, B. *ACS Nano* **2017,** *11*, 4825-4831.

(28) Kim, J.; Choi, W.; Park, J. W.; Kim, C.; Kim, M.; Song, H. *J. Am. Chem. Soc.* **2019,** *141*, 6986-6994.

Chapter 7

Summary

7.1. Summary

The first part of this thesis explored the effects of the first and second coordination sphere of first row transition metal complexes on their H_2 evolution activity. The synthesis and characterisation of Ni and Co TAML complexes, and salen-type Ni complexes were presented. A systematic investigation of their reactivity towards H_2 evolution in different conditions was performed and mechanistic studies were conducted through various spectroscopic techniques such as TAS and TES, coupled with DFT calculation. In the second part of the thesis, the effect of the crystal facets on the product distribution of OD-Cu was studied. We found that the selectivity is greatly affected by the crystal facets in addition to the proposed grain boundary by Kanan and co-workers.[1,2] We hypothesised that the major crystal facets can greatly influence the products and the overpotentials required to obtain them.

In Chapter 3 of this thesis, the effect of the first coordination sphere on H_2 evolution activity was explored. The Co and Ni TAML complexes were synthesized and characterised. Due to the strongly electron donating TAML, we hypothesised that the formation of a metal hydride complex will be facilitated with the increase in basicity by these late nucleophilic-ate complexes, and hence resulting in higher H_2 evolution activity. The synthesis and characterisation of the Ni and Co TAML were presented. It was found that the Co TAML possessed a square planar geometry and is paramagnetic instead of the more common low-spin diamagnetic, octahedral Co complex. Of the two different TAML complexes synthesised, only the Co TAML complex showed activity towards H_2 evolution. However, further investigation suggested that the formation of Co nanoparticles was responsible for the H_2 evolution activity as the Faradaic efficiency of the reaction was found to be only 18.2%.

In Chapter 4, the effect of the secondary coordination sphere on H_2 evolution reactivity were presented. In this chapter, the focus was on the effect of the non-amino pendant arm and its role in the H_2 evolution reaction in a photocatalytic system. It was found that the salen–type Ni complex, modified with pendant ether arms, was able to catalyse H_2 evolution with a TON of 3800 in a photocatalytic system with $[Ir]^+$ as the photosensitizer and TEA as the sacrificial reagent. This study used TAS and TES to understand the electron transfer process in the photocatalytic system. It was found that the $[Ir]^+$ first gets excited by irradiation and reduced by the TEA before it reduced the Ni complex that catalysed the H_2 evolution. Using the combination of both experimental data and DFT calculations, it is suggested that a ligand- based reduction of the complex may play an important role in its H_2 evolution reactivity. Furthermore, the pendant ether arms were also found to play a key role in H_2 evolution activity by promoting a proton relay similar to that of [FeFe] hydrogenase.

In Chapter 6 of the thesis, OD-Cu nano-scrolls were synthesized via a chemical oxidation method follow by electrochemical reduction. XPS and EDS were carried out before and after reduction to verify that the Cu oxide layer was fully converted to Cu metal. The reactivity of the OD-Cu nano-scrolls were then studied using GC and NMR methods. The OD-Cu obtained possessed high surface roughness and show high Faradaic efficiency towards the formation of CO. A comparison with other literature work suggests that the selectivity of the OD-Cu can be attributed to the crystal facets that were studied.

7.2. Future Outlook

As the salen-type Ni complex has shown to be able to catalyse H_2 evolution using $[Ir]^+$ as a light-harvester and TEA as a sacrificial electron donor and reductive quencher,[3] we are interested in anchoring the salen-type Ni complex to an artificial photosynthesis scaffold to test the efficiency of the system and to improve the lifetime of this homogenous

catalyst.[4] This will allow us to replace the use of the expensive Ir-based metal complex with other cheaper visible-light absorbing semiconductors. The use of TEA as a sacrificial electron donor can also be eliminated.[5] As discussed in chapter 2, Shao *et al.* have shown that modification of the secondary ether arms can aid coordination to alkali metal cations to facilitate the hydride transfer resulting in enhanced H_2 evolution activity.[6] Other groups have also shown that the appended ether arms on the secondary coordination sphere are effective in chelating alkali metal cations to form bimetallic complexes.[7,8] Therefore, the reactivity of this hybrid system towards H_2 evolution in seawater, which contains copious amount of alkali cations, will be an interesting area of study. In addition, the incorporation of the homogenous catalyst in an artificial photosynthesis scaffold allows the catalyst to be recovered and reused via a simple filtration process. This will greatly improve the viability of the catalyst for applications in water splitting reactions.

We are also interested in the development of catalysts that can utilised sunlight photovoltaically in order to catalyse the reduction of CO_2 into fuels. In Chapter 6 of the thesis, we looked at the modification of the Cu surface in order to tune the selectivity of the products from electrocatalytic reduction of CO_2 with Cu metal. In particular, we showed that the major crystal facets of the OD-Cu can greatly affect the overpotential and the distribution of products. Ager and co-workers demonstrated the high selectivity of C_2H_4 at low overpotentials using OD-Cu with (111) as the major crystallite facet as opposed to the high selectivity towards CO by the OD-Cu nano-scrolls with (220) as the major crystal facets.[9] Dinh *et al.* reported a high Faradaic efficiency towards ethylene formation with the use of highly concentrated alkaline electrolyte. Furthermore, the introduction of a polymer-based gas diffusion layer in a flow cell has shown to improve the stability, reactivity and selectivity of CO_2 reduction on Cu surfaces for CO_2 reduction under alkaline conditions. This is due to the abrupt interface in which the CO_2 reduction take place.[10] Therefore, in the future, we are interested in the synthesis of OD-Cu with majority (111) crystallite

surface with high surface roughness to incorporate into a flow cell modified with a polymer-based gas diffusion layer to study the product selectivity for CO_2 reduction.

In addition, most of the OD-Cu materials that are synthesised pay little to no attention the effect of the crystal facets on the selectivity of the products.[1,11-13] Hence, more research is required in this field to understand the mechanism behind this selectivity of C_2 products. The effect of the crystal facets can be studied in-depth by first comparing the current efficiency of the OD-Cu with regular polycrystalline Cu that has similar crystal facets. Calculations can be performed to understand how the different crystal facets on OD-Cu result in different distribution of products and how the grain boundary plays a role in the selectivity.

In conclusion, we have successfully synthesized a series of first row transition metal complexes and their reactivity towards H_2 evolution were explored. It was found that the salen-type Ni complex with modified ether arms is able to catalyse H_2 evolution in a photocatalytic system. In the future, we hope to integrate this catalyst into an artificial photosynthesis system for H_2 evolution. Furthermore, we have also successfully synthesised an OD-Cu nanoscrolls and found that the major crystal facets can influence the product distribution. The effect of crystal morphology in OD-Cu can be further explored to show its effect on the products selectivity during CO_2 reduction experiments in order to achieve high C_2 to C_3 selectivity.

References

(1) Feng, X.; Jiang, K.; Fan, S.; Kanan, M. W. *ACS Cent. Sci.* **2016**, *2*, 169-174.

(2) Li, C. W.; Kanan, M. W. *J. Am. Chem. Soc.* **2012**, *134*, 7231-7234.

(3) Ho, X. L.; Shao, H.; Ng, Y. Y.; Ganguly, R.; Lu, Y.; Soo, H. S. *Inorg. Chem.* **2019**, *58*, 1469-1480.

(4) Klepser, B. M.; Bartlett, B. M. *J. Am. Chem. Soc.* **2014**, *136*, 1694-1697.

(5) Tachibana, Y.; Vayssieres, L.; Durrant, J. R. *Nat. Photonics* **2012**, *6*, 511-518.

(6) Shao, H.; Muduli, S. K.; Tran, P. D.; Soo, H. S. *Chem. Commun.* **2016**, *52*, 2948-2951.

(7) Kumar, A.; Lionetti, D.; Day, V. W.; Blakemore, J. D. *Chem. Eur. J.* **2018**, *24*, 141-149.

(8) Van Staveren, C. J.; Van Eerden, J.; Van Veggel, F. C. J. M.; Harkema, S.; Reinhoudt, D. N. *J. Am. Chem. Soc.* **1988**, *110*, 4994-5008.

(9) Lum, Y.; Yue, B.; Lobaccaro, P.; Bell, A. T.; Ager, J. W. *J. Phys. Chem. C* **2017**, *121*, 14191-14203.

(10) Dinh, C. T.; Burdyny, T.; Kibria, M. G.; Seifitokaldani, A.; Gabardo, C. M.; Garcia de Arquer, F. P.; Kiani, A.; Edwards, J. P.; De Luna, P.; Bushuyev, O. S.; Zou, C.; Quintero-Bermudez, R.; Pang, Y.; Sinton, D.; Sargent, E. H. *Science* **2018**, *360*, 783-787.

(11) Kwon, Y.; Lum, Y.; Clark, E. L.; Ager, J. W.; Bell, A. T. *ChemElectroChem* **2016**, *3*, 1012-1019.

(12) Lum, Y.; Ager, J. W. *Angew. Chem. Int. Ed.* **2018**, *57*, 551-554.

(13) Verdaguer-Casadevall, A.; Li, C. W.; Johansson, T. P.; Scott, S. B.; McKeown, J. T.; Kumar, M.; Stephens, I. E.; Kanan, M. W.; Chorkendorff, I. *J. Am. Chem. Soc.* **2015**, *137*, 9808-9811.

Appendix

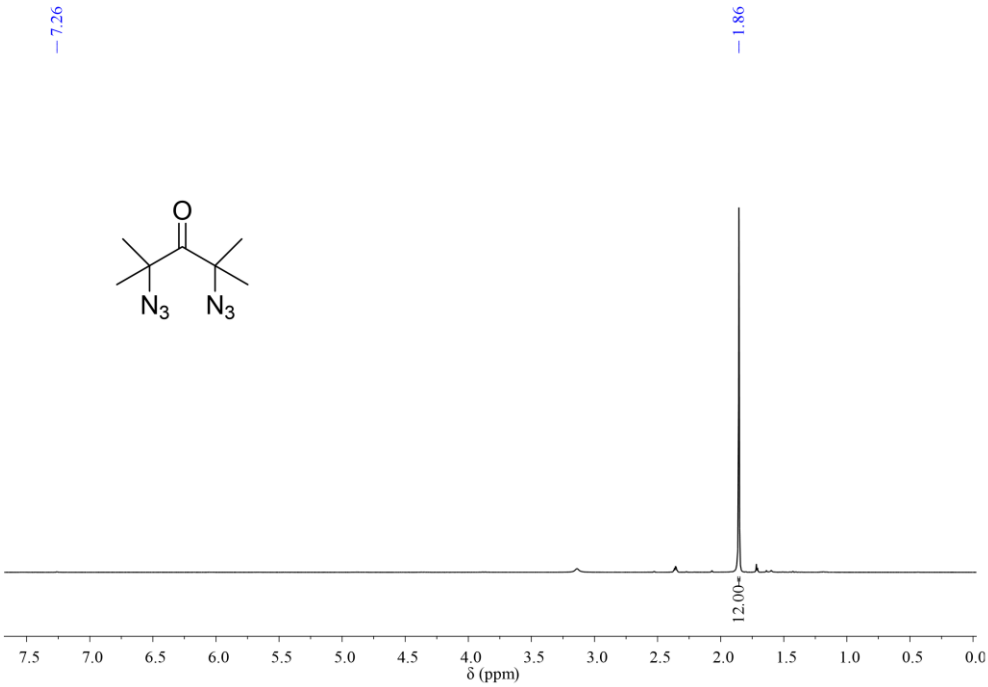

Figure A.1. The ^{1}H NMR spectrum of **3.2** in $CDCl_3$.

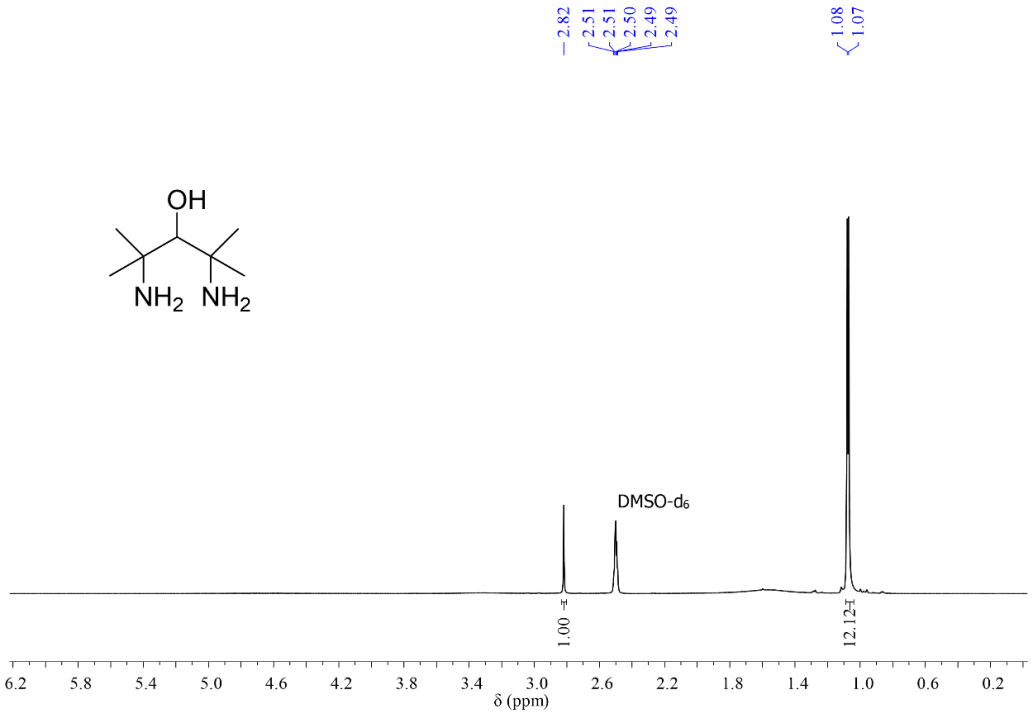

Figure A.2. The ^{1}H NMR spectrum of **3.3** in DMSO-d_6.

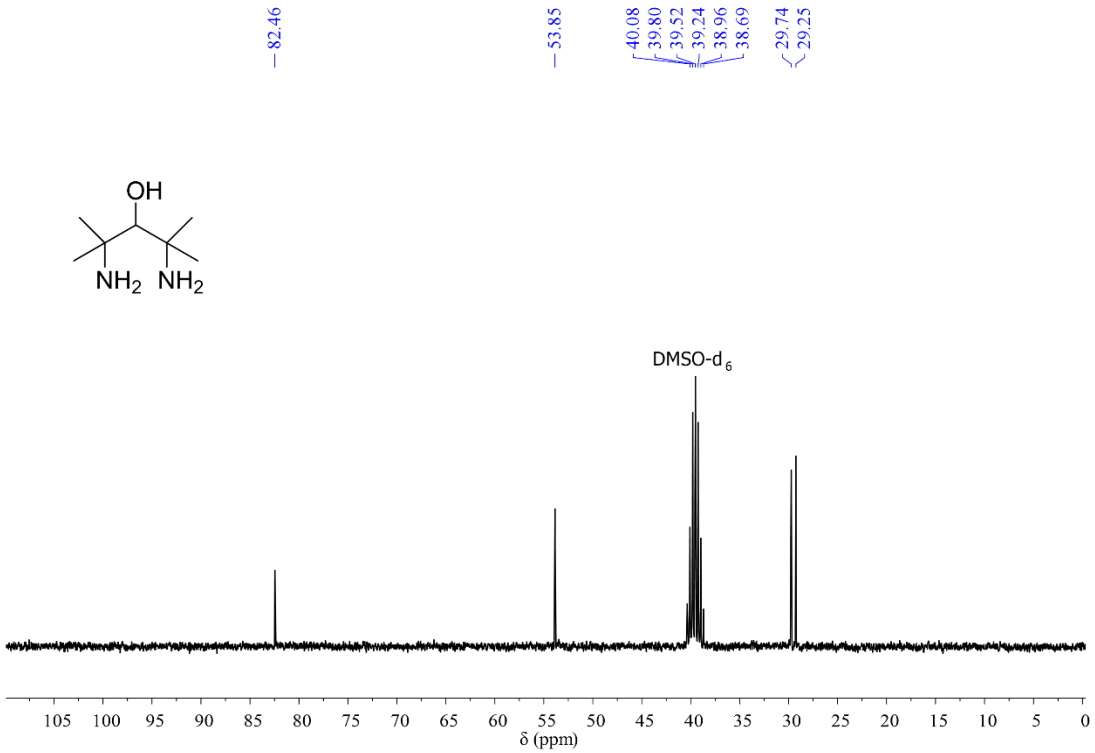

Figure A.3. The ^{13}C NMR spectrum of **3.3** in DMSO-d_6.

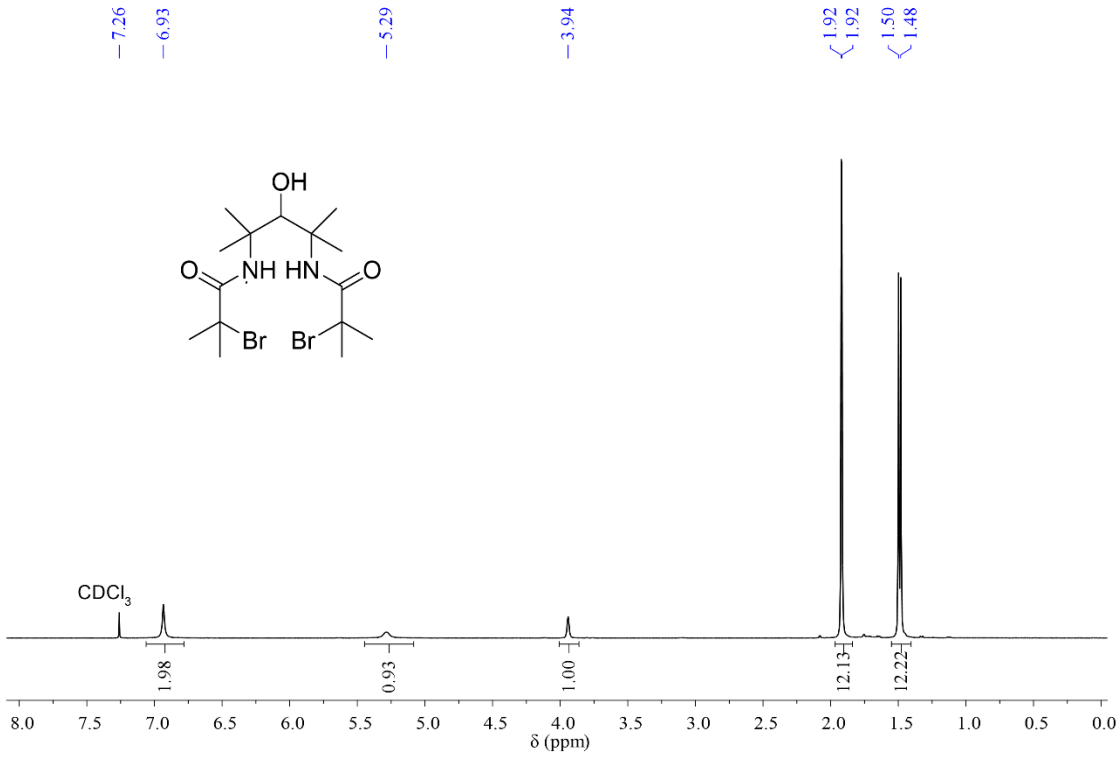

Figure A.4. The ^{1}H NMR spectrum of **3.4** in $CDCl_3$.

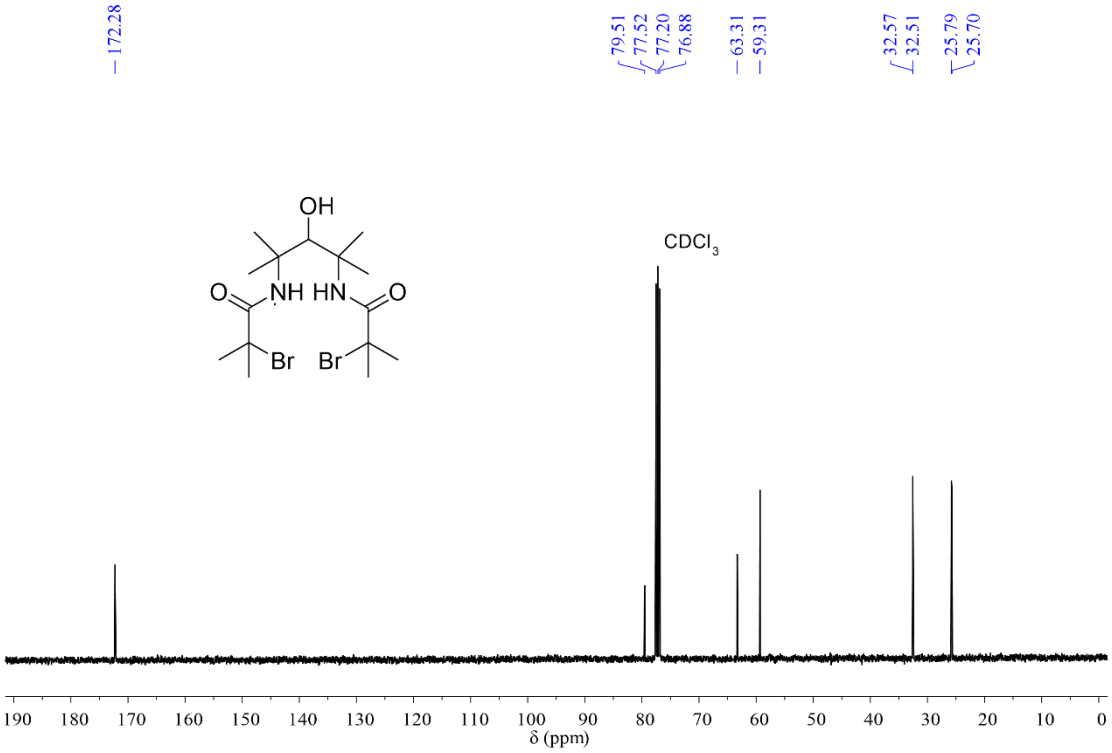

Figure A.5. The ^{13}C NMR spectrum of **3.4** in $CDCl_3$.

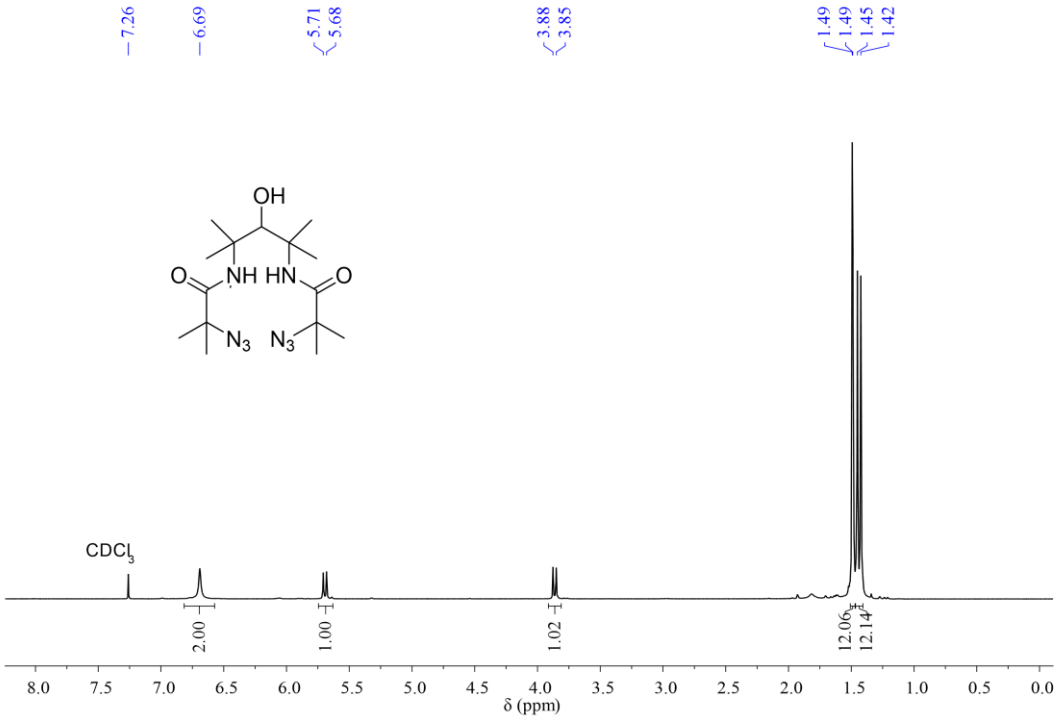

Figure A.6. The ^{1}H NMR spectrum of **3.5** in $CDCl_3$.

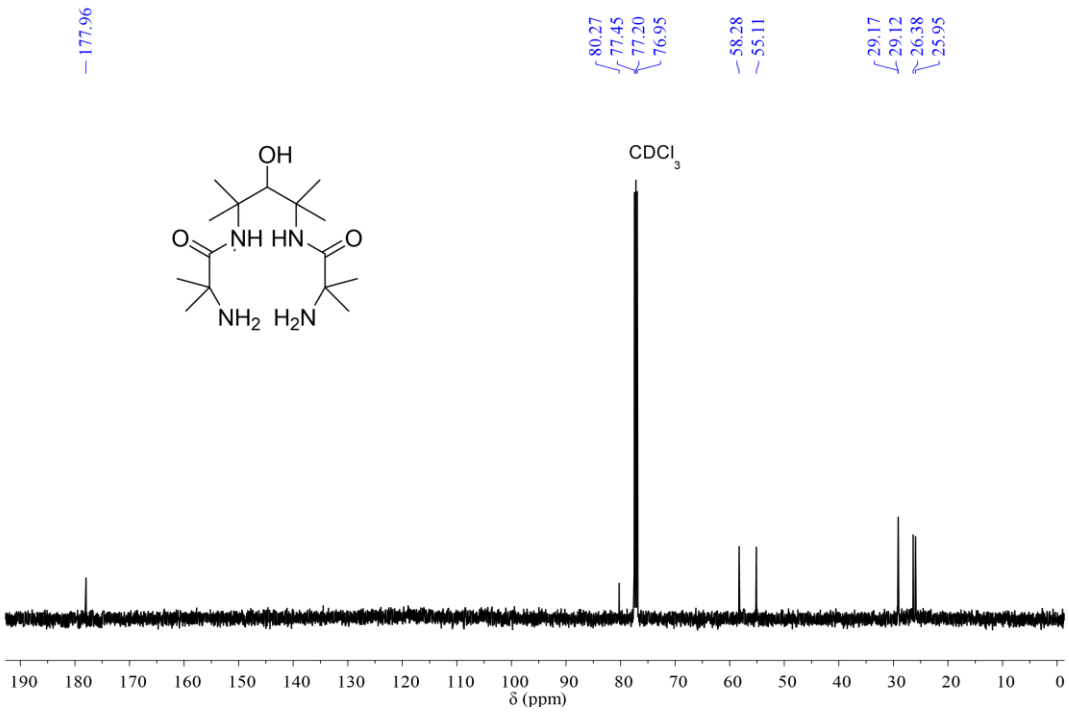

Figure A.7. The ^{13}C NMR spectrum of **3.5** in $CDCl_3$.

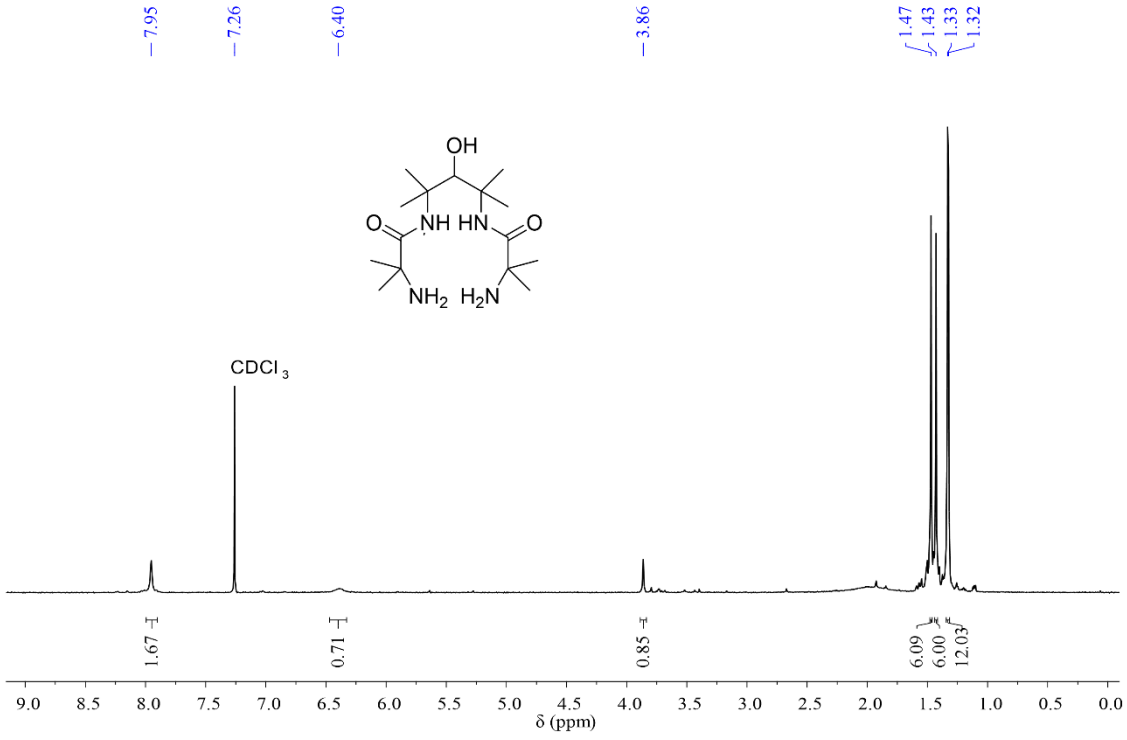

Figure A.8. The ^{1}H NMR spectrum of **3.6** in $CDCl_3$.

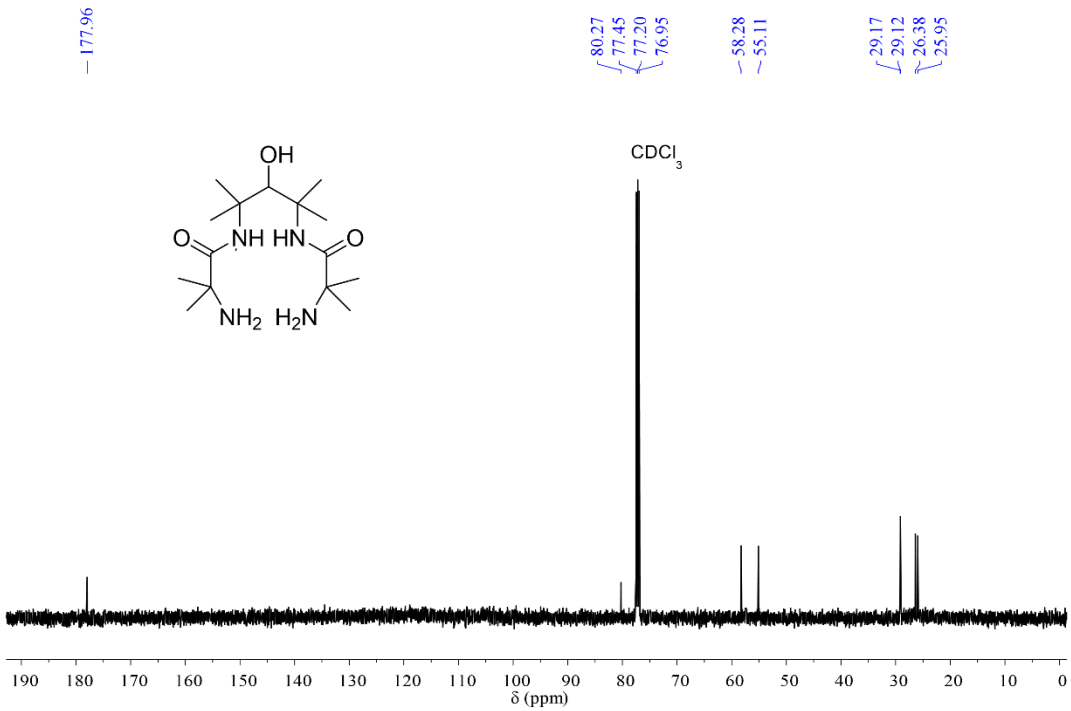

Figure A.9. The ^{13}C NMR spectrum of **3.6** in $CDCl_3$.

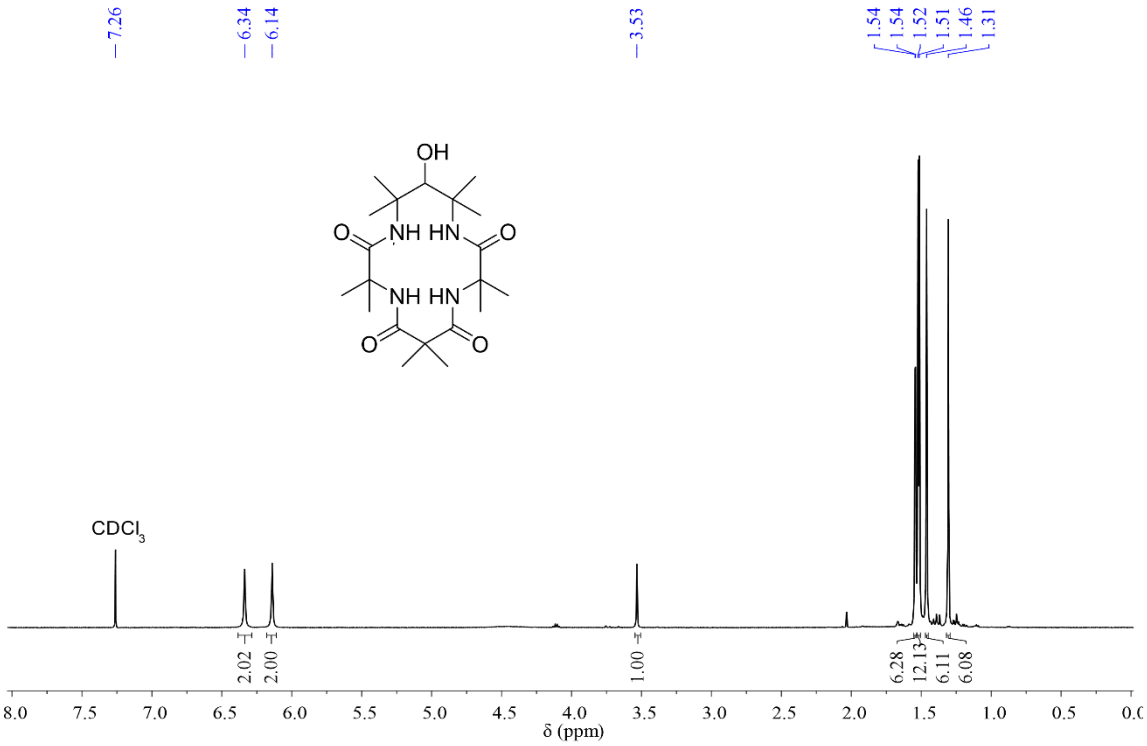

Figure A.10. The ^{1}H NMR spectrum of **3.7** in $CDCl_3$.

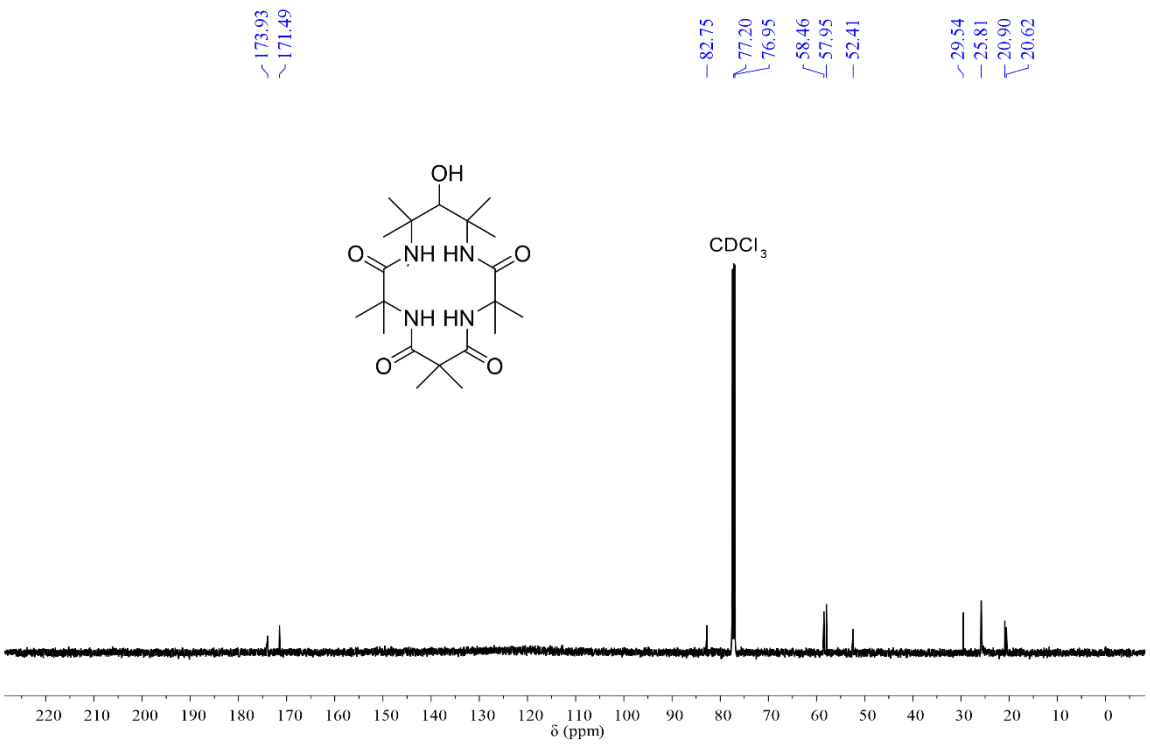

Figure A.11. The ^{13}C NMR spectrum of **3.7** in $CDCl_3$.

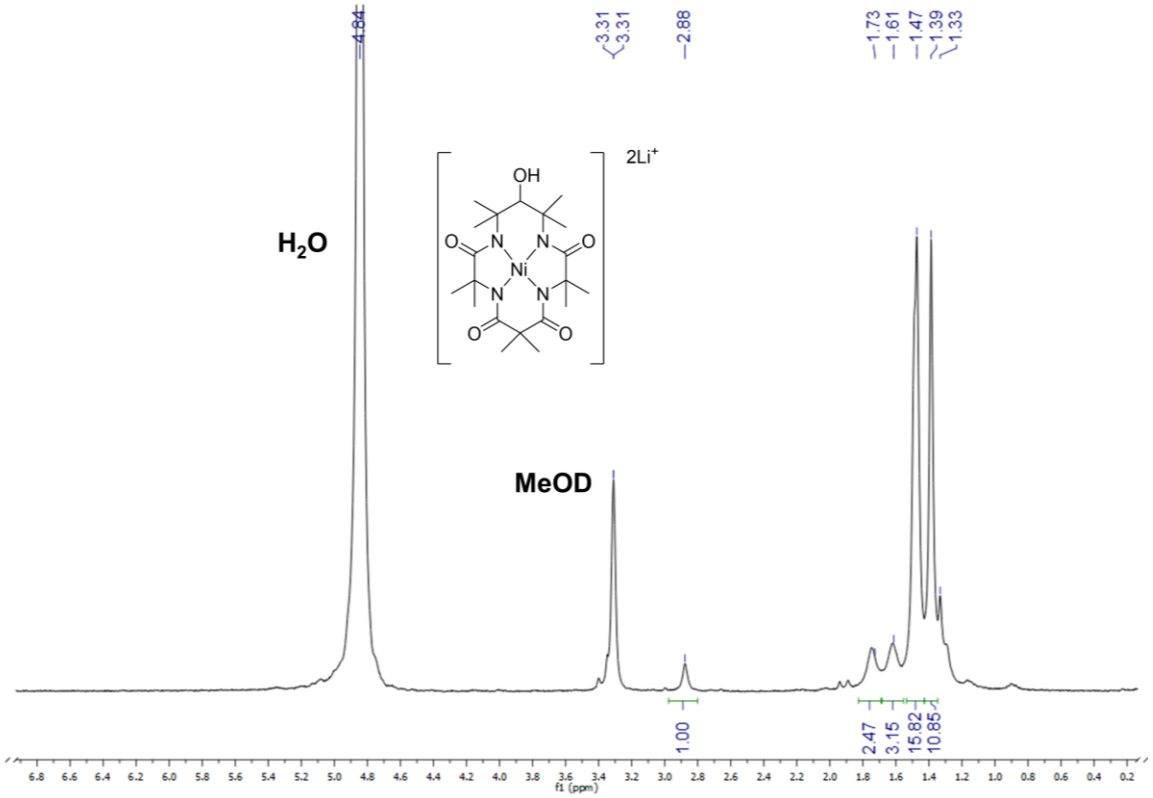

Figure A.12. The ^{1}H NMR spectrum of **3.9** in MeOD.

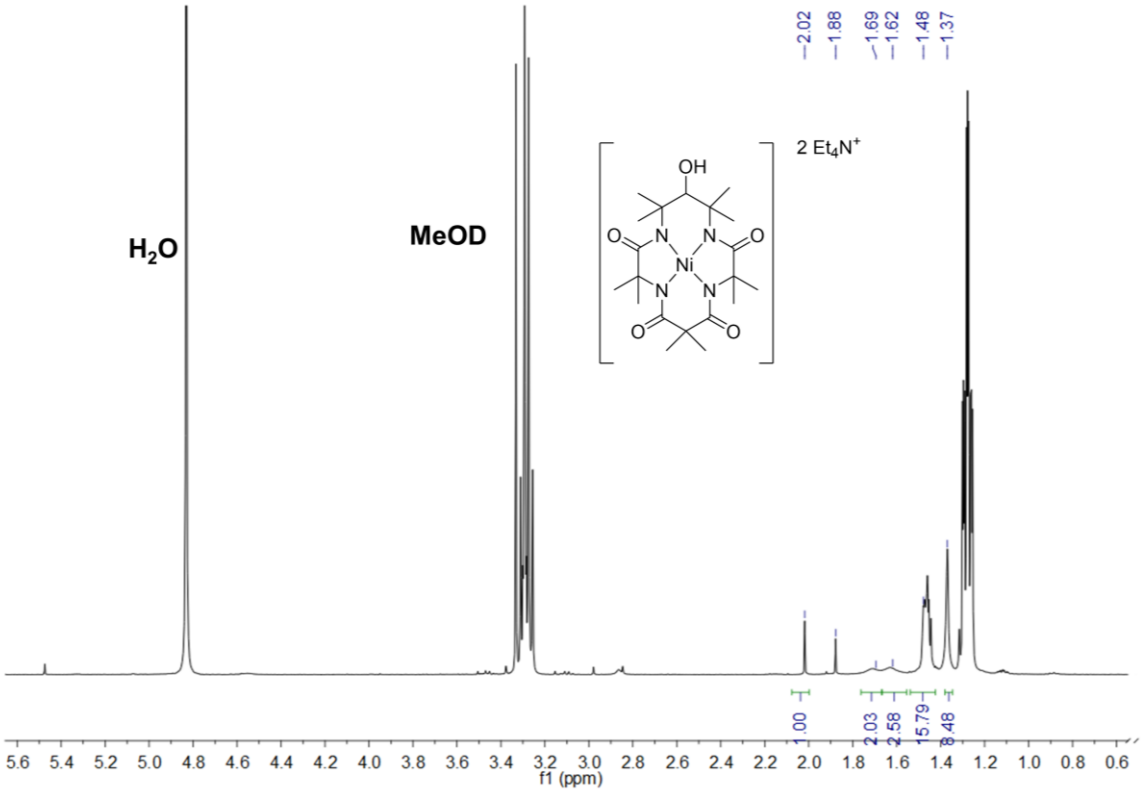

Figure A.13. The ^{1}H NMR spectrum of **3.11** in MeOD.

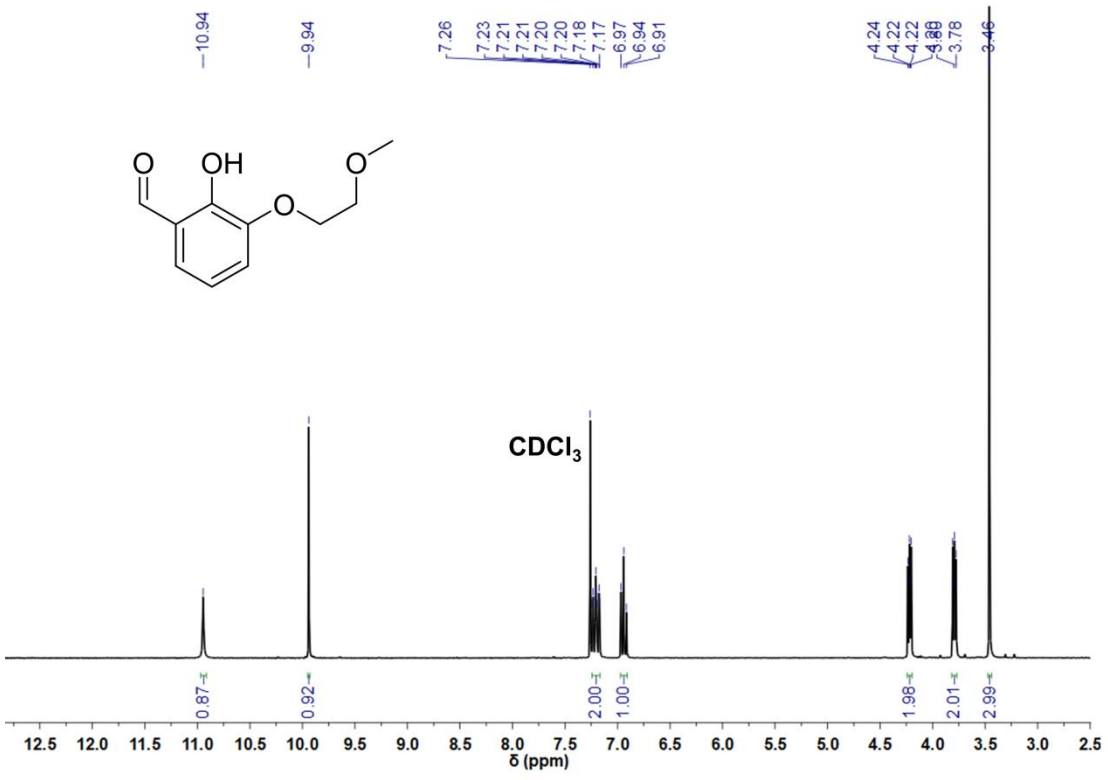

Figure A.14. The ^{1}H NMR spectrum of **4.1** in $CDCl_3$.

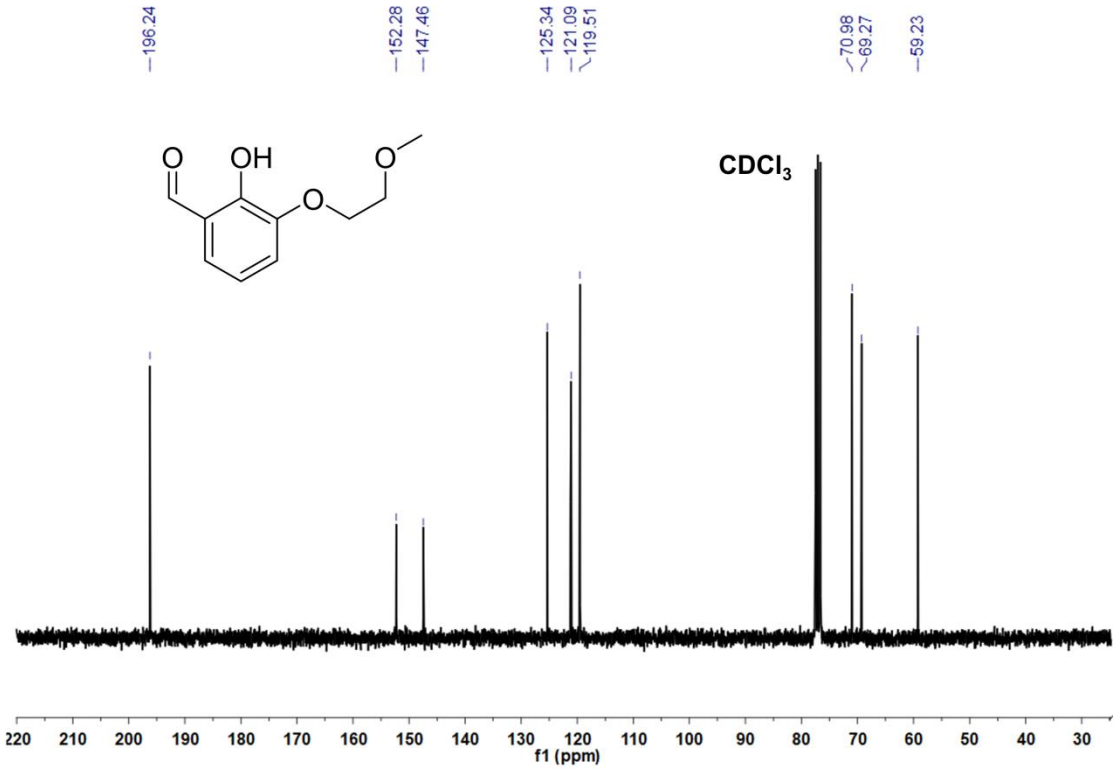

Figure A.15. The ^{13}C NMR spectrum of **4.1** in $CDCl_3$.

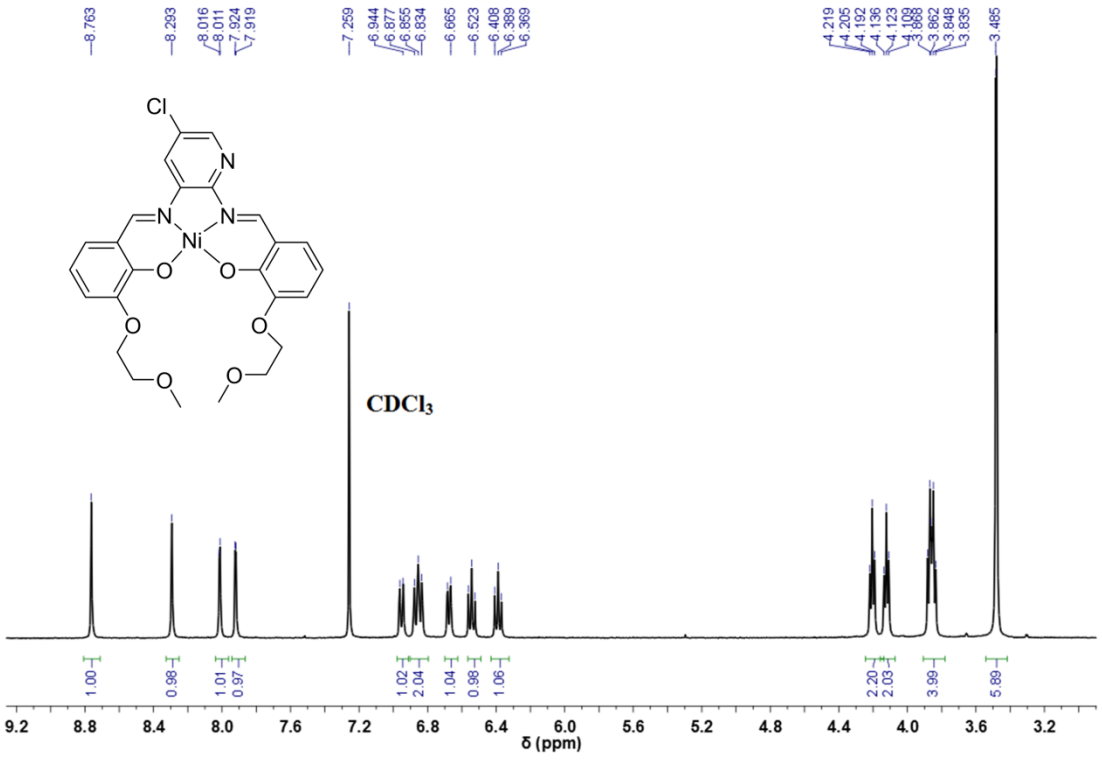

Figure A.16. The ^{1}H NMR spectrum of **4.2** in $CDCl_3$.

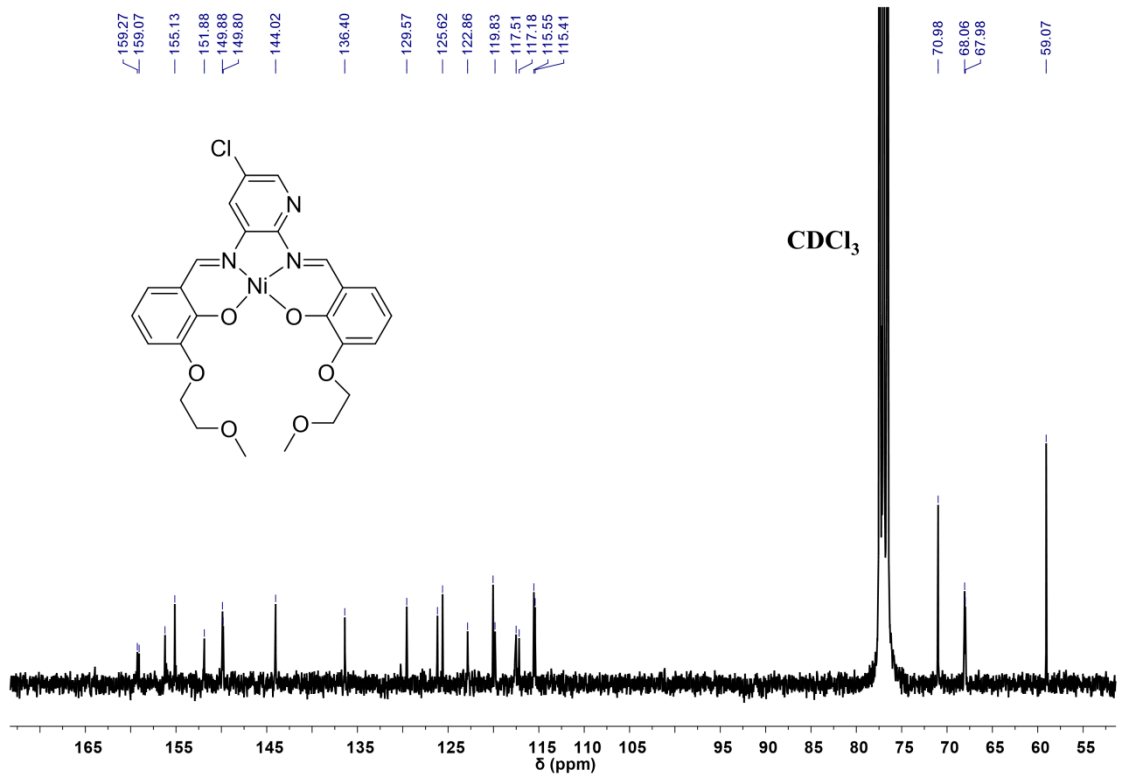

Figure A.17. The ^{13}C NMR spectrum of **4.2** in $CDCl_3$.

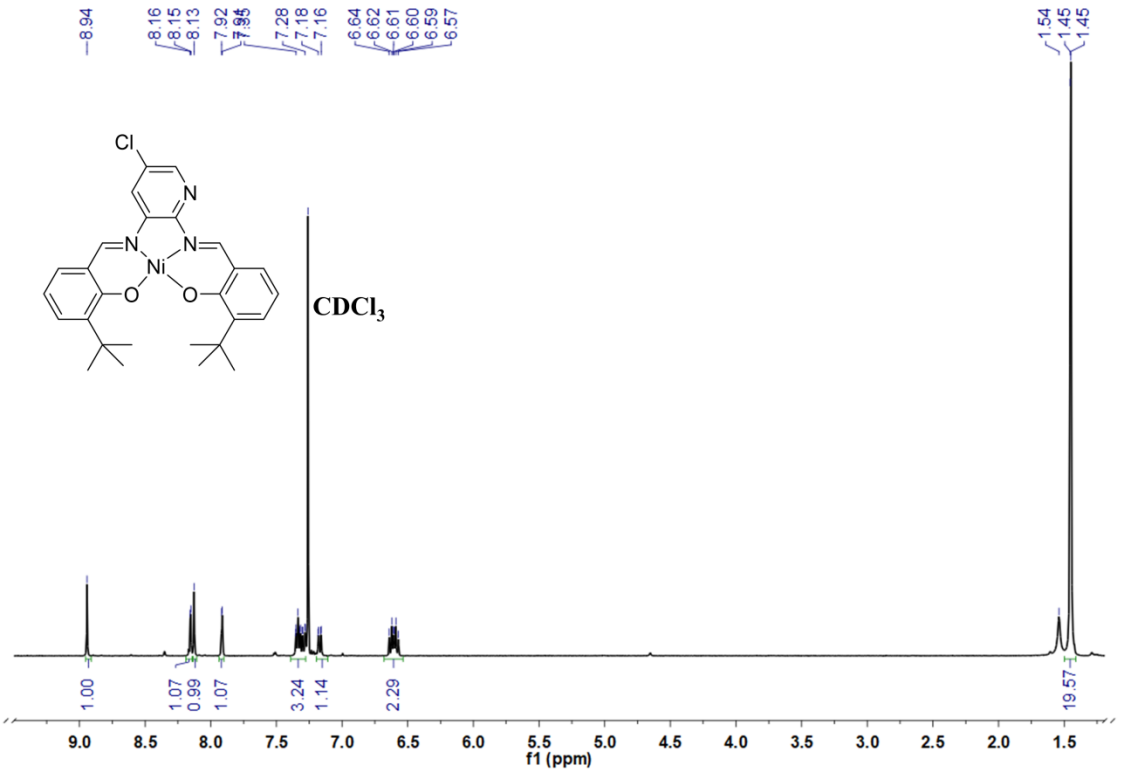

Figure A.18. The ^{1}H NMR spectrum of **4.3** in $CDCl_3$.

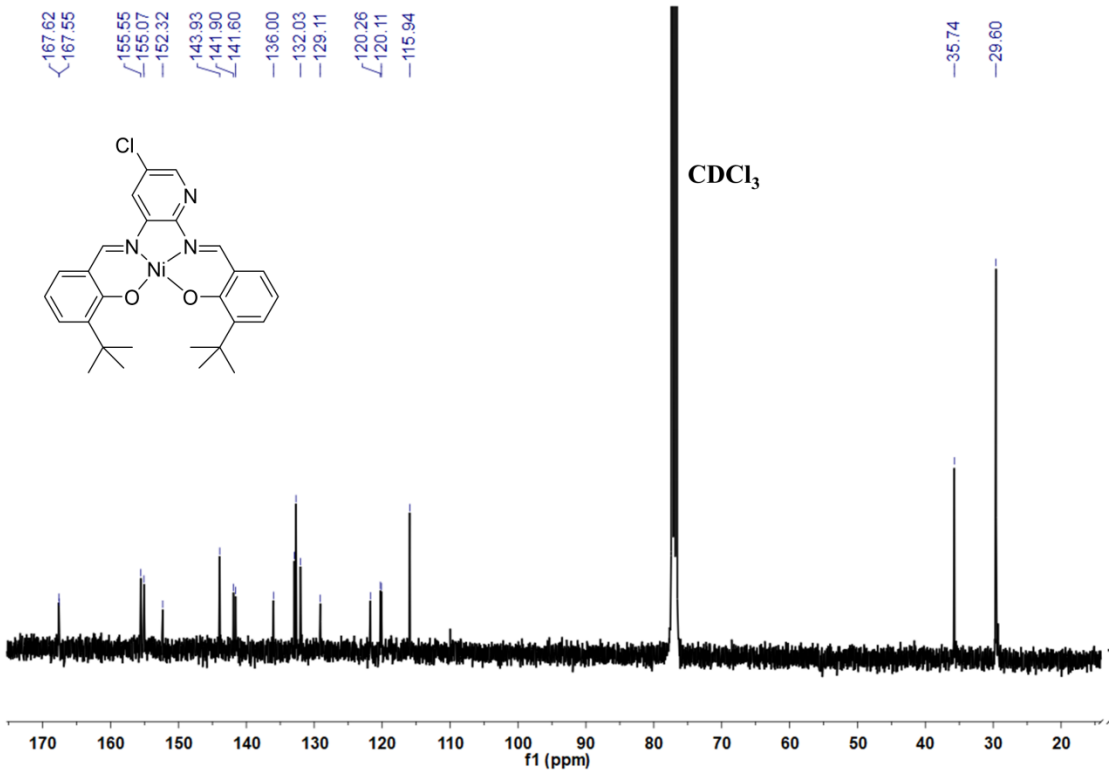

Figure A.19. The ^{13}C NMR spectrum of **4.3** in $CDCl_3$

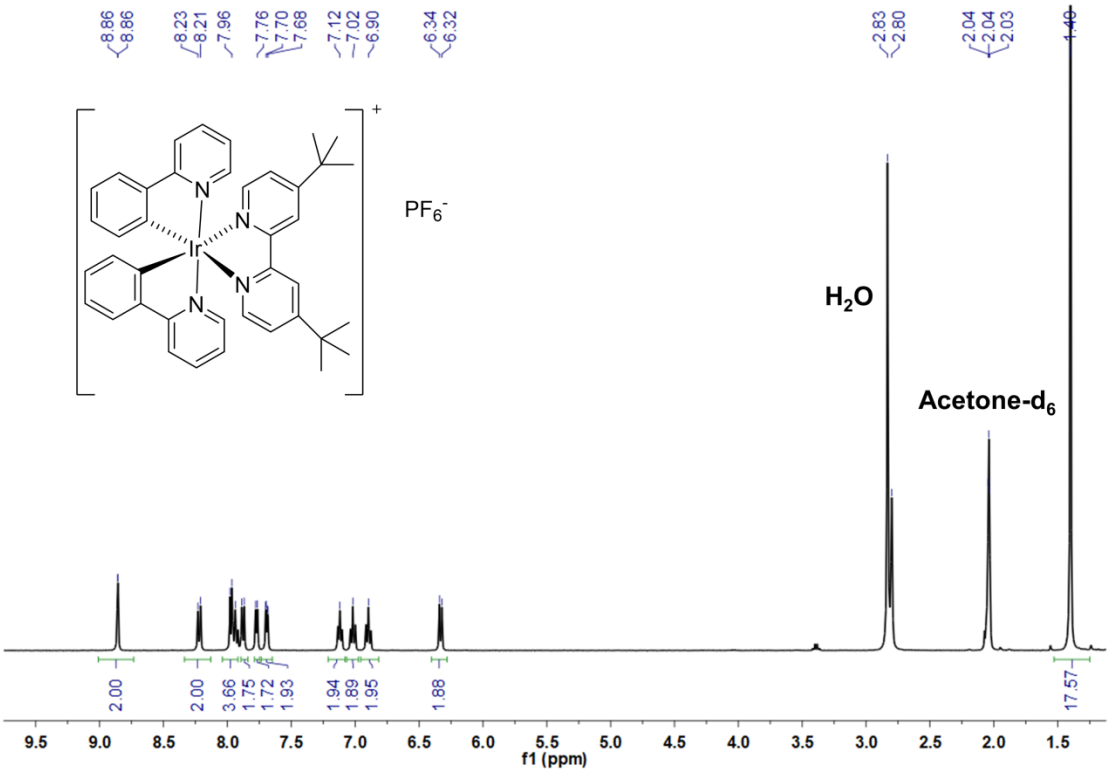

Figure A.20. The ^{1}H NMR spectrum of $[Ir]^{+}$ in acetone-d_6.

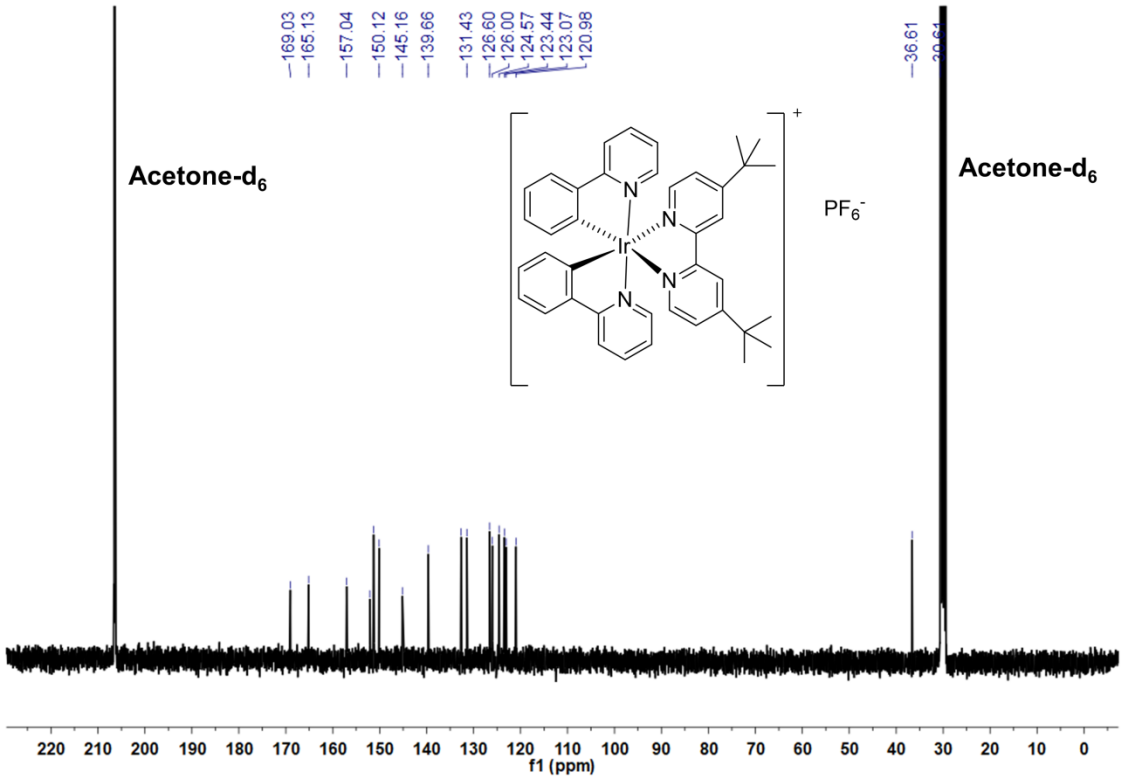

Figure A.21. The ^{13}C NMR spectrum of $[Ir]^+$ in acetone-d_6.

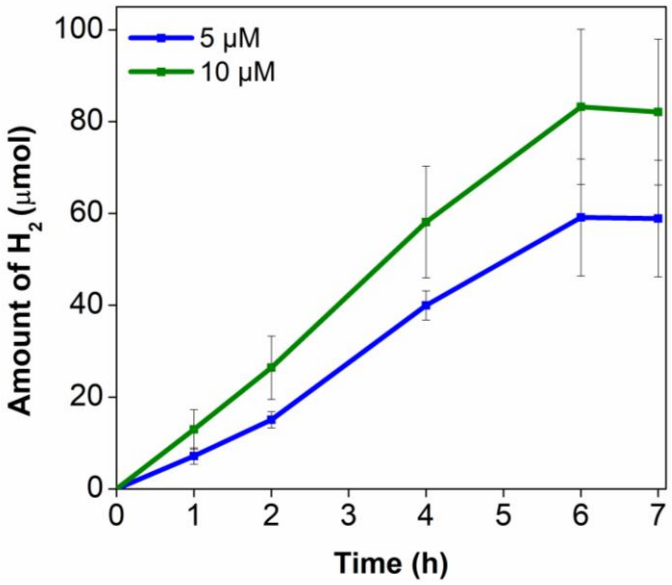

Figure A.22. The (a) amount in μmol of H_2 produced with **[4.2]** = 5.0 μM (blue), and 10 μM (green) in a methanol (5% H_2O) solution containing 0.10 mM of $[Ir]^+$ and 0.10 M TEA under 6 h of visible light irradiation

Table A1. Sample and X-ray crystallographic data of **3.10**.

Identification code	shs102
Chemical formula	$C_{28}H_{54}CoN_5O_6$
Formula weight	615.69 g/mol
Temperature	153(2) K
Wavelength	0.71073 Å
Crystal size	0.040 x 0.180 x 0.400 mm
Crystal habit	red plate
Crystal system	monoclinic
Space group	P 1 21/m 1
Unit cell dimensions	a = 11.6287(8) α = 90°
	b = 11.4553(8) β = 112.652(2)°
	c = 13.1234(9) γ = 90°
Volume	1613.32(19) Å^3
Z	2
Density (calculated)	1.267 g/cm^3
Absorption coefficient	0.578 mm^{-1}
F(000)	664
Theta range for data collection	2.67 to 29.15°
Index ranges	-10<=h<=15, -15<=k<=15, -17<=l<=17
Reflections collected	25507
Independent reflection	4543 [R(int) = 0.0880]
Coverage of independe reflections	99.7%
Absorption correction	multi-scan
Max. and min. transmission	0.9770 and 0.8020
Refinement method	Full-matrix least-squares on F2
Refinement program	SHELXL-2014/6 (Sheldrick, 2014)
Function minimized	Σ w(Fo2 - Fc2)2
Data/restraints/parameters	4543 / 0 / 220
Goodness-of-fit on F2	1.029
Δ/σ_{max}	0.001
Final R indices	3084 data; I>2σ R1 = 0.0504, wR2 = 0.1175
	all data R1 = 0.0935, wR2 = 0.1382
Weighting schen	w=1/[$\sigma^2(F_o^2)$+(0.0643P)^2+0.6065P] where P=(F_o^2+2F_c^2)/3
Largest diff. pea and hole	1.473 and -0.688 eÅ^{-3}
R.M.S. deviation from mean	0.104 eÅ^{-3}

Table A2. Crystal and structure refinement data of **4.2**.

Identification code	shs292m5_sq	
Empirical formula	C100 H100 Cl4 N12 Ni4 O28	
Formula weight	2294.55	
Temperature	100(2) K	
Wavelength	0.71073 Å	
Crystal system	Triclinic	
Space group	P-1	
Unit cell dimensions	a = 9.2016(13) Å	a= 113.693(4)°.
	b = 21.742(3) Å	b= 91.995(5)°.
	c = 26.419(4) Å	g = 90.139(5)°.
Volume	4836.2(12) $Å^3$	
Z	2	
Density (calculated)	1.576 Mg/m^3	
Absorption coefficient	0.966 mm^{-1}	
F(000)	2376	
Crystal size	0.140 x 0.120 x 0.080 mm^3	
Theta range for data collection	2.296 to 26.722°.	
Index ranges	-11<=h<=11, -27<=k<=27, -33<=l<=33	
Reflections collected	19769	
Independent reflections	19769 [R(int) = 0.1144]	
Completeness to theta = 25.242°	99.8 %	
Absorption correction	None	
Refinement method	Full-matrix least-squares on F2	
Data / restraints / parameters	19769 / 2904 / 1419	
Goodness-of-fit on F2	1.024	
Final R indices [I>2sigma(I)]	R1 = 0.1144, wR2 = 0.3137	
R indices (all data)	R1 = 0.1617, wR2 = 0.3581	
Extinction coefficient	0.0069(8)	
Largest diff. peak and hole	1.760 and -1.456 $e.Å^{-3}$	

Magnetic susceptibility by the Evans method

The Evans method is used to determine the spin-only magnetic moment for a sample and provide an estimate of the number of unpaired electrons present. In a typical experiment, the difference in the NMR chemical shift caused by the presence of paramagnetic species in solution is measured. It is summarized in the following equation:

$\chi_M = 3\Delta f/4\pi fm + \chi_0 + \chi_0(d_0 - d_s)/m$

- χ_M: mass susceptibility in $cm^3\ g^{-1}$
- Δf: observed frequency difference in Hz
- f: 400 MHz on Bruker AV 400 NMR spectrometer
- m: mass of paramagnetic substance in $g\ mL^{-1}$
- χ_0: mass susceptibility of solvent in $cm^3\ g^{-1}$
- d_0: density of solvent in $g\ cm^{-3}$
- d_s: density of solute in $g\ cm^{-3}$

Since d_s is not applicable,

$$\chi_M = 3\Delta f/4\pi fm + \chi_0$$

$$\mu_{eff} = \sqrt{(8\,\chi_M T)}$$

In our experiment, 5.0 mg of **8** was dissolved in 0.50 mL solvent and used for a ^{1}H NMR spectroscopic measurement. A 400 MHz NMR spectrometer was used. A peak separation of 0.281 ppm was observed, which was then introduced into the equations above to give a χ_M of 3.55×10^{-3} and hence a μ_{eff} of 2.91 μ_B. This μ_{eff} value is close to the expected spin-only magnetic moment of an $S = 1$ complex, which has 2 unpaired electrons.

Table A3. Summary of the data used for the calculations of the magnetic susceptibility *via* the Evans method.

	8	**acetonitrile**
Mass (g)	5.0 mg	0.39
MW (g/mol)	474.2	N.A.
n (mol)	1.05×10^{-5}	N.A.
Density (g/mol)	N.A.	0.79
Volume (mL)	N.A.	0.50
Concentration (mol/ mL)	2.10×10^{-5}	
NMR shift		
δ (ppm)	2.245	1.964
Δ (ppm)	0.281	

Computational Methods

All calculations were performed with the Gaussian 09 (Rev. E.01) program. Geometry optimization was conducted using the M06 functional. The Def2-SVP basis set was employed for all atoms. The vibrational analysis and thermodynamic information at 298.15 K were calculated with the keyword Freq in Gaussian. The PCM solvent model was used in the geometry optimizations for all calculations. The TD-DFT calculations were performed on the optimized geometry of **2** by using PBE0 functional (Gaussian Keyword: PBE1PBE) and the def2-TZVP basis set. The calculated 467 nm transition can likely be correlated with the experimental absorption band maximum around 488 nm. The nature of this excitation is a HOMO (Orbital 144) to LUMO (Orbital 145) transition, which is a local excitation (MLCT) process from the nickel and the phenoxy fragments to the pyridine motif, as observed from the frontier MO shapes.

Table A4. Geometry-optimized XYZ coordinates of **2.**

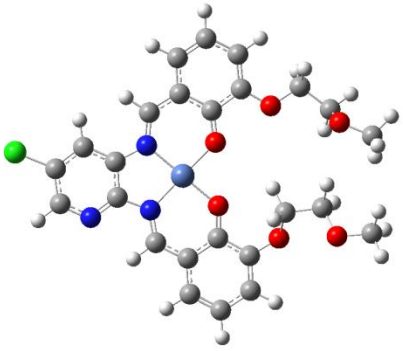

Compound **2:**

Ni	-0.953336	-0.133100	-0.172433
C	-3.627743	0.343500	0.110777
C	-4.904975	0.884645	0.245809
H	-5.084319	1.959892	0.316746
C	-5.981546	0.004144	0.286951
C	-5.764671	-1.373842	0.195767
H	-6.616507	-2.063244	0.229472

C	-3.514843	-1.058279	0.024157
C	-2.333727	2.329233	0.131533
H	-3.267659	2.894851	0.267556
C	-1.155353	3.106221	0.063773
C	-1.274070	4.522843	0.169051
H	-2.269690	4.954712	0.311541
C	-0.165622	5.319238	0.088054
H	-0.247725	6.406043	0.164852
C	1.109936	4.731892	-0.101562
H	1.980574	5.388115	-0.165907
C	1.267369	3.364607	-0.200422
C	0.122257	2.487921	-0.122006
C	3.584976	3.535769	-0.622544
H	3.778722	4.209856	0.235113
H	3.420702	4.169073	-1.516268
C	4.794533	2.674635	-0.836755
H	4.574688	1.881924	-1.584244
H	5.589294	3.315989	-1.271991
C	6.528444	1.626983	0.306066
H	6.634398	0.832922	-0.460921
H	6.794066	1.201464	1.285215
H	7.255485	2.427531	0.062943
C	-1.948062	-2.803920	-0.177515
H	-2.816792	-3.478039	-0.128689
C	-0.664047	-3.384316	-0.294697
C	-0.547242	-4.800683	-0.343380
H	-1.461823	-5.400289	-0.292862
C	0.683405	-5.399615	-0.448864
H	0.776478	-6.487591	-0.485569
C	1.842394	-4.592386	-0.491710
H	2.838681	-5.040693	-0.555495
C	1.770607	-3.215992	-0.455032
C	0.499976	-2.554048	-0.377392

C	3.160494	-1.502113	0.442770
H	2.773007	-1.848067	1.420977
H	2.653199	-0.554550	0.195256
C	4.637340	-1.281112	0.539315
H	5.040125	-1.032625	-0.468945
H	4.819265	-0.391355	1.179620
C	6.644555	-2.271117	1.167838
H	7.121379	-2.074881	0.185384
H	7.066501	-3.200207	1.577610
H	6.918690	-1.435270	1.844054
N	-2.407829	1.025544	0.044560
N	-2.197357	-1.520856	-0.110031
O	0.307442	1.228069	-0.227855
O	0.478951	-1.273594	-0.392438
O	2.450339	2.737202	-0.382278
O	5.223203	2.121459	0.375692
O	2.912515	-2.490210	-0.548434
O	5.263180	-2.419272	1.056375
N	-4.547060	-1.882463	0.066804
Cl	-7.598997	0.608303	0.448527

Table A5. Geometry-optimized XYZ coordinates of TEA.

TEA: 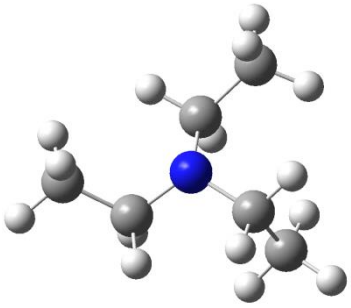			
C	0.254577	1.119711	-0.471671
H	-0.619265	1.777793	-0.620929
H	0.539656	0.781578	-1.498387
C	-1.360192	-0.643760	-0.163978
H	-1.258414	-0.879743	-1.250797
H	-1.458360	-1.620634	0.342914
C	0.889904	-0.926220	0.709723
H	1.654407	-0.388720	1.298917
H	0.458372	-1.667838	1.406351
C	1.558896	-1.650468	-0.449418
H	2.080371	-0.953805	-1.127050
H	2.308631	-2.367660	-0.079681
H	0.828918	-2.217704	-1.051233
C	-2.631107	0.151958	0.060516
H	-2.634502	1.105559	-0.491529
H	-3.511869	-0.417275	-0.275787
H	-2.757365	0.383471	1.130558
C	1.378929	1.938659	0.125574
H	2.337800	1.395377	0.140666
H	1.537588	2.858749	-0.457341
H	1.139026	2.227525	1.162399
N	-0.170147	0.006293	0.358064

Table A6. Geometry-optimized XYZ coordinates of TEA^+

TEA^+:	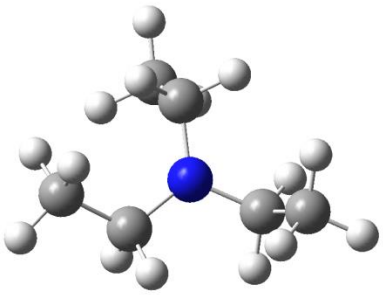		
C	-0.528065	-1.236787	-0.498237
H	0.236907	-2.035922	-0.496180
H	-0.778731	-1.108031	-1.575121
C	1.494600	0.192706	-0.592382
H	1.613598	-0.364998	-1.534379
H	1.608008	1.268793	-0.803714
C	-0.491783	1.017165	0.656141
H	-1.120822	0.552077	1.429768
H	0.299868	1.596734	1.156141
C	-1.326358	1.919121	-0.251982
H	-2.128452	1.356694	-0.752278
H	-1.784577	2.704374	0.364613
H	-0.699429	2.398639	-1.017920
C	2.516791	-0.263683	0.442595
H	2.421518	-1.340187	0.646698
H	3.523721	-0.073351	0.046857
H	2.405670	0.289553	1.386625
C	-1.741712	-1.610841	0.310133
H	-2.549105	-0.868298	0.231360
H	-2.134984	-2.561440	-0.074657
H	-1.492210	-1.758618	1.371677
N	0.148311	-0.023158	-0.111014

Table A7. Geometry-optimized XYZ coordinates of **Int 1**

	Int 1: 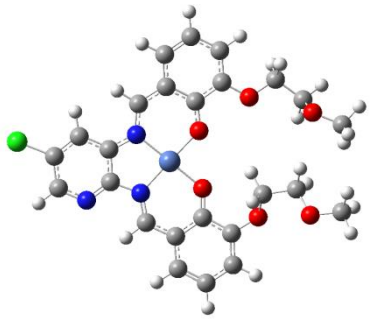		
Ni	-0.971527	-0.130914	-0.165852
C	-3.615599	0.354572	0.085187
C	-4.918148	0.896168	0.199426
H	-5.098463	1.971007	0.269882
C	-5.987914	0.014891	0.209433
C	-5.794875	-1.369424	0.113336
H	-6.652400	-2.051975	0.123031
C	-3.533805	-1.066346	-0.005661
C	-2.345939	2.359794	0.202360
H	-3.274739	2.911509	0.401369
C	-1.152346	3.119919	0.144667
C	-1.226617	4.530609	0.317776
H	-2.211566	4.978491	0.494614
C	-0.100078	5.322350	0.259470
H	-0.175106	6.406325	0.389650
C	1.157217	4.736689	0.027006
H	2.043256	5.373426	-0.017636
C	1.265776	3.355497	-0.135674
C	0.121667	2.504231	-0.087423
C	3.571728	3.514470	-0.654097
H	3.827269	4.181115	0.194606
H	3.366578	4.162981	-1.529856
C	4.765803	2.653314	-0.946970
H	4.498400	1.861061	-1.679596

H	5.535313	3.292484	-1.428972
C	6.562481	1.587910	0.076436
H	6.607689	0.788592	-0.691511
H	6.892967	1.165243	1.036946
H	7.279082	2.379378	-0.222434
C	-1.956315	-2.815306	-0.148953
H	-2.821064	-3.495078	-0.096838
C	-0.663547	-3.395299	-0.243750
C	-0.540457	-4.809307	-0.258924
H	-1.454303	-5.410362	-0.199228
C	0.693121	-5.412590	-0.344550
H	0.785515	-6.501634	-0.355117
C	1.849194	-4.605901	-0.402478
H	2.848052	-5.050811	-0.452337
C	1.767803	-3.227663	-0.399014
C	0.497951	-2.563828	-0.340953
C	3.160093	-1.505098	0.474708
H	2.799431	-1.854046	1.462697
H	2.628844	-0.568600	0.235203
C	4.635298	-1.260551	0.539895
H	5.012417	-1.017477	-0.479517
H	4.822903	-0.362658	1.167141
C	6.667956	-2.220854	1.137595
H	7.122818	-2.008314	0.148028
H	7.111116	-3.147656	1.530121
H	6.944614	-1.387921	1.816536
N	-2.430137	1.015822	0.050378
N	-2.213464	-1.534646	-0.108210
O	0.285202	1.224533	-0.260311
O	0.471046	-1.283036	-0.384556
O	2.454587	2.720966	-0.360912

O	5.271418	2.095397	0.234683
O	2.911975	-2.500901	-0.506179
O	5.287450	-2.387399	1.051970
N	-4.567594	-1.880322	0.006940
Cl	-7.617272	0.629328	0.339569

Table A8. Geometry-optimized XYZ coordinates of **Int 2.**

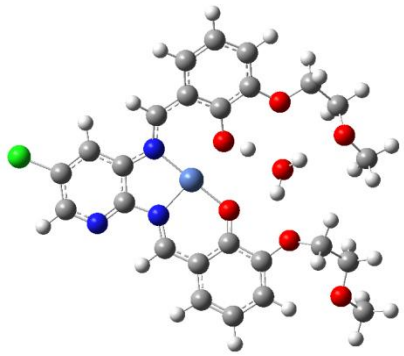

Int 2:

Ni	-1.003596	-0.158926	-0.052569
C	-3.703290	-0.308312	-0.167394
C	-5.081360	-0.086054	-0.312311
H	-5.496137	0.919774	-0.413234
C	-5.916845	-1.196287	-0.361671
C	-5.393174	-2.489964	-0.263841
H	-6.061521	-3.357694	-0.303806
C	-3.282845	-1.658991	-0.070873
C	-2.960346	1.893184	0.265512
H	-3.972028	2.128858	0.629634
C	-2.009715	2.946908	0.335271
C	-2.442346	4.224613	0.784349
H	-3.503107	4.352802	1.021948
C	-1.566757	5.278348	0.923703
H	-1.929073	6.250474	1.268889
C	-0.205679	5.114185	0.628461
H	0.487899	5.949688	0.743357
C	0.249318	3.871181	0.193155
C	-0.634430	2.789595	0.040503
C	2.511837	4.601196	-0.092064
H	2.704075	4.928880	0.949629
H	2.194144	5.488730	-0.674350
C	3.762147	4.034745	-0.701174

H	3.529173	3.653415	-1.718311
H	4.520712	4.838431	-0.808161
C	5.350903	2.349144	-0.470632
H	5.060616	1.816496	-1.398605
H	5.740144	1.617922	0.253883
H	6.165278	3.059914	-0.712928
C	-1.346525	-2.960667	0.302363
H	-2.031857	-3.819291	0.388994
C	0.048730	-3.204709	0.416142
C	0.491720	-4.524139	0.696406
H	-0.262774	-5.307923	0.821064
C	1.829068	-4.814630	0.805167
H	2.164816	-5.832885	1.015773
C	2.782523	-3.789391	0.622873
H	3.853047	-4.011129	0.654717
C	2.380398	-2.498324	0.358176
C	0.995346	-2.147702	0.250208
C	4.439927	-1.346846	0.870864
H	4.423667	-1.995828	1.766192
H	4.519250	-0.299613	1.220316
C	5.642127	-1.659152	0.021253
H	5.561850	-1.090414	-0.931802
H	6.557067	-1.291863	0.540128
C	6.759745	-3.374786	-1.088583
H	6.641260	-2.899923	-2.083361
H	6.751274	-4.465680	-1.221104
H	7.750342	-3.077974	-0.686892
N	-2.704250	0.628731	-0.107528
N	-1.893528	-1.796501	0.092379
O	-0.164118	1.584370	-0.384150
O	0.694331	-0.922977	0.001263

O	1.537023	3.599015	-0.127800
O	4.254598	2.998337	0.106255
O	3.233954	-1.452800	0.156049
O	5.724825	-3.028081	-0.222573
N	-4.087737	-2.698741	-0.123865
Cl	-7.631038	-0.986686	-0.557233
H	2.356026	0.185825	-0.582640
O	2.346950	1.113089	-0.891293
H	0.832822	1.534236	-0.602758
H	2.846617	1.627458	-0.235769

Table A9. Geometry-optimized XYZ coordinates of **TS 1.**

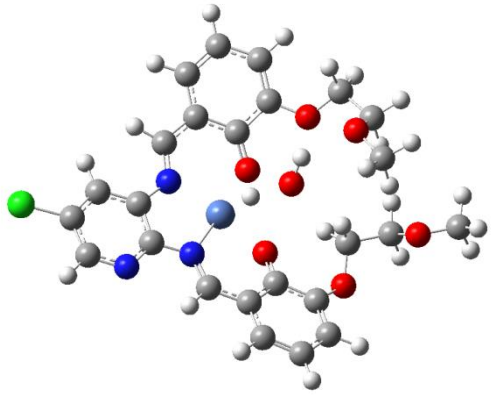

TS 1:

Ni	-0.808357	-0.196211	-0.614277
C	-3.559259	0.077509	-0.099365
C	-4.892976	0.473594	0.001468
H	-5.206097	1.500665	-0.204763
C	-5.846194	-0.471038	0.365772
C	-5.450386	-1.785897	0.622621
H	-6.200232	-2.532831	0.912199
C	-3.259376	-1.291982	0.165132
C	-2.532786	2.190050	-0.476437
H	-3.498393	2.699727	-0.295142
C	-1.416912	3.067604	-0.622793
C	-1.643277	4.461386	-0.448217
H	-2.678383	4.817632	-0.402475
C	-0.600746	5.340459	-0.300179
H	-0.784074	6.410279	-0.175307
C	0.724929	4.848480	-0.252335
H	1.549929	5.542475	-0.065773
C	0.976674	3.504559	-0.421388
C	-0.074380	2.578110	-0.751741
C	3.184224	3.549664	0.481324
H	2.725775	4.149004	1.292880
H	3.790724	4.234103	-0.143064

C	4.055966	2.492027	1.097074
H	4.392747	1.774518	0.315922
H	4.967929	2.960984	1.523432
C	4.046770	0.742985	2.647293
H	4.363024	0.022970	1.866765
H	3.389310	0.228255	3.362222
H	4.948519	1.094806	3.185165
C	-1.502380	-2.864832	0.307311
H	-2.232837	-3.571841	0.738926
C	-0.173675	-3.332577	0.135140
C	0.121632	-4.641487	0.611701
H	-0.686575	-5.214409	1.079115
C	1.379947	-5.172179	0.497484
H	1.602192	-6.175816	0.868284
C	2.401038	-4.400005	-0.098134
H	3.420251	-4.786757	-0.192985
C	2.163955	-3.135247	-0.589876
C	0.848700	-2.548401	-0.520322
C	3.383105	-1.109087	-1.034589
H	3.059287	-0.795777	-0.024956
H	2.796250	-0.529591	-1.768278
C	4.844482	-0.801629	-1.178181
H	5.258756	-1.347669	-2.052800
H	4.967364	0.285750	-1.390839
C	6.889931	-0.899045	-0.074475
H	7.374689	-1.461947	-0.898000
H	7.353426	-1.207258	0.874155
H	7.106623	0.179439	-0.236229
N	-2.476051	0.890225	-0.430324
N	-1.929578	-1.664421	0.008989
O	0.249712	1.385584	-1.071989

O	0.655297	-1.400755	-1.043767
O	2.192947	2.911928	-0.282097
O	3.334387	1.823986	2.096589
O	3.189587	-2.497275	-1.207869
O	5.524622	-1.150124	-0.004875
N	-4.188384	-2.170684	0.518459
Cl	-7.519297	-0.027519	0.497690
H	-0.007200	0.038504	0.705431
O	1.278417	0.333838	1.118494
H	1.477984	0.719184	0.231196
H	1.555381	1.045910	1.732474

Table A10. Geometry-optimized XYZ coordinates of **Int 3.**

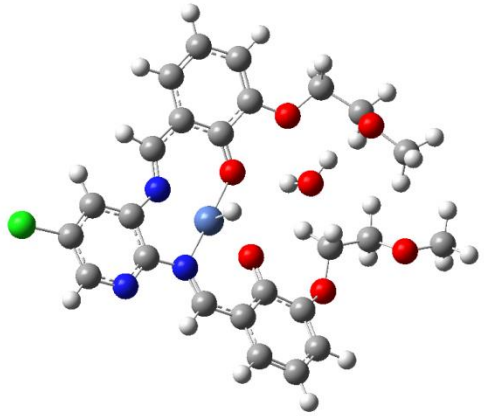

Int 3:

Ni	-0.907266	-0.169357	-0.385418
C	-3.679765	0.188511	-0.081613
C	-5.000213	0.634347	-0.010738
H	-5.262213	1.684086	-0.165687
C	-5.998353	-0.293953	0.257650
C	-5.663785	-1.636948	0.454246
H	-6.451723	-2.369069	0.668399
C	-3.443217	-1.198822	0.117338
C	-2.543239	2.271653	-0.303386
H	-3.493020	2.818941	-0.168809
C	-1.381202	3.095384	-0.388469
C	-1.574290	4.502262	-0.288492
H	-2.599382	4.883284	-0.238442
C	-0.507559	5.362286	-0.242831
H	-0.663022	6.441658	-0.174859
C	0.809629	4.850408	-0.260641
H	1.651461	5.545101	-0.202743
C	1.037125	3.491254	-0.342262
C	-0.054212	2.561926	-0.472203
C	3.392202	3.672264	-0.011624
H	3.193551	4.332497	0.854973
H	3.683200	4.311342	-0.866705

C	4.501014	2.723911	0.338988
H	4.578464	1.939692	-0.444448
H	5.467482	3.266814	0.357742
C	5.153992	1.159573	1.961977
H	5.108025	0.274618	1.295400
H	4.911464	0.835166	2.983813
H	6.189399	1.550740	1.952719
C	-1.750280	-2.847334	0.274895
H	-2.540422	-3.540280	0.609125
C	-0.435436	-3.367080	0.169787
C	-0.234476	-4.714974	0.582930
H	-1.089930	-5.265292	0.988088
C	0.996742	-5.309464	0.477869
H	1.151502	-6.341669	0.801177
C	2.074982	-4.572074	-0.059068
H	3.066807	-5.023142	-0.162313
C	1.927668	-3.269691	-0.489035
C	0.656223	-2.601286	-0.383885
C	3.327597	-1.321136	-0.855479
H	3.051047	-1.008104	0.168756
H	2.788386	-0.651929	-1.548107
C	4.806355	-1.181309	-1.059764
H	5.098390	-1.649453	-2.024806
H	5.063782	-0.101727	-1.141609
C	6.881020	-1.657252	-0.119816
H	7.250686	-2.125851	-1.053579
H	7.354352	-2.161546	0.734774
H	7.204217	-0.595244	-0.124509
N	-2.550898	0.970169	-0.314457
N	-2.115673	-1.619130	0.005158
O	0.240596	1.322679	-0.655683

O	0.550910	-1.400344	-0.805531
O	2.252824	2.904849	-0.322593
O	4.231836	2.150813	1.590855
O	2.987024	-2.680586	-1.092077
O	5.495336	-1.772917	0.005636
N	-4.411965	-2.063238	0.383030
Cl	-7.658780	0.199541	0.347594
H	-0.678530	-0.091532	1.016314
O	1.893682	0.509367	1.572191
H	1.525196	0.658462	0.684602
H	2.584512	1.191991	1.626606

Table A11. Geometry-optimized XYZ coordinates of **Int 3'.**

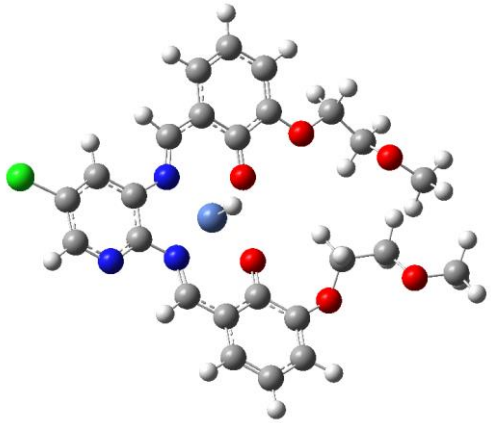

Int 3':

Ni	-0.869913	-0.128226	-0.307020
C	-3.612979	0.367437	0.030793
C	-4.887902	0.914783	0.188505
H	-5.047343	1.992595	0.272961
C	-5.978888	0.055674	0.223167
C	-5.782800	-1.323620	0.106908
H	-6.644776	-2.001330	0.132394
C	-3.518212	-1.046220	-0.084965
C	-2.312400	2.353610	0.210160
H	-3.223992	2.919854	0.467935
C	-1.118807	3.122147	0.193384
C	-1.236196	4.502266	0.533587
H	-2.229271	4.894263	0.776159
C	-0.138323	5.317481	0.559641
H	-0.231194	6.374264	0.821538
C	1.137938	4.790155	0.244588
H	2.001847	5.457858	0.275342
C	1.299042	3.462308	-0.090850
C	0.166278	2.562686	-0.132711
C	3.612027	3.715551	-0.505244
H	3.846169	4.168612	0.478800
H	3.425358	4.542484	-1.218000

C	4.792081	2.919887	-0.977383
H	4.523578	2.356516	-1.896917
H	5.592583	3.635260	-1.261872
C	6.468992	1.470168	-0.292949
H	6.410430	0.864599	-1.220015
H	6.769108	0.810578	0.534565
H	7.260775	2.232199	-0.438518
C	-1.989734	-2.841455	-0.221774
H	-2.852561	-3.519747	-0.107756
C	-0.701832	-3.437470	-0.291899
C	-0.623483	-4.852495	-0.176350
H	-1.558189	-5.416324	-0.088554
C	0.588011	-5.499645	-0.163523
H	0.640972	-6.587473	-0.075762
C	1.776038	-4.740337	-0.233460
H	2.757341	-5.222867	-0.189309
C	1.747596	-3.367002	-0.350858
C	0.500723	-2.658882	-0.439289
C	3.126055	-1.608253	0.463830
H	2.709871	-1.868068	1.457206
H	2.619523	-0.692238	0.115950
C	4.596770	-1.359352	0.585714
H	5.030885	-1.220504	-0.429561
H	4.750073	-0.400795	1.127712
C	6.590958	-2.237827	1.392271
H	7.101088	-2.133393	0.412501
H	7.012245	-3.111210	1.910774
H	6.826424	-1.332168	1.989297
N	-2.413193	1.073672	-0.031815
N	-2.231146	-1.558187	-0.244361
O	0.371695	1.348600	-0.466985

O	0.532760	-1.397480	-0.655194
O	2.478041	2.886720	-0.412913
O	5.242062	2.056939	0.027383
O	2.918933	-2.686913	-0.438739
O	5.217244	-2.422915	1.248300
N	-4.575225	-1.845568	-0.040137
Cl	-7.586560	0.683112	0.401228
H	-0.716508	-0.224133	1.100420

Table A12. Geometry-optimized XYZ coordinates of **Int 4.**

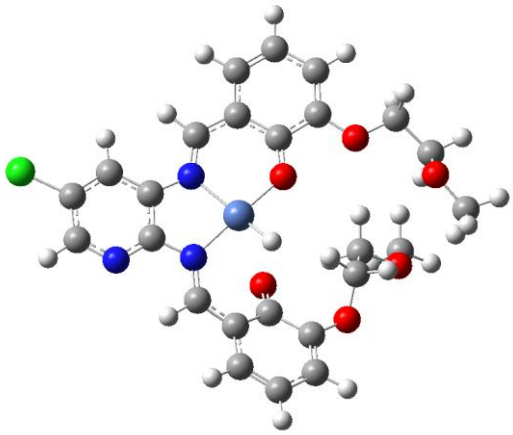

Int 4:

Ni	-0.800591	0.097938	-0.506535
C	-3.397890	-0.653056	0.051810
C	-4.606940	-1.322576	0.222859
H	-4.654689	-2.402561	0.384300
C	-5.783304	-0.577842	0.186769
C	-5.724926	0.801434	-0.010226
H	-6.652437	1.387310	-0.034447
C	-3.437922	0.752915	-0.151724
C	-1.895669	-2.484936	0.160338
H	-2.743068	-3.171087	0.330757
C	-0.617552	-3.106911	0.073246
C	-0.555235	-4.515678	0.270860
H	-1.487905	-5.049588	0.483676
C	0.634598	-5.190247	0.195663
H	0.677485	-6.273274	0.336708
C	1.827733	-4.472281	-0.059769
H	2.772962	-5.018895	-0.105498
C	1.809403	-3.105141	-0.243547
C	0.567756	-2.361441	-0.237919
C	4.169444	-2.956633	-0.503234
H	4.257578	-3.556644	-1.431683

H	4.323540	-3.643748	0.351484
C	5.231374	-1.896993	-0.450140
H	5.145853	-1.336615	0.506476
H	6.226217	-2.393347	-0.438844
C	6.033508	0.021181	-1.471138
H	5.892860	0.623323	-0.550577
H	5.883740	0.670638	-2.346010
H	7.079169	-0.348492	-1.484327
C	-2.115355	2.683871	-0.304256
H	-3.064100	3.227347	-0.456583
C	-0.939646	3.447009	-0.186691
C	-0.948355	4.789097	-0.672704
H	-1.900693	5.208856	-1.019333
C	0.210253	5.514837	-0.770838
H	0.206338	6.535219	-1.163733
C	1.443345	4.899923	-0.408582
H	2.393011	5.426659	-0.555723
C	1.486730	3.640355	0.130394
C	0.263617	2.906190	0.445226
C	2.910099	1.755869	0.021369
H	3.720397	1.782482	-0.733035
H	2.008502	1.337102	-0.456767
C	3.301176	0.855725	1.151626
H	2.549573	0.966435	1.958950
H	3.260788	-0.197496	0.798849
C	4.921385	0.516205	2.792639
H	4.219072	0.755935	3.616482
H	5.933849	0.818860	3.098084
H	4.912563	-0.586239	2.661954
N	-2.116759	-1.206994	0.045320
N	-2.193111	1.364716	-0.279174

O	0.612947	-1.112886	-0.513260
O	0.274906	1.921358	1.203743
O	2.908106	-2.341593	-0.442082
O	5.110901	-1.027724	-1.534382
O	2.682721	3.085934	0.476984
O	4.588238	1.186534	1.617036
N	-4.572898	1.441672	-0.164991
Cl	-7.325124	-1.357735	0.393922
H	0.014121	1.043033	-1.329429

Table A13. Geometry-optimized XYZ coordinates of hydronium.

	Hydronium: 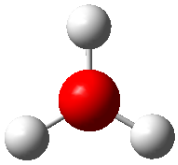		
O	-0.123203	0.852156	0.000000
H	0.847360	0.762974	0.000000
H	-0.531251	1.737280	-0.000000
H	-0.685719	0.056215	0.000000

Table A14. Geometry-optimized XYZ coordinates of H_2O.

	H_2O: 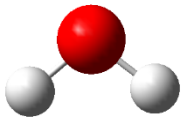		
O	-0.141963	0.825612	0.000000
H	0.820466	0.883599	-0.000000
H	-0.408567	1.752193	0.000000

Table A15. Geometry-optimized XYZ coordinates of H_2.

H_2:			
H	-0.912325	0.308008	0.000000
H	-1.670427	0.308008	-0.000000

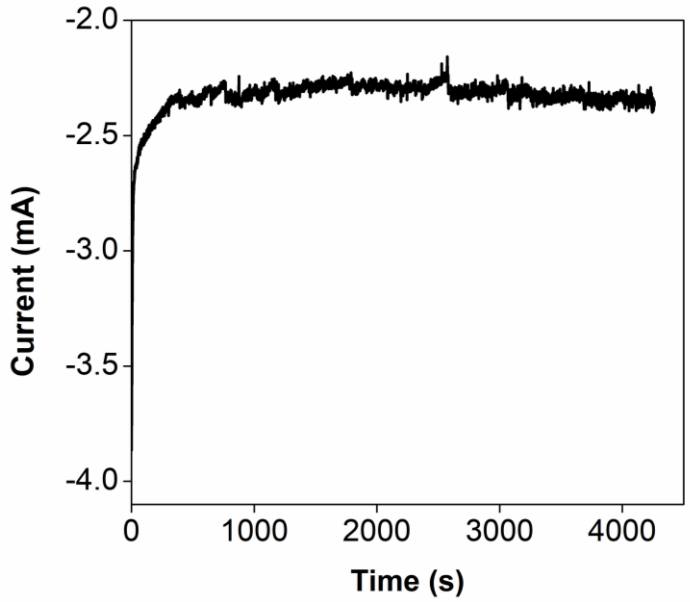

Figure A.23. Plots of current and against time using OD-Cu nano-scrolls as the working electrode in 0.10 M $KHCO_3$ solution saturated with CO_2 gas using a saturated calomel electrode as reference.

`